

BIOPHYSICAL STUDY OF TEAR FILM LIPID LAYER

A DISSERTATION SUBMITTED TO THE GRADUATE DIVISION OF THE
UNIVERSITY OF HAWAI‘I AT MĀNOA IN PARTIAL FULFILLMENT OF
THE REQUIREMENTS FOR THE DEGREE OF

DOCTOR OF PHILOSOPHY

IN

MECHANICAL ENGINEERING

AUGUST 2023

By

Xiaojie Xu

Dissertation Committee:

Yi Zuo, Chairperson

John S. Allen

Joseph J. Brown

Rui Sun

William Uspal

Zhengqing Yun

Acknowledgements

I would like to express my deepest gratitude to my supervisor and chair of my committee, Professor Yi Zuo for the continuous support of my Ph.D. study and related research, and his patience, motivation, and immense knowledge. His guidance helped me in all the time of research and writing of this thesis.

I would like to thank the rest of my committee: Prof. John Allen, Prof. Joseph Brown, Prof. Rui Sun, Prof. William Uspal, and Prof. Zhengqing Yun, for their criticism, insightful comments and encouragement.

I would also like to thank Prof. Yukiko Yamazaki for her support and assistance in my research, and Prof. Igor Butovich for providing me with animal samples. I learned a lot working with them.

I want to thank my labmates, especially Dr. Guangle Li, for the stimulating discussions, for the sleepless nights we were working together before deadlines, and for all the fun we have had in the last five years. My thanks also go to Christopher Kang, who helped me with the MD simulations presented in Chapter 3 of this dissertation.

I also want to thank my family for their enduring support and encouragement.

I would also like to thank National Science Foundation and Hawaii Community Foundation Grant for their financial support.

Finally, for all the people whom I love and who care about me, they deserve my sincere appreciation.

Abstract

Tear film lipid layer (TFLL) is the outmost layer of the tear film. The current consensus is that the 40-nm thick TFLL consists of two sublayers, *i.e.*, a polar lipid layer covering the air-water surface of the cornea, and a nonpolar lipid layer that resides upon the polar lipids and is directly exposed to air. The polar lipids account for 20 mol% of the TFLL, including ~ 12 mol% phospholipids, and ~ 4 mol% (O-acyl)- ω -hydroxy fatty acids (OAHFAs), which belongs to a newly discovered class of endogenous lipids termed fatty acid esters of hydroxy fatty acids (FAHFAs). The nonpolar lipids account for 80 mol% of the TFLL, with wax esters (WEs, accounting for ~ 43 mol%) and cholesteryl esters (CEs, accounting for ~39 mol%) being the most prevalent nonpolar lipid classes. The major physiological function of the TFLL is to stabilize the tear film by reducing surface tension and retarding evaporation of the aqueous layer. Dysfunction of the TFLL leads to dysfunctional tear syndrome, with the dry eye disease (DED) being the most prevalent eye disease affecting 10-30% of the world population. It is estimated that the DED directly and indirectly causes a \$55 billion annual economic burden in the United States alone. To date, except for treatments alleviating the dry eye symptoms, effective therapeutic interventions in treating the DED are still lacking. Therefore, there is an urgent need to better understand the biophysical function of the TFLL and to develop translational solutions in effectively managing the DED. The focus of this dissertation is to study biophysical properties of the TFLL using a newly developed experimental methodology called constrained drop surfactometry (CDS). Main contributions fell into the following four headings: 1. Study of the composition-functional correlations of a model TFLL, under physiologically relevant conditions. For the first time, this study unveiled that the primary biophysical function of FAHFAs is to optimize the interfacial rheological properties of the TFLL. 2. Study of the polymorphism and collapse mechanism of

FAHFA monolayers. This study revealed that FAHFA molecules at the air-water surface demonstrate unique polymorphic behaviors, which can be explained by configurational transitions of the molecules under various lateral pressures. 3. Development of a novel ventilated, closed-chamber, droplet evaporimeter with a constant surface area. This droplet-based evaporimeter is capable of a rigorous control of environmental conditions, including the temperature, relative humidity, airflow rate, surface area, and surface pressure, thus allowing for reproducible water evaporation measurements over a time period of only 5 minutes. The volumetric evaporation rate of this droplet evaporimeter is less than 2.7 $\mu\text{L}/\text{min}$, comparable to the basal tear production of healthy adults. This study demonstrated that the TFL resists water evaporation with a combined mechanism by increasing film compactness of the polar lipid film at the air-water surface, and, to a lesser extent, by increasing film thickness of the nonpolar lipid film. 4. Comparative study of the dynamic surface activity, interfacial rheology, evaporation resistance, and ultrastructure of the meibomian lipid films extracted from wild type (WT) and *Soat1* knockout (KO) mice. Inactivation of *Soat1* gene led to a complete stoppage of CE production in meibomian glands and a severe change in the eye phenotype in experimental animals. Lipidomic analysis with ultrahigh-pressure liquid chromatography – mass spectrometry showed that the pool of cholesterol rose seven times in the KO mice compared with their WT siblings, and, an almost complete ablation of CEs longer than $\text{C}_{18}\text{-C}_{20}$ was observed. This study revealed novel experimental evidence about the composition-structure-functional correlations of the meibomian lipid films. Overall, research in this dissertation advanced the biophysical understanding of the TFL, and provided novel implications in the pathophysiological and translational understanding of DED.

Table of Contents

Acknowledgements	i
Abstract	ii
List of Tables	xi
List of Figures	xii
List of Abbreviations	xvi
Chapter 1 Ocular drug delivery.....	1
1.1 Introduction	1
1.2 Anatomy of the eye	2
1.2.1 Anterior segment	3
1.2.1.1 Cornea.....	3
1.2.1.2 Conjunctiva	4
1.2.1.3 Iris	4
1.2.1.4 Lens.....	4
1.2.1.5 Ciliary body	5
1.2.1.6 Aqueous humor	5
1.2.2 Posterior segment	5
1.2.2.1 Vitreous humor	5
1.2.2.2 Retina	6
1.2.2.3 Choroid	7
1.2.2.4 Sclera.....	7
1.3 Physical barriers for ocular drug delivery	8

1.3.1 Tear film	8
1.3.2 Corneal barrier	10
1.3.3 Conjunctival barrier	11
1.3.4 Blood-aqueous barrier	11
1.3.5 Blood-retinal barrier	12
1.4 Nanomedicine for treating ocular diseases.....	13
1.4.1 Routes for ocular drug delivery	13
1.4.1.1 Topical administration	13
1.4.1.2 Systemic administration.....	14
1.4.1.3 Intravitreal administration.....	14
1.4.1.4 Transscleral administration	15
1.4.2 Nanomedicine formulations	15
1.4.2.1 Nanomicelle	15
1.4.2.2 Liposome.....	16
1.4.2.3 Nanoparticle.....	18
1.4.2.4 Dendrimer	19
1.4.2.5 Nanogel	19
1.4.3 Treatments of anterior segment eye diseases	20
1.4.3.1 Dry eye disease	20
1.4.3.2 Cataract	23
1.4.4 Treatments of posterior segment eye diseases.....	24
1.4.4.1 Glaucoma	25
1.4.4.2 Age-related macular degeneration	27
1.4.4.3 Diabetic retinopathy.....	30

1.5 Ocular nanotoxicology	31
1.5.1 Impact on the ocular surface.....	33
1.5.2 Impact on the lens.....	33
1.5.3 Impact on the retina	33
1.6 Summary and scope of this dissertation.....	35
Chapter 2 Surface tension and interfacial rheology of the tear film lipid layer	36
2.1 Introduction	36
2.2 Materials and methods	40
2.2.2 Constrained drop surfactometry (CDS).....	41
2.2.3 Interfacial dilational rheology	43
2.2.4 Statistical analysis.....	44
2.3 Results	44
2.3.1 Surface activities of the tear lipid films.....	44
2.3.2. Surface rheological properties of the tear lipid films	50
2.4 Discussion	52
2.5 Summary	57
Chapter 3 Polymorphism of fatty acid esters of hydroxy fatty acids	58
3.1 Introduction	58
3.2 Materials and methods	60
3.2.1 Materials	60
3.2.2 Constrained drop surfactometry (CDS).....	61
3.2.3 Atomic force microscopy (AFM).....	61
3.2.4 Molecular dynamics simulations	62

3.3 Results	62
3.3.1 Compression isotherms of the PAHSA film.....	62
3.3.2 Lateral structure and topography of the PAHSA film.....	65
3.3.3 Molecular dynamics simulations of the PAHSA film.....	66
3.4 Discussion	68
3.5 Summary	73
Chapter 4 Effect of the tear film lipid layer on water evaporation.....	74
4.1 Introduction	74
4.2 Material and methods	76
4.2.1 Materials	76
4.2.2 Constrained drop surfactometry (CDS).....	77
4.2.3 Ventilated closed-chamber droplet evaporimeter with a constant surface area	78
4.2.4 Atomic force microscopy (AFM).....	79
4.2.5 Statistical analysis.....	80
4.3 Results and discussion.....	80
4.3.1 Development of a constant-surface-area droplet evaporimeter for study in evaporation retardation by lipid films	80
4.3.2 Effect of the model TFLL on water evaporation	84
4.3.3 Lateral structure and topography of the model TFLL	87
4.4 Summary	90
Chapter 5 Comparative study of meibomian lipids of wild type and <i>Soat1</i> -null mice	91
5.1 Introduction	91

5.2.1 Reagents.....	93
5.2.2 Mouse Meibomian lipids	93
5.2.3 Lipidomic analysis.....	95
5.2.4 Dynamic surface activity	96
5.2.5 Surface dilational rheology.....	96
5.2.6 Evaporation resistance	97
5.2.7 Ultrastructure and film topography	97
5.2.8 Statistical analysis.....	98
5.3 Results	98
5.3.1 Lipidomic characterization of the mouse Meibomian samples	98
5.3.2 Dynamic surface activity of the mouse Meibomian lipid films	98
5.3.3 Interfacial rheology of the mouse Meibomian lipid films	101
5.3.4 Evaporation resistance of the mouse Meibomian lipid films	101
5.3.5 Ultrastructure and topography of the mouse Meibomian lipid films	104
5.4 Discussion	106
5.5 Summary	109
Chapter 6 Adsorbed pulmonary surfactant at physiologically relevant high	
concentrations	110
6.1 Introduction	110
6.2 Materials and methods	113
6.2.1 Pulmonary surfactant.....	113
6.2.2 Constrained drop surfactometry (CDS).....	114
6.2.3 Subphase replacement and Langmuir-Blodgett (LB) transfer.....	115

6.2.4 Atomic force microscopy (AFM).....	115
6.2.5 Statistics.....	116
6.3 Results.....	117
6.3.1 Dynamic surface activity of the adsorbed surfactant film.....	117
6.3.2 Optimization of the subphase replacement for AFM imaging.....	118
6.3.3 Ultrastructure and topography of the adsorbed surfactant film.....	120
6.4 Discussion.....	122
6.4.1 High phospholipid concentration optimizes surface activity of the surfactant film during normal tidal breathing.....	122
6.4.2 Multilayers of the adsorbed surfactant film act as a safety net for deep breathing....	125
6.5 Summary.....	127
Chapter 7 S2 subunit of SARS-CoV-2 spike protein induces domain fusion in natural pulmonary surfactant monolayers.....	129
7.1 Introduction.....	129
7.2 Materials and methods.....	131
7.2.1 Materials.....	131
7.2.2 Constrained Drop Surfactometry (CDS).....	132
7.2.3 Atomic Force Microscopy (AFM).....	134
7.3 Results and discussion.....	135
7.3.1 Effect of the S2 subunit on biophysical properties of the PS film.....	135
7.3.2 Effect of the S2 subunit on quasi-static compression isotherms of the PS monolayer	136
7.3.3 Effect of the S2 subunit on domain fusion of the PS monolayer.....	138

7.3.4 Biological implications.....	141
7.4 Summary	142
Chapter 8 Summary of main contributions and future directions	143
8.1 Summary of main contributions.....	143
8.2 Future directions.....	146
8.2.1 Biophysical studies of Meibomian lipids of healthy donors and dry eye patients	146
8.2.2 Evaporation resistance of tear film lipid layer.....	146
8.2.3 Nanomedicine for ocular drug delivery	147
8.2.4 Nanotoxicity to the eyes	147
List of awards and publications produced during the PhD	148
References	151

List of Tables

Table 1.1 Summary of representative nanomedicine formulations for treating ocular diseases..	17
Table 1.2 Summary of nanomedicine formulations currently studied in clinical trials and/or obtained FDA approval for treating ocular diseases.....	21
Table 1.3 Summary of representative nanotoxicological studies about the eye.	32
Table 2.1 Lipids studied in the biophysical simulations of the tear lipid films.	41

List of Figures

Figure 1.1 Anatomy of the human eye.....	2
Figure 1.2 Physical barriers for ocular drug delivery, including the tear film, corneal barrier, conjunctival barrier, blood-aqueous barrier, and blood-retinal barrier.....	7
Figure 1.3 Structure and composition of the tear film.....	9
Figure 1.4 Commonly used routes for ocular drug administration, including topical administration, systemic administration, intravitreal administration, and transscleral administration.....	13
Figure 1.5 Nanomedicine formulations studied for ocular drug delivery, including nanomicelle, liposome, nanoparticle, dendrimer, and nanogel.....	16
Figure 1.6 Nanomedicine formulations for treating dry eye disease.....	22
Figure 1.7 Nanomedicine formulations for treating glaucoma.....	27
Figure 1.8 Nanomedicine formulations for treating age-related macular degeneration.....	29
Figure 1.9 Adverse effects of silver (Ag) and gold (Au) nanoparticles (NPs) on mouse retina..	34
Figure 2.1 Schematics of (a) the tear film and (b) the constrained drop surfactometry (CDS) for biophysical simulations of the tear film lipid layer (TFLL)..	37
Figure 2.2 Effect of temperature and compression rate on the surface activity of tear lipid films (TLFs).....	45
Figure 2.3 Effect of subphase composition on the surface activity of tear lipid films (TLFs)....	47
Figure 2.4 Statistical analysis of the surface activity of tear lipid films (TLFs).....	49
Figure 2.5 Interfacial dilational rheological properties of tear lipid films (TLFs)..	51
Figure 3.1 Compression isotherms of the PAHSA monolayer under four experimental conditions, i.e., 20 °C and a low compression rate of 0.15 A%/s, 20 °C and a high compression rate of 15 A%/s, 34 °C and 0.15 A%/s, and 34 °C and 15 A%/s.....	63

Figure 3.2 Lateral structure and topography of the PAHSA film at three characteristic surface pressures, i.e., 10, 20, and 25 mN/m, each under four experimental conditions..	64
Figure 3.3 Atomistic molecular dynamics simulations of the PAHSA monolayer at the air-water surface.	67
Figure 3.4 Cartoons of the compressed PAHSA monolayer at three characteristic surface pressures, i.e., 10, 20, and 25 mN/m, each under four experimental conditions.	71
Figure 4.1 Schematic of a ventilated, closed-chamber, droplet evaporimeter with a constant surface area for studying evaporation resistance of the tear film lipid layer (TFLL).	78
Figure 4.2 Typical experimental results for water evaporation determined within 5 min using the new droplet evaporimeter.	81
Figure 4.3 Superimposed compression isotherm of a DPPC monolayer at 34 °C, and the corresponding evaporation resistance at various surface pressures. Surface pressure 0 indicates a pure lipid-free air-water surface.	82
Figure 4.4 Effects of lipid films on water evaporation.	85
Figure 4.5 AFM topography and lateral structure of lipid films at various surface pressures.	89
Figure 5.1 Schematics of the constrained drop surfactometer (CDS) as a versatile biophysical model for studying mouse MLFs.	94
Figure 5.2 Ultrahigh-pressure liquid chromatography-mass spectrometry (UHPLC-MS) lipidomic characterization of the meibomian samples extracted from wild-type (WT) and Soat1-knockout (KO) mice.	99
Figure 5.3 Dynamic surface activity of the MLFs of the WT and KO mice at 34 °C.	100
Figure 5.4 Interfacial dilational rheological properties of the MLFs of the WT and KO mice.	102

Figure 5.5 Effects of the MLFs of the WT (a) and KO (b) mice, under various surface pressures, on water evaporation.....	103
Figure 5.6 Ultrastructure and topography of the MLFs of the WT (a-c) and KO (d-f) mice at three characteristic surface pressures, i.e., 20, 30, and 40 mN/m.....	105
Figure 6.1 Schematic of the constrained drop surfactometry (CDS).....	116
Figure 6.2 Dynamic surface activity of the Infasurf film adsorbed from a series of phospholipid concentrations, i.e., 1, 10, 20, and 35 mg/mL.....	117
Figure 6.3 Ultrastructure and topography of the Infasurf film after de novo adsorption from a phospholipid concentration of 10 mg/mL.....	119
Figure 6.4 Ultrastructure and topography of the Infasurf film after de novo adsorption from phospholipid concentrations of 1 mg/mL (A), 10 mg/mL (B), 20 mg/mL (C), and 35 mg/mL (D).	121
Figure 6.5 Maximum height (nm), area fraction (%), and the area-averaged equivalent number of bilayers of the multilayer structures of the Infasurf film adsorbed from various subphase concentrations from 1 to 35 mg/mL.....	124
Figure 7.1 (A) Primary structure of the SARS-CoV-2 S protein. It is composed of the S1 and S2 subunits. (B) Cryo-EM structures of the S2 subunit from the Protein Data Bank ID 6VXX. (C) Schematic of the constrained drop surfactometry (CDS) for studying biophysical interactions between the S2 subunit and natural pulmonary surfactant.	133
Figure 7.2 Effect of the S2 subunit (0.15 mol% and 0.75 mol%) on the biophysical properties of 1 mg/mL Infasurf, with various compression ratios (CRs).....	136
Figure 7.3 Effect of the S2 subunit on the quasi-static compression isotherms of spread Infasurf monolayers.....	137

Figure 7.4 Lateral structure and topography of Infasurf with/without the addition of the S2 subunit, under two environmental temperatures of 20 °C and 37 °C, respectively..... 138

Figure 7.5 Quantification results for the Infasurf monolayer coverage of tilted-condensed (TC) microdomains and nanodomains at surface pressure 30 mN/m..... 140

List of Abbreviations

AFM	atomic force microscopy
ARDS	acute respiratory syndrome
BO	behenyl oleate
CDS	constrained drop surfactometry
CE	cholesteryl ester
CL-ADSA	closed-loop axisymmetric drop shape analysis
CO	cholesteryl oleate
CR	compression ratio
DED	dry eye disease
DPPC	dipalmitoyl phosphatidylcholine
FAHFA	fatty acid esters of hydroxy fatty acid
KO	knockout
LB	Langmuir-Blodgett
LE	liquid-expanded
MD	molecular dynamics
MGD	Meibomian gland dysfunction
ML	Meibomian lipids
OAHFA	(O-acyl)- ω -hydroxy fatty acid
PAHSA	palmitic acid-9-hydroxy stearic acid
PBS	phosphate buffered saline
PS	pulmonary surfactant
TC	tilted-condensed
TFL	tear film lipid layer
WE	wax ester
WT	wild type

Chapter 1 Ocular drug delivery ¹

1.1 Introduction

The eyes are one of the most important and complex sensory organs of the body. They act as a gateway to collect external images and transmit them to the brain as signals through the optic nerve. Genetic or acquired disorders in different compartments of the eye lead to various ocular diseases that can cause mild to severe symptoms from burning and itching, to visual impairment or even blindness. So far, pharmaceutical interventions for ocular diseases have demonstrated rather limited efficacy, mostly due to difficulties for drugs to cross the physiological and biological barriers of the eye. Nanotechnology provides new opportunities for the development of drug delivery systems particularly adapted to overcoming the eye-associated barriers. To date, a number of nanomedicine formulations, such as nanomicelles, liposomes, nanoparticles, dendrimers, and nanogels, have demonstrated the capacity of reducing the degradation of labile drugs and increasing the residence time and bioavailability of drugs in various ocular tissues. This chapter introduces these commonly studied nanomedicine formulations for treating various ocular diseases, including dry eye, cataracts, glaucoma, age-related macular degeneration, and diabetic retinopathy. Emerging toxicological studies about nanoparticle interactions with the ocular surface and tissues will also be briefly discussed.

¹ Xu X, Zuo YY (2023) Nanomedicine for ocular drug delivery. In: Gu N (ed) *Nanomedicine*. pp. 755-786, Series of Micro/Nano Technologies, Springer, Singapore.

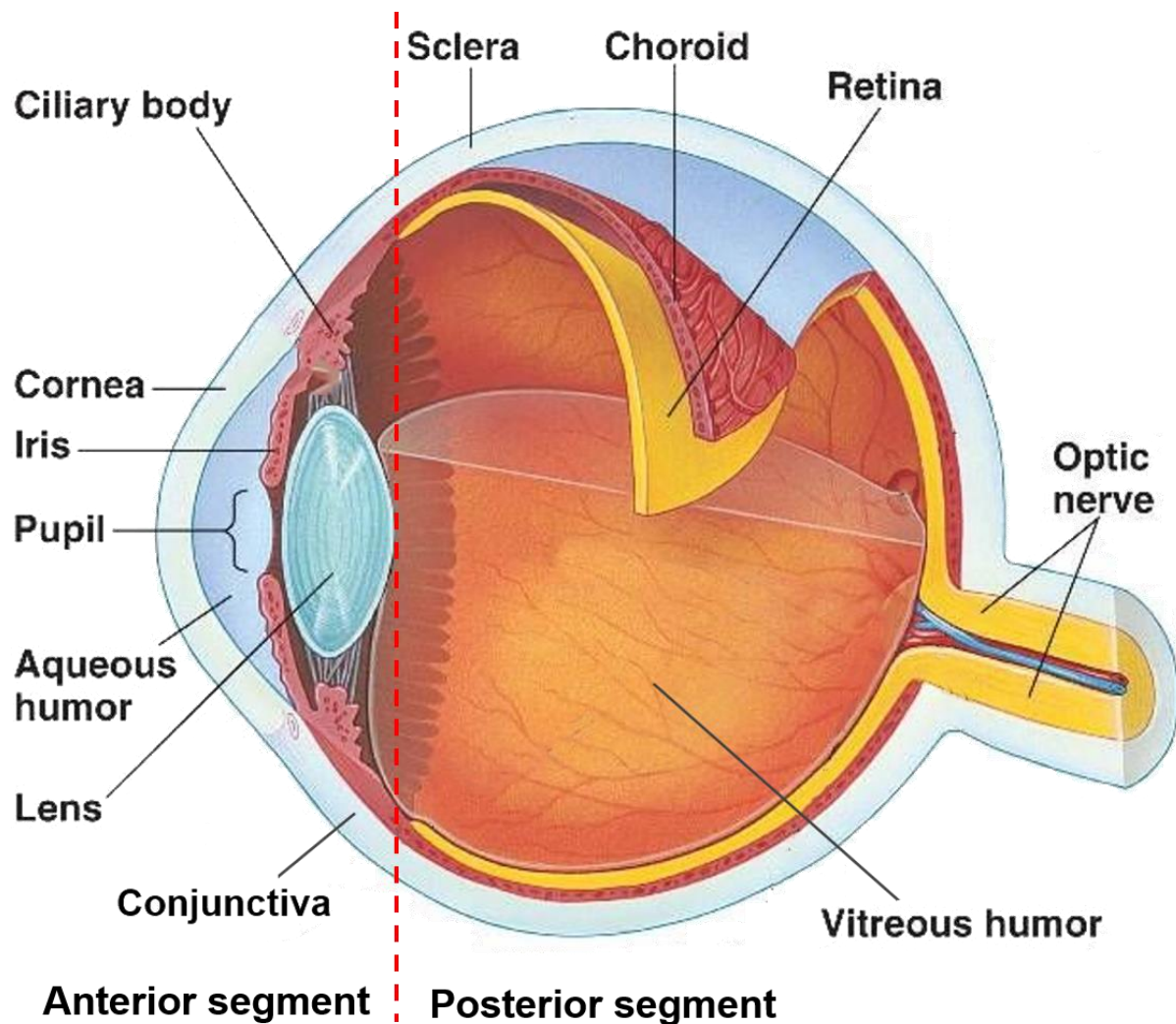


Figure 1.1 Anatomy of the human eye. The eye can be broadly divided into two segments: the anterior segment that occupies the front third of the eye, and the posterior segment that occupies the remaining two-thirds of the eye. The anterior segment is composed of the cornea, conjunctiva, iris, lens, ciliary body, and aqueous humor. The posterior segment comprises the vitreous humor, retina, choroid, sclera, and optic nerve.

1.2 Anatomy of the eye

The eyes are one of the most important and complex sensory organs of the body. They act as a gateway to collect external images and transmit them to the brain as signals through the optic nerve.

As shown in **Figure 1.1**, the eye can be broadly divided into two segments: the anterior segment

that occupies the front third of the eye, and the posterior segment that occupies the remaining two-thirds of the eye (1). The anterior segment is composed of the cornea, conjunctiva, iris, lens, ciliary body, and aqueous humor. The posterior segment comprises the vitreous humor, retina, choroid, sclera, and optic nerve. This section introduces the detailed anatomy of the eye.

1.2.1 Anterior segment

1.2.1.1 Cornea

Cornea is a transparent structure, with an average thickness of approximately 540 μm , which covers the front portion of the eye. It is made up of proteins and cells that do not rely on blood vessels to provide nutrients. The main function of cornea is to refract or bend light, thus focusing most of the light that enters the eye. The cornea comprises five layers: the epithelium, Bowman's layer, the stroma, Descemet's membrane, and the endothelium. The front layer, i.e., corneal epithelium, prevents foreign matters from entering the eye and absorbs nutrients and oxygen from tears and the aqueous humor in the anterior chamber. Bowman's layer is a tough layer composed of collagen (mainly type I collagen fibrils), laminin, nidogen, and perlecan that protects the corneal stroma. The stroma is a thick, transparent middle layer, accounting for more than 90% thickness of the cornea. It consists of regularly arranged collagen fibers along with sparsely distributed interconnected keratocytes that are cells for general repair and maintenance. Descemet's membrane is a dense and cell-free basement membrane that anchors the epithelium or endothelium to connective tissues. The corneal endothelium is a simple squamous monolayer responsible for regulating fluid and solute transport between the aqueous humor and the stromal compartment. Unlike the corneal epithelium, the endothelium cannot be regenerated if it were damaged.

1.2.1.2 Conjunctiva

Conjunctiva is a clear, thin membrane that covers a part of the front surface of the eye and the inner surface of the eyelids. Unlike the cornea, the conjunctiva has many small blood vessels that supply nutrients to the eye and eyelids. It also contains special cells that secrete a component of the tear film to help prevent dry eye. The conjunctiva has two continuous segments: the bulbar conjunctiva, covering the anterior part of the sclera, and the palpebral conjunctiva, also called tarsal conjunctiva, covering the inner surface of both upper and lower eyelids. The primary functions of the conjunctiva are to keep the front surface of the eye and the inner surface of the eyelids moist and lubricated, and to protect the eye from dust and pathogens.

1.2.1.3 Iris

Iris is a thin circular structure with an aperture in the center, i.e., the pupil, acting as a diaphragm that regulates the amount of light entering the eye. The iris, with a diameter in the general range of 11-13 mm, roughly consists of two layers: a pigmented fibrovascular layer known as the stroma and a second layer of pigmented epithelial cells. The color of iris is established genetically, and it depends on the pigments in the iris. The iris separates the space between the cornea and the lens into two chambers: the anterior chamber between the cornea and the iris, and the posterior chamber between the iris and the lens.

1.2.1.4 Lens

Lens is a transparent and biconvex structure that resides behind the iris with the support of the ciliary body's zonular fibers. It is made up of unusual, elongated cells that have no blood supply but obtain nutrients from the surrounding fluids, mainly the aqueous humor that bathes the front of the lens. The lens of adult humans is approximately 10 mm in diameter and 4 mm in thickness. The main function of the lens is to focus light rays onto the retina. The shape of the lens can be

altered by relaxation and contraction of the ciliary muscles surrounding it, thus enabling the eye to focus clearly on objects at widely varying distances.

1.2.1.5 Ciliary body

Ciliary body is a heavily muscled ring of tissue with an extensive capillary bed that is anterior to the lens. The ciliary body includes two main functional areas: the ciliary muscle that controls the shape of the lens, and the ciliary epithelium that produces the aqueous humor. The ciliary body is part of the uvea, i.e., the layer of tissue that delivers oxygen and nutrients to the eye tissues. The ciliary body joins the ora serrata of the choroid to the root of the iris.

1.2.1.6 Aqueous humor

Aqueous humor is a transparent water-like fluid similar to plasma, filling the space between the cornea and the lens. 99.9% of the aqueous humor is water, while the other 0.1% consists of sugars, vitamins, proteins and other nutrients. The aqueous humor is produced in the non-pigmented portion of the ciliary body at a rate of about 2 $\mu\text{L}/\text{min}$. It nourishes the cornea and lens, and gives the eye its shape by maintaining the intraocular pressure.

1.2.2 Posterior segment

1.2.2.1 Vitreous humor

Vitreous humor, also known as vitreous body, is a clear, avascular, and elastic colloidal gel that fills the space between the lens and the retina. It supports the retina and maintains the intraocular pressure. The vitreous humor is mainly composed of collagen fibers and acidic mucopolysaccharides, with its nutrients coming from the choroid and the aqueous humor. The volume of vitreous humor in adult humans is about 3-4 mL/eye, accounting for four-fifths of the eye's volume. Different from the aqueous humor, the metabolism of the vitreous humor is so low

that it has no ability to regenerate. Loss, liquefaction, or degeneration of the vitreous humor not only affects its transparency, but could also lead to retinal detachment.

1.2.2.2 Retina

Retina is a thin layer of tissue that lines the back of the eye. The main function of retina is to receive light that the lens has focused, convert the light into neural signals, and send these signals to the brain for visual recognition. The retina is composed of ten distinct layers. From the vitreous humor to the choroid, these layers are the following: 1) Internal limiting membrane that represents the structural boundary between the vitreous and the retina; 2) nerve fiber layer that contains the axons of ganglion cells; 3) ganglion cell layer that contains nuclei of ganglion cells. The photosensitive ganglion cell is important for entrainment of circadian rhythms and reflexive responses such as the pupillary light reflex; 4) inner plexiform layer; 5) inner nuclear layer; 6) outer plexiform layer; 7) outer nuclear layer; 8) external limiting membrane that separates the inner photoreceptors from supporting cells; 9) photoreceptor layer that comprises two types of photoreceptors: rods and cones. Rods function mainly in dim light and provide the black-and-white vision. Cones function in well-lit conditions and are responsible for the perception of colors, as well as the high-acuity vision used for tasks such as reading. In each human retina, there are 110–125 million rods and 6.3–6.8 million cones. When light hits the photoreceptor, it is absorbed by the light-sensitive photopigment, transformed into electrical impulses, and further relayed to the brain via the optic nerve; and 10) retinal pigment epithelium that supplies the photoreceptors with nutrients. The retinal pigment epithelium contains granules of melanin pigment that enhance visual acuity by absorbing light not captured by the photoreceptor cells, thus reducing glare. Another important function of the retinal pigment epithelium is to store and synthesize vitamin A, which is essential for the production of visual pigments.

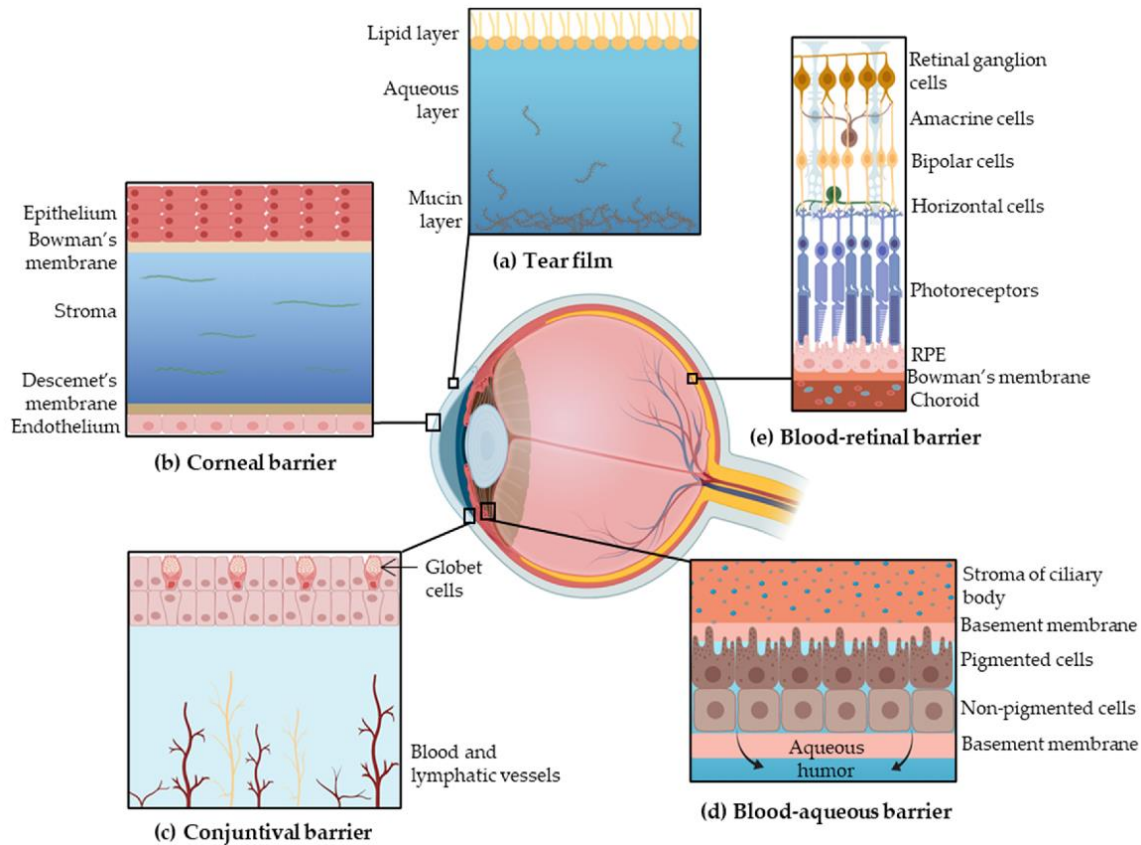


Figure 1.2 Physical barriers for ocular drug delivery, including the tear film, corneal barrier, conjunctival barrier, blood-aqueous barrier, and blood-retinal barrier. (Reproduced with permission from Ref. (2). Copyright 2022 MDPI)

1.2.2.3 Choroid

Choroid lies between retina and sclera. It is primarily composed of a dense capillary plexus, as well as small arteries and veins. As it contains numerous blood vessels and cells, the choroid supplies most necessary nutrients and oxygen to the back of the eye.

1.2.2.4 Sclera

Sclera is the white part of the eye, which occupies about 80% of the external surface of the eye. It is an opaque and elastic layer that is mainly composed of collagen fibers. The sclera is avascular, with nutrients coming from anterior vessels and the choroid. The main function of sclera is to

maintain the globe shape of the eye to resist external forces and injury.

1.3 Physical barriers for ocular drug delivery

Drugs administered topically or systemically to the eye must cross several physiological and biological barriers. As shown in **Figure 1.2**, the main barriers for ocular drug delivery include the tear film, the corneal barrier, the conjunctival barrier, the blood-aqueous barrier, and the blood-retina barrier (2).

1.3.1 Tear film

Tear film is a multilayered biological barrier that protects our eyes from potential risks of the environment. It is rapidly reorganized and spread as a continuous layer over the ocular surface following the upward movement of the eyelid during a blink. The tear film of healthy adults has a thickness of 6-10 μm and should be able to maintain its integrity during the 6-s interblink period. As shown in Figure 1.3, the tear film is composed of three consecutive layers: the inner mucin layer, the intermediate aqueous layer, and the outermost lipid layer. The mucin layer mainly consists of viscous, high molecular-weight sugar-rich glycosylated proteins that function as lubricants to facilitate spreading of the tear film on the ocular surface. The aqueous layer, representing the largest portion of the tear film with a thickness of approximately 4 μm , is made of solutions of electrolytes, peptides, and proteins, such as lipocalin, lysozyme, and lactoferrin. These proteins not only contribute to wound healing and anti-inflammatory processes, but also interact with the lipid layer to affect its stabilization and organization. The lipid layer, commonly known as the tear film lipid layer (TFLL), is approximately 40 nm thick. It is generally believed that the TFLL consists of two sublayers: a polar lipid layer adjacent to the aqueous layer, and a nonpolar lipid layer that resides upon the polar lipids and is directly exposed to air (3). The polar lipids account for 20 mol% of the TFLL, with phospholipids being the most abundant lipid class

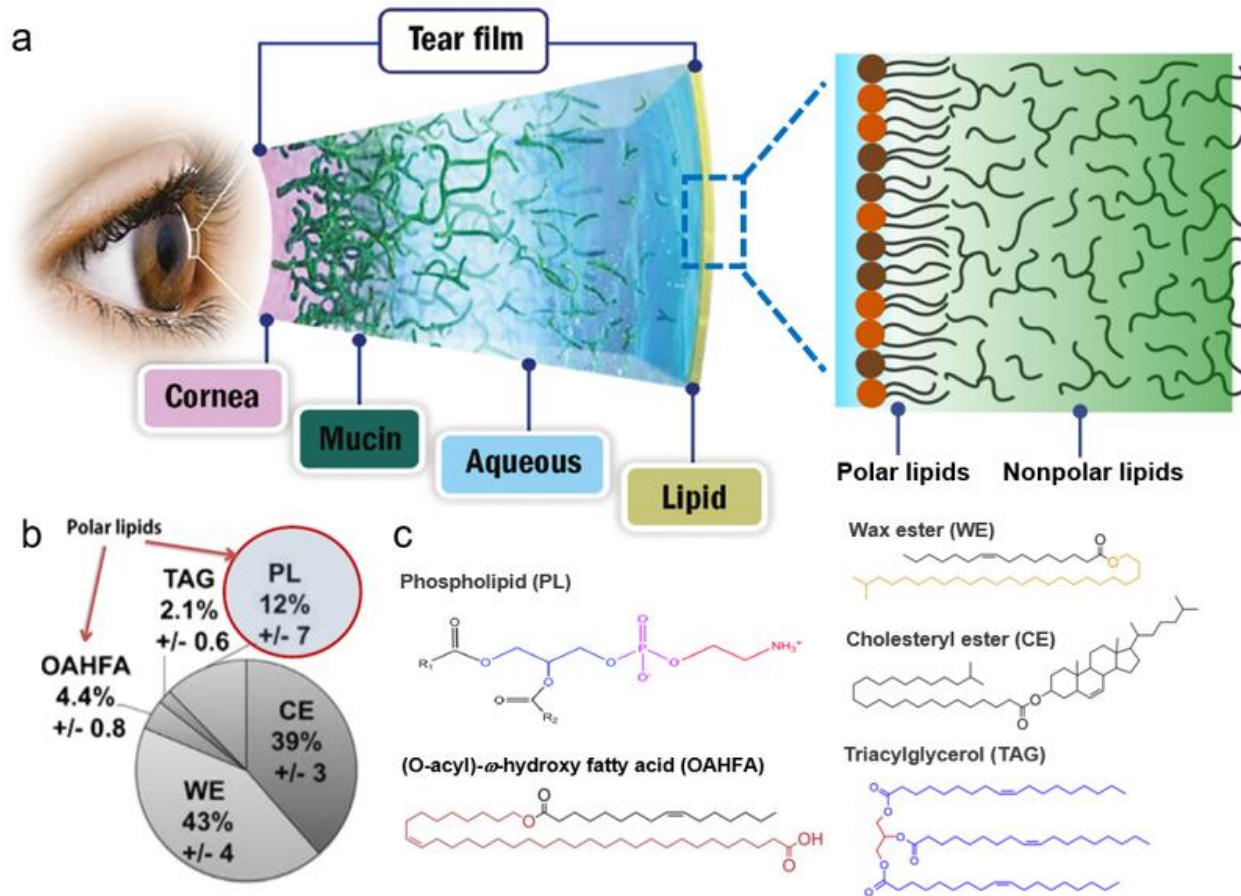


Figure 1.3 Structure and composition of the tear film. (a) The tear film is composed of three layers: the inner mucin layer, the intermediate aqueous layer, and the outmost lipid layer that consists of two sublayers, i.e., the polar lipid layer and nonpolar lipid layer. (b) Chemical composition of the tear film lipid layer: 20% polar lipids, including phospholipids (PL) and (O-acyl)- ω -hydroxy fatty acids (OAHFA), and 80% nonpolar lipids, including wax esters (WE), cholesteryl esters (CE), and a small amount of triacylglycerol (TAG). (c) Chemical structures of major tear film lipids. (Reproduced with permission from Ref. (3). Copyright 2016 Elsevier)

(~12 mol%) in human tears, and a new class of polar lipids, (O-acyl)- ω -hydroxy fatty acids (OAHFAs), accounting for ~4 mol% of the TFL (4). The nonpolar lipids account for 80 mol% of the TFL, with wax esters (WEs, i.e., esters of a fatty acid and a fatty alcohol, accounting for ~43 mol%) and cholesteryl esters (CEs, i.e., esters of a fatty acid and a cholesterol, accounting for ~39 mol%) being the most prevalent nonpolar lipid classes, and a small amount of triacylglycerol (5). The TFL plays a key biophysical role in stabilizing the tear film by decreasing surface tension,

optimizing interfacial rheology, and retarding evaporation of the aqueous layer (6, 7). The TFLL also provides antimicrobial activities and serves as a barrier against environmental particles and pathogens.

Being the outermost layer of the eye, the tear film represents the initial physical barrier for topically administered drugs to the eye. Tears are characterized by a high turnover rate with a restoration time of 2-3 min, thus limiting the ocular residence time for a drug (usually 5-6 min before drugs being completely washed away) and consequently minimizing the time period during which the drug can penetrate the ocular tissues. Reflex stimulation by some ophthalmic drugs with low pH may increase lachrymation by 100-fold, which would dramatically decrease the bioavailability of drugs. Another factor that makes tear film a barrier for ocular drug delivery is that tears contain proteins and mucins. With approximately 2-3 mL mucus secreted daily, mucin in the tear film has a protective role by forming a hydrophilic gel layer that moves over the glycocalyx of the ocular surface and clears cell debris, particles, and pathogens, as well as drugs. Mucin may bind with drug molecules, thereby reducing the effective concentration of drugs in contact with the cornea. Furthermore, tears contain buffering systems in the form of carbonic acid and weak organic acids. Due to their considerable volume compared to the volume of topically administered drugs, tears may modify the degree of ionization (pKa) of a drug, and thus its bioavailability (8).

1.3.2 Corneal barrier

As introduced in section “Cornea”, the cornea is composed of five layers of alternating polarities: the epithelium, Bowman’s layer, the stroma, Descemet’s membrane, and the endothelium. The sandwich-like structure of the cornea makes it an effective barrier not only to microorganisms but also to most hydrophilic and lipophilic drugs. On the one hand, the corneal

epithelium consists of five to six layers of cells closely packed and connected with tight junctions. The high lipid contents of the epithelium and the endothelium make them crucial barriers to hydrophilic molecules. The presence of tight junctions between the corneal epithelial cells retards paracellular drug permeation, thus limiting corneal permeability to hydrophilic and ionized molecules. On the other hand, the corneal stroma, which is constituted by an extracellular matrix consisting of a lamellar arrangement of collagen fibrils, is characterized by a high water content that makes this layer impermeable to lipophilic molecules. Furthermore, both the corneal epithelium and stroma represent a barrier to macromolecules, only allowing molecules smaller than 50 kDa to diffuse into the stroma (9).

1.3.3 Conjunctival barrier

Drugs can be absorbed into the anterior segment through the conjunctival/scleral route. As introduced in section “Conjunctiva”, the conjunctiva is a vascularized tissue that lines the inside of the eyelids and covers the sclera. The external epithelial cells of conjunctiva form junctions that limit paracellular drug penetration. Conjunctiva is a major rate-limiting barrier for hydrophilic drugs due to rapid drug elimination by the conjunctival blood and lymphatic flow. Therefore, only hydrophobic drugs with low molecular weights are able to cross the conjunctiva (10). Once surviving conjunctival clearance, drugs can penetrate to the sclera, in which they have a higher permeability than in cornea.

1.3.4 Blood-aqueous barrier

The blood-aqueous barrier (BAB) is an anterior barrier of the eye for systemically administrated drugs. The BAB is composed of the nonpigmented cell layer of the ciliary body epithelium and endothelial cells of blood vessels in the iris. As introduced in section “Ciliary Body,” the ciliary body epithelium is responsible for secretion of aqueous humor into the posterior chamber of the

eye. The ciliary body extends posteriorly from the iris root to the retina, forming a ring around the globe of the eye. The ciliary body is a bilayer comprised of two distinct cell layers: a pigmented cell layer and a nonpigmented cell layer. The pigmented and nonpigmented cells are coupled via gap junctions. The pigmented cells contact the choroidal blood supply, whereas the basolateral membrane of the nonpigmented epithelium contacts the aqueous humor. Tight junctions are present in the nonpigmented epithelial cells, but not in the pigmented cells. Thus, the physical barrier to drugs across the ciliary body is mostly due to the nonpigmented epithelium.

1.3.5 Blood-retinal barrier

The blood-retinal barrier (BRB) is an important posterior barrier of the eye for systemically administered drugs. Presence of the BRB is essential for the structural and functional integrity of the retina. Functions of the BRB are to regulate fluids and molecular movement between the ocular vascular beds and retinal tissues, and to prevent leakage of macromolecules and other potentially harmful agents into the retina. Under disease conditions where BRB breakdown occurs, vision can be seriously compromised. The BRB consists of an inner barrier (iBRB) and an outer barrier (oBRB). The iBRB is established by the tight junctions, also known as zonulae occludentes, between neighboring retinal endothelial cells. These specialized junctions restrict the diffusional permeability of the retinal endothelial layer to values in the order of 0.14×10^{-5} cm/s for sodium fluorescein that is used as a fluorescent tracer in ophthalmology and optometry. The oBRB is established by the tight junctions between neighboring retinal pigment epithelial cells. The retinal pigment epithelium separates the neural retina from the fenestrated choriocapillaris and plays a fundamental role in regulating nutrients from the blood to photoreceptors as well as eliminating waste products and maintaining retinal adhesion (11).

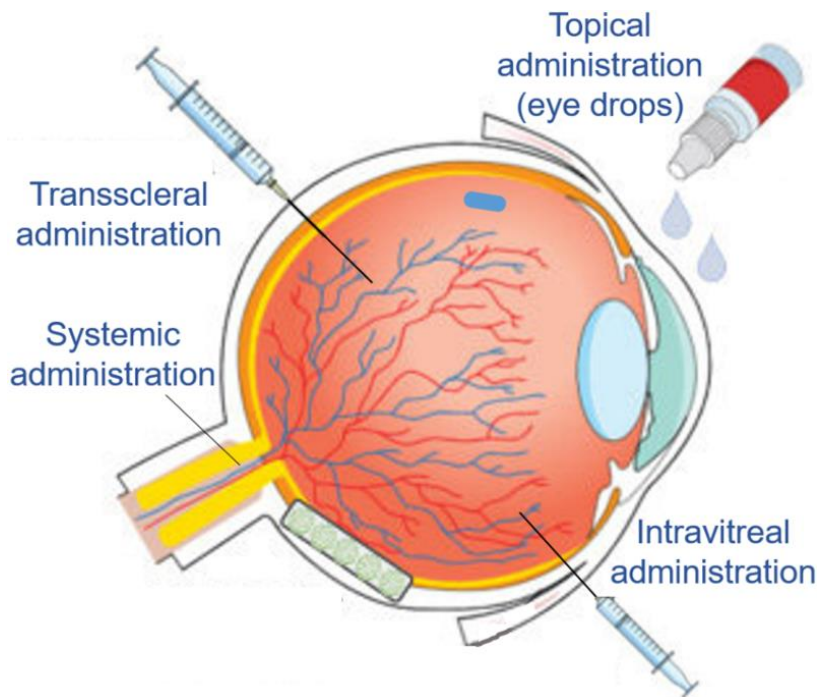


Figure 1.4 Commonly used routes for ocular drug administration, including topical administration, systemic administration, intravitreal administration, and transscleral administration. (Reproduced with permission from Ref. (12). Copyright 2019 MDPI)

1.4 Nanomedicine for treating ocular diseases

1.4.1 Routes for ocular drug delivery

As demonstrated in **Figure 1.4**, there are four general routes for administering therapeutic agents to the anterior and posterior segments of the eye, i.e., topical, systemic, intravitreal and transscleral administrations (12).

1.4.1.1 Topical administration

Topical administration mostly refers to the use of eye drops, accounting for over 90% ophthalmic products on the current market. In spite of their convenience to use, eye drops are very inefficient in delivering drugs, due to their limited administration volumes and fast clearance. In most cases, only 1% or less of a topically applied dose can enter the anterior segment of the eye, and less than 0.001% is expected to reach the posterior segment. Because of this restriction, eye

drops are mostly used to treat dry eye and corneal diseases, but they have very limited success in treating posterior segment eye diseases.

1.4.1.2 Systemic administration

Similar to the topical route, systemic administration also fails to achieve satisfactory ocular bioavailability since systemically administered drugs need to overcome the BRB. Orally administered drugs have to survive the harsh environment of the gastrointestinal tract and the first-pass metabolism. Although intravenous administration may be used to overcome these challenges, the dilution effect of the blood and the selective permeability of the BRB further limit drug entry into the eye. The poor delivery efficiency entails more frequent delivery with higher doses, thus increasing the risk of systemic side effects.

1.4.1.3 Intravitreal administration

Intravitreal administration is an intervention of directly injecting drugs into the anterior chamber or the vitreous humor of the eye. It is a topical drug delivery method that can deliver a high dose of drugs to the target while avoiding the side effects of first-pass metabolism for systemically administered drugs. Intravitreal injection is the main route of delivering macromolecules to the posterior segment of the eye. The drugs most commonly delivered via the intravitreal route are antibiotics, corticosteroids, and antiangiogenic agents such as vascular endothelial growth factor (VEGF) inhibitors. Repeated intravitreal injections of anti-VEGF drugs have become the first-line treatment for age-related macular degeneration (see section “Age-Related Macular Degeneration” for details). However, being an invasive procedure, intravitreal injection could be associated with complications such as endophthalmitis, retinal detachment, and intraocular hemorrhage.

1.4.1.4 Transscleral administration

The transscleral route includes subconjunctival, posterior juxta scleral, peribulbar, subtenon, and retrobulbar injections. Drugs delivered by this route can enter the posterior segment of the eye through the conjunctiva-sclera-choroid-retina pathway, achieving a superior ocular bioavailability (~0.01-0.1%), compared to the topical route ($\leq 0.001\%$). However, it still fails to deliver sufficient drugs to the retina due to drug losses from the periocular space, the choroidal circulation, etc.

1.4.2 Nanomedicine formulations

Nanotechnology provides new opportunities for the development of drug delivery systems particularly adapted to overcoming the eye-associated barriers. To date, a few nanomedicine formulations have demonstrated the capacity of targeted delivery and controlled release, reducing the degradation of labile drugs, and increasing the penetration, residence time, and bioavailability of drugs in various ocular tissues (13, 14). This section will introduce some commonly studied nanomedicine formulations for treating ocular diseases. As shown in **Figure 1.5**, these nanomedicine formulations include nanomicelle, liposome, nanoparticle, dendrimer, and nanogel (15, 16). **Table 1.1** summarizes representative nanomedicine formations that have been studied for ocular drug delivery (17).

1.4.2.1 Nanomicelle

Nanomicelles are made of self-assembled amphiphilic molecules that form nanosized colloidal structures with a hydrophobic core shielded by a hydrophilic shell. Nanomicelles have a common size range of 10-100 nm. Nanomicelles are one of the most studied nanomedicine formulations for ocular drug delivery. For instance, Civiale et al. developed dexamethasone-loaded nanomicelles made of copolymers of polyhydroxyethylaspartamide (PHEA) and PEGylated PHEA for anterior segment delivery (18). In vivo dexamethasone concentration profiles were determined in rabbits

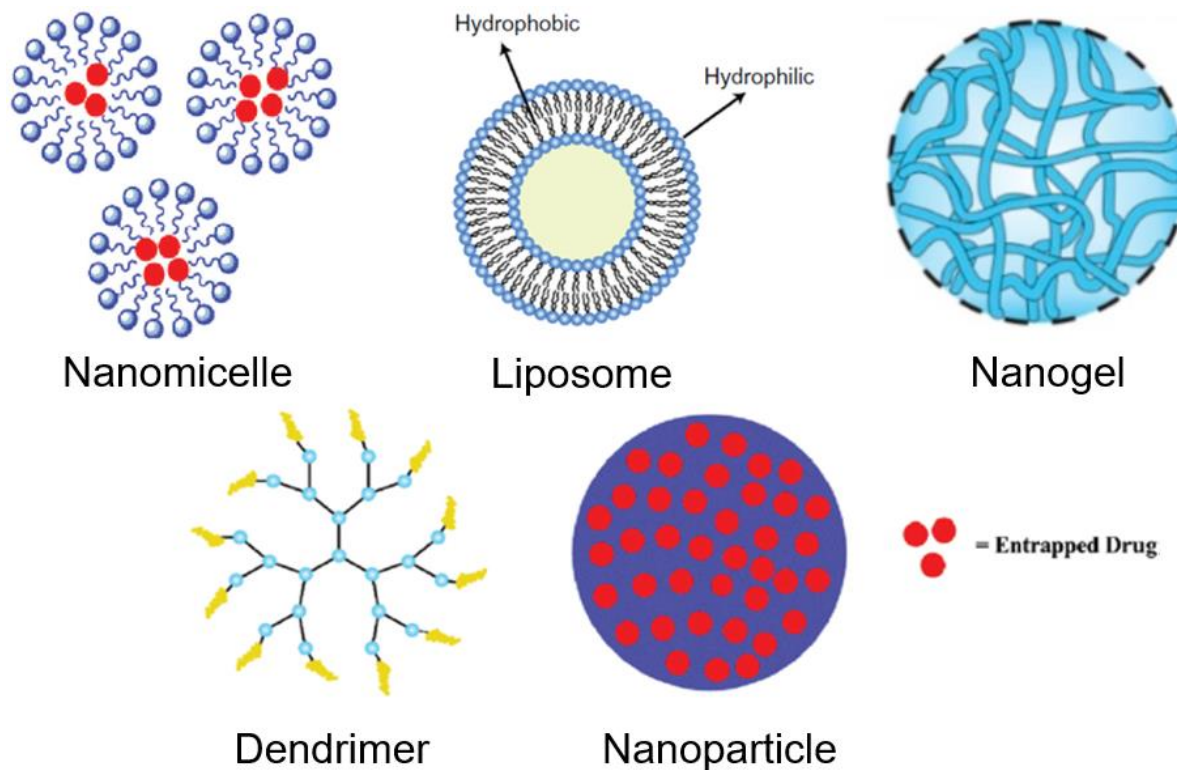


Figure 1.5 Nanomedicine formulations studied for ocular drug delivery, including nanomicelle, liposome, nanoparticle, dendrimer, and nanogel. (Reproduced with permission from Ref. (15, 16). Copyright 2013 Wolters Kluwer and 2013 Dove Press)

with aqueous humor sampling. Results showed that dexamethasoneloaded PHEA nanomicelles produced a higher ocular bioavailability in comparison to dexamethasone suspensions. There were also studies using nanomicelles for posterior segment delivery. All studies suggested that formulations based on nanomicelles help penetrate ocular barriers and deliver more drugs to the posterior segment (19).

1.4.2.2 Liposome

Liposomes are lipid vesicles with one or more phospholipid bilayers enclosing an aqueous core. Liposomes include small unilamellar vesicles (20-100 nm) made of a single bilayer, large unilamellar vesicles (200-800 nm), and multilamellar vesicles (500-5000 nm) that contain multiple concentric bilayers. Liposomes have several advantages that make them ideal for drug delivery.

Table 1.1 Summary of representative nanomedicine formulations for treating ocular diseases. (Reproduced with permission from Ref. (17). Copyright 2022 Wiley)

Nanoformulations	Cargos	Administrations	Functions/Applications
Liposomes	CRISPR-Cas9 ribonucleoprotein complex	Subretinal injection	Inducing efficient genome editing in vivo
Nanostructured lipid carriers	Dasatinib	Topical administration	Increasing the solubility of dasatinib, sustaining drug release, reducing ocular toxicity, and facilitating its penetration into cornea
Solid lipid nanoparticles	RS1 DNA plasmid	Intravitreal injection	Improvement of retinal structure by extending therapeutic period up to 2 weeks
DSPE-PEG2000-Crgd nanomicelle	Flurbiprofen	Eye drops	Specifically targeted combining to integrin receptors on cornea surface and facilitated rapid mucoadhesion
Boronic acid-rich dendrimer	Superoxide dismutase	Intravitreal injection	Protecting retinal function and reducing cell apoptosis by high levels of cellular uptake without immunogenicity and cytotoxicity
DNA/PLGA hybrid hydrogel	Dexamethasone	Topical administration	Improving dexamethasone accumulation and mediating gradual dexamethasone release
Chitosan-based self-assembly nanofilms	Heparin	Cornea in situ self-assembly	Rescuing corneal defective wound healing
Mesenchymal stem cell-derived exosomes	-	Intravitreal injection / eye drops	Significantly anatomical and functional restoration of retina, optic nerve, or cornea by modulating angiogenesis and inflammation, and improving immunomodulation and tissue regeneration
Palladium-coated gold nanorods	-	Being pasted to lacrimal gland	Sensing diverse visible light irradiations and spontaneously responded by heating up to secrete more tears to prevent dry eye
Nanoceria	Doxorubicin	Intravitreal injection	Sensitive to extracellular acidic pH conditions, targeted to tumor cells, instantaneously inducing ROS, and releasing doxorubicin intracellularly to enhance the chemotherapeutic activity in retinoblastoma cells
Gold nanoparticles-based nanobubbles	Hyaluronic acid	Intravitreal injection	Mechanically ablating the vitreous opacities upon local pulsed-laser illuminates to generate vapor nanobubbles
Dichalcogenides quantum dots	-	Eye drops	Antibacterial agent with a fast response and no reliance on light
Mesoporous silica nanoparticles	Bevacizumab	Intravitreal / subconjunctival injection	Suppressing corneal and retinal neovascularization
Spermidine-derived carbon quantum dots	-	Eye drops	Strong antibacterial capabilities for treatment of bacterial keratitis
Graphene-coated contact lens	-	Wearing on the ocular surface	Monitoring changed water evaporation rate and protecting eyes from electromagnetic wave damage
Thermosensitive triblock copolymer	Acriflavine hydrochloride and sunitinib malate	Topical administration	Increasing the intraocular absorption of hydrophilic and hydrophobic drugs and extending the drug–ocular–epithelium contact time
PEG-b-poly(propylene sulfide nanomicelles)	Actin depolymerizer latrunculin A	Intravitreal injection	Selectively modulating stiffness of Schlemm’s canal cells for therapeutic reducing intraocular pressure

Because liposomes are noncovalent aggregates, their size, lipid composition, and electric charge can be easily designed and engineered. Liposomes are capable of carrying both hydrophobic (when embedding drugs in the lipid bilayers) and hydrophilic (when encapsulating drugs in the aqueous core) drugs. The surface of liposomes can be easily modified with polymers, carbohydrates, and

antibodies, thus realizing stealth and targeting functions for drug delivery. Liposomes are made of biodegradable materials and, hence, in general have a high-membrane permeability and low cytotoxicity. All these advantages make liposomes a promising nanomedicine formation for ocular drug delivery.

Liposomes have demonstrated a good effectiveness for both anterior and posterior segment delivery (16). For drug delivery to the anterior segment of the eye, efforts are mainly put toward improving precorneal residence time by incorporating positively charged lipids or mucoadhesive polymers in liposomes. Positively charged liposomes have exhibited a better efficacy for ocular delivery than negatively charged and neutral liposomes due to their capacity in binding with the negatively charged corneal surface. For posterior segment delivery, liposome development is more focused toward improving the half-life of drugs by reducing clearance from the vitreous humor, protecting labile molecules such as peptides and oligonucleotides from degradation, and providing a sustained and controlled release. Drugs bound to liposomes can increase their bioavailability and prolong their half-life in the ocular environment. For instance, it was found that the vitreous half-life of fluconazole in rabbit eyes increased from 3.08 to 23.40 h after formulating into liposomes (20).

1.4.2.3 Nanoparticle

Nanoparticles, also known as nanospheres or nanocapsules, are solid drug carriers with a particle size of 10–1000 nm. Nanoparticles for ocular drug delivery are generally made of proteins, such as human serum albumin, or polymers, such as sodium alginate, chitosan, poly(lactide-co-glycolide) (PLGA), polylactic acid, and polycaprolactone. Drugs can be loaded either on the surface and inside the shell of the nanoparticles. Because topically administrated nanoparticles can be rapidly eliminated from the precorneal pocket, it is a common practice to modify the

nanoparticles with mucoadhesive polymers, thus improving their precorneal residence time. Polyethylene glycol, chitosan, and hyaluronic acid are most commonly used molecules to modify nanoparticles for ocular drug delivery. Among these molecules, chitosan is positively charged and hence can help bind to the negatively charged corneal surface, thereby improving the precorneal residence time and decreasing clearance of the drug (21). Once administrated, deposition and retention of nanoparticles depend on their size and surface properties. It was found that after transscleral administration, nanoparticles in the range of 200–2000 nm retained for more than 2 months, while smaller nanoparticles were rapidly cleared from periocular tissues (22).

1.4.2.4 Dendrimer

Dendrimers are nanosized, highly ordered, branched polymeric molecules. Dendrimers are available in different molecular weights with their terminals ended with various (amino, hydroxyl, carboxyl, etc.) functional groups. Drugs can be either entrapped in the dendrimer network through hydrogen bonds, hydrophobic interactions, and ionic interactions, or conjugated through covalent bonds. The highly branched structure of dendrimers allows incorporation of both hydrophobic and hydrophilic drugs. Molecular weight, size, surface charge, molecular geometry, and functional group are all important factors to design dendrimer formulations for drug delivery (23). However, there are relevantly less results reported with dendrimer formulations for ocular drug delivery, likely due to their poor ability in loading the same amount of drugs as other nanocarriers.

1.4.2.5 Nanogel

Nanogels are nanoscale hydrogel particles composed of highly cross-linked hydrophilic polymers. Nanogels can be directly loaded with drugs by equilibration or swelling in water, followed by reduction in solvent volume and gel collapse, leading to the formation of tightly packed nanoparticles. Nanogels can be used for controlled release of both hydrophilic and

hydrophobic drugs by varying the composition and conformation of polymers, and the degree of crosslinking (24).

1.4.3 Treatments of anterior segment eye diseases

Anterior segment eye diseases (ASED) refer to a range of disorders that affect the front of the eye, i.e., the anterior segment, which includes the cornea, conjunctiva, iris, lens, and ciliary body. ASED can be congenital, hereditary, or acquired. Typical disorders in this category include dry eye disease, blepharitis, contact lens-related disorders, corneal ulcers, cataract, conjunctivitis, refractive errors, and so on. This section will be focused on two most common ASED, i.e., the dry eye disease and cataracts, and their treatments with nanomedicine formulations. **Table 1.2** gives a comprehensive summary of nanomedicine formulations currently studied in clinical trials for treating both anterior and posterior segment eye diseases (17).

1.4.3.1 Dry eye disease

Dry eye is a multifactorial disease, characterized by an irritation of the eye due to deficiencies in producing enough tears or maintaining the stability of tear film on the ocular surface. Dry eye could result in damage of the corneal epithelium, inflammation of the ocular surface, ocular fatigue, and impaired vision. Dry eye disease (DED) is the most prevalent eye disease that affects 10–30% of the world population. The current treatment of dry eye is mostly palliative rather than curative. It mainly relies on the use of drug-free artificial tears and over-the-counter eye drops and lubricants to hydrate the ocular surface. Effective therapeutic interventions in treating DED are still lacking. It is estimated that DED directly and indirectly causes a \$55 billion annual economic burden in the United States alone. Therefore, there is an urgent need to develop translational solutions to effectively manage DED.

Table 1.2 Summary of nanomedicine formulations currently studied in clinical trials and/or obtained FDA approval for treating ocular diseases. (Reproduced with permission from Ref. (17). Copyright 2022 Wiley)

Products/nanoformulations (cargos)	Conditions/disease	Administrations	Number enrolled	Status	Phase	ClinicalTrials.gov Identifier
Nanoparticles (urea)	Cataract	Eye drops	50	Completed	II	NCT03001466
Albumin (paclitaxel)	Melanoma	Intravitreal injection	4	Completed	II	NCT00738361
Cyclodextrin (dexamethasone)	Diabetic macular edema	Eye drops	40	Unknown	II / III	NCT01523314
Lecithin/glycerin (coenzyme Q10)	Ataxia with ocular apraxia type 1	Oral	19	Completed	III	NCT02333305
Liposome (latanoprost)	Ocular hypertension	Subconjunctival injection	6	Completed	I / II	NCT01987323
Liposomes (latanoprost)	Ocular hypertension and open-angle glaucoma	Subconjunctival injection	81	Completed	II	NCT02466399
Liposomes (vincristine)	Metastatic malignant uveal melanoma	Intravitreal injection	54	Completed	II	NCT00506142
Liposomes (vincristine)	Retinoblastoma	Intravitreal injection	331	Unknown	III	NCT00335738
Lipid (TLC399)	Retinal vein occlusion, macula edema	Intravitreal injection	61	Active, not recruiting	II	NCT03093701
Lipid (TLC399)	Central/branch retinal vein occlusion with macula edema	Intravitreal injection	30	Recruiting	I / II	NCT02006147
INVELTYS/Mucus penetrating particles (Loteprednol etabonate)	Postoperative inflammation and pain following ocular surgery	Topical administration	900	Completed	FDA approved	NCT02163824 and NCT02793817
Bromfenac DuraSite /synthetic polymer of cross-linked polyacrylic acid (bromfenac)	Post cataract surgery inflammation and pain	Topical administration	268	Completed	FDA approved	NCT01576952
DexaSite/Synthetic polymer of crosslinked polyacrylic acid and chitosan (dexamethasone)	Post cataract surgery inflammation and pain	Topical administration	260	Completed	Phase III	NCT03192137
Cyclosporine nanomicellar	Dry eye	Eye drops	258	Completed	III	NCT02845674
Cyclosporine nanomicellar	Dry eye	Eye drops	745	Completed	III	NCT02688556
Mesenchymal stem cells-derived exosomes	Macular holes	Intravitreal injection	44	Recruiting	Early Phase I	NCT03437759
Serum exosomal miRNA	Diabetic retinopathy	-	200	Not yet recruiting	I	NCT03264976

Topical administration of immunosuppressive drugs such as cyclosporine A (CyA) helps control ocular surface inflammation so that it increases tear secretion and the stability of the tear film. Topical CyA also effectively restores epithelial damage and reduces disease recurrences in the long term, thus alleviating dry eye symptoms (25). As shown in **Figure 1.6a**, a number of nanomedicine formulations, such as nanomicelles, liposomes, and nanoparticles, have been developed to deliver CyA in the preclinical stage (26). For example, it has been shown that CyA-

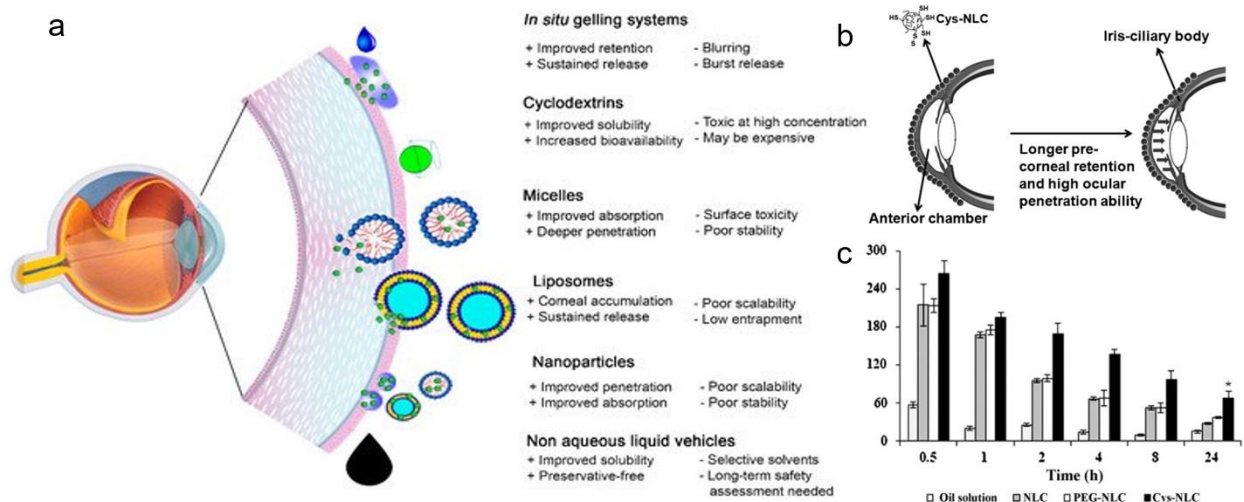


Figure 1.6 Nanomedicine formulations for treating dry eye disease. (a) Schematic representation of various nanomedicine formations, such as nanomicelles, liposomes, nanoparticles, to enhance topical drug delivery for dry eye therapy. (b) Schematic representation of intraocular drug delivery using cysteine-functionalized nanostructured lipid carrier (Cys-NLC). (c) Biodistribution of CyA in rabbits' tear fluids after topical administration of CyA-loaded nanomedicine formulations, in comparison with traditional oil solutions. (Reproduced with permission from Ref. (26, 28). Copyright 2021 MDPI and 2010 Elsevier)

loaded poly- ϵ -caprolactone (PECL) nanocapsules were able to increase CyA concentration in cornea five-times higher than that of the traditional oily formulation of CyA (27). The increased bioavailability was attributed to internalization of the PECL nanocapsules in the corneal epithelium. Similar enhancement in bioavailability can be achieved by encapsulating CyA in a variety of nanoscale polymer shells, such as a double shell of hyaluronic acid and PECL, cysteine polyethylene glycol monostearate, or mixtures of surfactants and propylene glycol. **Figure 1.6b** shows the synthesis of cysteine-functionalized nanostructured lipid carrier (Cys-NLC) for the topical administration of CyA (28). It was found that after topical administration to rabbits, the CyA concentration in tear fluids of the Cys-NLC treated group was significantly higher than the group treated with the traditional oil solutions of CyA (**Figure 1.6c**) (28). In general, these novel nanomedicine formulations led to higher drug concentrations and longer-lasting periods (up to 24

h) in a broad range of ocular tissues including the cornea, conjunctiva, iris, ciliary body, and aqueous humor, in comparison to the traditional oily formulation of CyA. More recently, it has been reported that topical administration of CyA-loaded polymeric nanomicelles based on polyoxyl 40 stearate and methoxy poly(ethylene glycol) hexylsubstituted poly (lactide) led to a 28.5-fold increase of drug concentration in comparison to the traditional oily CyA solution (29).

1.4.3.2 Cataract

A cataract is a cloudy area of the lens of the eye that leads to a decrease in vision. Cataracts are a leading cause of blindness globally. According to the World Health Organization (WHO), cataracts affect approximately 65.2 million people worldwide and cause moderate to severe vision loss in over 80% cases. Cataracts are a leading cause of age-related vision loss in the United States. More than half of all Americans of 80 years older have cataracts. Symptoms of cataracts include blurry vision, abnormal color perception, monocular diplopia, glare, and impaired vision. Cataracts are mostly caused by electrolyte disturbances and oxidative damage. Transparency and refractive properties of the lens are regulated by the concentration of lens proteins in lens fibers. Mutations of these proteins can increase the oxidative stress, thus leading to the formation of cataracts. To date, the only available treatment for cataracts is surgical removal of the opacified lens and replacement with an artificial one. However, surgical treatments suffer from side effects such as implant disintegration, corneal wounds, postsurgical inflammation, and posterior capsular cataract formation. Hence, there is a general need for nonsurgical preventative and treatment interventions for cataracts.

Anticataract agents have been investigated in two distinct categories: chemical agents and antioxidants (30). Some nonsteroid anti-inflammatory drugs such as aspirin, paracetamol, ibuprofen, and bendazac were found to delay cataract formation by effectively increasing blood

pressure or inhibiting posttranslational protein modifications. Antioxidants are reducing agents that accept electrons from free radicals and reactive oxygen species, and therefore can protect tissues from oxidative stress and damage. Many antioxidant molecules have been found to be effective anticataract agents, such as glutathione, cysteine, cysteine prodrug L-2-oxothiazolidine-4-carboxylic acid, N-acetyl carnosine, N-acetylcysteine, and N-acetylcysteine amide. Some flavonoids, such as curcumin and quercetin, and β -carotenes, such as lutein and lycopene, have also demonstrated anticataract properties (31). However, most of these drugs have very low delivery efficiencies due to their inability to overcome physical barriers of the eye (see section “Physical Barriers for Ocular Drug Delivery” for details).

Nanomedicine formulations have been studied to improve the bioavailability, biocompatibility, and biodegradability of anticataract drugs. Curcumin was encapsulated in PLGA nanoparticles for systemic administration, which increased the oral bioavailability of the drug by ninefold compared to free curcumin. Lutein can be loaded with Labrasol® (a nonionic surfactant excipient) to form a nanoemulsion, which demonstrated a shorter lag time and two times more cellular accumulation compared with free lutein. Liposomes have also been reported as an efficient formulation for preventing cataracts. For example, it was found that vitamin E-containing liposomes made of dipalmitoyl phosphatidylcholine and dioleoyl phosphatidylcholine delayed cataract progression in a rat model (32). Cytochrome C-loaded freeze-dried liposomes also exhibited significant efficacy in retarding the onset and progression of cataracts in rats (33).

1.4.4 Treatments of posterior segment eye diseases

Posterior segment eye diseases (PSED) refer to a spectrum of disorders that affect the back of the eye, i.e., the posterior segment, which includes the retina, choroid, and optic nerve (see section “Posterior Segment” for details). The most prevalent PSED include glaucoma, age-related macular

degeneration, and diabetic retinopathy. These PSED are now recognized as a major cause of visual impairment worldwide and are more prevalent than infectious causes of visual impairment such as trachoma and corneal ulcers. Novel nanomedicine formulations to treat these PSED will be introduced in this section.

1.4.4.1 Glaucoma

Glaucoma is a group of eye conditions characterized by damage of the optic nerve. The symptoms of glaucoma include vision loss, eye pain, mild-dilated pupil, redness of the eye, and nausea. It was estimated that about 80 million people had glaucoma worldwide in 2020, and this number is expected to increase to over 111 million by 2040. The WHO estimated that 4.5 million people worldwide are blind due to glaucoma. Although most of the genetic bases of glaucoma are still not completely understood, increased intraocular pressure (IOP), ischemia of the optic nerve, and the activation of oxidative stress-related pathways are found in the progression of this disease. At present, the major aim in controlling glaucoma is to prevent or delay the loss of visual field. This is because neuronal cell death is irreversible. Once the visual field is lost, there is no cure available. It was found that an effective IOP reduction resulted in a delay of onset and progression of glaucoma in 80-90% patients in clinical trials.

Drugs to treat glaucoma are classified by their active ingredients, including prostaglandin analogs, beta blockers, alpha agonists, carbonic anhydrase inhibitors, and Rho-kinase inhibitors. Most of these drugs are lipophilic and hard to penetrate physical barriers of the eye. Nanomedicine formulations are able to increase the drug concentration in target tissues and result in improved and long-lasting therapeutic effects. The first study of using nanomedicine formulations to treat glaucoma was reported in 1986 (34). The study showed a more prolonged myosis after administration of pilocarpine-containing poly(butylcyanoacrylate) nanospheres, compared to

traditional pilocarpine solutions. Liao et al. synthesized pilocarpine-loaded gelatin-covered mesoporous silica nanoparticles (p/GM) (35). The gelatin coating was controlled by varying its thickness on the mesoporous silica nanoparticles, thereby realizing a sustained drug release. It was found that p/GM0.05, i.e., with 0.05 mg gelatin coating per mg of nanoparticles, was able to release pilocarpine in a long-lasting (up to 36 days) and high-concentration (~50%) fashion, thus maintaining a normal IOP for a period up to 21 days (35).

More recently, antiglaucoma drugs, such as beta blockers (betaxolol) or carbonic anhydrase inhibitors (dorzolamide), have been encapsulated in chitosan nanoparticles. It was found that betaxolol-loaded chitosan nanoparticles led to a significant decrease in IOP compared to traditional formulations (36). Hyaluronic acid-modified chitosan nanoparticles codelivered with timolol maleate and dorzolamide hydrochloride showed a high efficacy in reducing IOP. Other examples of antiglaucoma drug-loaded nanoparticles include Eudragit® RL100 and RS100-based nanoparticles, PLGA nanoparticles, and cationic solid lipid nanoparticles (13). Nanoemulsions have also been studied to deliver antiglaucoma drugs. Topical administration of nanoemulsions to hypertensive rabbits was able to reduce IOP up to 8 hours (37). Liposomes have also been tested for delivering antiglaucoma drugs. In general, it was found that cationic liposomes were more effective than neutral and negatively charged liposomes, likely due to stronger interactions of these liposomes with the ocular mucosa. For example, Natarajan et al. reported a long-lasting unilamellar liposome formulation for delivering a prostaglandin derivative, latanoprost (Xalatan®) (38). It was found that a single subconjunctival injection of latanoprost-loaded liposomes led to IOP reduction for up to 120 days (**Figure 1.7**). The IOP was further reduced over another 180 days after a second injection was administered (38).

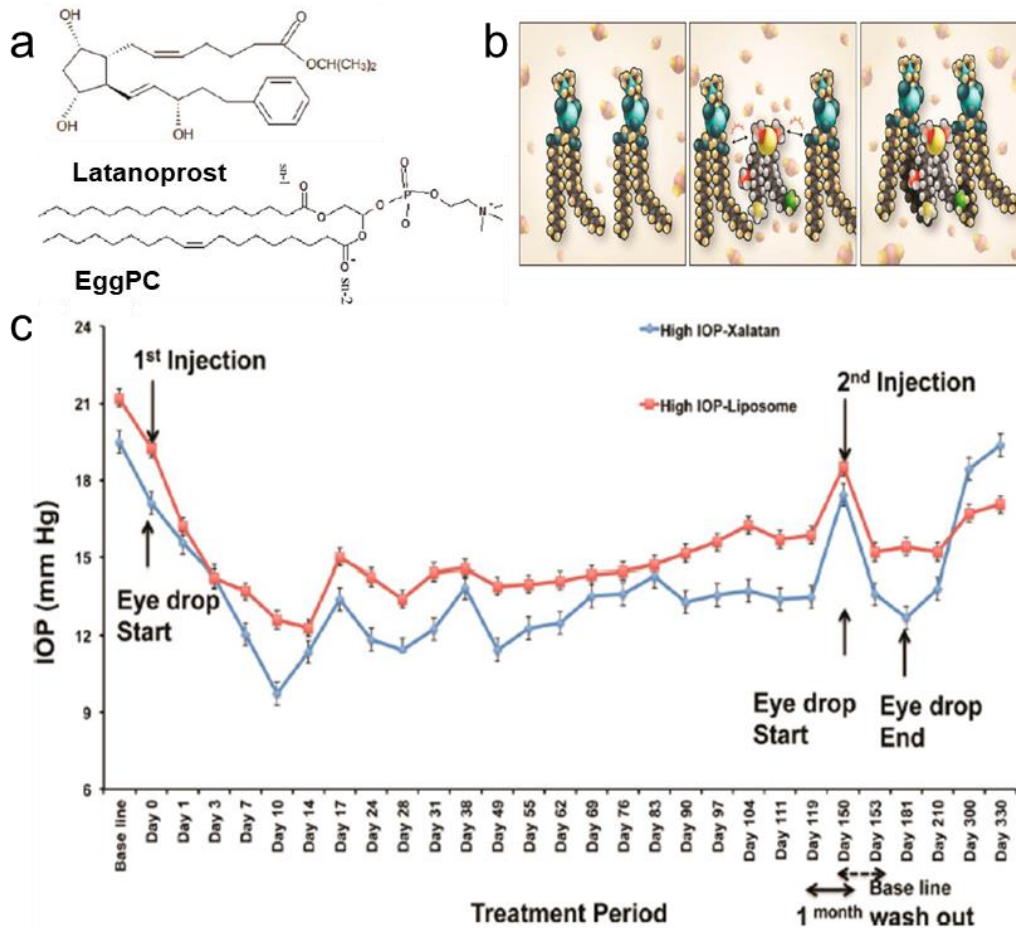


Figure 1.7 Nanomedicine formulations for treating glaucoma. (a) Chemical structures of latanoprost and EggPC. (b) Schematic representations of the process of loading liposomes with latanoprost: phospholipid molecules in liposomes prior to loading latanoprost, hydrogen bonding between the polar moiety of latanoprost and the phospholipid headgroups, and the hydrophobic moiety of latanoprost buried between phospholipid acyl chains. (c) A single subconjunctival injection of latanoprost-loaded (Xalatan[®]) liposomes led to IOP reduction for up to 120 days. The IOP was further reduced over another 180 days after a second injection was administered. (Reproduced with permission from Ref. (38). Copyright 2014 American Chemical Society)

1.4.4.2 Age-related macular degeneration

Age-related macular degeneration (AMD) is a complex eye disease characterized by a progressive loss of central vision due to degenerative and neovascular changes at the macular area, which is responsible for central and sharp vision at the posterior segment of the eye. AMD can be divided into the slowly developing dry (~80%) and the rapidly blinding wet (~20%) forms. The

disease impairs abilities to read and to recognize faces, thus severely compromising the patients' independency. AMD is the leading cause of blindness in the elderly population in developed countries. Its prevalence increases with age. It is estimated that the incidence of AMD in people of age 65-75 is 1%, and the incidence increases to 13% in people of age 85 and above. With improved mortality conditions at advanced ages, it is projected that in 2050, 20% of the world population will be older than 65. As a consequence, the prevalence of AMD is expected to double during the next two decades. In general, patients with AMD incur twice the annual costs per patient compared with individuals without AMD. The economic burden of AMD is estimated to be above \$35 billion/year in the United States alone.

Currently, AMD is treated with the photodynamic therapy, transpupillary thermotherapy, macular surgery, radiation, retinal translocation, and most commonly, antivascular endothelial growth factor (anti-VEGF) agents. The three most widely used anti-VEGF drugs at present are Avastin® (bevacizumab), Lucentis® (ranibizumab), and Eylea® (aflibercept). Bevacizumab is a whole anti-VEGF-A immunoglobulin, while ranibizumab is a fab fragment of an antibody against VEGF-A. Aflibercept is a new recombinant fusion protein that is composed of two main components, i.e., the VEGF-binding portions from the extracellular domains of human vascular endothelial growth factor receptor-1 (VEGFR-1) and VEGFR-2. Aflibercept has the ability to bind VEGF-A, VEGF-B, or placental growth factor and to inhibit angiogenesis.

To deliver drugs directly to retina, anti-VEGF agents are administered intravitreally, which reduces the dosage required and avoids the side effects associated with systemic administration. However, intravitreal injections are associated with various complications, such as endophthalmitis, a sight-threatening infection with reported incidences of 0.019-0.09%. Multiple monthly to bimonthly injections are required for long periods of time for the treatment of AMD,

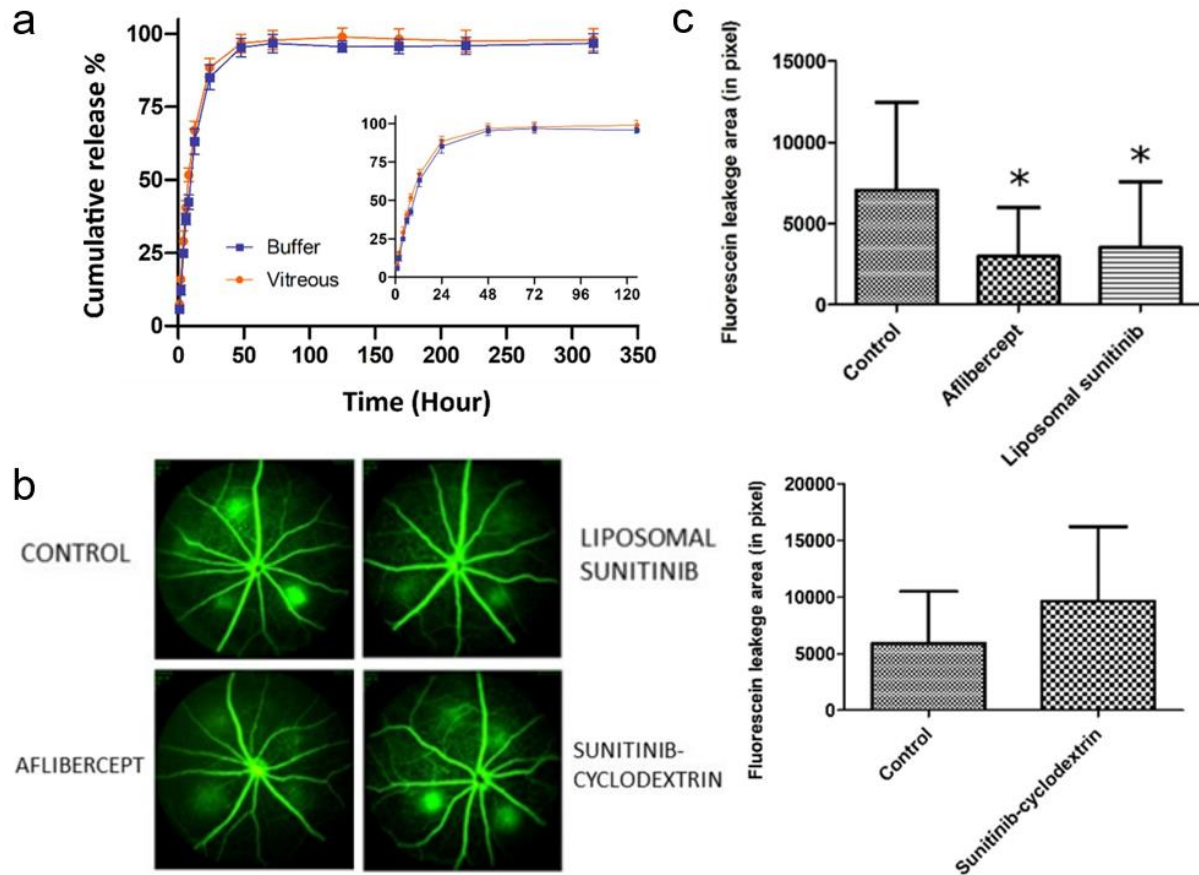


Figure 1.8 Nanomedicine formulations for treating age-related macular degeneration. (a) Cumulative release of sunitinib (%) from a liposomal formulation. The insert shows a magnified view of the release profile over 5 days. (b) Representative late-phase fluorescein angiograms in control mice and in aflibercept, liposomal sunitinib and sunitinib-cyclodextrin treated mice, three days after photocoagulation. (c) Vascular leakage measured by fluorescein angiography. (Reproduced with permission from Ref. (41). Copyright 2022 Elsevier)

thus increasing the risk of infection. Apart from the endophthalmitis risk, the need for frequent intravitreal injections poses a significant burden to the patients and healthcare providers. Hence, there is an urgent need and a great interest of developing a noninvasive topical ocular formulation, ideally in the form of eye drops, to deliver anti-VEGF drugs to patients with retinal vascular diseases such as AMD.

Liposomes have been studied for the treatment of AMD. The biodegradable and biocompatible nature of phospholipids makes liposomes attractive for ocular delivery. There are several liposome

formulations currently under study for the treatment of AMD, such as peptide-modified PEGylated liposomes, vector-mediated liposomes, and PEGylated cationic liposomes (39, 40). Tavakoli et al. synthesized sunitinib-loaded liposomes to block the neovascularization signaling pathway through inhibition of the tyrosine kinase of vascular endothelial growth factor receptors (VEGFRs). By comparing the encapsulation efficiency, loading capacity, and drug release profile in buffer and vitreous, they showed that liposomes with the mean size of 104 nm could effectively carry sunitinib and release it up to 3 days (**Figure 1.8**) (41). de Cogan et al. reported that therapeutic levels of bevacizumab in the posterior segment were achieved in rats following topical administration when this anti-VEGF drug was conjugated with a cell-penetrating peptide, i.e., short cationic sequences (less than 30 amino acids) with a remarkable capacity for biomembrane translocation (42). Although being tested only in rodents, this research demonstrated the feasibility of a potentially promising noninvasive formulation for topical administration of anti-VEGF drugs to treat patients with AMD.

1.4.4.3 Diabetic retinopathy

Diabetic retinopathy (DR) is a diabetes complication that affects the eye. It can be defined as a microvascular disease that leads to capillary occlusion, and damage of blood vessels and light-sensitive tissues in the retina. In its early stage, the patient might not have symptoms. As the condition progresses, patients with DR may have blurred vision, impaired color vision, and even blindness. DR can be divided into two broad categories: the nonproliferative DR (NPDR) and the proliferative DR (PDR). NPDR is further subdivided into mild, moderate, and severe (43). In the mild and moderate NPDR stages, the walls of blood vessels in retina weaken. Tiny bulges (microaneurysms) protrude from the walls of smaller vessels, sometimes leaking fluid and blood into the retina. Larger retinal vessels then begin to dilate and become irregular in diameter. When

it reaches the severe stage, too much sugar can lead to severe block of the blood vessels. PDR is the result of further development from severe NPDR. In this stage, due to the damage of blood vessels, capillary endothelial cells begin to proliferate, and hypoxic retinal tissue releases vascular proliferation substances to promote the growth of abnormal retinal blood vessels, i.e., neovascularization, which grow in an attempt to supply oxygen to the hypoxic retina. This could result in retinal detachment and blindness.

The mechanisms by which hyperglycemia results in retinal pathology remain inconclusive. The main biochemical pathways that influence DR include protein kinase C activation, advanced glycation end product (AGE) pathway, oxidative stress, and expression of growth factors, such as VEGFs. Typical drugs to treat DR include corticosteroids, AGE inhibitors such as carnosine, and antioxidants. Polymeric nanospheres have been studied to deliver these drugs to treat DR. PLGA, chitosan, polyvinyl alcohol, and poly(methyl methacrylate) nanospheres all have a high drug encapsulation rate to prolong the resident time of the free drugs. Liposome formulations are mainly based on biodegradable lipids, such as phospholipids, ceramides, and glycerides. Dendrimers, such as polyamidoamine, are also studied. Drugs can be entrapped in the dendrimer network composed of the functional groups to promote a sustained drug delivery to the retina.

1.5 Ocular nanotoxicology

The ocular surface serves as a potential biological portal for environmental particulate matters and pathogens to enter the human body. Hence it is important to understand the nano-bio interactions at the ocular surface, and the health impact of natural, incidental, and engineered nanoparticles that enter the body *via* the eye (44). This section will briefly introduce emerging toxicological studies about nanoparticle interactions with the ocular surface and tissues. **Table 1.3** summarizes a few representative ocular nanotoxicological studies (44).

Table 1.3 Summary of representative nanotoxicological studies about the eye. (Reproduced with permission from Ref. (44). Copyright 2022 Wiley)

Compound	Biological model	Mechanism	Outcome
Au NP	Zebrafish eye		Disrupt eye development and pigmentation
Ag/Au NP	Cell and tissue culture of mouse retina	Oxidative stress	Apoptosis, Neurotoxic effect, and even visual impairment
Ag NP	Bovine retinal endothelial cells	Oxidative stress	Cytotoxicity and apoptosis
Ag NP	New Zealand white rabbits		Conjunctival redness, edema, and discharge
Ag NP Fe NP	Guinea pigs Human corneal epithelial cells	Elevated inflammatory response, cell death-related pathway indicators and generated mistranscribed RNA	Grade 1 conjunctivae irritation Cell death
CeO ₂ NP	Rat retina primary cells, tubby mutant mice, and very low density lipoprotein receptor knockout mouse	Antioxidative effect	
SiO ₂ NP	Human corneal epithelial cells and Sprague–Dawley rats	Cell membrane damage, cell death, and mitochondrial dysfunction	Corneal injury
TiO ₂ NP	Rabbits		Reversible ocular conjunctival redness
TiO ₂ NP ZnO NP	New Zealand white rabbits Rat retinal ganglion cells	Overproducing ROS, caspase 12, decreasing plasma membrane calcium ATPase and bcl 2/caspase 9, disrupting intracellular calcium homeostasis	Ocular surface damage Cell death
ZnO NP	Sprague–Dawley rats		Retinopathy
Fullerene	Rabbit		Conjunctival redness and corneal epithelial defects
Fullerene	Rabbits		Conjunctiva redness and blood vessel hyperemia
SWCNT	ARPE-19	Changes in SOD levels, membrane integrity and cell apoptosis increase in LDH release, ROS generation and apoptosis	Cell death
MWCNT	Human retinal pigment epithelium cells		Decrease in cell survival rate
MWCNT	Rabbit		Conjunctival redness/discharge and vessel hyperemia
GO NP	Primary human corneal epithelium cells and human conjunctiva epithelium cells; Sprague–Dawley rats	Oxidative stress	Cell death
GO NP	Kunming mice and corneal epidermal cells	Inflammation and apoptosis	Incrassated corneal stromal layer and iris neovascularization

NP: nanoparticle; SWCNT: single-walled carbon nanotubes; MWCNT: multi-walled carbon nanotubes; GO: graphene oxide; ROS: reactive oxygen species; SOD: superoxide dismutase; LDH: lactate dehydrogenase.

1.5.1 Impact on the ocular surface

Nanoparticles mostly affect the ocular surface, which is composed of the corneal epithelium in the center and the surrounding conjunctival epithelium. It was found that nanoparticles could induce a series of inflammatory events at the ocular surface, featured by symptoms such as dryness, burning, itching, gritty eyes, conjunctival chemosis, limbitis, redness, and swelling of eyelids. Ocular surface inflammation may cause tear film dysfunction. Dry eye is one of the most common ocular surface disorders directly associated with exposure to particles. Han et al. found that exposure to titanium dioxide nanoparticles worsened dry eye symptoms (45). Researchers have also showed that exposure to PM_{2.5} induced allergic conjunctivitis (46).

1.5.2 Impact on the lens

It has been reported that cigarette smoke, diesel exhaust, and aerosols of iron nanoparticles all have an adverse impact on the lens (47). Exposure to these metal-containing particles and aerosols leads to accumulation of metals, such as cadmium, in the lens, which could induce oxidative stress and trigger cataractogenesis (48). In addition to direct exposure to metal-containing particles, inhaled metal nanoparticles may also enter the blood and then accumulate in the aqueous humor by penetrating the blood-aqueous barrier (see section “Blood-Aqueous Barrier”), thus increasing the toxic metal concentration in the eye. Increasing metal ions in the eye may promote cataract formation by inducing oxidative stress, inhibiting antioxidant pathways, and modifying the structure/formation of the lens extracellular matrix. It was proposed that iron nanoparticles could cause oxidative damage to lens through the metal-catalyzed Fenton reaction (49).

1.5.3 Impact on the retina

Nanoparticles may cause retinal vascular layer damage and cell degeneration by inducing oxidative stress. Söderstjerna et al studied the effects of 20 and 80 nm silver and gold nanoparticles

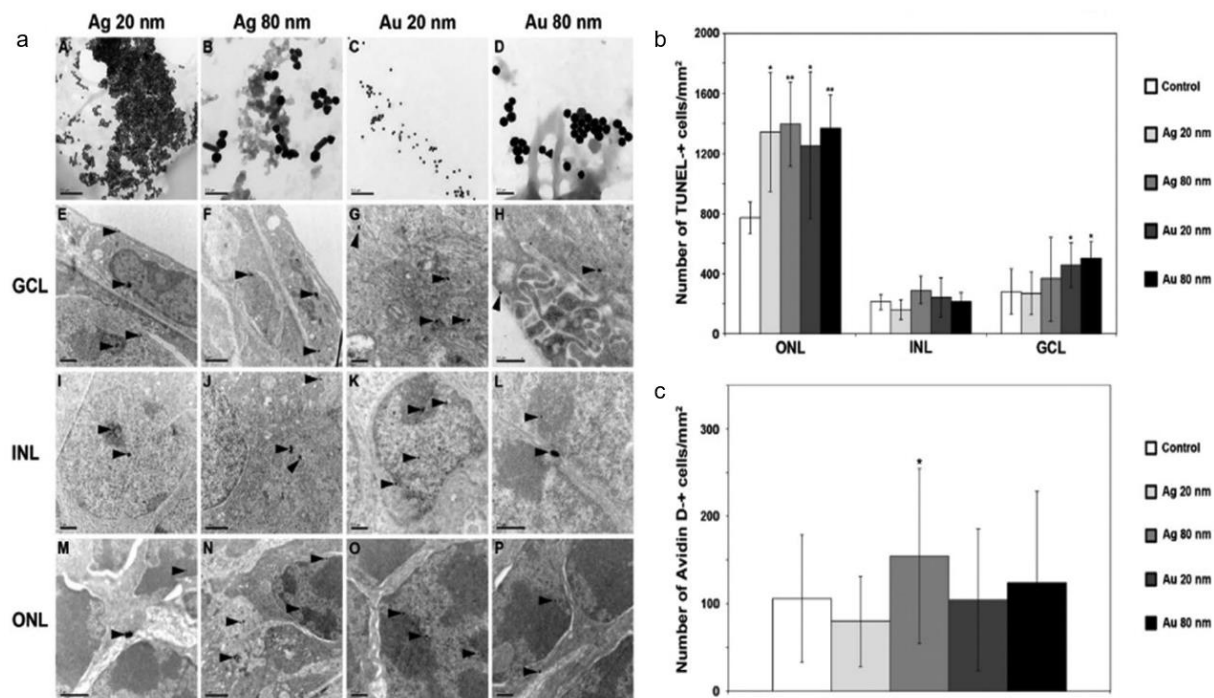


Figure 1.9 Adverse effects of silver (Ag) and gold (Au) nanoparticles (NPs) on mouse retina. (a) TEM images demonstrating uptake of Ag and Au NPs found in all three retinal nuclear neuronal layers, i.e., the ganglion cell layer (GCL), the inner nuclear layer (INL), and the outer nuclear layer (ONL). Arrowheads show NPs that have been taken up by the retinal cells. Scale bars equal to 0.2 μ m for images (A-D); 1 μ m for (E, F), (I, J), and (M, N); and 0.5 μ m for (G, H), (K, L), and (O, P). (b) Retinal cell apoptosis was detected with the TUNEL assay. Apoptosis was detected in the ONL, INL and GCL after exposure to 20 and 80 nm Ag and Au NPs. (c) Oxidative stressed cells were detected using AvidinD as a marker. AvidinD-positive cells were detected after exposure to 20 and 80 nm Ag and Au NPs. (Reproduced with permission from Ref. (50). Copyright 2014 PLOS)

on an *in vitro* cell culture model of the mouse retina (50). It was found that exposure to these nanoparticles by 72 h, even at low particle concentrations, caused significant oxidative stress and apoptosis of the retinal cells (**Figure 1.9**), which could lead to visual impairment or even blindness. Cytotoxicity of these nanoparticles was attributed to their neurotoxic effects especially on the sensory neurons of the retina, i.e., the photoreceptors, which are the most vulnerable neurons of the retina and the key for a proper vision (50). In addition, it has been reported that nanoparticles can increase serum homocysteine levels, which in turn reduces the retinal blood flow velocity.

Moreover, dissolution of excess metal ions in the eye was found to be associated with retinal detachment, age-related macular degeneration, and intraocular bleeding.

1.6 Summary and scope of this dissertation

Nanotechnology provides new opportunities for the development of drug delivery systems particularly adapted to overcoming the eye-associated barriers. A number of nanomedicine formulations, such as nanomicelles, liposomes, nanoparticles, dendrimers, and nanogels, have demonstrated the capacity of increasing the residence time and bioavailability of drugs in the treatments of various ocular diseases, including dry eye, cataracts, glaucoma, age-related macular degeneration, and diabetic retinopathy. Despite the preliminary success achieved by these novel drug delivery systems, it should be noted that development of nanomedicine formations for preventing and treating ocular diseases is still in its infancy. Potential toxicity of nanoparticles due to interactions with the ocular surface and tissues should be further investigated.

The rest of the dissertation is organized as follows. Chapter 2 investigates distinctive composition-functional correlations for major lipid components in a model TFL. Chapter 3 discusses the molecular biophysical mechanisms of fatty acid esters of hydroxy fatty acids (FAHFAs) using palmitic acid-9-hydroxy stearic acid (PAHSA) as a model. Chapter 4 develops a novel droplet-based biophysical model to study the effects of TFL on water evaporation. Chapter 5 establishes the composition-structure-functional correlations of the Meibomian lipid (ML) films extracted from wild type (WT) and *Soat1*-knockout (KO) mice. Chapter 6 introduces a side work of studying pulmonary surfactant films adsorbed from the subphase at physiologically relevant high surfactant concentrations. Chapter 7 focuses on another side work of studying interactions between the recombinant S2 subunit of the SARS-CoV-2 S protein and an animal-derived clinical surfactant. Chapter 8 concludes the dissertation research and provides several future directions.

Chapter 2 Surface tension and interfacial rheology of the tear film lipid layer ¹

2.1 Introduction

The tear film is a multilayered biological barrier that protects our eyes from potential risks from the environment (51, 52). The thickness of a normal tear film is 6-10 μm (53). As shown in **Figure 2.1a**, it is composed of three consecutive layers, *i.e.*, the inner mucin layer, the intermediate aqueous layer, and the outermost lipid layer (54). The mucin layer mainly consists of sugar-rich glycosylated proteins that function as lubricants to facilitate spreading of the tear film at the ocular surface (55). The aqueous layer, representing the largest portion of the tear film with a thickness of approximately 4 μm , is made of solutions of electrolytes, peptides, and proteins (56).

The lipid layer, commonly known as the tear film lipid layer (TFLL), is approximately 40 nm thick (57). It consists of two sublayers, *i.e.*, a polar lipid layer adjacent to the aqueous layer, and a non-polar lipid layer that resides upon the polar lipids and is directly exposed to the environment (58, 59). The polar lipids account for 20 mol% of the TFLL, with phospholipids (PLs) being the most abundant lipid class (~12 mol%) in human tears (60). Recent lipidomics study identified a new class of polar lipids, (O-acyl)- ω -hydroxy fatty acids (OAHFAs), accounting for ~4 mol% of the TFLL (58, 61-63). The non-polar lipids account for 80 mol% of the TFLL, with wax esters (WEs, *i.e.*, esters of a fatty acid and a fatty alcohol, accounting for ~43 mol%) and cholesteryl esters (CEs, *i.e.*, esters of a fatty acid and a cholesterol, accounting for ~39 mol%) being the most prevalent non-polar lipid classes (64).

¹ Xu X, Li G, Zuo YY, Biophysical properties of tear film lipid layer I. Surface tension and surface rheology. *Biophys. J.* 121 (2022) 439-450.

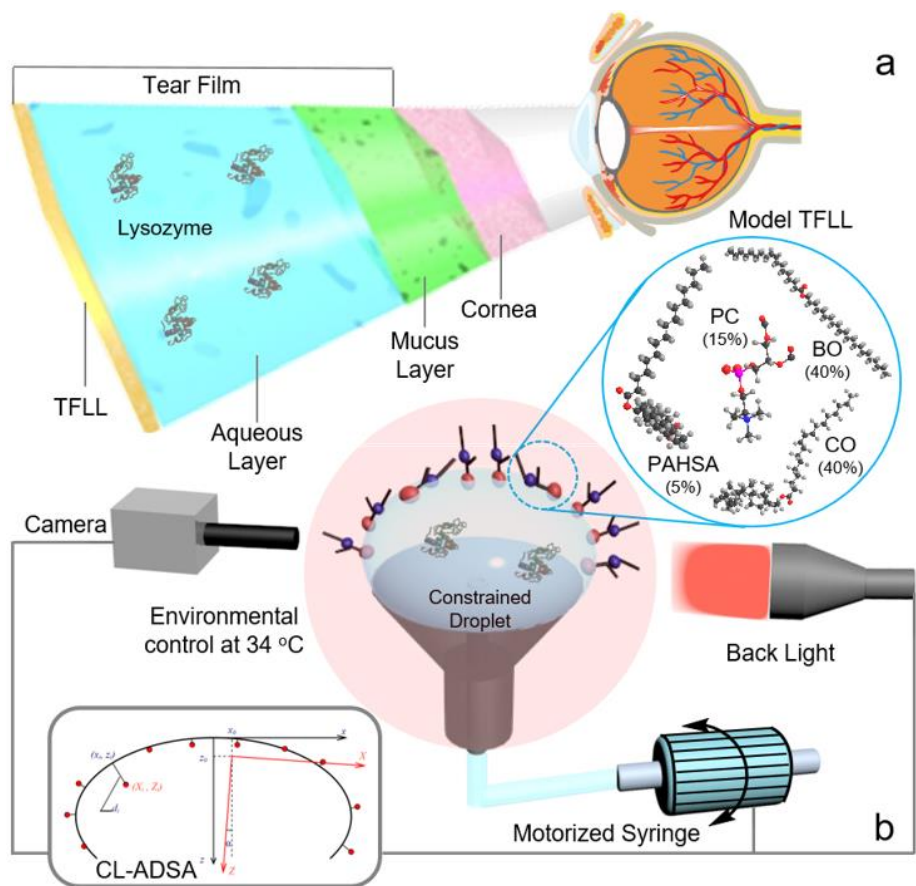


Figure 2.1 Schematics of (a) the tear film and (b) the constrained drop surfactometry (CDS) for biophysical simulations of the tear film lipid layer (TFLL). CDS uses the air-water surface of a sessile drop (~ 4 mm in diameter, ~ 0.3 cm² in surface area, and ~ 20 μ L in volume), constrained on a carefully machined pedestal with sharp-knife edges, to accommodate the spread TFLL. The buffer droplet, simulating the chemical compositions of the tear film aqueous layer, is enclosed in an environmental control chamber that maintains the physiologically relevant temperature of 34 °C. The model TFLL consists of BO:CO:PC:PAHSA (40:40:15:5). The TFLL is compressed and expanded at a highly dynamic rate of 15% relative area per second to simulate a blink, by regulating fluid flow into and out of the droplet using a motorized syringe. Dynamic surface tension of the TFLL is determined with closed-loop axisymmetric drop shape analysis (CL-ADSA), which measures surface tension of the TFLL remotely by analyzing the shape of the TFLL-covered droplet in real-time using photographic methods.

It is believed that the major physiological function of the TFLL is to stabilize the tear film by reducing surface tension and retarding evaporation of the aqueous layer (62, 65-67). Dysfunction of the TFLL leads to dysfunctional tear syndrome (DTS) (68, 69), with dry eye disease (DED) being the most prevalent eye disease affecting 10-30% of the world population (70). DED is a

multifactorial ocular disease characterized by damage of corneal epithelia, inflammation of ocular surface, eye discomfort and visual disturbance, as a result of compromised tear film stability (71, 72). To date, except for treatments alleviating the dry eye symptoms, effective therapeutic interventions in treating the DED are still lacking (73). It is estimated that the DED directly and indirectly causes a \$55 billion annual economic burden in the United States alone (74). Therefore, there is an urgent need to understand the biophysical properties of the TFLL and to develop translational solutions in effectively managing the DED.

There have been many *in vitro* studies that investigated the surface activities of either model TFLL (75-77) or meibomian lipids extracted from either human (78) or animal sources (79). Although providing valuable biophysical and physiological insights, these studies have a few common limitations. First of all, lipid composition of the model TFLL used in most previous studies deviated significantly from that of the natural TFLL. Polar lipids, mainly phosphatidylcholine (PC), have been commonly used *in vitro* to constitute the model TFLL (80). However, PC accounts for less than 20 mol% of the natural TFLL, while the other 80 mol% of the natural TFLL is composed of nonpolar lipids (66, 81). This discrepancy is at least in part due to the rapid development of lipidomics in recent years, which allows comprehensive lipid analysis of meibomian gland secretions and discovery of never-before-known lipid classes, such as OAHFAs (61, 82), whose biophysical function and contribution to the surface activity of TFLL are still poorly understood.

In addition, the experimental conditions used in most previous *in vitro* studies can hardly mimic the physiological conditions of the ocular surface and/or the dynamics of the TFLL. This limitation is largely due to existing *in vitro* biophysical methods used for studying the TFLL. These methods include the Langmuir trough (75-78, 83-85), capillary tube (86), pendent drop (87), sessile drop

and bubble (88, 89). Among these methods, the Langmuir trough is the most commonly used method for studying the TFL. However, Langmuir trough has a few limitations that prevent it from mimicking the physiological conditions of the ocular surface and the dynamics of the TFL. First, due to its large size, the Langmuir trough generally lacks rigorous temperature control. Hence most Langmuir trough experiments were conducted at room temperature (79, 90). However, the ocular surface is estimated to have a physiological temperature of 34 °C (78, 91). Second, the Langmuir trough is incapable of simulating the physiologically relevant tear film dynamics. The tear film is spread and replenished at the ocular surface, compressed and expanded rapidly during each individual blink. A healthy adult blinks approximately 10 times per minute with an average duration of 0.1-0.3 second per blink (92). It means that the TFL must undergo highly dynamic compression (during the closing phase of the blink) and expansion (during the opening phase of the blink) (93). Langmuir trough is unable to perform fast compression and expansion as doing so generates waves that disturb the surface tension measurements by the Wilhelmy plate (94). Third, the Langmuir trough has difficulties in studying the effect of biological ligands in the aqueous layer of the tear film. The aqueous layer contains electrolytes, peptides, and proteins, mainly lipocalin (95), lysozyme (96), and lactoferrin (97). It is not unexpected that these ligands interact with the TFL during normal physiological conditions. However, the Langmuir trough commonly requires a large aqueous subphase of at least 100 mL, which complicates the study of any potential surface interaction and molecular recognition between the TFL and biological ligands in the aqueous layer.

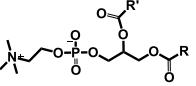
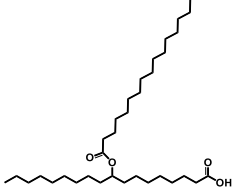
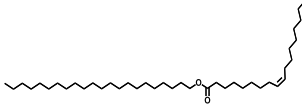
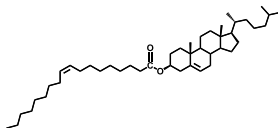
Here, we studied the biophysical properties of a model TFL using a novel experimental methodology called the constrained drop surfactometry (CDS). CDS is a new generation of droplet-based surface tensiometry that we developed initially for studying the biophysical

properties of pulmonary surfactant films (98, 99). We have shown that CDS is superior to previous *in vitro* methods in permitting high-fidelity biophysical simulations of pulmonary surfactant films by precisely controlling the physiologically relevant experimental conditions, such as the core body temperature, highly dynamic compression and expansion cycles, and adsorption from high surfactant concentrations (100-102). Given the biophysical similarities between the pulmonary surfactant film and the TFLL (103), we hypothesize that CDS would be an ideal *in vitro* model for biophysical simulations of the TFLL. Using CDS, we have systematically studied the surface properties of various tear lipid films (TLFs) closely relevant to the natural TFLL. These TLFs are behenyl oleate (BO) and cholesteryl oleate (CO) representing the most abundant wax ester (WE) and cholesteryl ester (CE) in the TFLL, respectively (104). Phosphatidylcholine (PC) and palmitic-acid-9-hydroxy-stearic-acid (PAHSA) represent the two predominant polar lipid classes in the TFLL. PAHSA and OAHFAs both belong to a structurally similar general class of lipids named fatty acid esters of hydroxy fatty acids (FAHFAs), which are lipids consisting of two acyl chains connected through a single ester bond (82). Although OAHFAs differ from PAHSA in the length of their hydroxy fatty acids and the location of the hydroxy esterification, the structural similarity shared by these two lipids could result in comparable surface activities. Our data suggest a distinctive composition-function correlation for the lipid components in the TFLL. While the major biophysical function of phospholipids in the TFLL is to reduce the surface tension, the primary function of FAHFAs is to optimize the surface rheological properties of the TFLL. These findings have novel implications in better understanding the physiological and biophysical functions of the TFLL, and may offer new translational insight in the treatment of DED.

2.2 Materials and methods

2.2.1 Materials

Table 2.1 Lipids studied in the biophysical simulations of the tear lipid films.

Lipid	Chemical formula	Chemical structure	Chemical supplier	Purity	Molecular weight (g/mol)	Melting temperature
L- α -phosphatidylcholine (PC)	C16:0 (33%) C18:1 (32%) C18:2 (17%) C18:0 (12%) Others (6%)		Sigma-Aldrich	99%	~770	-15 - -7 °C
Palmitic-acid-9-hydroxy-stearic-acid (PAHSA)	C ₃₄ H ₆₆ O ₄ (C18:0-C16:0)		Sigma-Aldrich	95%	539	33.5 °C
Behenyl oleate (BO)	C ₄₀ H ₇₈ O ₂ (C22:0-C18:1)		Larodan	99%	591	38 °C
Cholesteryl oleate (CO)	C ₄₅ H ₇₈ O ₂ (C18:1-Cholesterol)		Sigma-Aldrich	98%	651	44-47 °C

L- α -phosphatidylcholine (PC), palmitic-acid-9-hydroxy-stearic-acid (PAHSA), behenyl oleate (BO), and cholesteryl oleate (CO) were purchased and used without further purification. Physicochemical properties, chemical structures, and sources of these lipids are summarized in **Table 2.1**. Individual lipids were dissolved in chloroform as 1 mM stock solutions. Lysozyme, being a major protein found in the aqueous layer of the tear film (84), was purchased from Sigma-Aldrich. Phosphate-buffered saline (PBS) was purchased from Fisher Scientific. Water used was Milli-Q ultrapure water with a resistivity greater than 18 M Ω -cm at room temperature.

2.2.2 Constrained drop surfactometry (CDS)

Constrained drop surfactometry (CDS) is a new-generation of droplet-based surface tensiometry technique developed in our laboratory (98, 99). It uses the air-water surface of a sessile drop (~4 mm in diameter, ~0.3 cm² in surface area, and ~20 μ L in volume) to accommodate the

spread or adsorbed film. As shown in **Figure 2.1b**, a key design of the CDS is a carefully machined pedestal that uses its knife-sharp edge to prevent film leakage even at very low surface tensions. System miniaturization of the CDS facilitates rigorous control of the experimental conditions with an environmental control chamber. The spread/adsorbed film at the droplet surface can be compressed and expanded by precisely controlling oscillation of the surface area of the droplet using a newly developed mechatronic system called closed-loop axisymmetric drop shape analysis (CL-ADSA) (105). CL-ADSA determines the surface tension of the spread/adsorbed film by analyzing the shape of the film-covered droplet. The surface pressure (π) can be determined from the surface tension (γ) using $\pi = \gamma_0 - \gamma$, with γ_0 being the surface tension of a clean, surfactant-free air-water surface.

Specifically, a trace amount of the lipid sample was spread onto the air-water surface of a 10 μL droplet that works as an aqueous subphase to the TFL. To study the effect of chemicals in the subphase, the droplet was switched among the pure water, saline, PBS, or 1 mM lysozyme solution, respectively. The spread film was left undisturbed for 1 min to allow evaporation of solvent. The droplet was then slowly expanded to decrease the surface pressure to around zero (*i.e.*, increasing the surface tension to around 70 mN/m). Subsequently, the spread lipid film was compressed and expanded at two extreme rates, *i.e.*, 0.15 and 15 relative area per second (A%/s), and at two different environmental temperatures, *i.e.*, 20 and 34 $^{\circ}\text{C}$, respectively.

The TFL spread on the ocular surface of human eyes has an approximate surface area of 1-3 cm^2 (106), which is only three to ten times larger than the surface area of the sessile drop used in CDS (*i.e.*, approximately 0.3 cm^2). Given the maximum eyelid speeds in the range of 0.1-0.3 m/s and the time period of a typical unforced blink at 0.3 s (107), the film compression rate of the TFL during a typical blink is estimated at approximately 10 cm^2/s . The high compression rates

of 15 A%/s used in our experiments corresponds to 0.045 cm²/s, which is still 200 times slower than the actual blinking process. Nevertheless, the compression rate of 15 A%/s used in our experiments is significantly higher than the maximum possible compression rate of a Langmuir trough. This high compression rate is used to study the kinematic effect of TFL under physiologically relevant conditions, in comparison to quasi-static compressions at the rate of 0.15 A%/s.

The lipid film was compressed and expanded for a least of five cycles. Usually after the first cycle, the compression and expansion isotherms became repeatable. The fifth cycle was investigated as representative of the surface activity of lipid films. Surface activity of the lipid films were quantified with the maximum surface pressure (π_{\max}) reached at the end of film compression, and the average film compressibility $\kappa = \frac{1}{A} \frac{\partial A}{\partial \gamma}$.

2.2.3 Interfacial dilational rheology

Detailed experimental protocols for determining the surface dilational modulus $E = \frac{d\gamma}{d \ln A}$ of the lipid films using CDS can be found elsewhere (108, 109). Briefly, surface area of the spread lipid films was oscillated in a sinusoidal waveform, with a series of predefined frequencies (0.025, 0.05, 0.1, 0.25, 0.5, and 1 Hz) and amplitude (10% of the initial surface area), using CL-ADSA. The surface tension response to the surface area oscillation was recorded as the output, and was compared against the surface area oscillation waveform as the input. The elastic (E_r) and viscous (E_i) components of the surface dilational modulus were determined from the phase shaft (φ) between the input and output waveforms, and from the oscillation amplitudes of the surface area and the surface tension. The loss tangent ($\tan\varphi$) was calculated as the ratio between the viscous modulus and the elastic modulus (E_i/E_r). All measurements were carried out at 34 ± 1 °C for at least three times.

2.2.4 Statistical analysis

All results were shown as mean \pm standard deviation ($n > 3$). One-way ANOVA with Tukey's means comparison test was used to determine group differences (OriginPro, Northampton, MA). A value $p < 0.05$ was considered to be statistically significant.

2.3 Results

2.3.1 Surface activities of the tear lipid films

Figure 2.2 shows the compression and expansion isotherms of five characteristic tear lipid films (TLFs), at different temperatures (20 and 34 °C) and compression rates (0.15 and 15 A%/s), respectively. These lipid films are two individual polar lipids, *i.e.*, PC and PAHSA, the combined polar lipid films, *i.e.*, PC:PAHSA (3:1), the combined nonpolar lipid film, *i.e.*, BO:CO (1:1), and the recombinant model TFL, *i.e.*, BO:CO:PC:PAHSA (40:40:15:5). Pure water was used as the subphase in all of these experiments.

Figure 2.2a shows the compression and expansion isotherms of the five tear lipid films at room temperature with a quasi-static cycling rate of 0.15 A%/s. These results are comparable to those obtained with the Langmuir trough under similar experimental conditions (80, 85). As shown in Figure 2.2a, among the two polar lipid films, PC collapses at 46 mN/m; but PAHSA collapses at a much lower surface pressure of only 25 mN/m. The combined polar lipid film, *i.e.*, PC:PAHSA shows a similar surface activity as PC. But the compression isotherms shift slightly to the left, indicating gradual squeeze-out of PAHSA from the combined polar lipid film. The combined nonpolar film, *i.e.*, BO:CO (1:1), is nearly infinitely compressible, and shows moderate surface pressure increase only at an extreme film compression below $50 \text{ \AA}^2/\text{molecule}$. The recombinant model TFL, *i.e.*, BO:CO:PC:PAHSA (40:40:15:5), shows similar isotherm shape and collapse pressure as PC, except for significantly shifting the isotherms to the left. These results indicate that

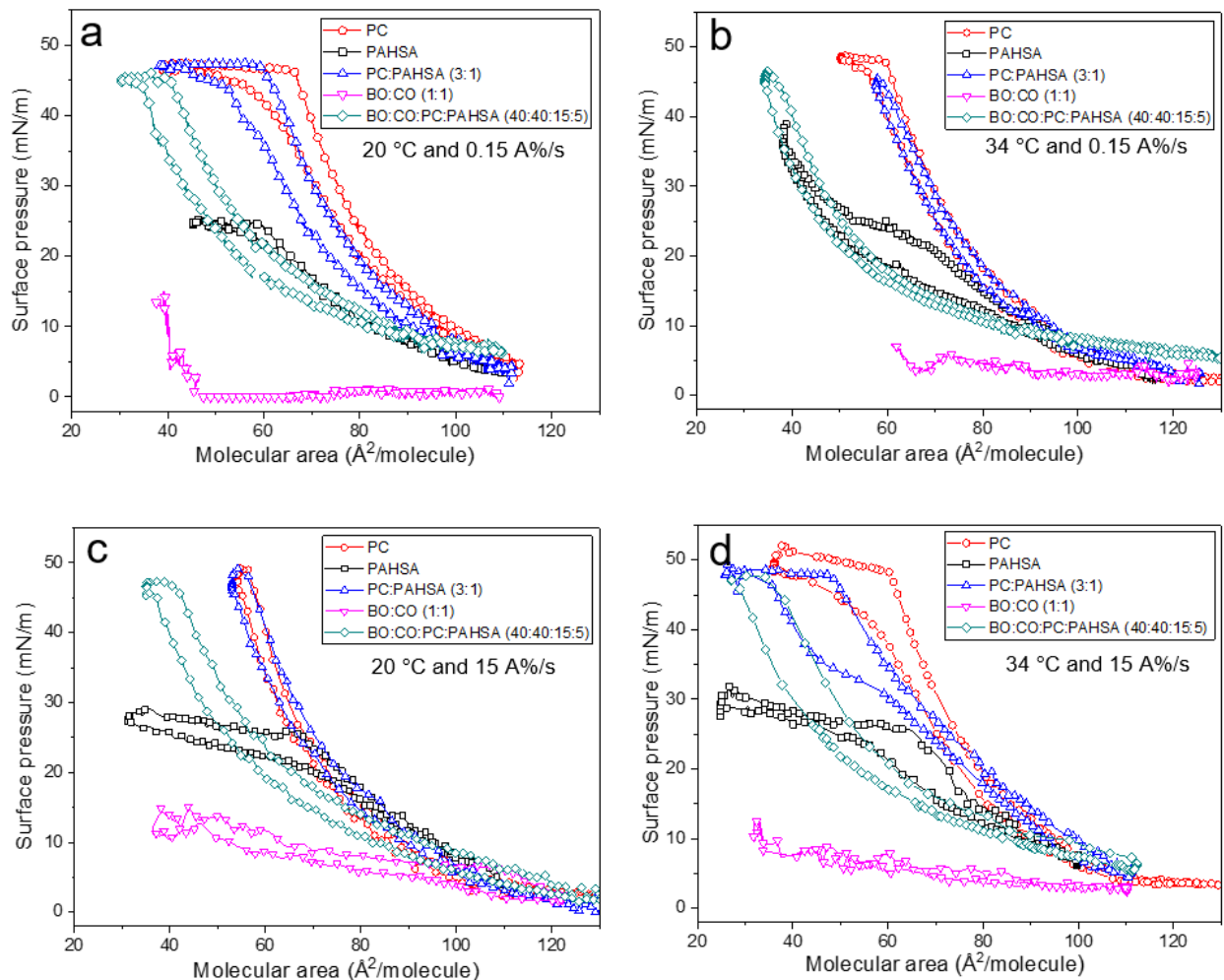


Figure 2.2 Effect of temperature and compression rate on the surface activity of tear lipid films (TLFs). Compression-expansion isotherms of PC, PAHSA, PC:PAHSA (3:1), BO:CO (1:1), and BO:CO:PC:PAHSA (40:40:15:5) at (a) room temperature and a low compression rate (0.15 A%/s), (b) 34 °C and the low compression rate (0.15 A%/s), (c) room temperature and a high compression rate (15 A%/s), (d) the physiologically relevant temperature (34 °C) and high compression rate (15 A%/s).

PC plays a predominate role in controlling the surface activity of the model TFL, while the nonpolar lipids are squeezed out from the interfacial monolayer almost instantaneously, and most likely residing atop of the lipid monolayer due to the strong hydrophobicity of these nonpolar lipids.

Figure 2.2b shows the quasi-static compression and expansion isotherms of the five TLFs at 34 °C. It is found that increasing temperature to 34 °C did not have a significant effect on the lipid films other than PAHSA. This is not unexpected because the melting temperature of PC, *i.e.*, -15~7 °C, is much lower than either room temperature or the physiological temperature. However, the melting temperature of PAHSA, *i.e.*, 33.5 °C (Table 2.1), is very close to the physiological temperature of the TFL. Surprisingly, it is found that the surface pressure of PAHSA increases to more than 40 mN/m at 34 °C; while it collapses at 25 mN/m at room temperature.

Figure 2.2c shows the dynamic compression and expansion isotherms of the five TLFs at room temperature. In comparison to quasi-static processes at the same temperature (Figure 2.2a), both PAHSA and nonpolar lipids shows kinetically-driven increase in surface pressure. Figure 2d shows the compression and expansion isotherms of the five TLFs under physiologically relevant conditions, *i.e.*, 34 °C and a high compression rate 100 times of that used in the quasi-static process. It is found that all TLFs containing PC collapse at around 50 mN/m. With reducing PC content, the compression isotherms shift to the left. Together with those shown in Figure 2a-c, all results indicate that PC, although accounting for only 15% of the model TFL, plays the predominant role in reducing surface tension (*i.e.*, increasing surface pressure) of the TFL. Another polar lipid, PAHSA collapses at the surface pressure around 30 mN/m, indicating that the primary biophysical role of PAHSA is not surface tension reduction. The nonpolar lipids are mostly not surface active.

Statistical analyses of the surface activity of the TLFs under various experimental conditions are summarized in **Figure 2.4a** and **b**, which shows the maximum surface pressure (π_{\max}) and film compressibility (κ), respectively. Since the nonpolar lipid film BO:CO is essentially infinitely compressible, its compressibility is not shown in Figure 2.4b. It can be seen that the π_{\max} of the model TFL is largely determined by PC. Film compressibility (κ) measures the “hardness” of a

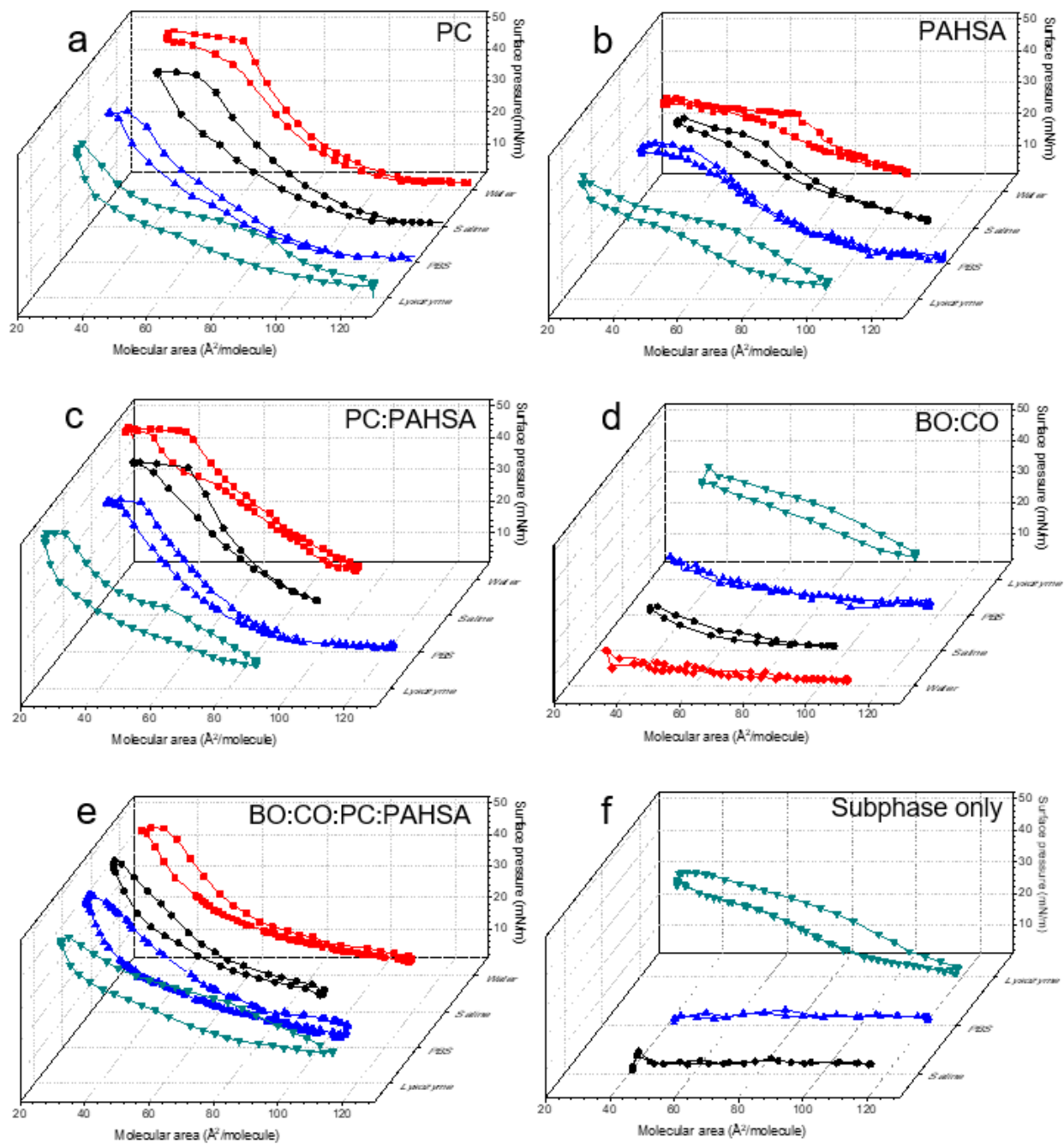


Figure 2.3 Effect of subphase composition on the surface activity of tear lipid films (TLFs). Compression-expansion isotherms of (a) PC, (b) PAHSA, (c) PC:PAHSA (3:1), (d) BO:CO (1:1), (e) BO:CO:PC:PAHSA (40:40:15:5), and (f) subphase alone without TLFs. For each TLF, four subphases with increasing complexity of chemical composition were studied. These were pure water, saline (0.9 wt%), PBS, and the lysozyme solution (1 mM), respectively. All biophysical simulations were conducted at the physiologically relevant temperature (34 °C) and high film compression rate (15 Å%/s).

two-dimensional material, such as the lipid film. A low κ indicates an incompressible “hard” film, while a high κ indicates a “soft” film (94). As shown in Figure 2.4b, among the two polar lipids studied, κ of PC at the physiologically relevant condition is 0.97 m/mN. In comparison, κ of PAHSA appears to be insensitive to the experimental conditions and maintains a nearly constant value of 1.7 m/mN at all temperatures and compression rates. Under the same experimental condition, κ increases with reducing PC contents of the lipid films. At the physiological relevant condition, κ of PC, PC:PAHSA, and BO:CO:PC:PAHSA gradually increases from 0.7 to 1.4. These results indicate that PAHSA, although not contributing to directly decreasing surface tension of the TFL, plays a role in “softening” the TFL by increasing its compressibility.

Figure 2.3 shows the effect of four different subphases on the surface activity of the TLFs. These subphases are, with the increasing chemical complexity, pure water, saline (0.9 wt%), PBS, and 1 mM lysozyme solution. All compression and expansion isotherms were obtained at the physiologically relevant conditions of 34 °C and high compression rate. Being a control, Figure 2.3f shows the compression and expansion isotherms of the subphases alone, *i.e.*, without TLFs. It is clear that neither saline nor PBS is surface active, but lysozyme demonstrates a moderate surface activity, up to surface pressure 30 mN/m at the end of compression.

For the three PC-containing TLFs (Figure 2.3a, c, and e), the effect of subphase on the compression and expansion isotherms is only moderate, expect that lysozyme increases the hysteresis of the compression and expansion loop. For PAHSA and BO:CO (Figure 2.3b and d), lysozyme significantly increases the surface pressure. In comparison with the TLF-free control (Figure 2.3f), the influence of lysozyme on PAHSA and BO:CO must be due to adsorption of lysozyme at the air-water surface, thus dominating the surface activity of these two less surface active TLFs.

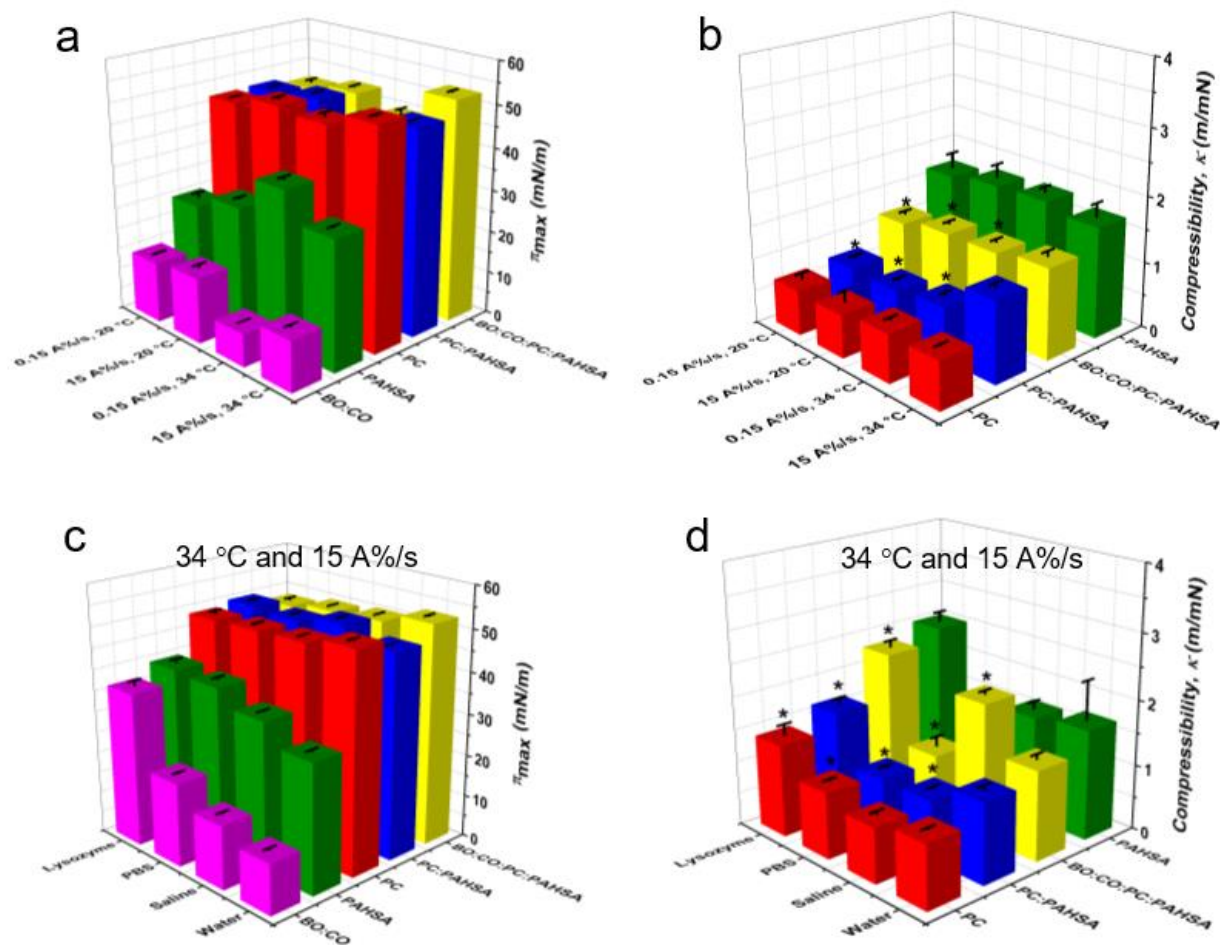


Figure 2.4 Statistical analysis of the surface activity of tear lipid films (TLFs). (a, b) The maximum surface pressure (π_{max}) and film compressibility (κ) of TLFs at different temperatures (20 and 34 °C) and compression rates (0.15 and 15 A%/s), with the pure water subphase. (c, d) The π_{max} and κ of TLFs at the physiologically relevant conditions (34 °C and 15 A%/s compression rate) in the presence of various subphases. * $p < 0.05$ indicates statistically significant differences.

Statistical analyses of the effect of subphase on the TLFs under the physiologically relevant conditions of 34 °C and high compression rate are summarized in **Figure 2.4c** and **d**, which shows the π_{max} and κ , respectively. As shown in Figure 2.4c, the three PC-containing TLFs, *i.e.*, PC, PC:PAHSA, and BO:CO:PC:PAHSA, are all capable of reaching a π_{max} around 50 mN/m regardless of the subphase. However, the subphase significantly affects the two lipid films without PC, *i.e.*, BO:CO and PAHSA. The π_{max} of these two TLFs increases with increasing chemical

complexity of the subphase. While the surface pressure increase of BO:CO with lysozyme may be easily explained by the adsorption of this protein to the air-water surface, as also found in previous studies (84, 89, 110), the case of PAHSA with lysozyme appears to be more complicated. The π_{\max} of PAHSA increases from 30 to 40 mN/m when the subphase is changed from pure water to 1 mM lysozyme. Since the π_{\max} of lysozyme alone is only 30 mN/m (Figure 2.3f), these results must indicate certain synergetic effect or molecular recognition between PAHSA at the surface and lysozyme in the subphase. Similar effect of molecular interactions is also revealed by the κ . As shown in Figure 2.4d, κ of PAHSA increases from 1.7 to 2.5 m/mN with lysozyme in the subphase. Consequently, κ of the model TFL increases from 1.5 to 2.1 m/mN, indicating a significant increase in softness.

2.3.2. Surface rheological properties of the tear lipid films

Figure 2.5a and b shows the elastic (E_r) and viscous (E_i) moduli of four TLFs, *i.e.*, PC, PAHSA, PC:PAHSA, and BO:CO:PC:PAHSA. All surface dilational moduli were determined at a characteristic surface pressure of 20 mN/m at 34 °C, using pure water as the subphase, under a series of frequencies of 0.025, 0.05, 0.1, 0.25, 0.5, and 1 Hz. Given the average duration of each blink for 0.1-0.3 second (92), the oscillation frequency of 1 Hz is of physiological relevance. The nonpolar lipid film, *i.e.*, BO:CO, was not studied since it does not reach the characteristic surface pressure of 20 mN/m.

It is found that the E_r of all TLFs at all frequencies is significantly larger than their E_i , indicating that all TLFs are more elastic than viscous. The E_r of all TLFs increases slightly with frequency. The E_r of PC is more than twice that of PAHSA (90 vs. 40 mN/m). Addition of nonpolar lipids, *i.e.*, BO:CO, significantly decreases the E_r of the model TFL. The E_r of PAHSA and BO:CO:PC:PAHSA is close at the physiologically relevant frequency of 1 Hz.

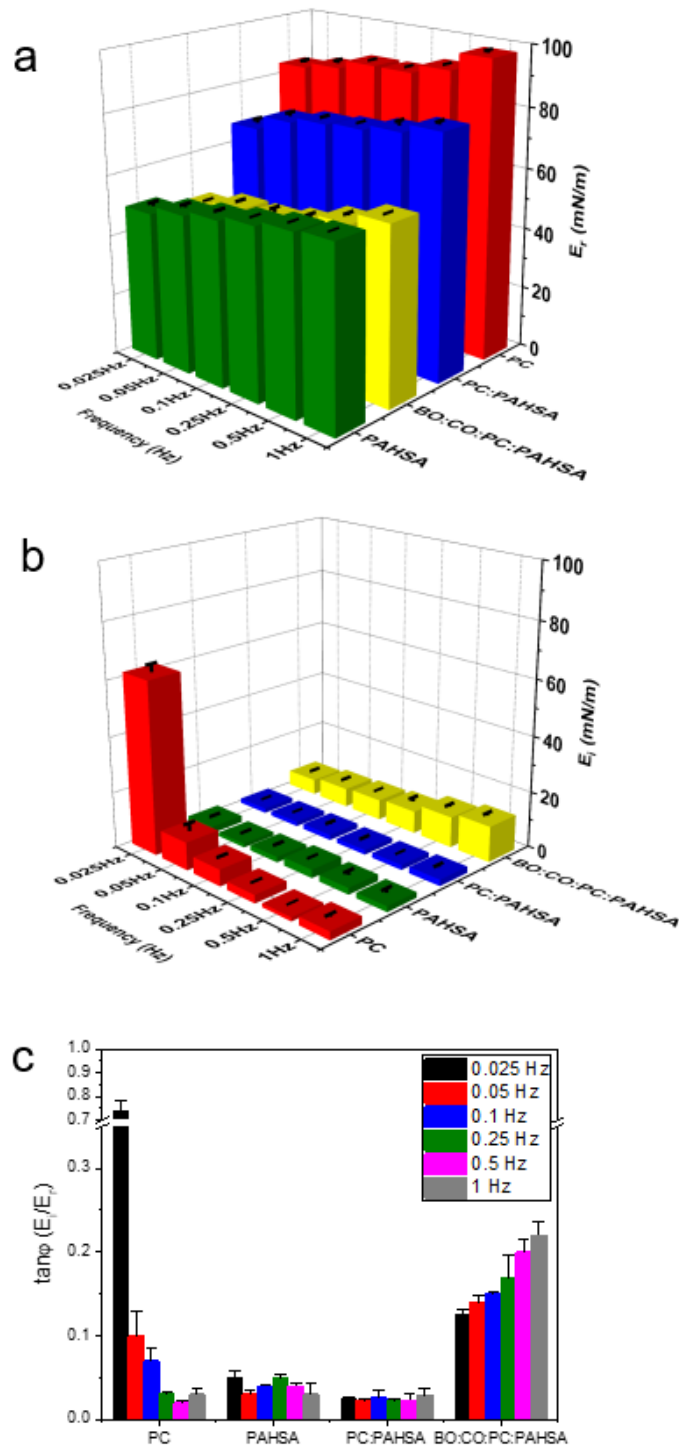


Figure 2.5 Interfacial dilational rheological properties of tear lipid films (TLFs). (a) Elastic (E_r) and (b) viscous (E_i) surface dilational moduli, and (c) the loss tangent ($\tan\phi$) of PC, PAHSA, PC:PAHSA (3:1), and BO:CO:PC:PAHSA (40:40:15:5), at frequencies of 0.025, 0.05, 0.1, 0.25, 0.5, and 1 Hz. All interfacial rheological properties were determined at the characteristic surface pressure of 20 mN/m and 34 °C.

The E_i of all TLFs at all frequencies is less than 15 mN/m, except for PC at a very low frequency of 0.025 Hz. The E_i of PC decreases to a value of 3 mN/m at 1 Hz. In comparison, the E_i of PAHSA and PC:PAHSA is relatively independent from the oscillation frequency and maintains a low value less than 3 mN/m for all studied frequencies. The E_i of BO:CO:PC:PAHSA, on the other hand, increases slightly with the increasing frequency, to approximately 13 mN/m at the physiologically relevant frequency of 1 Hz.

Figure 2.5c shows the tangent of loss angle, also known as the loss tangent ($\tan\phi$), as a function of the oscillation frequency. In general, the $\tan\phi$ of PC decreases with the increasing frequency, and reaches a value less than 0.05 when the oscillation frequency is higher than 0.25 Hz. In comparison, the $\tan\phi$ of PAHSA and PC:PAHSA is relatively insensitive to the frequency, and remains at a low value less than 0.05 at all tested frequencies. The addition of nonpolar lipids, *i.e.*, BO:CO, into the model TFL significantly increases the $\tan\phi$ above 0.1, indicating a more viscous film than those without the nonpolar lipids. Interestingly, the addition of nonpolar lipids not only increases the $\tan\phi$ of the TFL but also changes its frequency dependency. It is found that the $\tan\phi$ of BO:CO:PC:PAHSA increases with the oscillation frequency, and reaches a value larger than 0.2 at the physiologically relevant frequency of 1 Hz.

2.4 Discussion

The major physiological function of the TFL is to stabilize the tear film by reducing surface tension and retarding evaporation of the aqueous layer (67, 111). However, the specific surface active components of the TFL are still under investigation. Our biophysical studies found that a model TFL that consists of BO:CO:PC:PAHSA (40:40:15:5) is capable of reaching a surface pressure as high as 50 mN/m under physiologically relevant conditions (Figure 2.2). This surface pressure corresponds to a surface tension of 20 mN/m, which is much lower than the surface

tension of whole tears, reported to be around 43-46 mN/m (86, 106, 112). In addition, we found that these surface tension values of whole tears reported in literatures are in line with the surface tension of major proteins in the tear aqueous layer, such as lysozyme (Figure 2.3). Our study therefore suggested that the static surface tension of whole tears determined in previous studies mostly reflect the equilibrium surface tension of soluble proteins in the tear (113) rather than the dynamic surface tension of the TFLL. Being an insoluble lipid film, the TFLL is capable of reducing the surface tension significantly lower than that of the whole tears when the TFLL is compressed during a blink (65).

Using recombinant lipid films, we have studied the composition-function correlation of the individual lipid components in the TFLL. Our study suggests that phospholipids are most likely to be the primary components that are responsible for reducing the surface tension of the TFLL (Figures 2.2-2.4). The minimum surface tension of the model TFLL is close to the equilibrium surface tension (γ_e) of PC after *de novo* adsorption at the air-water surface (114). Since the model TFLL contains only 15% PC, the TFLL must reach the γ_e of PC by selectively removing other lipids during the highly dynamic process of film compression caused by a blink. Such a process is called “squeeze-out”, likely similar to the biophysical mechanism by which pulmonary surfactant films reduce the surface tension during respiration (94, 102, 115).

Most interestingly, we found that the major biophysical function of another polar lipid in the model TFLL, *i.e.*, PAHSA, is not to reduce the surface tension but to optimize the interfacial dilational rheology of the TFLL. When a monolayer that consists of a mixture of lipids is compressed, the maximum surface pressure that the monolayer can sustain, *i.e.*, its collapse pressure, depends on the lipid component with the highest collapse pressure (116). The maximum surface pressure of PAHSA is only 30 mN/m, which is significantly lower than that of PC. Hence,

it is unlikely that PAHSA contributes to the biophysical function of TFLM by reducing its surface tension.

Dilational rheological studies provide knowledge about the viscoelastic properties of the TFLM (65). At the physiologically relevant conditions and frequency of 1 Hz, we have measured the elastic (E_r) and viscous (E_i) moduli of the model TFLM to be 58 and 13 mN/m, respectively (Figure 2.5). These dilational rheological data are in good agreement with those reported by Raju *et al.* (117). Using a pendant drop method, these workers have determined the E_r and E_i of human Meibomian lipid films at 37 °C to be approximately 40 and 10 mN/m, respectively. Therefore, our study confirms that the TFLM is overwhelmingly more elastic than viscous under physiologically relevant conditions (117-119).

More importantly, using recombinant lipid films, we have found that there are distinct differences in the viscoelastic properties between the two polar lipid components in the model TFLM, *i.e.*, PC and PAHSA. One striking difference between these two polar lipids is that the E_i of PC decreases significantly with increasing frequency, especially in the low frequency range. But the E_i of PAHSA is relatively independent of the oscillation frequency and maintains a low value for all studied frequencies. Our dilational rheological measurements of PC are in general agreement with those reported by Wüstneck *et al.* (120). Using captive bubble surfactometry, these workers found that the E_r of dipalmitoyl phosphatidylcholine (DPPC) with 2 mol% surfactant protein C was relatively independent of the frequency, but its E_i decreases significantly with increasing frequency, especially in the low frequency range. In contrast, we found that not only does PAHSA alone demonstrate a low E_i in a large range of oscillation frequencies, addition of PAHSA, even at a small amount, such as in PC:PAHSA (3:1) and BO:CO:PC:PAHSA

(40:40:15:5), is able to significantly reduce the viscosity of the mixed lipid films for all tested frequencies (Figure 2.5b).

This unique property of PAHSA to damp down the viscosity of lipid films and thus to minimize energy dissipation during highly dynamic film oscillation is most likely attributed to its unique molecular structure (Table 2.1). Both PAHSA and OAHFAs belong to the general lipid class of fatty acid esters of hydroxy fatty acids (FAHFAs), which are lipids with potent anti-diabetic and anti-inflammatory activities (121, 122). OAHFAs differ from the other FAHFAs in that their hydroxy fatty acid backbones are ultra-long, typically around 26-34 carbons in length, and their hydroxy esterification is believed to be solely at the terminal (ω -) position (82). Being a palmitic acid (C16:0) ester of 9-hydroxy stearic acid (C18:0), the hydroxy fatty acid backbone of PAHSA is much shorter than that of OAHFAs. In addition, PAHSA lacks the acyl chain unsaturation in OAHFAs since oleic acid (C18:1) has been identified as the most abundant acyl chain in OAHFAs of the human TFL (123). In spite of these differences, PAHSA and OAHFAs share critical structural similarity that predominates their surface activities. Namely, both PAHSA and OAHFAs maintain their amphiphilicity through two hydrophilic moieties favoring contact with water, *i.e.*, a relatively strong contact point through the negatively charged carboxyl group and a relatively weak contact point *via* the polar ester group. Consequently, PAHSA appears to be a plausible alternative to understand the biophysical properties of FAHFAs in general and of OAHFAs in specific, to a reasonable extent.

In contrast to phospholipid molecules, which have only one hydrophilic moiety (*i.e.*, their phosphate headgroups), the unique structure of PAHSA molecules entails a new degree of rotational freedom when the lipid film is compressed. In other words, upon highly dynamic compression, the PAHSA molecules at the air-water surface may be able to fold and/or rotate with

either one or both hydrophilic moieties in contact with water, depending on the surface area available to the PAHSA molecules. Such intramolecular folding and/or rotation, in spite of not significantly increasing the surface activity, make PAHSA much more efficient than PC in storing the kinetic energy of lateral compression, thus rendering a highly elastic film. We have explored the molecular biophysical mechanism of PAHSA in more details in an accompanying chapter.

Similar conclusions can be drawn by examining the loss tangent ($\tan\phi$), which is the ratio between the viscous and the elastic moduli. A perfect elastic material, such as most metals, has a near-zero loss tangent (124). We found that different from PC, which has a very high loss tangent at low frequencies, PAHSA maintains a low loss tangent less than 0.05 for all tested frequencies. Addition of PAHSA to PC, *i.e.*, PC:PAHSA (3:1), decreases its loss tangent from ~ 0.7 to ~ 0.03 at the frequency of 0.025 Hz. The unique viscoelastic property of PAHSA makes the film behave as an elastic solid. This property of PAHSA, likely also that of OAHFAs, is of particular benefit for the TFL since it contains a large portion ($\sim 80\%$) of highly viscous, nonpolar lipids, such as BO and CO, with melting points significantly higher than those of the polar lipids in the TFL (Table 2.1). It can be seen that the addition of only 5% PAHSA helps maintain the loss tangent of the model TFL at a value not much higher than 0.2 (Figure 2.5c). It should be noted that the elasticity of the model TFL is significantly higher than that of natural pulmonary surfactant films. The loss tangent of natural pulmonary surfactants, which consist of mostly phospholipids without FAHFAs, was found to be approximately 0.4, determined under similar experimental conditions (102). This comparison highlights the importance of FAHFAs in optimizing the rheological properties of the TELL. It is known that the viscosity of TELL of patients with meibomian gland dysfunction increases (65, 118, 125), whereas the level of OAHFAs in dry eye diseases.

2.5 Summary

By studying surface and dilational rheological properties of recombinant lipid films under physiologically relevant conditions, we have studied the composition-function correlations of a model TFLL that consists of BO:CO:PC:PAHSA (40:40:15:5). We have concluded that the major biophysical function of phospholipids in the TFLL is to reduce the surface tension, while the primary function of PAHSA is to regulate interfacial rheology of the TFLL, thus optimizing the viscoelastic properties of the TFLL under physiologically relevant conditions. These findings have novel implications in better understanding the physiological and biophysical functions of the TFLL, and may offer new translational insight to the treatment of dry eye disease.

Chapter 3 Polymorphism of fatty acid esters of hydroxy fatty acids ¹

3.1 Introduction

Fatty acid esters of hydroxy fatty acids (FAHFAs) are molecules that contain a hydroxy fatty acid esterified by a fatty acid (126). Being a newly discovered class of endogenous lipids with potent anti-diabetic and anti-inflammatory activities (121, 122), FAHFAs exist in an extremely low abundance in natural sources, including humans, animals, plants and foods (127-129). Being a unique species of FAHFAs, (O-acyl)- ω -hydroxy fatty acids (OAHFAs) differ from other FAHFAs in that their hydroxy fatty acid backbones are ultra-long, typically around 26-34 carbons in length, and their hydroxy esterification is believed to be solely at the terminal (ω -) position (82).

Only in recent years with technological advances in lipidomics have OAHFAs been identified as an important component of the meibomian lipids (58, 61-63). Being the only polar lipid class other than phospholipids in the tear film lipid layer (TFLL), OAHFAs account for approximately 4 mol% of the total lipids and 20 mol% of the polar lipids (62, 130). OAHFAs appear to play a significant physiological and biophysical role in eye health since it is the only class of lipids found to decrease in dry eye (131, 132). Direct contribution of OAHFA deficiency to dry eye disease was recently established with Cyp4f39-knockout mice that exhibited damaged corneal epithelium and shortening of tear film break-up time (133). The latest human study suggested that OAHFAs might be used as a biomarker for dry eye disease (134). However, compared to other lipids, biophysical study of OAHFAs is still scarce, likely in part due to technical difficulties in purifying

¹ Xu X, Kang C, Sun R, Zuo YY, Biophysical properties of tear film lipid layer II. Polymorphism of FAHFA. *Biophys. J.* 121 (2022) 451-458.

large quantities of these lipids from complex meibomian gland secretions. The biophysical function of OAHFAs and their contribution to the TFL are still poorly understood (51, 123, 133).

In a companion paper, we have studied the composition function correlations of a recombinant artificial TFL, under physiologically relevant conditions (135). Our artificial TFL was composed of 40% behenyl oleate and 40% cholesteryl oleate that represent two nonpolar lipid classes, i.e., wax ester and cholesteryl ester in the natural TFL, and 15% phosphatidylcholine and 5% palmitic-acid-9-hydroxy-stearic-acid (PAHSA) that represent the two predominant polar lipid classes in the natural TFL (104). It should be noted that human meibomian lipids are composed of a complex mixture of different lipid classes, and each lipid class consists of numerous homologous lipid species varying in lengths, degrees of unsaturation, and branching (51, 62, 104). The major wax esters and cholesteryl esters found in human meibum are much longer than behenyl oleate and cholesteryl oleate used in our artificial TFL (63, 136, 137). Moreover, PAHSA used in our artificial TFL is only a remote model of OAHFAs. Due to its function in metabolic regulation and potential in glucose control, PAHSA has become the most extensively studied FAHFAs (126, 138), and it is readily available from commercial sources. We used PAHSA as an analog of OAHFAs to study the biophysics of TFL since they share critical structural similarity that predominates their surface activities. Namely, both PAHSA and OAHFAs maintain their amphiphilicity through two hydrophilic moieties favoring contact with water, i.e., a relatively strong contact point through the negatively charged carboxyl group and a relatively weak contact point via the polar ester group. On the other hand, it is also important to understand the structural differences between these two FAHFAs. First, the hydroxy fatty acid backbone of PAHSA (C18) is much shorter than that of OAHFAs (C26-34). Second, PAHSA lacks the acyl chain unsaturation in OAHFAs since oleic acid (C18:1) has been identified as the most abundant acyl chain in

OAHFAs (17). Third, with the ester group located at either the 9- or 5-position, PAHSA has a branched structure, whereas OAHFA should have a linear structure since its ester group is located at the ω -position (1).

In line with findings by other workers (139, 140), our biophysical study suggested that the primary function of FAHFAs in the TFL is not to reduce the surface tension (135). Rather, our study suggested that the main biophysical function of FAHFAs is to optimize the rheological properties of the TFL (135). To further scrutinize the molecular mechanism by which the FAHFAs regulate and optimize the biophysical function of the TFL, here we studied the detailed phase behavior of PAHSA molecules at the air-water surface, using combined *in vitro* biophysical simulations with constrained drop surfactometry (CDS), direct film imaging with atomic force microscopy (AFM), and *in silico* all-atom molecular dynamics (MD) simulations. We found that the biophysical properties of a dynamic PAHSA monolayer under physiologically relevant conditions depend on a balance between kinetics and thermal relaxation. Owing to their unique molecular structures of dual hydrophilic moieties, PAHSA molecules at the air-water surface demonstrate unique polymorphic behaviors and various collapse mechanisms. These findings could have novel implications in understanding the biophysical functions that FAHFAs, in general, or OAHFAs, specifically, play in the TFL.

3.2 Materials and methods

3.2.1 Materials

Palmitic-acid-9-hydroxy-stearic-acid (PAHSA, C:18:0-C16:0) was purchased from Sigma-Aldrich and used without further purification. PAHSA was dissolved in chloroform as 1 mM stock solutions. Water used was Milli-Q ultrapure water with a resistivity greater than 18 M Ω -cm at room temperature.

3.2.2 Constrained drop surfactometry (CDS)

CDS is a new-generation of droplet-based surface tensiometry technique developed in our laboratory (98). Detailed description of CDS can be found in the companion paper (135). Briefly, a trace amount of PAHSA was spread onto the air-water surface of a 10-mL droplet. The spread film was left undisturbed for 1 min to allow evaporation of solvent. The droplet was then slowly expanded to decrease the surface pressure to around zero (i.e., increasing the surface tension to around 70 mN/m). Subsequently, the spread lipid film was compressed at two extreme rates, i.e., 0.15 and 15 relative area per second (A%/s), and at two different environmental temperatures, i.e., 20 °C and 34 °C, with the latter representing the physiologically relevant temperature of the ocular surface. The low compression rate of 0.15 A%/s was used in our experiments to represent a quasi-static process, whereas the high compression rate of 15 A%/s was used to introduce sufficient kinematic effects into the study of the TFL.

3.2.3 Atomic force microscopy (AFM)

Lateral structure and topography of the PAHSA film were studied with the combination of *in situ* Langmuir-Blodgett (LB) transfer from the CDS and atomic force microscopy (AFM) (102). The lipid film was first LB transferred from the droplet by lifting a small piece of freshly peeled mica sheet at a speed of 1 mm/min. During the LB transfer process, the surface pressure of the lipid film was maintained at a constant value using closed-loop axisymmetric drop shape analysis (CL-ADSA) (105). Topographical images of the lipid film were obtained with an Innova AFM (Bruker, Santa Barbara, CA). Samples were scanned in air in contact mode using a silicon nitride cantilever with a spring constant of 0.12 N/m and a tip radius of 2 nm. Relative height differences between domains were determined with bearing analysis using Nanoscope Analysis (version 1.5).

3.2.4 Molecular dynamics simulations

All-atom molecular dynamics (MD) simulations were performed to study the molecular organization of PAHSA molecules at the air-water surface. The force field of PAHSA parameterization was carried out using existing molecules in the CHARMM lipid force field (29). The simulation box contained two symmetric PAHSA monolayers separated by a layer of TIP3 water of at least 4 nm thick. Periodic boundary conditions were enforced in all three directions. The system was generated using the PACKMOL software (141, 142) and contained a total of 162 PAHSA molecules, i.e., 81 PAHSA per monolayer, 6186 TIP3 water molecules, and 17 ions of both Na⁺ and Cl⁻ that mimic the physiological ionic concentration of 0.15 M. An illustration of the MD simulation system is depicted in **Figure 3.3a**. Steepest descent energy minimization was carried out, followed by 100 ns of equilibration. The axial, i.e., direction perpendicular to the monolayer, dimension of the system was ~25 nm after equilibrium, and the lateral dimension of the system was controlled at 5.2 nm × 5.2 nm, 6.2 nm × 6.2 nm, and 7.2 nm × 7.2 nm. The large axial dimension eliminates any possible interaction between the two PAHSA monolayers across the periodic boundaries. By varying the lateral dimension of the simulation box, the average area per lipid molecule and the corresponding surface tension were systematically controlled (143-146). Systems of each lateral dimension were simulated for 400 ns after the equilibrium. All simulations were conducted under NVT conditions and at a constant temperature of 34 °C using the Nose-Hoover thermostat (147) in the GROMACS 2020.4 software package (148).

3.3 Results

3.3.1 Compression isotherms of the PAHSA film

Figure 3.1 shows the compression isotherms of the PAHSA monolayer at different temperatures (20 and 34 °C) and compression rates (0.15 and 15 A%/s), respectively. It is found

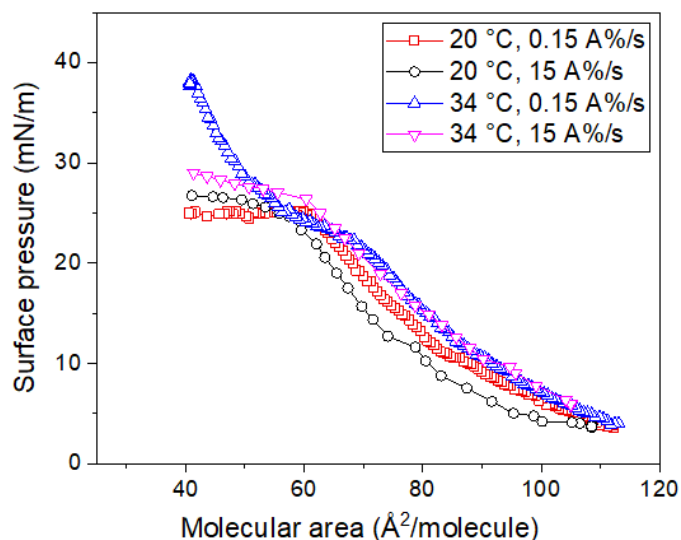


Figure 3.1 Compression isotherms of the PAHSA monolayer under four experimental conditions, i.e., 20 °C and a low compression rate of 0.15 A%/s, 20 °C and a high compression rate of 15 A%/s, 34 °C and 0.15 A%/s, and 34 °C and 15 A%/s.

that the compression isotherms of the PAHSA monolayer, at different temperatures and compression rates, are largely superimposed at the surface pressure lower than 25 mN/m. However, the collapse pressure (π_c) of the PAHSA monolayer differs under various experimental conditions. At 20 °C and slow compression, the PAHSA monolayer collapses at 25 mN/m. Increasing temperature to 34 °C, while maintaining the low compression rate, increases the π_c to 38 mN/m. The π_c of the PAHSA monolayer compressed at a high rate is found to be below 30 mN/m, at both 20 and 34 °C.

It should be noted that these results are rather surprising since the experimental temperature of 34 °C is higher than the melting temperature of PAHSA, i.e., 33.5 °C. Hence, the PAHSA monolayer at 34 °C is expected to be significantly more fluidic than that at 20 °C, while a lipid monolayer with a high fluidity usually instantaneously collapses upon quasi-static lateral compression without sustaining high surface pressures (149, 150). However, here we found that the π_c of the PAHSA monolayer at 34 °C, under quasi-static compression, is significantly higher

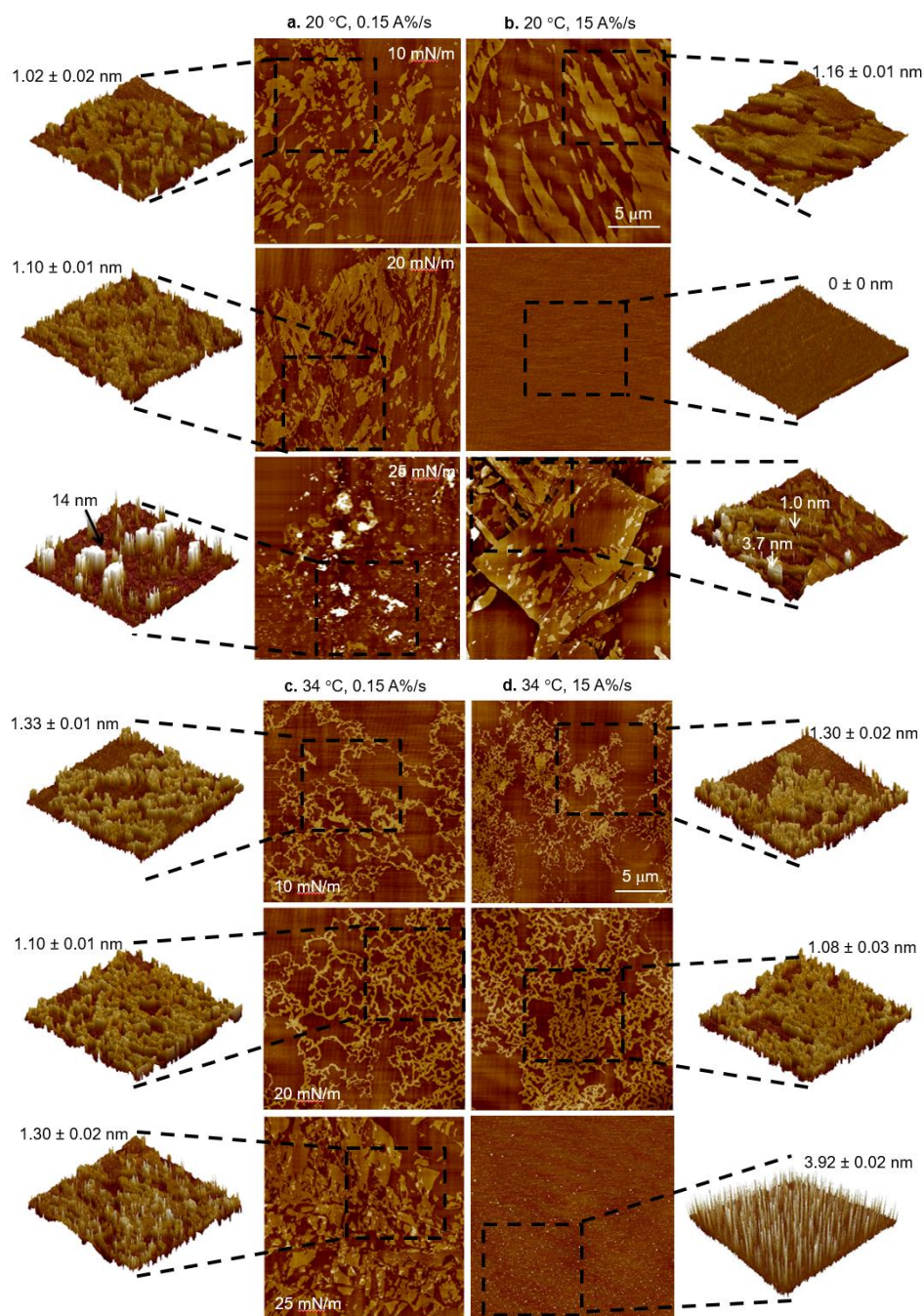


Figure 3.2 Lateral structure and topography of the PAHSA film at three characteristic surface pressures, i.e., 10, 20, and 25 mN/m, each under four experimental conditions. (a) 20 °C and a low compression rate of 0.15 A%/s, (b) 20 °C and a high compression rate of 15 A%/s, (c) 34 °C and 0.15 A%/s, and (d) 34 °C and 15 A%/s. All AFM images have the same scanning area of 20 μ m \times 20 μ m and the same z range of 5 nm. Images in the first and last columns show the 3D rendering of the film indicated by black squares. The average height differences are shown as mean \pm standard deviation. Arrows point to the height of specific features on the film. The bar is equal to 5 μ m.

than that at 20 °C (38 vs. 25 mN/m). A similar finding of the temperature dependence has been reported for the OAHFA monolayer (139), as will be discussed later.

3.3.2 Lateral structure and topography of the PAHSA film

Figure 3.2 shows the lateral structure and topography of the PAHSA monolayer at three characteristic surface pressures, 10, 20, and 25 mN/m, respectively, at different temperatures (20 and 34 °C) and compression rates (0.15 and 15 A%/s), matching the experimental conditions used in Figure 3.1.

As shown in Figure 3.2a, at 20 °C and slow compression, the PAHSA monolayer at 10 mN/m shows irregular flake-shaped domains about 1 nm higher than the surroundings. When the monolayer is compressed to 20 mN/m, these domains are further packed with relatively unchanged height differences. At 25 mN/m, *i.e.*, the π_c under this experimental condition, the PAHSA monolayer collapses to form isolated multilayered collapse structures up to 14 nm higher than the surroundings.

In comparison, at 34 °C and slow compression (Figure 3.2c), the PAHSA monolayer at 10 mN/m shows a network of ramified, fiber-like domains about 1 nm higher than the surroundings. When the monolayer is compressed to 20 mN/m, these higher domains form a denser network that covers most of the monolayer. At 25 mN/m, the fiber-like domains are compressed into larger pieces with a similar height as those at lower surface pressures, thus a large portion of the monolayer is covered with the higher domain. No collapse structure is found at 25 mN/m, which is consistent with the compression isotherm, *i.e.*, π_c close to 38 mN/m under this experimental condition.

At 20 °C and fast compression (Figure 3.2b), the PAHSA monolayer shows flake-shaped domains, similar to those shown in Figure 3.2a. However, in comparison to the slow compression

shown in Figure 3.2a, all higher domains in Figure 3.2b are rapidly compacted into a fully-packed monolayer without height contrasts at 20 mN/m. At 25 mN/m, liquid-crystalline collapse, revealed as large-piece folding, initiates in the fully-packed PAHSA monolayer, which is in contrast to the localized film collapse shown as individual protrusions at the same surface pressure shown in Figure 3.2a.

The domain structures at 34 °C and fast compression (Figure 3.2d) are similar to those at 34 °C and slow compression (Figure 3.2c). The PAHSA monolayer shows a network of ramified, fiber-like domains at 10 mN/m. These domains are compacted into a denser network at 20 mN/m, and then into a fully-packed monolayer without height variations at 25 mN/m. At this surface pressure, numerous protrusions 4 nm higher than the compacted monolayer appear, indicating localized film collapse.

3.3.3 Molecular dynamics simulations of the PAHSA film

Figure 3.3 shows the all-atom MD simulations of the PAHSA film at the air-water surface. Figure 3a shows the MD simulation model in which the two hydrophilic moieties of PAHSA are highlighted, with the more hydrophilic carboxyl group in blue and the less hydrophilic ester group in red. Figure 3b shows the density profiles of these two hydrophilic groups relative to the location of the air-water surface. It can be seen that at a low surface pressure both the carboxyl group and the ester are solvated in water, with the carboxyl groups ~ 0.3 nm into the water while the esters reside at the surface. When increasing surface pressure upon film compression, the esters are squeezed out of the bulk water. Figure 3c is a cartoon representation of the molecular conformation of PAHSA at the air-water surface with increasing surface pressure. At a low surface pressure, the vector connecting the carboxyl and ester groups of the PAHSA molecule assumes a configuration parallel to the air-water surface, with both the carboxyl and ester groups lying inside water. With

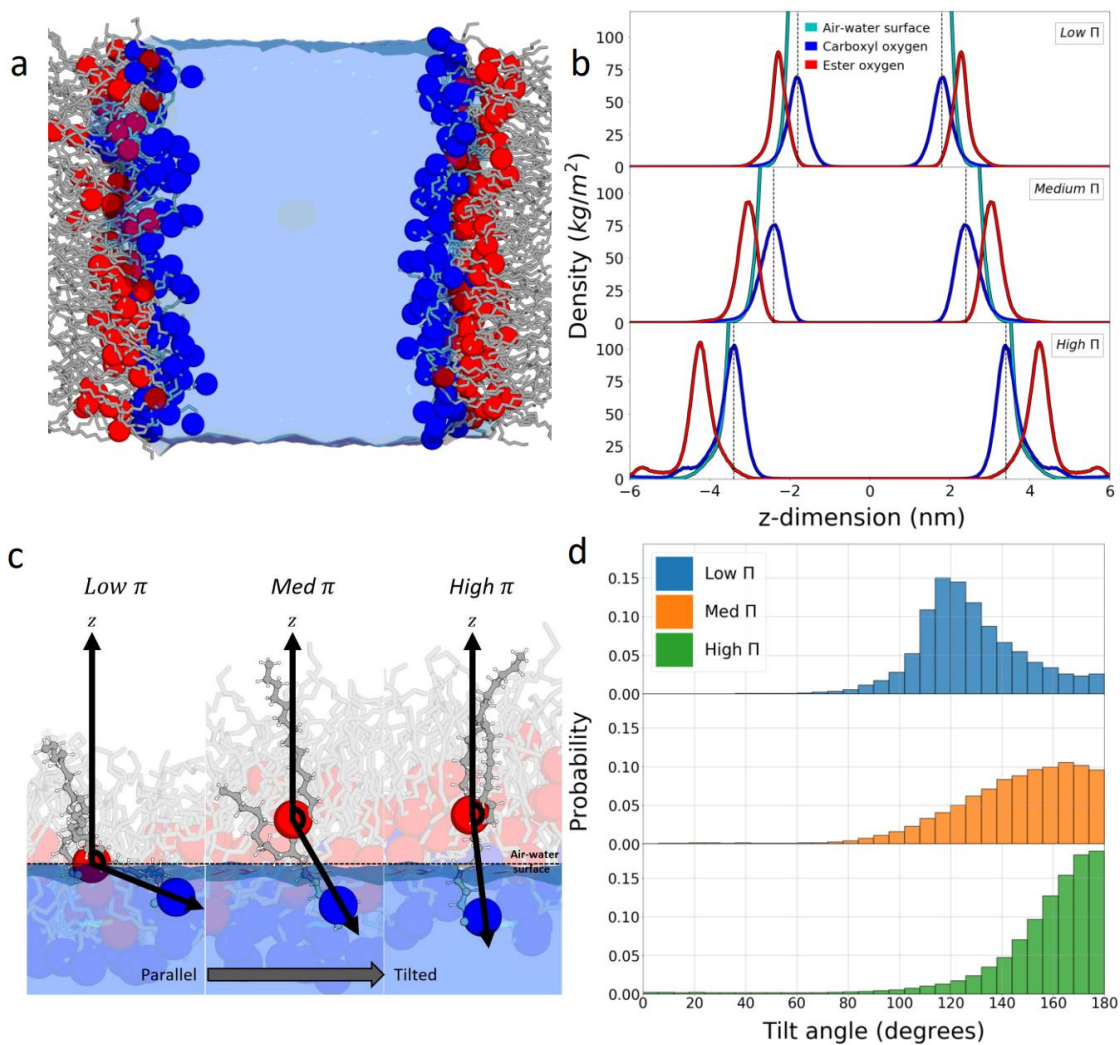


Figure 3.3 Atomistic molecular dynamics simulations of the PAHSA monolayer at the air-water surface. (a) Demonstration of the simulation box. The carboxyl oxygen is represented by blue beads and the ester oxygen is represented by red beads. Hydrocarbon chains are represented by gray sticks. (b) Density profiles of the carboxyl group (in blue) and ester group (in red) of the PAHSA relative to the air-water surface (in light blue) at increasing surface pressures. (c) Transition of the PAHSA molecule from a configuration “parallel” to the air-water surface, to a “tilted” configuration relative to the air-water surface, upon increasing surface pressure. The carbon atoms of the carboxyl oxygen are shown in blue, the ester oxygen is shown in red, and the rest of the carbon atoms are shown in grey. (d) Histograms of the average tilting angle of the vector connecting the carboxyl oxygen and the ester oxygen.

increasing surface pressure, the PAHSA molecule assumes a more and more tilted configuration, with the more hydrophilic carboxyl group remaining in water while the less hydrophilic ester is

squeezed out. Figure 3.3d shows the quantified tilting angle measure at various surface pressures. It can be seen that the average tilting angle increases from approximately 110 to 170 degrees with increasing surface pressure, indicating a transition of the PAHSA molecule from a parallel to a titled configuration. This surface pressure-dependent change in the molecular tilting angle is consistent with the density profile (Figure 3.3b), collectively suggesting that the ester groups are squeezed out from the water as the surface pressure increases.

3.4 Discussion

To date, most biophysical studies of artificial TFL have ignored the effects of FAHFAs, in general, or OAHFAs, in specific. To the best of our knowledge, there are only a few available biophysical studies of OAHFAs in artificial TFL (139, 140, 151, 152). The OAHFAs used in all of these studies were synthetic and contained only short hydroxy fatty acid backbones up to 20 carbons. In the past two years, Paananen and coworkers have developed a series of synthetic, oleic acid (C18:1) based OAHFAs with the hydroxy fatty acid backbone of various lengths, *i.e.*, C12:0, C15:0, and C20:0 (140, 151), and different chain saturation, *e.g.*, C20:1 (152). They have studied extensively the biophysical properties of these synthetic OAHFAs using Langmuir trough. In general, they found that the π_c of OAHFAs at 35 °C ranges from 35 mN/m for C20:1 (152), to 40 mN/m for OAHFAs with fully saturated backbones (140, 151). These findings are in good agreement with the π_c of PAHSA found here at 34 °C and slow compression (Figure 3.1).

Butovich *et al.* first synthesized a model OAHFA, (O-oleyl)- ω -hydroxy palmitic acid (OOHPA), *i.e.*, the C16:0-C18:1 OAHFA, in 2009 (63). Schuett and Millar have studied the surface activity of OOHPA (139). The compression isotherms obtained with OOHPA are in general agreement with those obtained here for PAHSA under slow compression (Figure 3.1). Interestingly, they found that increasing temperature from 20 to 35 °C significantly increased the

π_c of OOHPA from less than 10 to 45 mN/m. They were unable to explain this “unexpected” surface activity of OOHPA (139). A similar temperature dependence of the π_c is also found here with PAHSA (Figure 3.1). We have further shown that with a high compression rate, the PAHSA film reaches the same π_c of 29 mN/m at both 20 and 34 °C. These results indicate that the biophysical properties of a dynamic PAHSA monolayer under physiologically relevant conditions must depend on a balance between kinetics (mostly controlled by the speed of film compression) and thermal-relaxation (mostly controlled by temperature).

The different biophysical properties of the PAHSA monolayer under various temperatures and compression rates can be fully explained by the molecular organization and lateral structure of the monolayer revealed by AFM (Figure 3.2). It is clear that the lateral domain structures of the PAHSA monolayer are predominantly affected by temperature, which determines the mobility and fluidity of the molecules, while the compression rate mostly affects the kinetic compactness of the monolayer. At 20 °C, molecules in the PAHSA monolayer self-assemble into large flake-shaped crystalline domains. Such a loosely organized molecular structure can poorly absorb the kinetic energy of film compression, thus leading to film collapse at a low π_c (*i.e.*, < 30 mN/m). At 34 °C, however, molecules in the PAHSA monolayer self-assemble into a more flexible and uniform, fiber-like network. Compared to the isolated flake-shaped domains formed at 20 °C, this fiber-like network is more efficient in adsorbing the kinetic energy of film compression, especially at the low compression rate, thus maintaining a much higher π_c (*i.e.*, 38 mN/m for slow compressions). It should be noted that this fiber-like network was also observed in the C20-OAHFA monolayer at 35 °C using fluorescence microscopy (151), and in the human meibomian lipid film at 34 °C and surface pressures lower than 10 mN/m using Brewster angle microscopy (153).

The unique phase behavior of PAHSA molecules at the air-water surface can be better understood with MD simulations (Figure 3.3). It is well-known that both the time and length scales of all-atom MD simulations are too small to directly observe the phase behavior of biomembranes (154, 155). However, all-atom MD simulations shed light on molecular orientation and rotation, which are of vital importance for understanding molecular mismatch and phase separation in lipid monolayers and membranes. A distinct difference in the molecular structure between phospholipids and PAHSA, as well as OAHFAs, is that instead of having only one hydrophilic headgroup as in phospholipids, PAHSA has two individual hydrophilic moieties, *i.e.*, the more hydrophilic carboxyl group and the relatively less hydrophilic ester group. Both moieties are capable of interacting with water, albeit to different degrees. Consequently, the PAHSA monolayer at the air-water surface is expected to exhibit more complicated polymorphic behaviors than phospholipid monolayers. Our MD simulations have found that upon film compression, phase separations in the PAHSA monolayer are caused by a configurational transition from a parallel to a tilted configuration (Figure 3.3c). The findings from our MD simulations are consistent with the molecular model of OAHFAs proposed by Butovich who predicted the amphiphilicity of these molecules from their unique chemical structures (51). In general, OAHFAs have two hydrophilic moieties, the strongly hydrophilic carboxyl headgroup, which is ionized at the physiological pH, and the mildly hydrophilic ester bond in the middle of the molecules since esters are capable of forming hydrogen bonds with water (51). The unique molecular structure of OAHFAs thus facilitates their polymorphism at the air-water surface and their interactions with other polar and nonpolar lipids.

Taking together the results obtained from CDS, AFM, and MD simulations, **Figure 3.4** shows cartoons that describe the molecular organization of the PAHSA molecules at the air-water surface

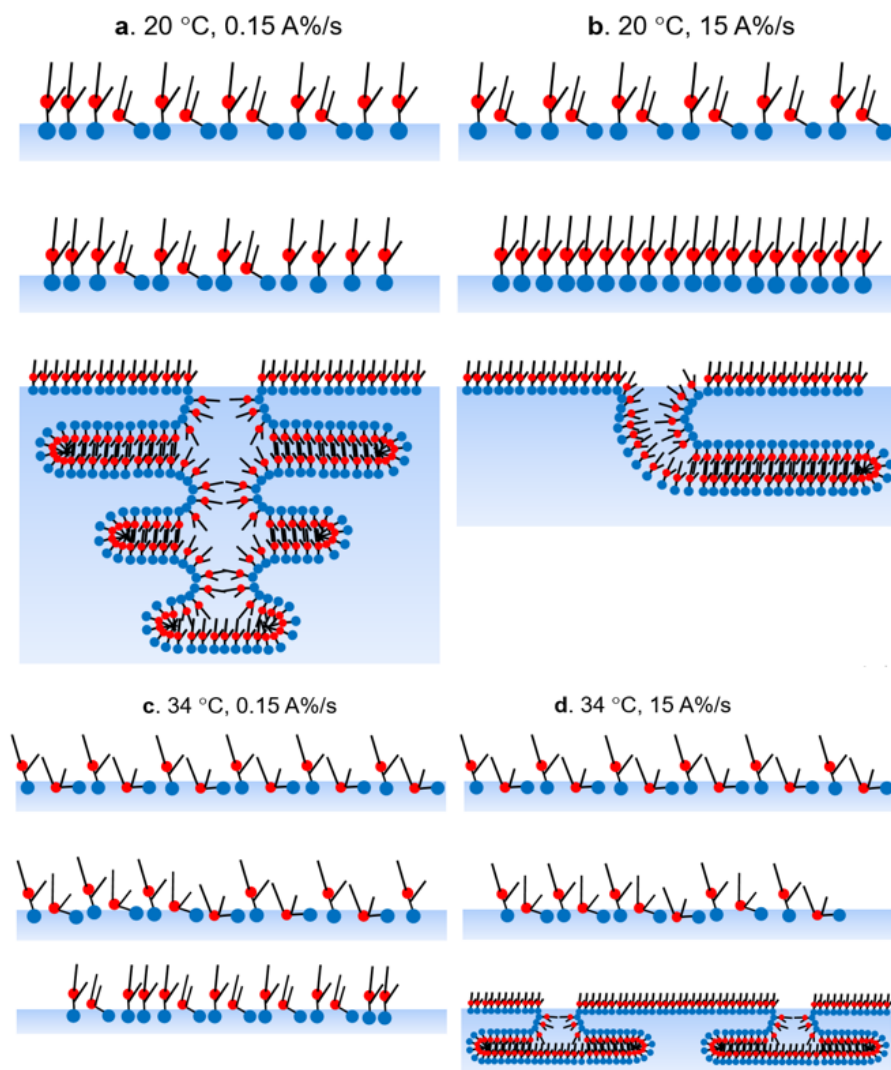


Figure 3.4 Cartoons of the compressed PAHSA monolayer at three characteristic surface pressures, i.e., 10, 20, and 25 mN/m, each under four experimental conditions. (a) 20 °C and a low compression rate of 0.15 A%/s, where the PAHSA monolayer collapses as isolated large protrusions up to three bilayer stacks. (b) 20 °C and a high compression rate of 15 A%/s, where the PAHSA monolayer collapses as large liquid-crystalline folds. (c) 34 °C and 0.15 A%/s, where the PAHSA monolayer does not collapse at the surface pressure of 25 mN/m. (d) 34 °C and 15 A%/s, where the PAHSA monolayer collapses as multiple, uniform-distributed, single bilayer budding. The carboxyl groups are represented by blue beads and the ester groups are represented by red beads.

with increasing surface pressures of 10, 20, and 25 mN/m, under the four experimental conditions matching those studied in Figure 3.1 and 3.2. Most importantly, Figure 3.4 demonstrates the molecular mechanisms that are responsible for the collapse of the PAHSA monolayer under

various kinetic and temperature conditions. At 20 °C and slow compression (Figure 3.4 a), the PAHSA monolayer collapses with isolated protrusions up to the thickness of three bilayer stacks (~14 nm). At 20 °C and fast compression (Figure 3.4 b), the PAHSA monolayer collapses as large liquid-crystalline folds since the monolayer is kinetically fully packed before the folding. At 34 °C and slow compression (Figure 3.4 c), the PAHSA monolayer does not collapse at the surface pressure of 25 mN/m. At 34 °C and fast compression (Figure 3.4 d), the PAHSA monolayer collapses with multiple, uniformly distributed, small protrusions of only one bilayer in thickness (~4 nm)

OAHFAs are the second most abundant amphiphilic lipid class found in meibum, accounting for ~4 mol% of the total meibomian lipids (131, 156). Hence, OAHFAs have been considered as a main surfactant in TFL (131). However, our study showed that the primary biophysical function of OAHFAs may not be surface tension reduction but optimizing rheological properties of the TFL (135). OAHFAs optimize the surface rheological properties of the TFL by maintaining a highly elastic film across a range of oscillation frequencies (135). This finding is consistent with the clinical evidence that OAHFAs decrease with dry eye (132). Such compositional changes have been linked to the biophysical malfunction of increasing TFL viscosity for patients with meibomian gland dysfunction (65, 118, 125). The optimal viscoelastic properties of OAHFAs are most likely related to their unique polymorphic behaviors at the air-water surface. Compared to phospholipid molecules, which have only one hydrophilic moiety, the dual hydrophilic groups of PAHSA molecules give them a new degree of rotational freedom when the lipid film is compressed. Consequently, the PAHSA monolayer may collapse with various molecular mechanisms (157, 158), depending on the balance of kinetic compression and thermal relaxation.

3.5 Summary

Using combined biophysical experiments, AFM observations, and all-atom MD simulations, we have studied the detailed biophysical properties of FAHFAs using PAHSA as a model. It is concluded that the biophysical properties of a dynamic PAHSA monolayer under physiologically relevant conditions depend on a balance between kinetics (mostly controlled by the speed of film compression) and thermal-relaxation (mostly controlled by temperature). We have revealed the unique lipid polymorphism and collapse mechanisms of the PAHSA monolayer at the air-water surface, under various kinetic and temperature conditions. Due to their structural similarities, the biophysical molecular mechanisms of PAHSA found here may be also applicable to OAHFAs. These findings could have novel implications in understanding biophysical functions that FAHFAs, in general, or OAHFAs, specifically, play in the TFL.

Chapter 4 Effect of the tear film lipid layer on water evaporation ¹

4.1 Introduction

Tear film is a multilayered biological barrier covering the ocular surface to protect and lubricate the cornea (5). The tear film can be divided into three distinct layers: an inner mucus layer with sugar-rich glycosylated proteins, an aqueous layer with dissolved proteins, metabolites, and electrolytes, and an outmost lipid layer made up of various lipid species (59, 159). This lipid layer, commonly known as the tear film lipid layer (TFLL), is approximately 100 nm thick (160). The current consensus is that the TFLL consists of two sublayers: a polar lipid layer at the air-water surface, mainly consisting of phospholipids and (O-acyl)- ω -hydroxy fatty acids (OAHFAs), and a nonpolar lipid layer, composed of wax esters and cholesteryl esters, residing atop the polar lipid layer and directly exposing to the environment (161-163). Nonpolar lipids in the TFLL are secreted by the Meibomian glands, while the source of phospholipids in the TFLL is still uncertain (164). The polar lipids may facilitate spreading of the nonpolar lipids, rather than forming aggregations or droplets, over the aqueous surface of the tear film (3, 165).

The TFLL has multiple physiological functions, such as host defense against ocular infection and retardation of water evaporation (62, 66, 166-168). Water evaporation is one of the most important mechanisms for tear film thinning (131). Rapid water evaporation leads to increased tear film instability and premature breakup, which happens in evaporative dry eye (167, 169). In

¹ Xu X, Li G, Zuo YY, Effects of model tear film lipid layer on water evaporation. *Invest. Ophthalmol. Vis. Sci.* 64 (2023) 13.

general, dysfunction of the TFLL results in dry eye disease that affects 10-30% of the world population (170-172).

Although it is generally accepted that the TFLL helps reduce water evaporation *in vivo* (173-177), *in vitro* findings remain controversial. Most *in vitro* studies with Meibomian lipid films and model tear film lipids only demonstrated relatively insignificant or nearly no retardation to water evaporation (178-184). These controversial results were likely related to the *in vitro* models used for studying water evaporation. Quantitative study of monolayer retardation on water evaporation can be traced back to the seminal work by Victor La Mer in the 1950s for the interests of conserving water in reservoirs (185-187). To date, a vast majority of these *in vitro* studies relied on the classical Langmuir trough (178-184), which has a few limitations that prevent accurate evaluation of water evaporation. First, due to its large size, the Langmuir trough generally lacks a rigorous control in environmental conditions, such as the temperature, relative humidity, and airflow rate, all of which are essential factors that can significantly affect the rate of water evaporation. Second, the evaporation rate is traditionally determined with gravimetric analysis, *i.e.*, directly measuring the mass of water lost by evaporation from a Langmuir trough, which requires a relatively long period of experiments (usually 0.5-2 hours) to reduce system errors (179). This further increases the difficulty of environmental control during such an extended period of experiments. Third, Langmuir trough can hardly reproduce the physiologically relevant high surface pressure of the TFLL. The surface tension of whole tears of healthy individuals was reported to be around 43-46 mN/m (188, 189), which most likely represents the surface tension of major proteins in tears, such as lysozyme (6). Upon film compression during the blinking process, the TFLL can reduce the surface tension to ~20 mN/m, corresponding to a surface pressure as high as 50 mN/m (6, 7). However, most existing *in vitro* evaporation studies only covered the surface pressure range

between 5 and 30 mN/m, because the TFLL rapidly collapses at higher surface pressures in a Langmuir trough. Hence, there is an urgent need for alternative biophysical models to evaluate the effect of TFLL on water evaporation under physiologically relevant conditions.

Here, we developed a novel droplet-based biophysical model to study the effect of TFLL on water evaporation. Owing to system miniaturization, droplet-based evaporation models offer a more rigorous environmental control than the classical Langmuir trough. Both pendant drop (190) and sessile drop (191) methods have been attempted in previous studies. A key novelty of this work was the invention of a ventilated, closed-chamber, droplet evaporimeter with a constant surface area, analogous to the evaporimeter used for measuring the tear evaporation rate *in vivo* (176, 192, 193). This *in vitro* evaporimeter was realized with the combination of constrained drop surfactometry and a novel feedback control system called closed loop-axisymmetric drop shape analysis that decoupled surface area of the droplet from water evaporation. Using this novel biophysical model, together with direct film imaging using atomic force microscopy, we have studied the effect of a model TFLL on water evaporation. Our data suggest that the model TFLL is capable of reducing the water evaporation rate by 11% at high surface pressures. Our experimental results may provide novel implications into better understanding the biophysical and physiological function of the TFLL.

4.2 Material and methods

4.2.1 Materials

Dipalmitoyl phosphatidylcholine (DPPC), L- α -phosphatidylcholine (PC) from egg yolk, palmitic-acid-9-hydroxy-stearic-acid (PAHSA), and cholesteryl oleate (CO) were purchased from Sigma-Aldrich (St. Louis, MO). Behenyl oleate (BO) was purchased from Larodan (Monroe, MI). Physicochemical properties of these lipids can be found elsewhere (6). Individual lipids were

dissolved in chloroform as 1 mM stock solutions. Water used was Milli-Q ultrapure water with a resistivity greater than 18 M Ω -cm at room temperature.

4.2.2 Constrained drop surfactometry (CDS)

CDS is a new generation of droplet-based surface tensiometry technique developed in our laboratory (194, 195). It uses the air-water surface of a millimeter-sized sessile drop to accommodate the spread or adsorbed film. As shown in **Figure 4.1**, a key design of the CDS is a carefully machined pedestal that uses its knife-sharp edge to prevent film leakage even at very low surface tensions. System miniaturization of the CDS facilitates rigorous control of experimental conditions with an environmental control chamber. The spread/adsorbed film at the droplet surface can be compressed and expanded by precisely controlling oscillation of the surface area of the droplet using a newly developed mechatronic system called closed-loop axisymmetric drop shape analysis (CL-ADSA) (196). CL-ADSA determines the surface tension of the spread/adsorbed film by analyzing the shape of the film-covered droplet. The surface pressure (π) can be determined from the surface tension (γ) using $\pi = \gamma_0 - \gamma$, with γ_0 being the surface tension of a clean, lipid-free air-water surface.

Specifically, a trace amount of the lipid sample was spread onto the air-water surface of a 15 μ L droplet serving as the aqueous subphase to the spread lipid film. The spread film was left undisturbed for 1 min to allow evaporation of the solvent and to reach equilibrium. The droplet was then slowly expanded to decrease the surface pressure to around zero (*i.e.*, increasing the surface tension to around 70 mN/m). Subsequently, the spread lipid film was compressed quasi-statically at a rate of 0.15 A%/s to a target surface pressure.

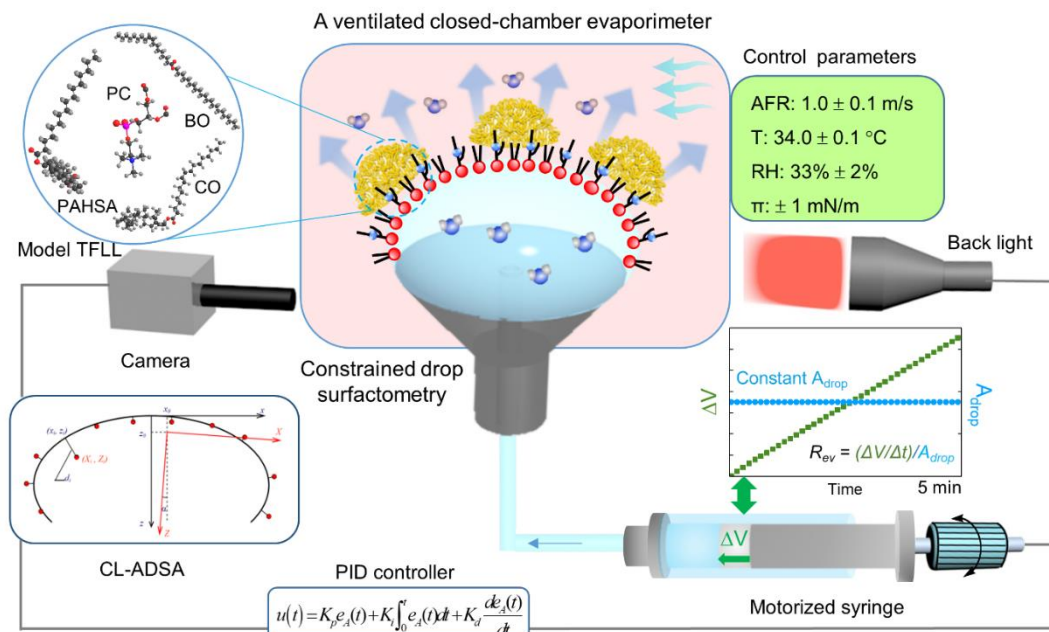


Figure 4.1 Schematic of a ventilated, closed-chamber, droplet evaporimeter with a constant surface area for studying evaporation resistance of the tear film lipid layer (TFL). This droplet evaporimeter is constructed based on constrained drop surfactometry (CDS), in which a 5-mm water droplet ($\sim 27 \mu\text{L}$ in volume and $\sim 0.35 \text{ cm}^2$ in surface area) is constrained on a carefully machined pedestal with knife-sharp edges. The water droplet is enclosed in an environmental control chamber that ensures a rigorous control of experimental conditions, including the temperature, relative humidity (RH), and airflow rate (AFR). The surface area of the droplet is maintained at a constant using closed-loop axisymmetric drop shape analysis (CL-ADSA) with a proportional-integral-derivative (PID) control loop. The measuring principle of ADSA is illustrated in a box: ADSA determines the surface tension by numerically fitting the experimental droplet profiles (indicated by red dots) to theoretical droplet profiles (indicated by black curves) obtained with numerical integration of the Laplace equation of capillarity. The PID controller is illustrated by a PID control function with the proportional, integral, and derivative terms. The evaporation rate (R_{ev} , mm/min) is calculated as $(\Delta V/\Delta t)/A_{drop}$, where ΔV is the volume of water replenished into the droplet, in order to compensate for the water lost by evaporation. Δt is the time period of the experiment, usually 5 min. A_{drop} was the surface area of the droplet, controlled at $0.35 \pm 0.01 \text{ cm}^2$. The model TFL consists of 40 mol% behenyl oleate (BO) and 40 mol% cholesteryl oleate (CO) that represent two nonpolar lipid classes, i.e., wax ester and cholesteryl ester in the natural TFL, and 15 mol% phosphatidylcholine (PC) and 5 mol% palmitic-acid-9-hydroxy-stearic-acid (PAHSA) that represent two polar lipid classes in the natural TFL, i.e., phospholipids and OAHFAs.

4.2.3 Ventilated closed-chamber droplet evaporimeter with a constant surface area

Figure 4.1 illustrates the schematic of the droplet-based evaporimeter. Lipid samples were spread onto the air-water surface of a 5-mm droplet ($27 \mu\text{L}$ in volume and 0.35 cm^2 in surface area)

to result in a target surface pressure. The environmental temperature and relative humidity (RH) were controlled at 34.0 ± 0.1 °C and $33.0 \pm 2.0\%$ with a closed environmental control chamber. The chamber was ventilated with a continuous airflow. The airflow rate was measured with a hot wire anemometer (TSI, Shoreview, MN) and was controlled at 1.0 ± 0.1 m/s to simulate the ambient environment (197).

A key feature of the droplet-based evaporimeter is its capacity of maintaining a constant surface area during water evaporation. As shown in Figure 4.1, CL-ADSA maintains the constant surface area of a droplet by determining its surface area in real-time and feeding this information back to a motorized syringe to automatically complete a proportional-integral-derivative (PID) control loop (196). The evaporation rate (mm/min) was calculated as $(\Delta V/\Delta t)/A_{\text{drop}}$, where ΔV was the volume of water replenished into the droplet, in order to compensate for the evaporated water and thus to maintain the constant surface area. Δt is the time period of the experiment, *i.e.*, 5 min. $\Delta V/\Delta t$ was determined from linear regression of the recorded ΔV - Δt curve. A_{drop} was the surface area of the droplet, controlled at 0.35 ± 0.01 cm². The volumetric evaporation rate (*i.e.*, $\Delta V/\Delta t$) of this droplet-based evaporimeter was determined to be less than 2.7 $\mu\text{L}/\text{min}$, comparable to the basal tear production of healthy adults (*i.e.*, 0.8-2.0 $\mu\text{L}/\text{min}$) (198, 199).

4.2.4 Atomic force microscopy (AFM)

Lateral structure and topography of the tear lipid films were studied with the combination of *in situ* Langmuir-Blodgett (LB) transfer from the CDS and atomic force microscopy (AFM) (7, 200). The lipid film was first LB transferred from the droplet by lifting a small piece of freshly peeled mica sheet at a speed of 1 mm/min. During the LB transfer process, the surface pressure of the lipid film was maintained at a constant (± 1 mN/m). Topographical images of the lipid film were obtained with an Innova AFM (Bruker, Santa Barbara, CA). Samples were scanned in air in contact

mode and tapping mode. The contact mode used a silicon nitride cantilever with a spring constant of 0.12 N/m and a tip radius of 2 nm, while the tapping mode used a silicon cantilever with the spring constant of 42 N/m and a resonance frequency of 300 kHz. Relative height differences between domains were determined with bearing analysis using Nanoscope Analysis (version 1.5).

4.2.5 Statistical analysis

All results were shown as mean \pm standard deviation ($n = 10$ unless otherwise indicated). One-way ANOVA with Tukey's means comparison test was used to determine group differences (OriginPro, Northampton, MA). A value $p < 0.05$ was considered to be statistically significant.

4.3 Results and discussion

4.3.1 Development of a constant-surface-area droplet evaporimeter for study in evaporation retardation by lipid films

Figure 4.2 demonstrates the capacity of this new evaporimeter in determining the rate of evaporation from a water droplet while maintaining a constant surface area of the droplet. Within a 5-min period, the RH of the environment was maintained at 33%, while the temperature and airflow rate were controlled at 34 °C and 1 m/s, respectively. Surface tension of the water droplet remained at a constant of 71 mN/m, indicating no contamination of the water surface. It can be seen that during the 5-min period, in spite of water evaporation, the surface area and volume of the droplet were maintained at 0.35 cm² and 27 μ L, respectively, using CL-ADSA. The volume of water replenished into the droplet, in order to maintain the constant surface area, increased linearly over the 5-min period, with a volumetric rate of 2.7 μ L/min. The water evaporation rate, $(\Delta V/\Delta t)/A_{\text{drop}}$, under the controlled experimental conditions, was determined to be 0.078 mm/min.

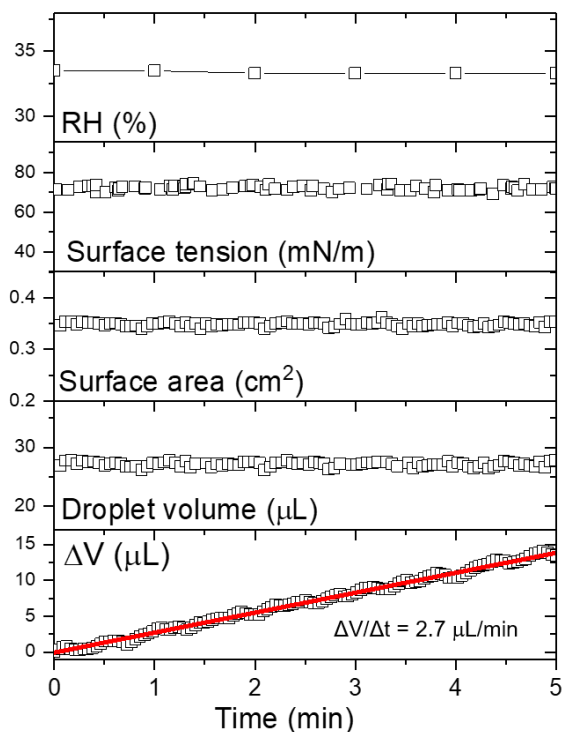


Figure 4.2 Typical experimental results for water evaporation determined within 5 min using the new droplet evaporimeter. Temperature and relative humidity (RH) were maintained at 34 °C and 33%, respectively. Surface tension of water was relatively unchanged at 70 mN/m, indicating no contamination. Surface area of the droplet was actively controlled at a constant of 0.35 cm² using CL-ADSA. Volume of the droplet was relatively unchanged at 27 µL. The volumetric rate of water replenished into the droplet ($\Delta V/\Delta t$) to complement the water lost by evaporation was determined by linear regression (red solid line), corresponding to a volumetric evaporation rate of 2.7 µL/min.

To demonstrate the effect of lipid monolayers on water evaporation, we have studied the evaporation resistance of a DPPC monolayer at 34 °C under various controlled surface pressures. DPPC (16:0, 16:0 PC) was selected as a model lipid monolayer because C16 fatty acids are able to balance the rigidity needed for a sufficient resistance to water evaporation and the “self-healing” effect after rupture by waves (186).

As shown in **Figure 4.3**, effects of the DPPC monolayer on water evaporation can be roughly divided into three regions as a function of surface pressure. First, at 10 mN/m, the DPPC monolayer shows no statistically significant effect on water evaporation ($p > 0.05$ in comparison

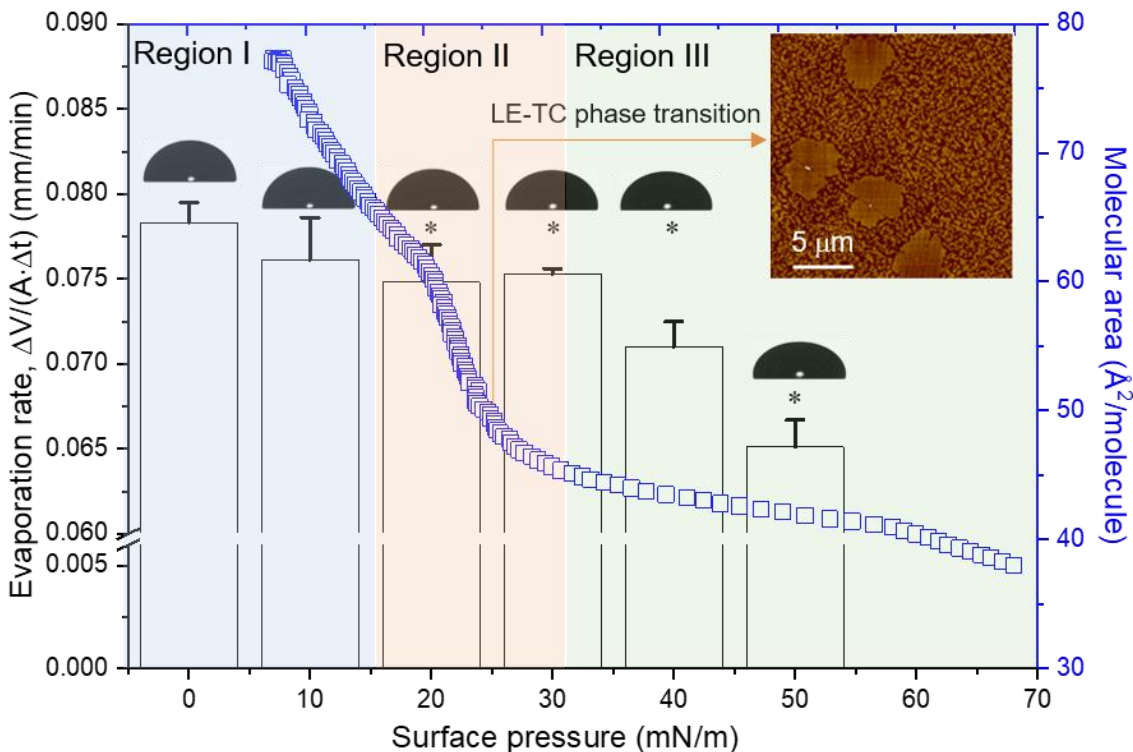


Figure 4.3 Superimposed compression isotherm of a DPPC monolayer at 34 °C, and the corresponding evaporation resistance at various surface pressures. Surface pressure 0 indicates a pure lipid-free air-water surface. The compression isotherm and evaporation resistance can be separated into three regions. Region I. No evaporation resistance for the DPPC monolayer in a disordered liquid-expanded (LE) phase; Region II. Moderate evaporation resistance for the DPPC monolayer undergoing LE to tilted-condensed (TC) phase transitions; and Region III. High evaporation resistance for the DPPC monolayer in a closely-packed ordered TC phase. Insets are an AFM image showing LE-TC phase coexistence at 25 mN/m, and droplet images demonstrating the constant surface area. * $p < 0.05$ indicates statistically significant differences.

to the clean air-water surface). Second, at 20 and 30 mN/m, the DPPC monolayer shows moderate, but statistically significant ($p < 0.05$), effects on water evaporation, by reducing the evaporation rate by 4%. Third, at 40 and 50 mN/m, the DPPC monolayer shows significant retardation effects on water evaporation, with 9% and 17% reduction in the evaporation rate, respectively. These findings are in qualitative agreement with those reported by Miano *et al.* who determined the effect of the DPPC monolayer on water evaporation up to the surface pressure of 35 mN/m, at 36 °C and 15% RH, using the pendant drop method (190). These workers found that at the surface pressure

below 12 mN/m, the DPPC monolayer showed no retardation effect on water evaporation. When the surface pressure was increased to 20 mN/m, the DPPC monolayer showed moderate effects on evaporation retardation, while increasing the surface pressure to 35 mN/m did not further increase the evaporation resistance (190).

Figure 4.3 also shows the compression isotherm of the DPPC monolayer at 34 °C, superimposed on the water evaporation data. The DPPC monolayer undergoes a liquid-expanded (LE) to tilted-condensed (TC) phase transition within the surface pressure range between 20 and 30 mN/m, indicated by a plateau region in the compression isotherm. This phase transition region of the DPPC monolayer at 34 °C is in good agreement with our previous observations (195). The LE-TC phase transition, or phase coexistence, can be visualized by the formation of TC domains ~1 nm higher than the surrounding LE phase, as demonstrated by the AFM image shown in the inset of Figure 4.3.

These findings suggest that the evaporation resistance of the DPPC monolayer is mainly determined by the phospholipid polymorphism. The LE-TC phase coexistence in the DPPC monolayer, *i.e.*, at 20-30 mN/m, corresponds to Region II in which the DPPC monolayer starts to show moderate resistance to water evaporation (Figure 4.3). At surface pressures lower than this phase transition pressure, the DPPC monolayer is in a disordered LE phase and hence does not significantly resist water evaporation (Region I). At surface pressures higher than this phase transition pressure, the DPPC monolayer is compressed into a tightly packed, ordered TC phase, thus showing significant resistance to water evaporation (Region III). These experimental data are in line with the theory of an active energy barrier to water evaporation through monolayers, originated from electrostatic and/or steric repulsions between lipid molecules upon monolayer compression (187).

4.3.2 Effect of the model TFLL on water evaporation

Figure 4.4a shows the quasi-static compression isotherms of three lipid films, *i.e.*, egg PC, PAHSA, and a synthetic model TFLL, at 34 °C. This model TFLL consists of 40 mol% behenyl oleate (BO) and 40 mol% cholesteryl oleate (CO) that represent two nonpolar lipid classes, *i.e.*, wax ester and cholesteryl ester in the natural TFLL, and 15 mol% PC and 5 mol% PAHSA that represent two polar lipid classes in the natural TFLL, *i.e.*, phospholipids and OAHFAs (104). It should be noted that human meibomian lipids are composed of a complex mixture of more than 200 lipid species, primarily including cholesterol esters, wax esters, (O-acyl)- ω -hydroxy fatty acids, and triacylglycerols (5, 162). Modern lipidomics data further suggested that the polar lipid content in healthy TFLL is generally less than 5 mol% (5, 162). Hence, the model TFLL used here, *i.e.*, BO:CO:PC:PAHSA (40:40:15:5), is not only overly simplified in its lipid composition but also likely has an augmented abundance in polar lipids. Nevertheless, our previous studies have demonstrated that this model TFLL represents the biophysical and rheological properties of the natural TFLL to a certain degree (6, 7).

Figure 4.4b-d shows the retardation effects of the PC, PAHSA, and model TFLL films at increasing surface pressures on water evaporation at 34 °C. Since the PAHSA monolayer collapses at 34 mN/m, effects of the PAHSA monolayer on water evaporation were only studied for surface pressures up to 30 mN/m. It can be seen that all lipid films, *i.e.*, PC, PAHSA, and the model TFLL, show statistically significant resistance to water evaporation, albeit to varying extents. For instance, at 30 mN/m, the PC, PAHSA and model TFLL monolayers reduce the water evaporation rate by 2.5%, 4.8%, and 5.1%, respectively. For all studied lipid films, the retardation effect increases with increasing surface pressure. For example, the model TFLL reduces the water evaporation rate by 3.4% at 10 mN/m, 6.1% at 40 mN/m, and 11% at 47 mN/m (Figure 4.4d).

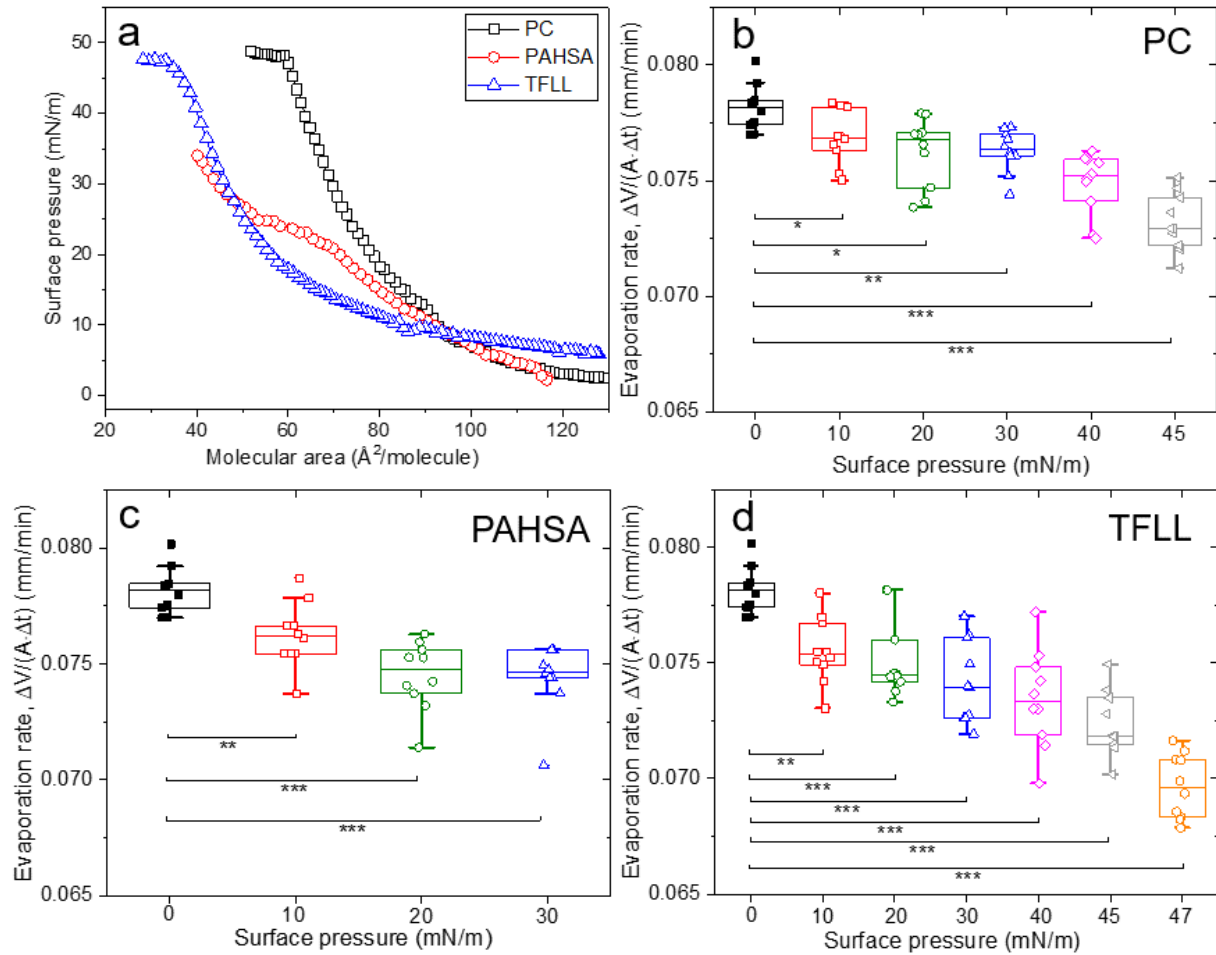


Figure 4.4 Effects of lipid films on water evaporation. (a) Compression isotherms of PC, PAHSA, and a model TFL, BO:CO:PC:PAHSA (40:40:15:5). (b-d) Evaporation rates of water (mm/min) through PC, PAHSA, and the model TFL at various surface pressures. * $p < 0.05$, ** $p < 0.01$, *** $p < 0.001$.

Our findings have a few novel implications in understanding the biophysical and physiological function of the TFL. First, our study qualitatively addressed the discrepancy between available *in vivo* and *in vitro* studies about the effect of TFL on water evaporation. Although *in vivo* studies in general predicted that the TFL significantly reduced the rate of water evaporation from the corneal surface (201, 202), a vast majority of *in vitro* measurements were unable to establish this finding (178-184). Using various synthetic models, animal, or human Meibomian lipids, numerous *in vitro* studies found no (< 1 %) (178, 180, 182, 183) or only limited (~8% with an intense airflow

of 2.5 m/s) evaporation resistance (181) in comparison to evaporation from the lipid-free air-water surface. Here we found that a model TFL was able to reduce the water evaporation rate up to 11% ($p < 0.001$; see Figure 4.4d), thus indicating a definite evaporation resistance. This finding is attributed to the new ventilated, closed-chamber, constant-surface-area droplet evaporimeter developed in this study (Figure 4.1). This novel evaporimetry technique provides a rigorous environmental control, including temperature, relative humidity, airflow rate, surface area, and surface pressure, thus allowing for highly sensitive, reproducible measurements within a short period of only 5 min, while most gravimetric methods require a least of 1-hour measurements (180-182). It is worth mentioning that our method is essentially different from the sessile drop method used by Svitova and Lin (191). To the best of our knowledge, the evaporimeter developed in this paper is the first and only *in vitro* evaporimetry technique capable of automatically controlling the constant surface area of a droplet without human intervention. This is done with the combination of CDS hardware and CL-ADSA software, both invented in our laboratory. In addition, no ventilation or airflow was introduced or controlled in those experiments by Svitova and Lin (191), which may contribute to the low basal evaporation rate found in their experiments, *i.e.*, $\sim 0.16 \mu\text{L}/\text{min}$, more than 15 times lower than the basal evaporation rate found in our experiments. Another factor that influences the evaporation rate is the temperature differences between the environment and the surface of the evaporating droplet.

Second, our study showcases the importance of lipid packing density in evaporation resistance. As shown in Figure 4.4d, when the surface pressure is increased from 10 to 47 mN/m, the evaporation resistance of the TFL increases by 3.2 times. Surface pressure 47 mN/m corresponds to a surface tension approximately 23 mN/m, which is significantly lower than the surface tension of whole tears but corresponds to the lowest surface tension of a highly compressed TFL (6).

Third, our study indicates that the long-chain nonpolar lipids may play a role in evaporation resistance of the TFLL. It has long been recognized that the evaporation resistance of polar lipid monolayers depends on both the chain length and packing density of the lipid molecules (185, 186). La Mer and coworkers found that the evaporation resistance of saturated fatty acids was an exponential function of the chain length (185, 186). Any addition of one carbon atom in the hydrocarbon chain increases the evaporation resistance by a factor of 1.65 (168, 185, 186). However, the chain length effect of nonpolar lipids on water evaporation is largely unknown. Nonpolar lipids, such as wax esters and cholesteryl esters, account for 80% of the TFLL (64). The model TFLL studied here contains 40% behenyl oleate (C22:0-C18:1) and 40% cholesteryl oleate (cholesterol-C18:1). Although these nonpolar lipids are incapable of directly spreading at the air-water surface, they somehow increase the evaporation resistance of the polar lipid monolayer, *e.g.*, 4.2% for PC versus 6.1% for TFLL at 40 mN/m; see Figure 4.4b vs. 4.4d).

4.3.3 Lateral structure and topography of the model TFLL

Figure 4.5 shows the lateral structure and topography of three lipid films (*i.e.* PC, PAHSA, and the model TFLL made up of BO:CO:PC:PAHSA [40:40:15:5]), at 34 °C. Films of the two polar lipids (*i.e.* PC; see Figure 4.5a-b) and PAHSA (see Figure 4.5c-d), assume a monolayer conformation with phase separation at surface pressures up to 30 mN/m. Lateral structures of the PC and PAHSA monolayers show a network of ramified, fiber-like ordered domains ~1 nm higher than the surrounding disordered phase. The network of the ordered domains increases in density upon increasing surface pressure from 20 to 30 mN/m, consistent with our previous observations (7).

At a low surface pressure of 20 mN/m (Figure 4.5e), the model TFLL also demonstrates a general monolayer conformation with phase separation, similar to the polar lipids. However, at

surface pressures equal to or higher than 30 mN/m (Figure 4.5f-h), the TFL shows a completely different topography and lateral structure, compared to those of the polar lipid monolayers. At all high surface pressures, *i.e.*, 30, 40, and 47 mN/m, the TFL shows discrete bead-like structures ranging from ~150 to ~700 nm in height (see Figure 4.5f1-h1 for three-dimensional renderings of the film topography). In comparison to lateral structures of the polar lipid films, the source of these high, bead-like structures must be the nonpolar lipids in the TFL, *i.e.*, BO and CO. Due to lack of affinity to water, these nonpolar lipids are squeezed out from the surface when the surface pressure is increased above 30 mN/m (corresponding to the surface tension of whole tears), thus forming nonpolar lipid multilayers/aggregates residing atop the polar lipid monolayer.

Formation of nonpolar lipid droplets or aggregates by squeezing out from the TFL at increasing surface pressure is supported by multiple experimental evidence. First, film compressibility of the TFL significantly decreases at surface pressures higher than 30 mN/m (Figure 4.4a). Second, AFM has detected a unique evaporation pattern closely analogous to the coffee-ring effect (203). These evaporation patterns have heights of either 4 nm (inset of Figure 4.5h1) or 8 nm (Figure 4.5f1), corresponding to 1 or 2 fully hydrated phospholipid bilayers. These “coffee-rings” are most likely formed by evaporation-driven self-assembly of reverse micelles of polar lipids mixed with the nonpolar lipids (3, 166). This also explains the various sizes of the oil “beads” found in the model TFL, which could be a consequence of different degrees of oil evaporation and oil droplet coalescence. Third, AFM has revealed structures similar to the polar lipid monolayers (PC or PAHSA) underneath the nonpolar multilayer, as shown in a high-resolution ($1 \times 1 \mu\text{m}$) AFM image scanned through a “pore” on the surface layer. This AFM observation provides direct evidence for layered structures of the TFL.

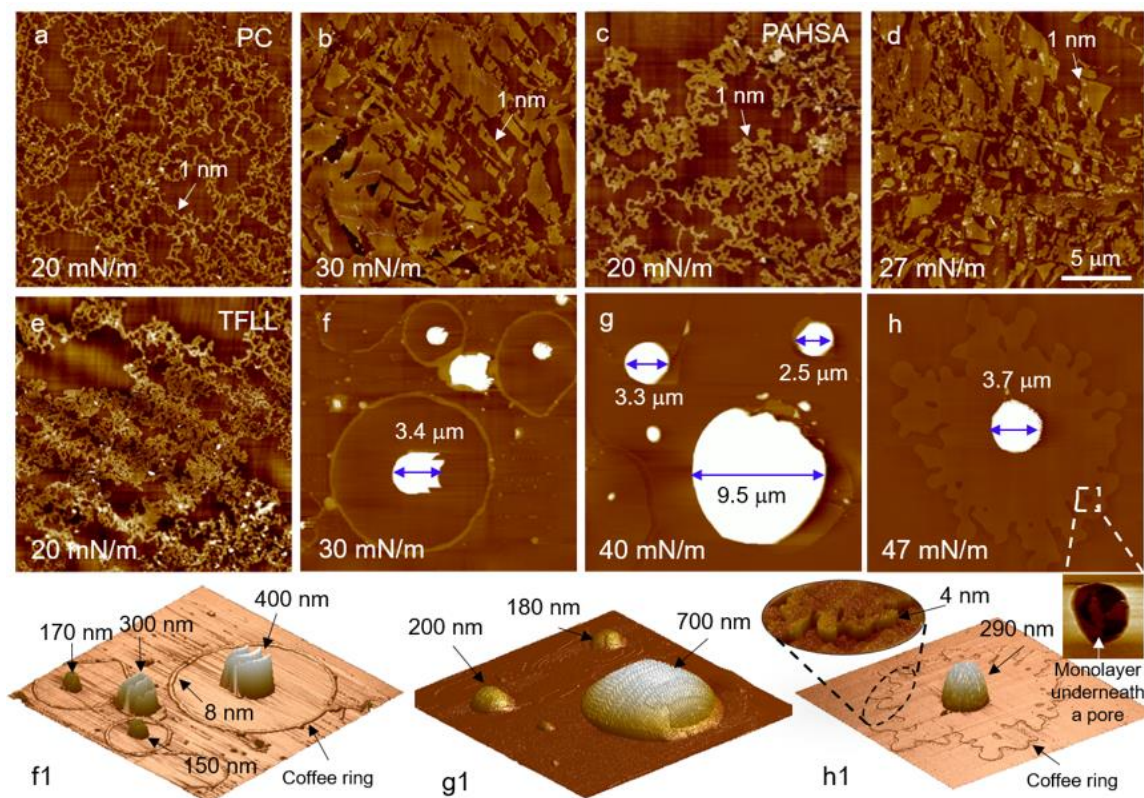


Figure 4.5 AFM topography and lateral structure of lipid films at various surface pressures. (a-b) PC monolayer at 20 and 30 mN/m. (c-d) PAHSA monolayer at 20 and 27 mN/m. (e-h) Model TFL, BO:CO:PC:PAHSA (40:40:15:5) at 20, 30, 40 and 47 mN/m. (f1-h1) Three-dimensional renderings of the TFL corresponding to AFM images shown in (f-h). All AFM images have the same scanning area of $20 \times 20 \mu\text{m}$. The z range for images in (f-h) is 100 nm, while 5 nm for all other images. Single-headed arrows indicate the heights of the structures, while double-headed arrows indicate the lateral dimensions of the structures.

Formation of the nonpolar lipid multilayer/aggregates in the TFL corresponds to a slight increase in the evaporation resistance of the TFL (Figure 4.4b-c vs. 4.4d). Therefore, the present study supports that the TFL resists water evaporation with a combined mechanism by increasing film compactness of the polar lipid film at the air-water surface, and to a lesser extent, by increasing film thickness of the nonpolar lipid film. It should be noted that the model TFL studied here only consists of four lipid components, *i.e.*, BO:CO:PC:PAHSA (40:40:15:5). Consequently, the squeezed-out nonpolar lipids formed discrete droplets/aggregates due to inadequate lipid mixing. Human Meibomian lipids are composed of many different lipid classes, and each of these

lipid classes consists of many homologous lipid species varying in lengths, degrees of unsaturation, and branching, which is essential for the natural Meibomian lipids to have proper melting and lipid mixing (5). Hence, the nonpolar lipid layer of natural TFLL is likely more continuous and more uniform than the model TFLL studied here, thus rendering more evaporation resistance (204). However, more recent studies, both *in vitro* (205) and *in vivo* (206, 207), suggested that the thickness of the TFLL, and especially that of the nonpolar lipid layer of the TFLL, is not uniform but with regions of thicker lipid droplets or aggregates. Using *in vitro* surface rheological study of bovine Meibomian lipids, Bhamla *et al.* also inferred that the TFLL is likely not uniform in thickness, with the thicker area acting as a more effective barrier to water evaporation (208). These studies, including the present work, are consistent with the finding that tear film evaporation is not necessarily correlated with a uniform thickness of the TFLL (209).

4.4 Summary

We have developed a novel ventilated, closed-chamber, droplet evaporimeter with a constant surface area for studying the effect of TFLL on water evaporation. This new evaporimeter is capable of a rigorous control of environmental conditions, including the temperature, relative humidity, airflow rate, surface area, and surface pressure, thus allowing for reproducible water evaporation measurements over a time period of only 5 min. The volumetric evaporation rate of this droplet evaporimeter is less than 2.7 $\mu\text{L}/\text{min}$, comparable to the basal tear production of healthy adults. With this new evaporimeter, we have established the *in vitro* evaporation resistance of a model TFLL that consists of 40% wax esters, 40% cholesteryl esters, and 20% polar lipids. It was found that the TFLL resists water evaporation with a combined mechanism by increasing film compactness of the polar lipid film at the air-water surface, and, to a lesser extent, by increasing film thickness of the nonpolar lipid film.

Chapter 5 Comparative study of meibomian lipids of wild type and *Soat1*-null mice¹

5.1 Introduction

Holocrine meibomian glands (MGs) are specialized glands that are embedded in the upper and lower tarsal plates of the eyelids of humans and most mammals(210). The main function of MGs is to produce a lipid-rich secretion, *a.k.a.* meibum, which is expressed through the set of ducts and orifices onto the ocular surface, where, after being mixed with aqueous tears, participates in the formation of a dynamic, ever-changing, multilayered structure called the tear film (TF) (210). The exact structure of the TF is a subject of undergoing studies (52, 56, 65, 123). However, a predominant view is that meibum forms its outermost sublayer called the TF lipid layer (TFLL), whose main function is believed to be reducing evaporation of the TF (5, 66, 168). Alterations in the TFLL may lead to TF instability and a loss of its protective function – an often-observed condition associated with various types of MG dysfunction (MGD) and Dry Eye Disease (DED) (211, 212). The major causes of these pathological conditions are a change in expressibility of meibum from the orifices due to its inspissation, changes in the ability of meibum to form TFLL, physical obstruction of MG ducts/orifices due to, for example, hyperkeratinization, or insufficient production of meibum in MGs due to MG dropout. The first two causes are closely related to alterations in the chemical composition of meibum, which is formed, predominantly, from wax esters (WEs, about 41% of all lipids), cholesteryl esters (CEs, 31%), (O-acyl)- ω -hydroxy fatty acids (OAHFAs), and a number of other classes of lipids (5, 58, 132, 213). The balance between

¹ Xu X, Wilkerson A, Li G, Butovich I, Zuo YY, Comparative Biophysical Study of Meibomian Lipids of Wild Type and *Soat1*-Null Mice: Implications to Meibomian Gland Dysfunction and Dry Eye Disease. Submitted to *Invest. Ophthalmol. Vis. Sci.*

these groups of lipids is absolutely essential for maintaining the health of the ocular surface and adnexa, as a number of studies with genetically-modified gene knockout (KO) mice demonstrated severe ocular abnormalities once biosynthesis of any of those lipids had been arrested (133, 214, 215). Specifically, inactivation of *Soat1* gene led to a complete stoppage of CE production in MGs and a severe change in the eye phenotype in experimental animals (216-218). Also noted were changes in meibum thermotropic characteristics, such as a multi-degree increase in its melting temperature, which affected its expressibility from MGs (219). However, no other characterization of the biophysical/physicochemical properties of meibomian lipids (MLs) of *Soat1*^{+/-} mice was conducted.

In this chapter, we report results of a comprehensive biophysical study of the dynamic surface activity, interfacial rheology, evaporation resistance, and ultrastructure of the ML films (MLFs) extracted from wild type (WT) and *Soat1* KO mice, using a novel experimental methodology called the constrained drop surfactometry (CDS). The CDS is a new generation of droplet-based tensiometry technique initially developed in our laboratory for studying the biophysical properties of pulmonary surfactants (194). Given the biophysical similarities between pulmonary surfactant and the TFLL (103), we have recently modified the CDS to make it an ideal and versatile *in vitro* model for studying the biophysics of the TFLL (6, 7, 220, 221). By correlating the lipidomic analysis and biophysical assays of the MLs of WT and *Soat1* KO mice, our study revealed novel experimental evidence on the composition-structure-functional correlations between nonpolar lipid components in the MLF and its biophysical properties. These results may provide novel insights into the pathophysiology of MGD and DED, and biophysical behavior of the TF and TFLL.

5.2 Materials and methods

5.2.1 Reagents

Lipid standards were purchased from Avanti Polar Lipids (Birmingham, AL), MilliporeSigma (St. Louis, MO), and NuChek Prep. (Elysian, MN). Acetonitrile, *iso*-propanol, chloroform, and methanol were of chromatography- or mass-spectrometry-grade were purchased from Millipore Sigma and Thermo Fisher Scientific (Waltham, MA). Compressed gasses (helium and nitrogen of ultra-high purity) were obtained from Airgas (Dallas, TX). Acetic and formic acids (each > 99.9% purity), anhydrous ammonium formate (> 99.995%), and leucine-enkephalin were purchased from Millipore Sigma.

5.2.2 Mouse Meibomian lipids

All animal procedures used in this study were approved by the Institutional Animal Care and Use Committee of the University of Texas Southwestern Medical Center and were conducted in accordance with the Association for Research in Vision and Ophthalmology Statement for the Use of Animals in Ophthalmic and Vision Research. *Soat1*^{+/-} founder mice on a C57BL/6J background were purchased from the Jackson Laboratory (B6.129S4-*Soat1*^{tm1Far}/Pgn, Stock #007147, Bar Harbor, ME). The targeted mutation resulted in *Soat1*-null mice, which do not have SOAT1 protein detected by immunoblotting samples from preputial gland, ovaries, and adrenals of these mice. MLs were extracted from the tarsal plates of WT and KO mice by following procedures detailed elsewhere.⁽²¹⁷⁾ Four tarsal plates from each mouse were excised from the eyelids, dissected free from epidermis, and placed in glass vials filled with ~0.5 mL of chloroform:methanol (*v/v* 2:1) for overnight extraction in a refrigerator. The lipids were repetitively extracted with 3 × 1 mL of the solvent mixture, and the extracts were pooled. To collect enough lipid material for biophysical evaluation, ML samples from 3 male WT mice and 3 male KO mice were combined in glass vials to produce two pooled WT and KO ML study samples.

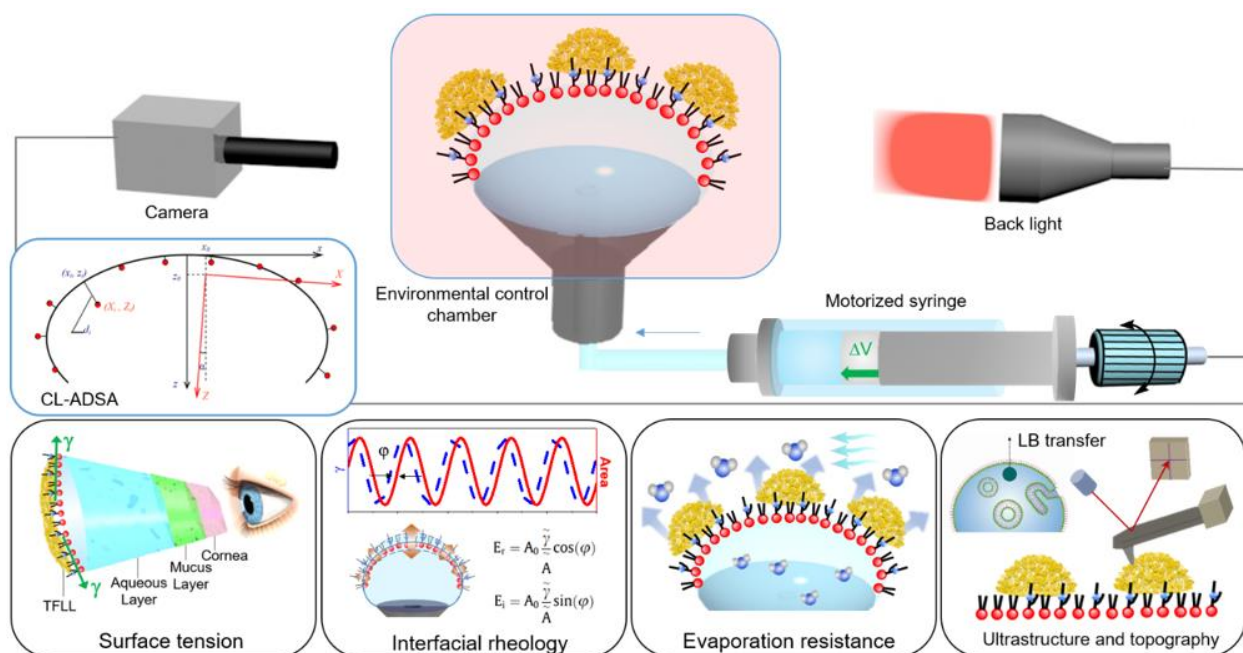


Figure 5.1 Schematics of the constrained drop surfactometer (CDS) as a versatile biophysical model for studying mouse MLFs. The CDS uses the air-water surface of a 4-mm sessile drop, constrained on a carefully machined pedestal with knife-sharp edges, to accommodate the spread MLF. The droplet is enclosed in an environmental control chamber that maintains a constant temperature, relative humidity, and ambient airflow rate. The spread MLF can be compressed and expanded at a highly dynamic rate of 20% relative area per second to simulate a blink, by regulating fluid flow into and out of the droplet using a motorized syringe. Dynamic surface tension of the film is determined with closed-loop axisymmetric drop shape analysis (CL-ADSA), which measures surface tension of the film remotely by analyzing the shape of the MLF-covered droplet in real-time. The CDS is capable of multiple biophysics assays of the MLFs, including dynamic surface tension, interfacial dilational rheology, evaporation resistance, and ultrastructure and topography of the MLFs, when being used in conjunction with the Langmuir-Blodgett (LB) technique atomic force microscopy (AFM).

Then, the samples were dried under a stream of nitrogen and weighed on an analytical microbalance, to produce pooled off-whitish-to-yellowish oily samples of sufficient physical size of about 0.5 mg each, and compared using ultrahigh-pressure liquid chromatography – mass spectrometry (UHPLC-MS; see lipidomic analysis below). The solvent was evaporated under a gentle stream of nitrogen. The remaining lipid materials were sealed and stored at -20 °C until analyses.

5.2.3 Lipidomic analysis

ML samples were analyzed using UHPLC-MS. The LC instrument was a Waters M-Class UHPLC binary system (Waters Corp., Milford, MA). Separation of lipids was conducted on an Acquity C8-BEH UHPLC column (2.0 mm × 100 mm, 1.7 μm) using isocratic elution with a 95% isopropanol : 5% acetonitrile (each with 5% of 10 mM aqueous ammonium formate as additive) solvent mixture as described before.(217) The elutions were conducted at a flow rate of 20 μL/min, with a column temperature of 35 °C. The MS instrument was a high resolution quadrupole Time-of-Flight Synapt G2-Si system equipped with a ZSpray atmospheric pressure ionization LC interface, an IonSabre-II atmospheric pressure chemical ionization (APCI) ion source and a LockSpray unit. The LockSpray was used with a 2 μg/mL Leucine-Enkephalin solution in 50% H₂O : 50% acetonitrile : 0.1% formic acid as calibrant (Waters Corp.). The lipid analytes were detected in positive ion mode as prominent (M + H)⁺, (M - H₂O + H)⁺ and (M - fatty acid + H)⁺ adducts. The APCI detector was used with the following settings: mode “Sensitivity”; resolution 10,000 FWHP; scan rate 1 scan/sec; corona current 1.7 μA; probe temperature 350 °C; source temperature 150 °C; sampling cone 30 V; cone gas flow (nitrogen) 100 L/hr; desolvation gas flow 400 L/hr; nebulizer gas pressure 3 bar; and the trap gas flow (ultra-high purity helium) 2 mL/min. The accuracy of measured *m/z* values for lipid analytes was better than 5 mDa.

The UHPLC-MS raw data were analyzed with the MassLynx v.4.1 software package (Waters Corp.). The total ion chromatograms (TIC) and extracted ion chromatograms (EIC) were used to estimate, respectively, the total lipid content and the apparent abundances of individual analytes as described before (217). Briefly, the signals for EIC were extracted with a mass window of 10 mDa, plotted, and integrated using the MassLynx's Integration routine. The results were statistically analyzed with the SigmaStat v.3.5 software (Systat Software, San Jose, CA).

Reproducibility of the analyses was established in a series of repetitive injections of samples and standard lipids as described earlier (222) and found to be better than $\pm 5\%$.

5.2.4 Dynamic surface activity

Dynamic surface activity of the mouse MLF was studied with constrained drop surfactometry (CDS) (6, 194), in which the MLF film can be spread at the air-water surface of a ~ 4 mm sessile drop enclosed in an environmental control chamber. As shown in **Figure 5.1**, the MLF is constrained at the air-water surface of the sessile drop using a pedestal with knife-sharp edges. The MLF film can be compressed and expanded by regulating the surface area of the droplet using closed-loop axisymmetric drop shape analysis (CL-ADSA) (105), which determines surface tension from the shape of the droplet. Surface pressure presents the differences between the surface tension of the clean air-water surface and that of the MLF-covered surface.

Specifically, ~ 0.1 μL mouse ML samples at ~ 1 mg/mL lipid concentration were spread onto the droplet surface, and left for 1 min to allow solvent evaporation. The spread MLF was compressed at 20% relative area per second (A%/s), corresponding to 0.1 cm^2/s , at 34.0 ± 0.1 $^\circ\text{C}$. At least five compression-expansion cycles were studied, and the fifth cycle was analyzed as representative. Dynamic surface activity of the MLF was quantified with the average film compressibility $\kappa = \frac{1}{A} \frac{\partial A}{\partial \gamma}$, and the hysteresis area of the compression-expansion loop.

5.2.5 Surface dilational rheology

Protocols for determining the surface dilational modulus $E = \frac{d\gamma}{d \ln A}$ of the mouse MLF can be found elsewhere (6, 223). Briefly, surface area of the MLF film was made to undergo a small-amplitude (*i.e.*, amplitude $< 10\%$) harmonic oscillation (*i.e.*, sinusoidal waveform) with frequencies from 0.01 to 0.25 Hz, at 34.0 ± 0.1 $^\circ\text{C}$. The elastic modulus (E_r) and the viscous

modulus (E_i) were determined from the phase shift (φ) between the surface area and the surface tension waveforms. The ratio between E_i and E_r defines the loss tangent ($\tan\varphi$).

5.2.6 Evaporation resistance

Evaporation resistance of the mouse ML film was evaluated with a ventilated, closed-chamber, droplet evaporimeter recently developed in our laboratory (220). As shown in Figure 5.1, this novel *in vitro* evaporimeter was designed based on the CDS. A key feature of the droplet-based evaporimeter is its capacity of maintaining a constant surface area during water evaporation. This was implemented by determining the surface area of the droplet in real-time and supplementing the evaporation loss by automatically injecting water into the droplet, controlled with the CL-ADSA. The evaporation rate (mm/min) was calculated as $(\Delta V/\Delta t)/A_{\text{drop}}$, where ΔV was the volume of water replenished into the droplet, in order to compensate for the evaporated water and thus to maintain the constant surface area. Δt is the time period of the experiment, typically 5 min. $\Delta V/\Delta t$ was determined from linear regression of the recorded ΔV - Δt curve. A_{drop} was the surface area of the droplet, controlled at $0.35 \pm 0.01 \text{ cm}^2$ using CL-ADSA. The environmental temperature and relative humidity (RH) were controlled at $34.0 \pm 0.1 \text{ }^\circ\text{C}$ and $33.0 \pm 2.0\%$ with a closed environmental control chamber. The chamber was ventilated with a continuous airflow. The airflow rate was measured with a hot wire anemometer (TSI, Shoreview, MN) and was controlled at $1.0 \pm 0.1 \text{ m/s}$ to simulate the ambient environment. The volumetric evaporation rate (*i.e.*, $\Delta V/\Delta t$) of this droplet-based evaporimeter was determined to be less than $2.7 \text{ }\mu\text{L/min}$, comparable to the basal tear production of healthy adults (*i.e.*, $0.8\text{-}2.0 \text{ }\mu\text{L/min}$) (198, 199).

5.2.7 Ultrastructure and film topography

Ultrastructure and topography of the mouse MLF were studied with combined Langmuir-Blodgett (LB) transfer technique and atomic force microscopy (AFM) (7). The MLF was first LB

transferred to a freshly peeled mica sheet, and was then scanned in air with the tapping mode using an Innova AFM (Bruker, Santa Barbara, CA).

5.2.8 Statistical analysis

Results were shown as mean \pm SD ($n \geq 3$). One-way ANOVA with Tukey's means comparison test was used to determine differences between groups (OriginPro, Northampton, MA). $p < 0.05$ was considered to be statistically significant.

5.3 Results

5.3.1 Lipidomic characterization of the mouse Meibomian samples

Figure 5.2 shows the lipidomic characterization of the ML samples extracted from the WT and KO mice. Compared with WT mice, the mutation resulted in a moderate 27% reduction in the total amount of produced MLs. Moreover, *Soat1* inactivation caused multiple changes in the composition of the meibomian lipidome of the KO mice, such as a 51% increase in the apparent abundance of triacylglycerols (TAGs), and a 39% decrease in total WEs (Figure 5.2a). Most importantly, the pool of Chl rose 7 times in the KO mice compared with their WT siblings, and, corroborating our previous results (217), an almost complete ablation of CEs longer than C₁₈-C₂₀ was observed (Figure 5.2b). These changes transformed Chl into the main, most abundant lipid species produced by *Soat1*-null MGs with the apparent abundance of ~50% in the tested pool of lipids. Simultaneously, the apparent abundance of CEs dropped from 38% to 1.5% or so, of which all CEs were of shorter chains in nature. Other changes were an apparent decline in the WE content from 38% to 23%, and an increase in the TAG fraction from 17% to 23%.

5.3.2 Dynamic surface activity of the mouse Meibomian lipid films

Figure 5.3 shows the comparison of dynamic surface activity of the ML films between WT and KO mice at the physiologically relevant temperature of 34 °C. Figure 5.3a shows the typical

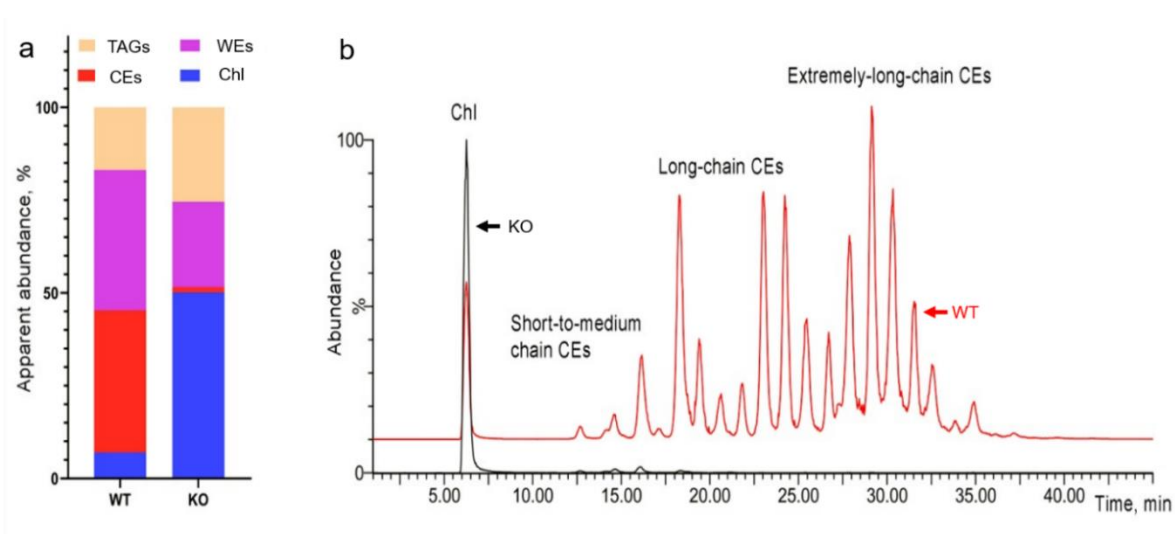


Figure 5.2 Ultrahigh-pressure liquid chromatography-mass spectrometry (UHPLC-MS) lipidomic characterization of the meibomian samples extracted from wild-type (WT) and *Soat1*-knockout (KO) mice. (a) Compositions of the MLs extracted from the WT and KO mice. (b) Effect of *Soat1* inactivation on the ML profiles of mice. Note the major shifts in the Chl/CE ratio in the KO MLs, and a much subtler effect of the mutation on TAGs and WEs.

compression-expansion isotherms of these two MLFs. Reproducibility of the compression-expansion isotherms can be found in Figure S1 of the Supporting Information. It can be seen that both WT and KO MLFs can be compressed to a maximum surface pressure of ~ 50 mN/m, corresponding to a minimum surface tension of ~ 20 mN/m. However, as shown in Figure 5.3b, the compressibility (κ) of the KO ML film is lower than that of the WT ML film (1.33 vs. 1.75 m/mN), indicating that the ML film of KO mice is less compressible, or in other words, “harder” than the ML film of WT mice. Most importantly, as shown in Figure 5.3c, the hysteresis area of the KO ML film is found to be significantly larger than that of the WT ML film (0.13 vs. 0.37 $\mu\text{J}/\text{cycle}$). The hysteresis area of a compression-expansion cycle indicates energy loss per cycle (224). Hence, our results suggest that the energy loss per compression-expansion cycle for the ML film of KO mice is three times that of the healthy WT mice.

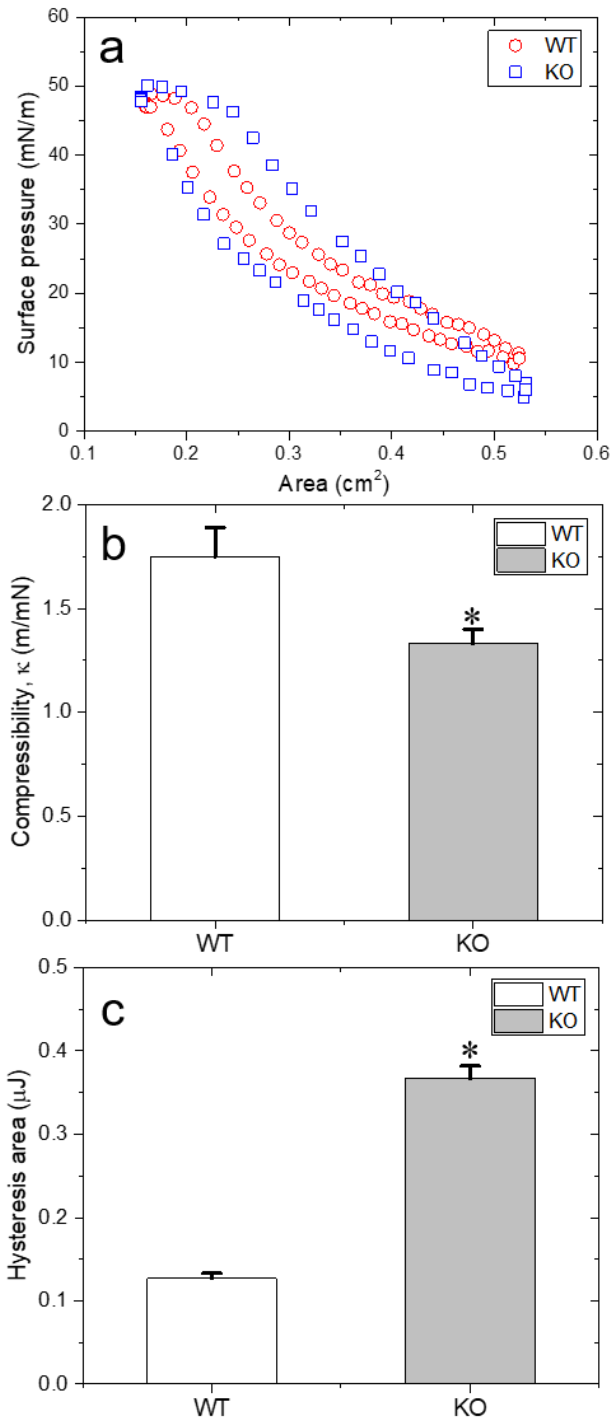


Figure 5.3 Dynamic surface activity of the MLFs of the WT and KO mice at 34 °C. (a) Typical compression-expansion isotherms of the WT and KO MLFs. (c) Statistical analysis of the compressibility (κ_{comp}) of the WT and KO MLFs. (c) Statistical analysis of the hysteresis area, i.e., the energy loss per cycle, for the WT and KO MLFs. * $p < 0.05$ represents statistically significant differences.

5.3.3 Interfacial rheology of the mouse Meibomian lipid films

Figure 5.4 shows the dilational rheological properties of the ML films of the WT and KO mice. All rheological properties were determined at a characteristic surface pressure of 30 mN/m at 34 °C. As shown in Figure 5.4a, the elastic modulus (E_r) of the KO MLF almost doubles that of the WT MLF at all tested frequencies, from 0.01 to 0.25 Hz, thus indicating that the MLF of the KO mice is significantly stiffer or more rigid than the WT mice. This conclusion is also consistent with the compressibility measurement shown in Figure 5.3b. Figure 5.4b shows the viscous modulus (E_i) of the MLFs. In comparison to the E_r measurements shown in Figure 5.4a, the E_i of all MLFs is significantly smaller than the corresponding E_r , indicating that these ML films are essentially more elastic than viscous. Moreover, the E_i of the KO MLF is higher than that of the WT MLF at all tested frequencies. Most importantly, as shown in Figure 5.4c, it is found that the loss tangent ($\tan\varphi = E_i/E_r$) of the KO MLF is in general smaller than that of the WT MLF. In addition, the $\tan\varphi$ of both WT and KO MLFs appears to decrease with increasing frequency, which is consistent with the frequency-dependence of the phospholipid film but has an opposite frequency-dependence as a simplified model TF lipid layer consisting of behenyl oleate (BO): cholesteryl oleate (CO): phosphatidylcholine (PC): palmitic-acid-9-hydroxy-stearic-acid (PAHSA) (40:40:15:5) (6).

5.3.4 Evaporation resistance of the mouse Meibomian lipid films

Figure 5.5 shows the evaporation resistance of the MLFs of the WT and KO mice, upon increasing surface pressure of these MLFs. It can be seen that both WT and KO MLFs demonstrate statistically significant resistance to water evaporation, and the evaporation resistance increases with increasing surface pressure of the MLFs. Nevertheless, the MLF of the WT mice shows significantly higher resistance to water evaporation than the MLF of the KO mice, especially at high surface pressures. For instance, at 30 mN/m, the MLFs of the WT and KO mice reduce the

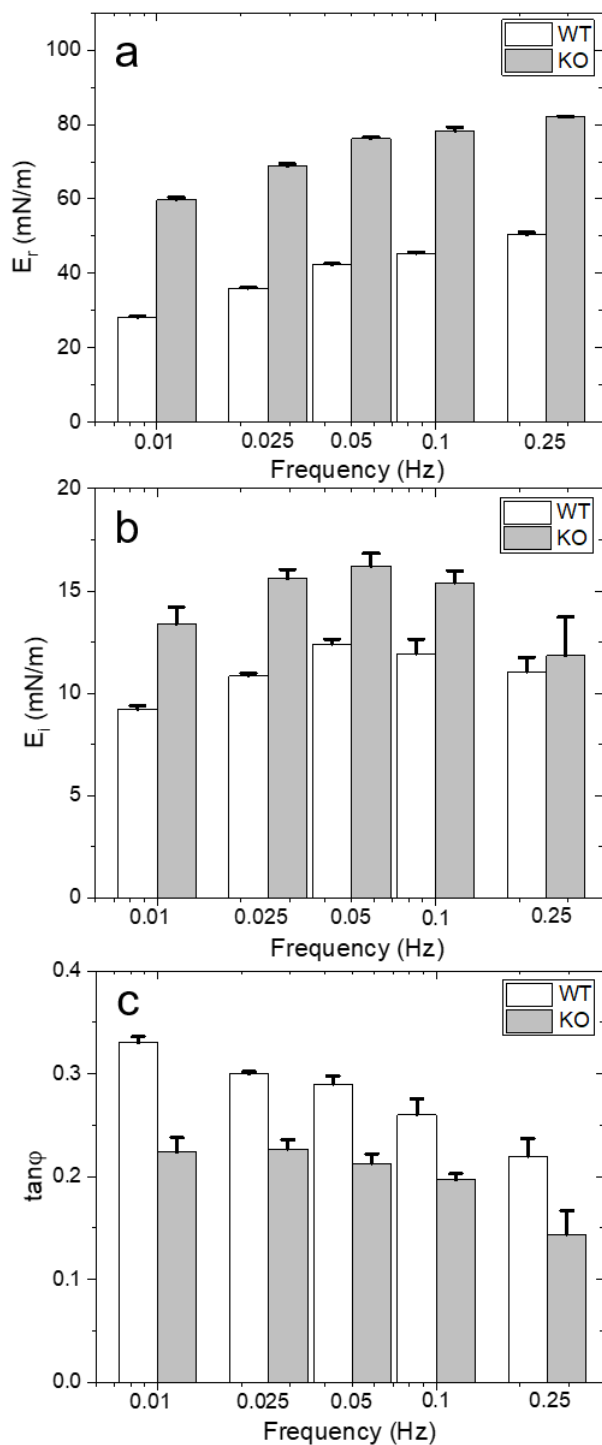


Figure 5.4 Interfacial dilational rheological properties of the MLFs of the WT and KO mice. (a) Elastic modulus (E_r) of the WT and KO MLFs. (b) Viscous modulus (E_i) of the WT and KO MLFs. (c) Loss tangent ($\tan\phi$) of the WT and KO MLFs. All interfacial rheological properties were determined at the characteristic surface pressure of 30 mN/m at 34 °C.

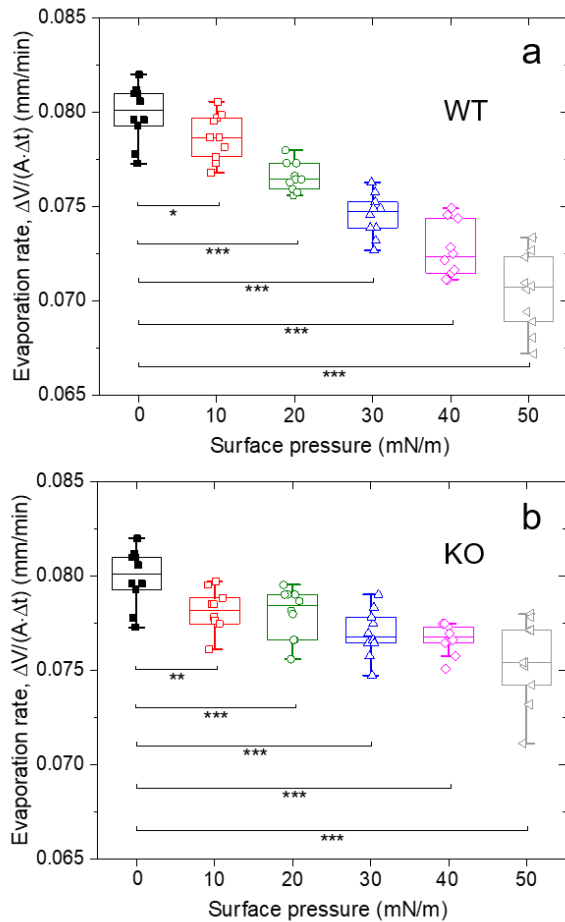


Figure 5.5 Effects of the ML films of the WT (a) and KO (b) mice, under various surface pressures, on water evaporation. *p<0.05, **p<0.01, ***p<0.001.

water evaporation rate by 6.8 % and 3.7%, respectively. At 50 mN/m, however, the MLFs of the WT and KO mice reduce the water evaporation rate by 11.9 % and 5.6%, respectively, thus indicating that the evaporation resistance of the WT MLF more than doubles that of the KO MLF at this high surface pressure. In fact, linear regression of the data shown in Figure 5 indicates that the dependence of the evaporation resistance on surface pressure for the WT MLF more than doubles that of the KO MLF, indicating that the MLF of WT mice has a much better retardation effect to water evaporation than the MLF of KO mice.

5.3.5 Ultrastructure and topography of the mouse Meibomian lipid films

Figure 5.6 shows the ultrastructure and topography of the ML film of WT and KO mice, at three characteristic surface pressures, *i.e.*, 20, 30, and 40 mN/m, obtained at 34 °C. As shown in Figure 5.6a, the WT MLF at a low surface pressure of 20 mN/m demonstrates a multilayered structure with a network of lipid folds 40-60 nm in height. This structure is very different from that of the simplified model TFL investigated in our previous studies (7, 220). Single-component or 4-component model lipid films at such low surface pressures typically exhibit a monolayer conformation (7, 220). With increasing surface pressure to 30 mN/m (Figure 5.6b), the WT MLF shows discrete bead-like structures, with a lateral diameter of $\sim 1.4 \mu\text{m}$ and a height of $\sim 15 \text{ nm}$, surrounded with coffee-ring-like structures of $\sim 3 \mu\text{m}$ in diameter and $\sim 4 \text{ nm}$ in height. A similar structure has been detected in the model TFL of BO:CO:PC:PAHSA (40:40:15:5) at the same surface pressure (220). These bead-like structures must be formed by the squeeze-out nonpolar lipids in the ML film, due to lack of affinity to the air-water surface. The coffee-ring-like structures are most likely formed by evaporation-driven self-assembly of reverse micelles of polar lipids mixed with nonpolar lipids (220). With further increasing the surface pressure to 40 mN/m (Figure 5.6c), the MLF is compressed into a lipid multilayer with a compacted bilayer ($\sim 4 \text{ nm}$ in height) cover the air-water surface, and large aggregates of 50-100 nm in height atop the compacted bilayer.

The MLF of the KO mice shows a completely different ultrastructure and topography in comparison to that of the WT mice. As shown in Figure 5.6d, the KO MLF at the low surface pressure of 20 mN/m shows only limited amounts of multilayered protrusions 10 to 30 nm in height. At 30 mN/m (Figure 5.6e), a large portion of the film is still covered with a monolayer, while only isolated multilayer protrusions appear in the lipid film. At 40 mN/m (Figure 5.6f), the KO MLF

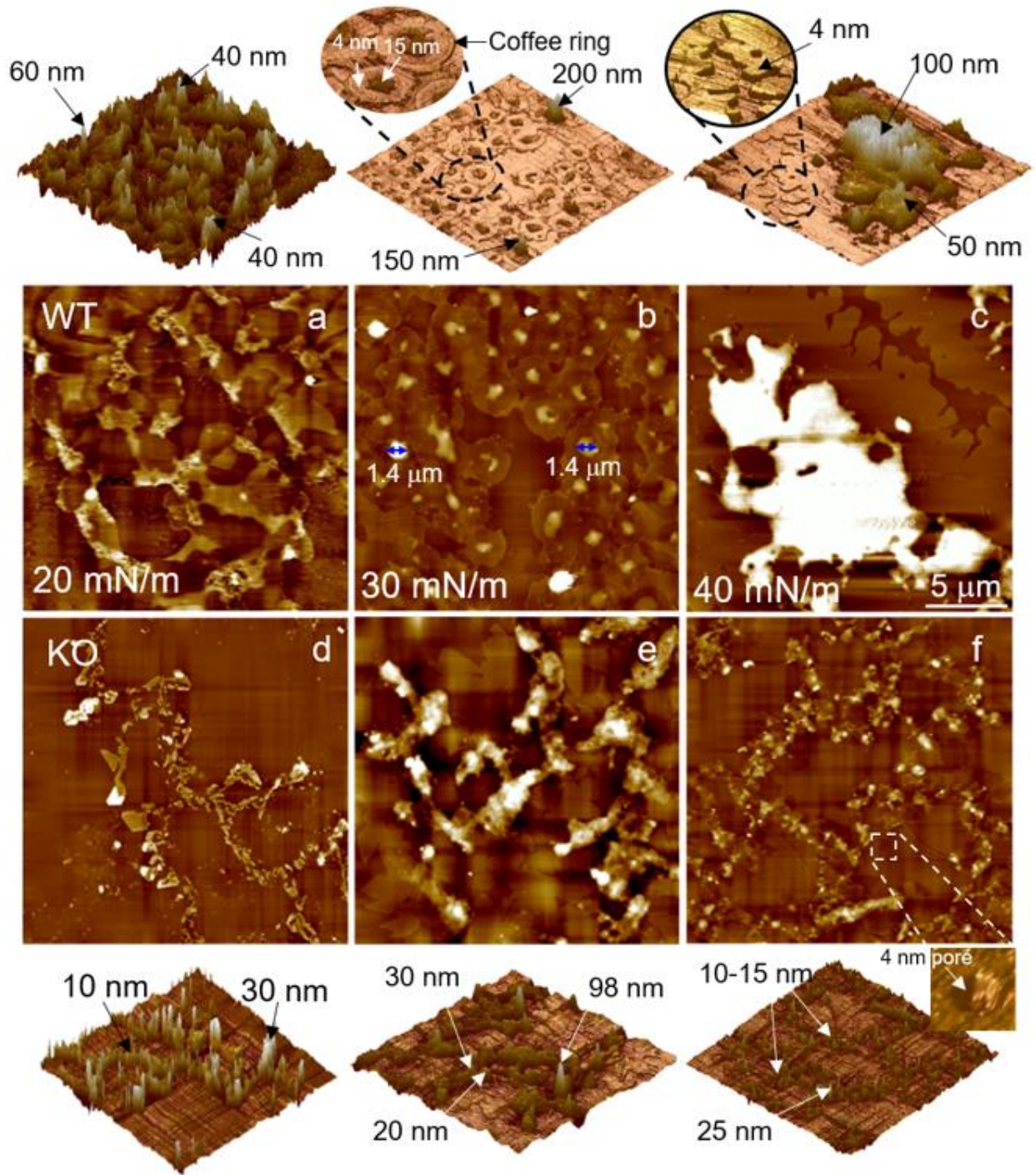


Figure 5.6 Ultrastructure and topography of the MLFs of the WT (a-c) and KO (d-f) mice at three characteristic surface pressures, i.e., 20, 30, and 40 mN/m. All AFM images shown in the two middle rows have the same scanning area of $20 \times 20 \mu\text{m}$, and the same z range of 50 nm. Images in the top and bottom rows show the 3D renderings of the WT and KO ML films, respectively. Single-headed arrows indicate the heights of the structures, while double-headed arrows indicate the lateral dimensions of the structures. The bar represents $5 \mu\text{m}$.

still appears to be mostly in a monolayer conformation without significant amounts of multilayered structures detected even at this high surface pressure. Neither bead-like structures nor coffee-ring-like structures, as appearing in the WT MLF, are detected in the KO MLF. These structural variations are consistent with the compositional variations of the MLFs of the WT and KO mice, since the KO MLF lacks the most important nonpolar lipid, *i.e.*, CEs, and are enriched in Chl.

5.4 Discussion

Composition-structure-functional correlations revealed by comparison of the Meibomian lipid films between WT and *Soat1*-null mice

Corroborating our previous result (225), inactivation of *Soat1* almost completely eliminated long- and extremely long-chain CEs from meibum, and led to a multifold increase in non-esterified free Chl (Figure 5.2). The remaining CEs were based on C₁₄-C₁₈ fatty acids with one, two or three double bonds, *i.e.*, similar to those found in serum of mice and humans. As a result of this, free Chl became the major lipid species found in ML of the *Soat1*-null mice, comprising $\geq 50\%$ of the lipid pool. It is well known that Chl has a profound impact on the phospholipid phase behavior (153). Hence, it is not unexpected that enrichment of lipid mixtures (such as MLs) with Chl would noticeably change their rheological/thixotropic properties, especially at the physiologically relevant temperature around 34 °C.

Indeed, in comparison to the MLF of healthy WT mice, we found multiple biophysical variations to the MLF of KO mice, and such biophysical variations appear to be closely correlated with the alternation of the lipid profile. Both surface tension and interfacial rheological measurements consistently suggested that the MLF of KO mice is stiffer than the MLF of WT mice, revealed by the reduced film compressibility (Figure 5.3b), increased elastic modulus (Figure 5.4a), and decreased loss tangent (Figure 5.4c) of the KO MLF. These biophysical

variations can be correlated with the dramatic increase of free Chl in the ML samples of KO mice. How does Chl affect the phase behavior of lipid monolayers and bilayers largely depends on the temperature and the molar fraction of Chl in the mixture (226). The overall biophysical effect of Chl is to fluidize lipids in a rigid gel phase by disrupting lipid packing, or to condense lipids in a fluid phase by interacting with their disordered chains and thus stabilizing the fluid lipids (227-230). At 34 °C, most lipids in meibum, especially those with relatively shorter fatty acid chains (C₁₄-C₁₈), exist in a fluid phase. Hence, the increased Chl fraction in ML of KO mice is expected to condense and rigidify the MLF. One direct adverse biophysical consequence of the increasing film rigidity is to cause more energy loss per compression-expansion cycle that mimics the blinking cycle of the MLF (Figure 5.2c). Indicatively, thermotropic transitions in meibum of *Soat1*-null mice were distinctively different from those of WT mice (217). The melting transition of KO meibum, which began at -10 °C similarly to WT meibum, started to deviate from the trajectory of WT meibum after reaching a normal physiological temperature of cornea of around 34 °C, at which only a portion of the KO meibum is melted, while the other part remains solidified, which is consistent with a large presence of high-melting fraction of free Chl. In term of interfacial rheological properties, such a phase-mixing KO MLF demonstrates a decreased loss tangent in comparison to the WT MLF (Figure 5.4c). The MLF formed from the CE-depleted/Chl-enriched KO mouse meibum seems to replicate many features of MLFs formed of human meibum with increased levels of Chl (231).

Directly imaging the MLFs of WT and KO mice using AFM revealed further evidence about the composition-structure-functional correlations. The ML film of WT mice mostly depicts a multilayer conformation (Figure 5.6a-c). Especially at the physiologically relevant high surface pressures, e.g., 40 mN/m, the MLF consists of a compacted bilayer (~4 nm in height) and large

aggregates of 50-100 nm in height atop the compacted bilayer (Figure 5.6c). In contrast, the multilayer structures largely, if not completely, disappear from the MLF of KO mice (Figure 5.6d-f). Thinning of the ML film for the KO mice is most likely related to the depletion of CEs from meibum, since our previous studies suggested that the multilayer structures are mostly composed of nonpolar lipids (220), which can be easily squeezed out of the interfacial film at high surface pressure, because of their low affinity to the air-water surface. Interestingly, the same type of thinning of the MLF was also observed for human samples enriched with Chl (231), thus indicating that the enrichment of Chl in the KO mouse sample may also contribute to the transition from multilayer to monolayers.

Implications to Meibomian gland dysfunction and dry eye

Meibomian gland dysfunction (MGD) is the leading cause of DED (232, 233). It is believed that alternation of the ML profile, especially those nonpolar lipids in MLs, may significantly compromise the evaporation resistance of TFLL, thus leading to DED. The present study shows that at the physiologically relevant high surface pressures, the evaporation resistance of the WT MLF more than doubles that of the KO MLF (Figure 5.5). In addition, the dependence of the evaporation resistance on surface pressure for the WT MLF also more than doubles that of the KO MLF, indicating that the MLF of WT mice has a much better retardation effect on water evaporation than the MLF of the KO mice (Figure 5.5). These data suggest that long- and extremely long-chain CEs, *i.e.*, those longer than C₁₈-C₂₀, may play an important role in reducing tear evaporation. Another factor to consider is the effect of accumulation of Chl in meibum. Being an amphiphilic compound with a high melting temperature, Chl mixed well with Meibomian lipids causes an increase in their melting temperature, and rigidity and collapsibility of Chl-enriched MLF.(217, 231) Clinical studies linked hypercholesterolemia and MGD(234-236). Considering

that blood Chl can be transported to, and accumulated in, MGs in unaltered form, these observations provide an opportunity for Chl to play a role in inspissation of meibum of certain types of MGD (*e.g.*, its obstructive variant) and DED patients, and poor stability of their TF (237, 238). We are confident that future experiments with MLF will reveal the intricate mechanisms of molecular interactions between different types of Meibomian lipids, and their impact on the ocular surface homeostasis in the norm and pathology.

5.5 Summary

Using a novel experimental methodology called the constrained drop surfactometry (CDS), we reported a comprehensive biophysical study of the dynamic surface activity, interfacial rheology, evaporation resistance, and ultrastructure of the Meibomian lipid films (MLF) extracted from wild type (WT) and *Soat1* knockout (KO) mice. By correlating the lipidomic analysis and biophysical assays of the MLs of WT and KO mice, our study revealed novel experimental evidence on the composition-structure-functional correlations of the MLFs, and suggested a potential biophysical function of long-chain CEs in optimizing the surface activity, interfacial rheology, and evaporation resistance of the MLFs. This study may provide novel implications to pathophysiological and translational understanding of MGD and DED.

Chapter 6 Adsorbed pulmonary surfactant at physiologically relevant high concentrations ¹

6.1 Introduction

Pulmonary surfactant is a lipid-protein complex synthesized by the alveolar type II epithelial cells (94). It forms a thin film at the air-water surface of the lungs *via* rapid adsorption, immediately after inflating the lungs with air on the newborn's first breath (239). The adsorbed pulmonary surfactant film plays a dual physiological role of host defense against inhaled particles and pathogens, and surface tension reduction that increases lung compliance and stability of the alveolar architecture (240). Deficiency or dysfunction of endogenous pulmonary surfactant leads to life-threatening respiratory diseases (241). Neonatal respiratory distress syndrome (RDS) is a major disease of surfactant deficiency caused by premature birth (242). In addition to assisted ventilation and continuous positive airway pressure, surfactant replacement has been used as a standard clinical intervention to treat premature newborns with or at high risk for RDS (243). Surfactant replacement therapy has also been attempted to treat pediatric and adult patients with acute respiratory distress syndrome (ARDS) (244), but with only limited success (245). Amid the COVID-19 pandemic, surfactant replacement has been tested as a supportive therapy to treat patients with COVID-19-induced ARDS (246, 247).

Several *in vitro* biophysical models have been developed to assess the dynamic surface activity of pulmonary surfactant preparations. Three most widely used *in vitro* methods are the Langmuir

¹ Xu X, Li G, Zuo YY. Constrained drop surfactometry for studying adsorbed pulmonary surfactant at physiologically relevant high concentrations. Submitted to *Am. J. Physiol. Lung Cell Mol. Physiol.*

film balance, pulsating bubble surfactometry (PBS), and captive bubble surfactometry (CBS). Comparing to the other two methods, the Langmuir film balance is usually only used for studying the compression of surfactant monolayers spread with an organic solvent, and thus has only limited capacity for biophysical simulations (94). The PBS determines the minimum and maximum surface tensions of pulmonary surfactant by oscillating a small air bubble (~1 mm in diameter) suspended in pulmonary surfactant, with a fixed rate of 20 cycles/min and a fixed surface area reduction of 50% (248). Because of its simplicity and small sample consumption (~20 μ L), the PBS has gained popularity in medical research and quality control of clinical surfactant preparations (249). Nevertheless, the PBS only provides approximate biophysical simulations of pulmonary surfactant, mostly because of film leakage at the capillary tube to which the air bubble is suspended (94). To reduce surface tension to physiologically relevant low values, the surfactant film in PBS needs to be compressed and expanded up to 100 cycles, *i.e.*, 5 min, and in each cycle, the surfactant film is compressed by 50% of its initial surface area, which has little physiological relevance since the surface area of the lungs does not vary more than 20% during normal tidal breathing (250).

The CBS is the first *in vitro* model capable of simulating biophysical properties of pulmonary surfactant films under physiologically relevant conditions (251). It uses a large air bubble of 2-7 mm in diameter floating in a few milliliters of the surfactant suspension held in a transparent chamber. The bubble is separated from the chamber's ceiling, treated with a hydrophilic coating, by a thin wetting film, and hence the bubble is "captured" by the liquid phase, thus eliminating all potential pathways for film leakage (252). The CBS is capable of assaying the biophysical properties of adsorbed pulmonary surfactant films undergoing dynamic compression-expansion cycles that simulate tidal breathing (253, 254). In spite of its superb performance in biophysical

simulations, the CBS has a technical limitation in studying pulmonary surfactants. The surfactant suspension becomes murky or even opaque at high concentrations, which makes surface tension measurements from the shape of the bubble challenging or even impossible (255, 256). Consequently, the maximum surfactant concentration that can be *in vitro* simulated with the CBS is usually no more than 3 mg/mL (253, 254). This technical limitation can be somehow circumvented by spreading a high-concentration aqueous surfactant suspension around the bubble surface using a microsyringe, and meanwhile modifying the saline subphase with 10 wt% sucrose to help reduce precipitation of the surfactant vesicles (257).

The surfactant concentration used in clinical preparations varies but is consistently higher than 25 milligram phospholipids per milliliter (243). Survanta, a bovine surfactant prepared from minced lung tissues and supplemented with synthetic dipalmitoyl phosphatidylcholine (DPPC), palmitic acid, and tripalmitin, is clinically used at a concentration of 25 mg/mL. BLES, a bovine surfactant extracted from the lunge lavage of adult cows, is clinically used at 27 mg/mL. Infasurf, a bovine surfactant prepared from the lung lavage of newborn calves, is used at 35 mg/mL. Curosurf, a porcine surfactant prepared from minced lung tissues, is used at a high lipid concentration of 80 mg/mL.

The concentration of endogenous pulmonary surfactant in the alveolar hypophase of adult mammals could be estimated based on the total surfactant phospholipids recovered from bronchoalveolar lavage (258-260), the alveolar surface areas of various mammal species (261), and the overall area-weighted average thickness of the alveolar lining layer (*i.e.*, 0.2 μm) (262). Based on these data, it can be estimated that the endogenous surfactant concentration in adult mammals' lungs likely ranges between ~15 and ~50 mg/mL. To the best of our knowledge, *in vitro*

biophysical simulations of pulmonary surfactants at these physiologically relevant high concentrations (*i.e.*, >10 mg/mL) are still scarce.

Here, we report *in vitro* biophysical simulations of an animal-derived natural pulmonary surfactant, Infasurf, at the physiologically relevant high surfactant concentrations up to 35 mg/mL, using a novel experimental methodology called constrained drop surfactometry (CDS), developed in our laboratory (263). The CDS is capable of simulating the intra-alveolar microenvironment of pulmonary surfactants under physiologically relevant conditions. We have recently developed a novel subphase replacement technique and an *in situ* Langmuir-Blodgett (LB) transfer technique that allows direct atomic force microscopy (AFM) imaging of the ultrastructure and topography of adsorbed pulmonary surfactant films with submicron resolutions (102). These findings have novel implications in better understanding the physiological and biophysical functions of the pulmonary surfactant film, and may offer new translational insights into the design of clinical surfactant preparations to treat respiratory distress syndrome.

6.2 Materials and methods

6.2.1 Pulmonary surfactant

Infasurf was a gift from ONY Biotech (Amherst, NY). It is prepared from the lung lavage of newborn calves with centrifugation and organic extraction. Infasurf contains all hydrophobic components of the natural bovine surfactant, whereas hydrophilic surfactant proteins (SP-A and SP-D) were removed during the extraction process. Infasurf was stored at -20 °C in sterilized vials with an initial phospholipid concentration of 35 mg/mL. It was diluted with a saline buffer to various phospholipid concentrations on the day of the experiment.

6.2.2 Constrained drop surfactometry (CDS)

The CDS is a new generation of droplet-based tensiometry technique developed in our laboratory for biophysical simulations of pulmonary surfactants (99, 263). As illustrated in **Figure 6.1**, the CDS uses the air-water surface of a sessile droplet (~ 3 mm in diameter, ~ 0.14 cm² in surface area, and ~ 7 μ L in volume) to accommodate the adsorbed surfactant film. The surfactant droplet is constrained on a carefully machined pedestal that uses its knife-sharp edges to prevent film leakage, even at low surface tensions. The adsorbed surfactant film can be compressed and expanded periodically at physiologically relevant rates and compression ratios by controlling liquid flow out of and into the droplet using a motorized syringe. The surface tension and surface area of the adsorbed surfactant film are determined from the shape of the droplet using newly developed closed-loop axisymmetric drop shape analysis (CL-ADSA) (264). Owing to system miniaturization, the CDS enables a high-fidelity simulation of the intra-alveolar environment, including the core body temperature of 37 °C and a relative humidity close to 100%, using an environmental control chamber.

Specifically, a 7- μ L Infasurf droplet, with a specific surfactant concentration, was dispensed onto the CDS pedestal using a micropipette. Immediately after dispensing the droplet, its surface tension was continuously recorded, and was found to quickly (within seconds) reduce to an equilibrium value around 22-25 mN/m, indicating rapid adsorption of the pulmonary surfactant film at the air-water surface of the droplet (94). To mimic exhalation and inhalation, the adsorbed surfactant film was compressed and expanded at 20 cycles per minute with the compression ratios controlled at 15, 25, and 35%, respectively.

6.2.3 Subphase replacement and Langmuir-Blodgett (LB) transfer

To facilitate direct imaging of the ultrastructure and topography of the adsorbed surfactant film, we have developed a novel subphase replacement technique and an *in situ* LB transfer technique (102). As shown in Figure 6.1, the subphase replacement was implemented using a coaxial CDS pedestal connected with two motorized syringes, with one withdrawing the phospholipid-vesicle-containing subphase from the droplet at a flowrate of 10 $\mu\text{L/s}$, and the other one simultaneously injecting buffer into the droplet with the same flowrate. Consequently, phospholipid vesicles in the aqueous subphase, *i.e.*, the droplet, were washed away without disturbing the adsorbed Infasurf film at the air-water surface. After the subphase replacement, LB transfer of the adsorbed Infasurf film was performed by first quickly inserting a freshly peeled mica sheet into the droplet, followed by slowly lifting the mica across the air-water surface of the droplet at a rate of 1 mm/min. During the LB transfer process, the Infasurf film was maintained at a constant surface pressure (± 1 mN/m) using CL-ADSA. All measurements were conducted at 37 $^{\circ}\text{C}$ at least three times. The deposition ratio of the LB transfer, defined as the ratio between the lost area of the surfactant film during the LB transfer and the total surface area of the mica sheet (265), was estimated to be ~ 1.24 (102), thus indicating a complete transfer of the surfactant film from the air-water surface to the mica surface.

6.2.4 Atomic force microscopy (AFM)

The ultrastructure and topography of the adsorbed surfactant films were imaged using an Innova AFM (Bruker, Santa Barbara, CA). Samples were scanned in air using the tapping mode with a silicon cantilever of the spring constant 42 N/m and a resonance frequency of 300 kHz. Images were taken at multiple locations to ensure reproducibility. Lateral structures, topography, bearing

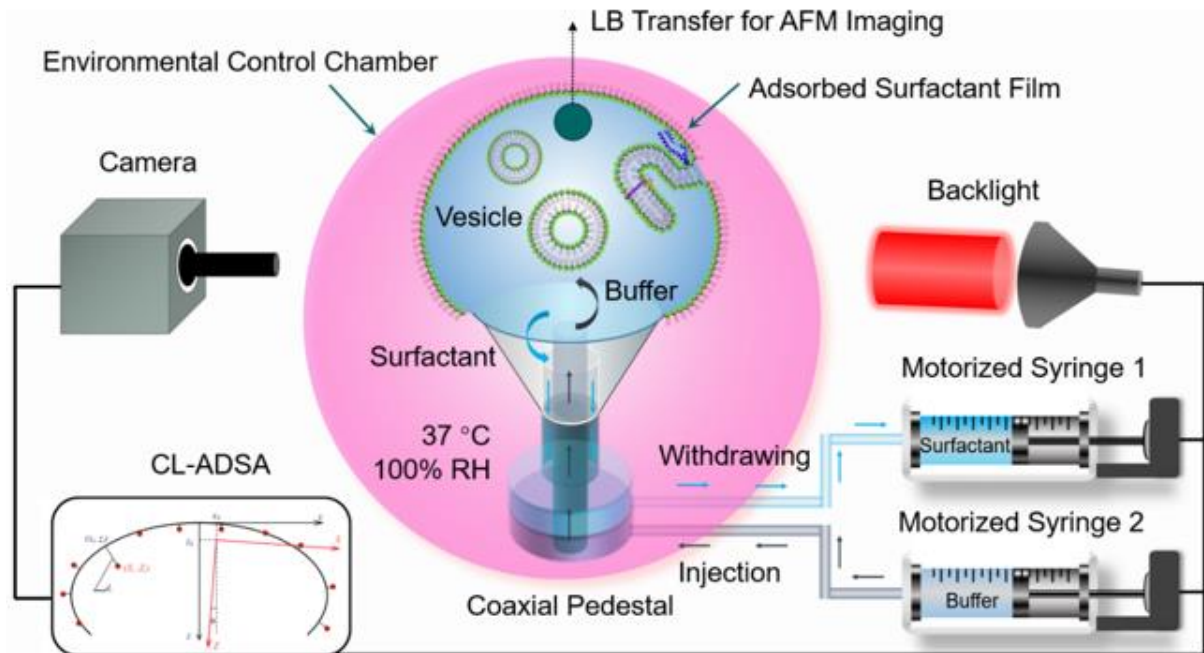


Figure 6.1 Schematic of the constrained drop surfactometry (CDS). Pulmonary surfactant is adsorbed to the air-water interface of a surfactant droplet. The sessile droplet is constrained on a 3-mm pedestal with knife-shape edges, and is enclosed in an environmental control chamber maintained at 37 °C. Surface tension and surface area of the adsorbed surfactant film are determined simultaneously from the shape of the droplet using close-loop axisymmetric drop shape analysis (CL-ADSA). Subphase replacement is implemented with a coaxial pedestal connected to two motorized syringes, with one withdrawing the vesicle-containing subphase from the droplet and another one simultaneously injecting buffer into the droplet with the same volumetric rate. The adsorbed surfactant film is subsequently Langmuir-Blodgett (LB) transferred from the air-water interface to a freshly peeled mica substrate for atomic force microscopy (AFM) imaging.

area, and bearing volume of the surfactant samples were analyzed using NanoScope Analysis (version 1.5).

6.2.5 Statistics

All results are shown as mean \pm standard deviation ($n > 3$). One-way ANOVA with the Tukey means comparison test was used to determine group differences (OriginPro, Northampton, MA). $p < 0.05$ was considered to be statistically significant.

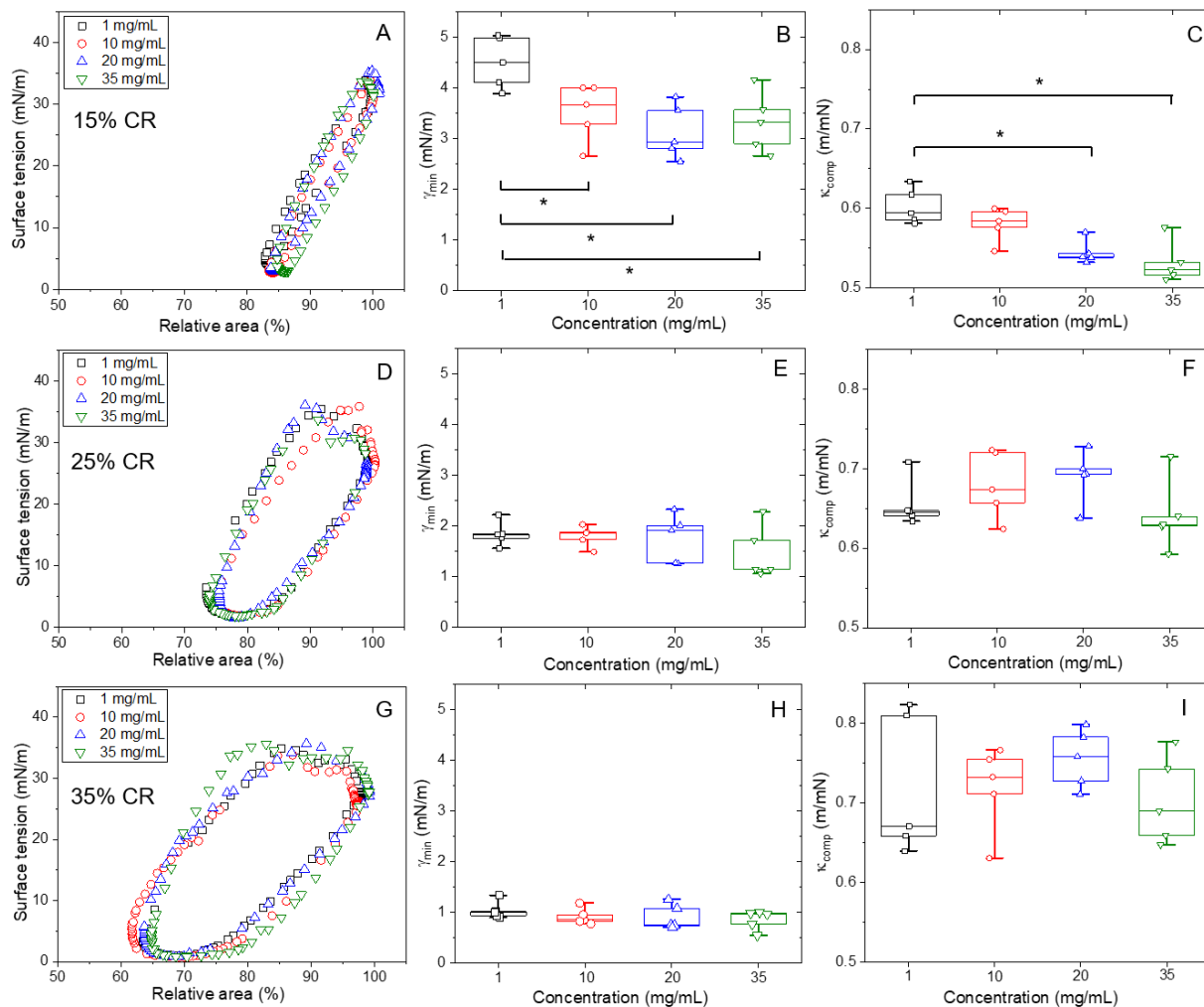


Figure 6.2 Dynamic surface activity of the Infasurf film adsorbed from a series of phospholipid concentrations, i.e., 1, 10, 20, and 35 mg/mL. Results shown are typical compression-expansion cycles (the 10th cycle), minimum surface tension (γ_{\min}), and film compressibility (κ_{comp}) for three different film compression ratios (CRs), i.e., 15% (A-C), 25% (D-F), and 35% (G-I). All dynamic cycling experiments were performed at 37 °C with a cycling rate of 3 seconds per cycle using the CDS. * $p < 0.05$ in comparison to Infasurf at the phospholipid concentration of 1 mg/mL.

6.3 Results

6.3.1 Dynamic surface activity of the adsorbed surfactant film

Figure 6.2 shows the dynamic surface activity of the Infasurf film adsorbed at physiologically relevant phospholipid concentrations of 10, 20, and 35 mN/m. A relatively low surfactant

concentration of 1 mg/mL was also studied as a reference. Three area compression ratios, *i.e.*, 15%, 25%, and 35%, were studied. The dynamic surface activity of the adsorbed surfactant film was quantified with the minimum surface tension (γ_{\min}) and the film compressibility (κ_{comp}), all based on data of the tenth consecutive cycle.

As shown in Figure 6.2A-C, at the physiologically relevant 15% compression ratio, the γ_{\min} of Infasurf at 1 mg/mL is 4.5 mN/m. When the surfactant concentration is increased to 10, 20, and 35 mg/mL, the γ_{\min} is reduced to 3.5, 3.1, and 3.0 mN/m, respectively, all below 4 mN/m. The κ_{comp} of the Infasurf film at 1 mg/mL is 0.60 m/mN, which gradually decreases to 0.52 m/mN, when the surfactant concentration is increased to 35 mg/mL. At the 25% compression ratio (Figure 6.2D-F), the γ_{\min} of Infasurf at all studied concentrations is consistently lower than 2 mN/m. The κ_{comp} of the Infasurf film varies between 0.65 and 0.70 m/mN. No statistically significant differences can be found among various concentrations from 1 to 35 mg/mL. At the 35% compression ratio (Figure 6.2G-I), the γ_{\min} of Infasurf at all studied concentrations reaches values lower than 1.0 mN/m, and the κ_{comp} varies between 0.7 and 0.8 m/mN, without statistically significant differences among these surfactant concentrations.

6.3.2 Optimization of the subphase replacement for AFM imaging

For imaging the ultrastructure and topography of the adsorbed surfactant film, subphase replacement is needed to wash away the non-adsorbing phospholipid vesicles from the droplet. Otherwise the solid substrate for LB transfer would be contaminated *prior to* the LB transfer, thus compromising the quality of AFM imaging. A key parameter that affects the subphase replacement process is the replacement volume. An optimal replacement volume should be the minimum volume capable of removing all non-adsorbing vesicles from the droplet, while effectively preserving the structure and functionality of the multilayer structures of the adsorbed surfactant

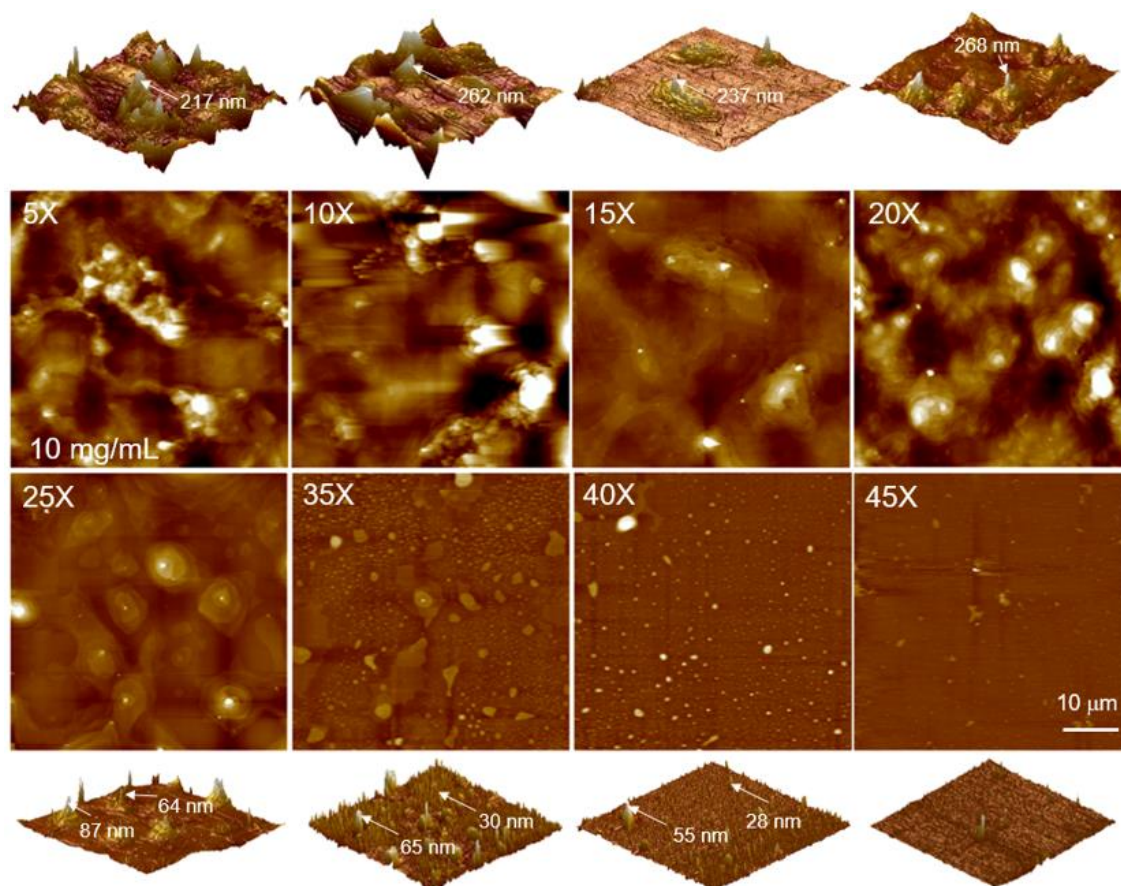


Figure 6.3 Ultrastructure and topography of the Infasurf film after de novo adsorption from a phospholipid concentration of 10 mg/mL. AFM images of the adsorbed surfactant film were obtained after subphase replacement with buffer volumes from 5-fold (5X) to 45-fold (45X) of the original droplet volume. Images in the top and bottom rows show the 3D rendering of the corresponding 2D AFM images shown in the middle rows. All AFM images have the same scanning area of $50 \times 50 \mu\text{m}$. AFM images for 5X, 10X, 15X, and 20X have a z range of 200 nm. AFM images for 25X and 35X have a z range of 100 nm, while the z range for the images of 40X and 45X is 30 nm. The 25X replacement volume was found to be an optimal subphase replacement volume because it efficiently removed the non-adsorbing vesicles from the droplet and, meanwhile, preserved the multilayers of the adsorbed Infasurf film. Arrows indicate the heights of structures.

film (102). For the Infasurf film adsorbed from a relatively low phospholipid concentration of 1 mg/mL, our previous study has determined the optimal subphase replacement volume to be threefold (3X) of the droplet volume (102).

Figure 6.3 shows the optimization process for the Infasurf film adsorbed from a phospholipid concentration of 10 mg/mL. It can be seen that subphase replacement from 5X to 20X volumes

did not effectively remove all vesicles. Large unilamellar and multilamellar vesicular structures with a height range between 200 and 300 nm were found to adsorb to the mica surface. With the 25X replacement volume, the AFM images demonstrate well-organized multilayer structures consisting of bilayer stacks of 60-90 nm in height (see Figure 4B for detailed topographic analysis). With the 35X replacement volume, the adsorbed Infasurf film also shows an organized multilayer structure. However, with further increasing the replacement volumes to 40X and 45X, the adsorbed Infasurf film depicts a primary monolayer conformation with only isolated multilayer protrusions, thus indicating compromised multilayer structures due to excessive washing. These AFM observations therefore collectively indicate that the optimal subphase replacement volume for 10 mg/mL Infasurf is around 25X, which balances the sufficient removal of non-adsorbing vesicles from the droplet and the effective preservation of functional multilayer structures.

A similar optimization process has been performed for imaging the Infasurf film adsorbed from 20 and 35 mg/mL surfactant suspensions, respectively. The optimal replacement volumes for 20 and 35 mg/mL Infasurf were found to be 45X and 80X, respectively.

6.3.3 Ultrastructure and topography of the adsorbed surfactant film

Figure 6.4 shows the ultrastructure and topography of the Infasurf film adsorbed from the surfactant concentrations of 1, 10, 20, and 35 mg/mL, respectively. As shown in Figure 6.4a, at a low concentration of 1 mg/mL, the Infasurf film shows a large number of uniformly distributed protrusions between 16 and 28 nm in height. Given the thickness of a fully hydrated phospholipid bilayer to be around 4 nm (266), these protrusions correspond to 4-7 stacked bilayers, in good agreement with our previous observation of the adsorbed Infasurf film from the same surfactant concentration, *i.e.*, 1 mg/mL (102).

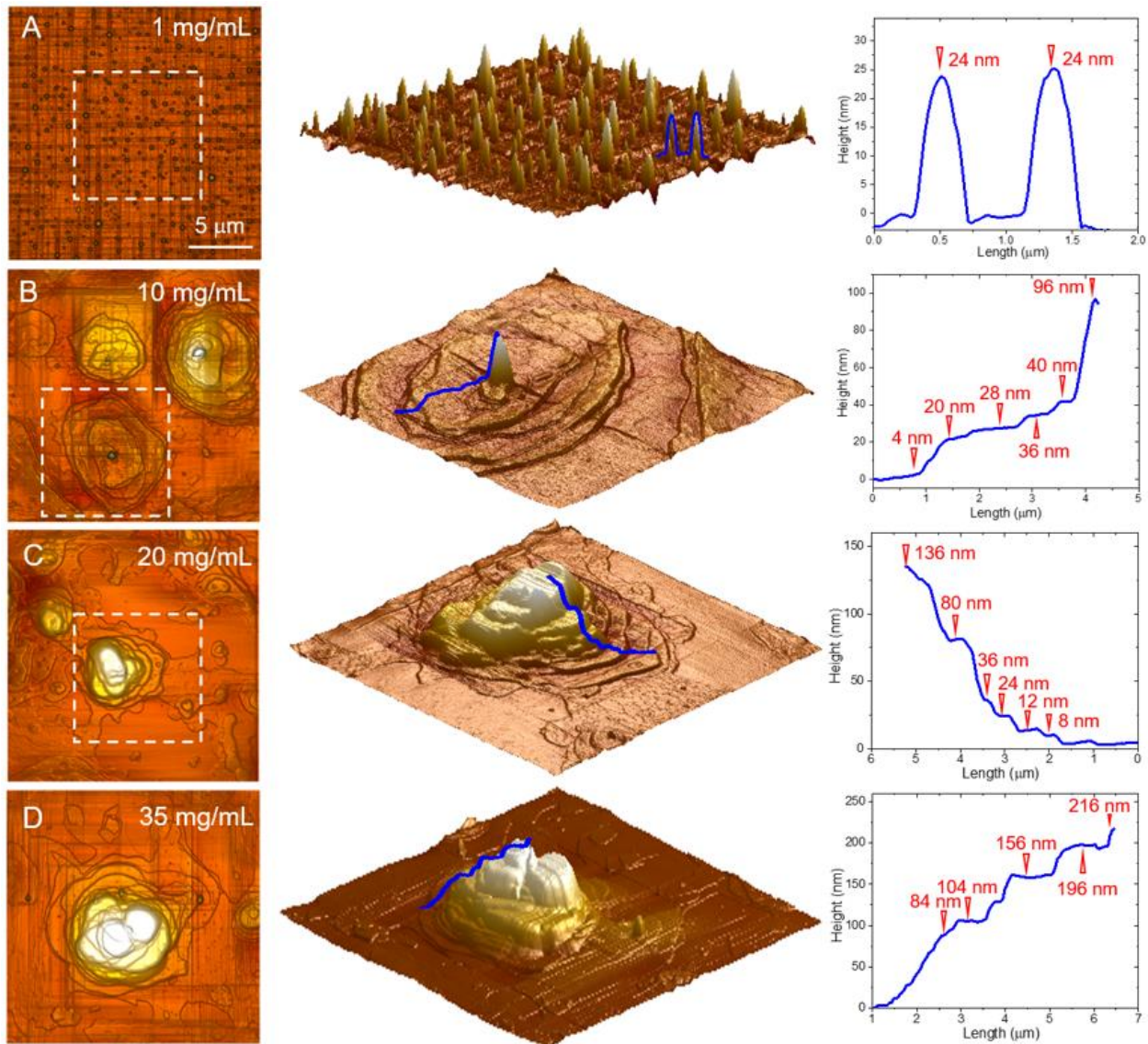


Figure 6.4 Ultrastructure and topography of the Infasurf film after de novo adsorption from phospholipid concentrations of 1 mg/mL (A), 10 mg/mL (B), 20 mg/mL (C), and 35 mg/mL (D). All AFM images were obtained with optimal subphase replacement conditions demonstrated in Figures 6.3. Images in the left column show the topographic map of the Infasurf film adsorbed from various surfactant concentrations. Each contour line of the topographic map connects points of equal height of the multilayers. All images have the same scanning area of $20 \times 20 \mu\text{m}$. The z range is 150 nm for images in A and B, and 400 nm for images in C and D. Images in the middle column show the 3D rendering of the adsorbed Infasurf films, indicated inside the white boxes shown in the images on the left. To better illustrate the multilayer structures, the corresponding topographic map was rotated in the clockwise direction by 45° . Images in the right column show the height profile of the multilayer structures indicated by the blue lines superimposed onto the 3D rendering of the adsorbed Infasurf film.

Increasing the surfactant concentration to physiologically relevant levels, the adsorbed Infasurf film demonstrates significantly larger multilayer structures both in the lateral and height dimensions. These multilayer structures depict a well-defined conformation of layer-by-layer assembly of stacked bilayers with the height of the multilayers proportional to the surfactant concentration of the subphase. The height profile of these multilayers shows a stair-like structure with the height of each “stair” to be a multiplier of ~ 4 nm (*i.e.*, the thickness of a single bilayer).

Figure 6.5 shows the statistical analysis of the maximum height, the area fraction, and the surface area-averaged equivalent number of phospholipid bilayers stored in the multilayers of the Infasurf film adsorbed from various surfactant concentrations. The maximum height of the multilayer structure is 36, 96, 148, and 228 nm, corresponding to stacks of 9, 24, 37, and 57 lipid bilayers, for the Infasurf film adsorbed from the surfactant concentrations of 1, 10, 20, and 35 mg/mL, respectively. The area fraction of the multilayers increases from 9% of the entire surfactant film at 1 mg/mL, to $\sim 70\%$ at 35 mg/mL. The equivalent number of phospholipid bilayers stored in the multilayers of the Infasurf film, averaged over the entire surface area of the adsorbed Infasurf film, can be estimated from the volume of all multilayer structures found in the Infasurf film with a surface area of $20 \times 20 \mu\text{m}^2$. The equivalent number of phospholipid bilayers stored in the multilayers is found to be 0.7, 3.1, 3.9, and 4.6 bilayers for surfactant concentrations of 1, 10, 20, and 35 mg/mL, respectively.

6.4 Discussion

6.4.1 High phospholipid concentration optimizes surface activity of the surfactant film during normal tidal breathing

Using CDS, we have studied the dynamic surface activity of the Infasurf film adsorbed from surfactant suspensions at the physiologically relevant phospholipid concentrations, *i.e.*, ≥ 10

mg/mL (Figure 6.2). Two conclusions can be drawn from these biophysical simulations. First, the effect of surfactant concentration on the dynamic surface activity of the Infasurf film appears to be only important for the physiologically relevant compression ratio of 15%. For 25% and 35% compression ratios, no statistically significant differences about the γ_{\min} and κ_{comp} can be found for surfactant concentrations between 1 and 35 mg/mL. Numerous lung physiological studies have demonstrated that variations in the alveolar surface area during normal tidal breathing are less than 20%, and usually no more than 30% for a deep breath (250, 267, 268). In contrast to the 15% compression ratio (Figure 6.2A), the compression-expansion cycles with 25% and 35% compression ratios (Figure 6.2D and 6.2G) show apparent hysteresis areas. The hysteresis between the compression and expansion branches is a result of reversible film collapse (269), when the surfactant film is compressed beyond 20% of its initial surface area, at which the surface tension remains a constant in spite of film compression. Such a phenomenon in *in vitro* biophysical simulations of pulmonary surfactant is termed as “overcompression” of the surfactant film (254, 270), which is unlikely to occur *in vivo* during normal tidal breathing, since the hysteresis area indicates energy loss per cycle due to partial collapse of the surfactant film (94). The hysteresis area, *i.e.*, the energy loss, for the Infasurf film at 15%, 25%, and 35% compression ratios are calculated to be approximately 0.01, 0.05, and 0.09 $\mu\text{J}/\text{cycle}$, respectively.

Second, at the physiologically relevant 15% compression ratio, the compressibility (κ_{comp}) of the Infasurf film decreases with increasing surfactant concentration from 1 to 35 mg/mL. Film compressibility measures the “hardness” of a two-dimensional film, with a lower compressibility indicating a “harder” film since the film is less compressible (271). Hence, these data suggest that the adsorbed Infasurf film becomes harder with increasing surfactant concentration. This is an interesting finding because it indicates that the surfactant concentration in the subphase influences

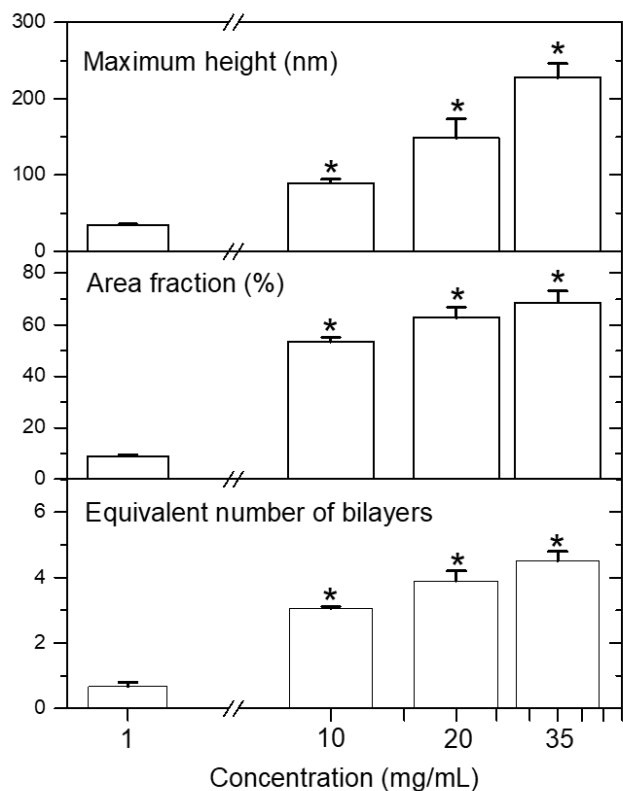


Figure 6.5 Maximum height (nm), area fraction (%), and the area-averaged equivalent number of bilayers of the multilayer structures of the Infasurf film adsorbed from various subphase concentrations from 1 to 35 mg/mL. The equivalent number of bilayers stored in the multilayers was determined from bearing analysis of the AFM topographic images. * $p < 0.05$ in comparison to Infasurf at the phospholipid concentration of 1 mg/mL.

the dynamic surface activity of the surfactant film after *de novo* adsorption at the air-water surface. Similar findings have been reported in literature (270, 272-274), but the biophysical mechanism responsible for the synergetic effect of the surfactant concentration on surface activity of the surfactant film is still unknown (275). Recently, using grazing incidence X-ray diffraction (GIXD), Andreev *et al.* showed that increasing the subphase concentration of an Infasurf film in a Langmuir film balance increases the lateral area of an ordered phase in the surfactant film at the air-water surface (276). This ordered phase resembles the properties of a DPPC:cholesterol (3:1) monolayer (276), thus indicating that it is the liquid-ordered (LO) phase in the surfactant monolayer (94).

Consequently, the decreased film compressibility at high surfactant concentration found here might be, at least in part, due to the formation of more LO phase at the interfacial monolayer. It should also be noted that although the compressibility appears to increase with increasing the film compression ratio from 15% to 35% (Figure 6.3C vs. 6.3F and 6.3I), it most likely does not indicate that the surfactant film becomes “softer” with increasing compression ratio. This is because the evaluation of film compressibility assumes no molecules leave the surface, *i.e.*, no film collapse (271). Hence, the increase in film compressibility when increasing the compression ratio to 25% and 35% is most likely linked to film collapse instead of hardness of the surfactant film.

6.4.2 Multilayers of the adsorbed surfactant film act as a safety net for deep breathing

Many *in vitro* studies have directly and indirectly demonstrated that the adsorbed pulmonary surfactant film has a complex conformation, consisting of an interfacial monolayer at the air-water surface and phospholipid multilayers closely and functionally fused with the interfacial monolayer (102, 240, 277-281). Hydrophobic surfactant proteins (SP-B and SP-C) likely play an important role in stabilizing the negative curvatures needed for the membrane fusion (274, 282-284). Such a monolayer-multilayer fusion structure facilitates rapid exchange of surface active materials between the monolayer and the multilayer, upon highly dynamic compression-expansion cycles of the surfactant film during normal tidal breathing (285, 286). Under pathophysiological conditions of protein denaturation, such as exposure to excessive nanoparticles (101, 287) or menthol-flavored e-cigarette aerosols (288, 289), it was found that the multilayer structure of the natural pulmonary surfactant film was compromised and downgraded into a monolayer conformation. The change of surfactant film conformation was found to be associated with *in vitro* biophysical inhibition of the surfactant film, and acute respiratory failure in animal models (100, 290, 291).

The preset study showed that the ultrastructure and topography of the adsorbed Infasurf film depend on the phospholipid concentration of the surfactant suspension (Figures 6.4 and 6.5). The multilayers of the Infasurf film adsorbed from a surfactant concentration of only 1 mg/mL appear as individual spear-like protrusions uniformly distributed throughout the surface of the surfactant film (Figure 6.4A). Although each of these protrusions could account for up to 9 stacked phospholipid bilayers, since they only have a limited surface coverage (< 10%), the area-averaged equivalent number of phospholipid bilayers stored in these multilayers was found to be only 0.7 (Figure 6.5).

Using transmission electron microscopy (TEM), Schürch et al. (253) and Ochs (292) have shown convincing evidence that a large portion of the surfactant film adsorbed to the air-water surface of the alveolar lining layer appears to be multilayers with a varying number of 2-7 bilayers. AFM images shown in the present study depict that the Infasurf film adsorbed from physiologically relevant high surfactant concentrations (between 10 and 35 mg/mL) are multilayers with an area-averaged number of 3-5 bilayers (Figure 6.5). These AFM observations are in good agreement with the TEM observations of the surfactant film at the alveolar lining layer (253, 292).

Interestingly, it appears that the biophysical function of the excessive lipids stored in the multilayers at high surfactant concentrations is not to increase the dynamic surface activity of the adsorbed surfactant film when the surface area compression ratio is increased to suprphysiological levels (*i.e.*, 25% and 35% shown in Figure 6.2). Rather, the beneficial effect of the high surfactant concentration on surface activity of the adsorbed Infasurf film only appears to be significant at the physiologically relevant 15% compression ratio, at which no collapse of the interfacial monolayer occurs at the end of compression (Figure 6.2A-C). These experimental

results likely indicate that the biophysical function of these multilayer structures formed after *de novo* adsorption is to act as a buffer zone to store surface active materials ejected from the interfacial monolayer under extreme conditions such as deep breathing or forced breathing. Under these conditions, the surfactant film is stretched beyond its normal compression ratio, which occurs as the expense of partial collapse of the interfacial surfactant film (Figure 6.2D and G). Instead of losing these surface active materials to the subphase, *e.g.*, in form of small vesicular aggregates (293), these materials can be temporarily absorbed by and stored in the adsorbed multilayer structures. As a result, these materials can respread back to the interfacial monolayer sufficiently fast so that low surface tensions can be achieved in the subsequent respiratory cycle immediately following a deep breath.

6.5 Summary

In conclusion, using constrained drop surfactometry (CDS), we have studied the biophysical properties, ultrastructure and topography of the pulmonary surfactant film adsorbed from the subphase at physiologically relevant high surfactant concentrations (*i.e.*, 10-35 mg/mL). It was found that the effect of surfactant concentration on the dynamic surface activity of the Infasurf film was only important for the physiologically relevant compression ratio of 15%. For supraphysiological compression ratios, at which the surfactant film partially collapses at the end of compression, no statistically significant differences in the minimum surface tension and film compressibility can be found between these high surfactant concentrations and a relative low concentration of 1 mg/mL. Atomic force microscopy (AFM) observed that the adsorbed Infasurf film depicts a multilayer conformation consisting of layer-by-layer assembly of stacked bilayers with the height of the multilayers proportional to the surfactant concentration in the subphase. At 35 mg/mL, the phospholipids stored in these multilayer structures are equivalent to 4.6 lipid

bilayers throughout the entire surfactant film. Our experimental data suggest that the biophysical function of these multilayer structures formed after *de novo* adsorption is to act as a buffer zone to store surface active materials ejected from the interfacial monolayer under extreme conditions such as deep breathing.

Chapter 7 S2 subunit of SARS-CoV-2 spike protein induces domain fusion in natural pulmonary surfactant monolayers ¹

7.1 Introduction

Severe acute respiratory syndrome coronavirus 2 (SARS-CoV-2), the virus responsible for coronavirus disease 2019 (COVID-19), has caused a global pandemic. SARS-CoV-2 is an enveloped, positive-sense, single-stranded RNA virus with a genome size of ~30 kb (294). It is made up of four structural proteins, *i.e.*, nucleocapsid (N), membrane (M), envelope (E), and spike (S) (294). Among these proteins, the S protein is the major mediator of cellular infection, which determines the attachment of SARS-CoV-2 onto the host cell membrane and the subsequent membrane fusion. During infection, the S protein recognizes and binds to angiotensin-converting enzyme 2 (ACE2) on the host cell membrane and thus mediates viral cellular entry (295).

The S protein is a heavily glycosylated, trimeric, type I membrane protein anchored on the exterior surface of the mature virion (296). Each monomer of the trimeric S protein is about 180 kDa with 1,273 amino acids. It is composed of a signal peptide (residues 1-13) and two functional subunits, *i.e.*, the S1 (residues 14-685) and S2 (residues 686-1,273) subunits, which are responsible for binding to the host cell receptor and fusion of the viral and cellular membranes, respectively (297). Once binding to the cell membrane, the S protein undergoes cleavage by proteases, such as furin, into the S1 and S2 subunits (298). As illustrated in **Figure 7.1A**, the S1 subunit contains an N-terminal domain and a receptor-binding domain that interacts with ACE2. The S2 subunit

¹ Xu X, Li G, Sun B, Zuo YY, S2 subunit of SARS-CoV-2 spike protein induces domain fusion in natural pulmonary surfactant monolayers. *J. Phys. Chem. Lett.* 13 (2022) 8359-8364.

consists of a fusion peptide, central helix, connecting domain, heptad repeat 1 and 2, transmembrane domain, and cytoplasm domain (Figure 7.1A and B). After S protein cleavage and membrane fusion, a fusion pore forms between viral and cellular membranes, which allows the virus to deliver its genetic information into the host cell cytoplasm for further replication and transcription.

In COVID-19 associated acute respiratory distress syndrome (ARDS) (299), SARS-CoV-2 attacks both type I and type II alveolar epithelial cells, where the ACE2 receptor is highly expressed (300). Damage to type II alveolar epithelial cells could compromise the synthesis and function of the endogenous pulmonary surfactant (PS) that plays a crucial physiological role in host defense and alveolar surface tension reduction. The PS is composed of ~80 wt% phospholipids, with dipalmitoyl phosphatidylcholine (DPPC) being the most abundant individual lipid species, ~10 wt% neutral lipids, mainly cholesterol, and ~10 wt% surfactant associated proteins, SP-A, -B, -C, and -D.(224) The hydrophilic proteins, SP-A and SP-D, presenting in airways and the alveolar regions, were found to bind to the S protein, thus mitigating infection of the epithelial cells through viral neutralization, agglutination, and enhanced phagocytosis (301, 302). In addition, a recent clinical trial showed that the DPPC levels in the bronchoalveolar lavage fluids of COVID-19 patients were lower than those in healthy controls (303). All this evidence justified the hypothesis that exogenous surfactant therapy, in which clinical surfactant preparations extracted from animals' lungs are delivered to patients' lungs, may be used as a supportive therapy to treat patients with COVID-19 and COVID-19 associated ARDS (246, 247, 304). There have been multiple ongoing clinical trials in the past two years (246). Although the verdict is still out, preliminary reports have demonstrated promise for the surfactant therapy in managing the progress of COVID-19 (305, 306).

Clinical application of the exogenous surfactant therapy in COVID-19 entails biophysical understanding of specific interactions between the PS film and the functional group of SARS-CoV-2 responsible for mediating membrane fusion. It is mechanistically accepted that the fusion peptide (FP) in the S2 subunit of the S protein plays a key role in mediating the initial penetration of the virus into the host cell membrane (298, 307). There have been a few *in silico* studies based on molecular dynamics simulations that investigated the specific FP-lipid interactions in the initial stage of SARS-CoV-2 infection (308, 309). However, it is still unknown how the FP of the S2 subunit interacts with or adversely impacts the natural PS film.

Here, we experimentally studied the specific biophysical interactions between the recombinant S2 subunit and an animal-derived clinical surfactant preparation, *i.e.*, Infasurf, using a novel experimental methodology called constrained drop surfactometry (CDS). CDS is a new generation of droplet-based surface tensiometry technique that we developed for studying the biophysical properties of the PS film, lipid-protein, and bio-nano interactions at the PS film (Figure 7.1C) (102, 194). With biophysical simulations using CDS and molecular visualization using atomic force microscopy (AFM), we found that the S2 subunit inhibited the biophysical properties of PS, and most importantly, directly induced fusion of phospholipid microdomains in the Infasurf monolayer. These results may provide novel insight into the understanding of biophysical mechanisms responsible for PS interactions with SARS-CoV-2, and may have translational implications in further developing the surfactant replacement therapy for COVID-19 patients.

7.2 Materials and methods

7.2.1 Materials

Infasurf was a gift from ONY Biotech (Amherst, NY). It was prepared from the lung lavage of newborn calves by centrifugation and organic extraction. Infasurf contains most phospholipids and

neutral lipids, mainly cholesterol, of the natural PS, as well as two hydrophobic surfactant proteins, SP-B and SP-C (310). The hydrophilic surfactant proteins, SP-A and SP-D, however, were removed during the extraction process. Infasurf was stored in sterilized vials with an initial phospholipid concentration of 35 mg/mL. It was diluted to 1 mg/mL using phosphate-buffered saline (PBS) on the day of experiments. For the study of spread monolayers, Infasurf was extracted with chloroform-methanol, dried under a nitrogen stream, and re-suspended in chloroform to a final concentration of 1 mg/mL.

The recombinant SARS-CoV-2 spike S2 subunit protein was purchased from Sigma-Aldrich (St. Louis, MO) and used without further purification. It was produced by the Baculovirus-Insect Cells expression system and expressed with sequence Ser686-Pro1213 of the SARS-CoV-2 spike S2 ECD fused with a His-tag at the C-terminus. The S2 subunit protein was received in the form of lyophilized powder, and was dispersed in Milli-Q water to form a 1 mg/mL stock solution.

7.2.2 Constrained Drop Surfactometry (CDS)

CDS is a new generation of droplet-based surface tensiometry technique developed in our laboratory (102, 194). It uses the air-water surface of a sessile drop (~3 mm in diameter, ~0.3 cm² in surface area, and ~20 μ L in volume) to accommodate the spread or adsorbed surfactant film. As shown in Figure 7.1C, a key design of the CDS is a carefully machined pedestal that uses its knife-sharp edge to prevent film leakage even at very low surface tensions. System miniaturization of the CDS facilitates rigorous control of the experimental conditions with an environmental control chamber. The spread/adsorbed film at the droplet surface can be compressed and expanded by precisely oscillating the surface area of the droplet using a motorized syringe. The surface tension and surface area of the film were determined with closed-loop axisymmetric drop shape analysis (CL-ADSA) by analyzing the shape of the film-covered droplet (105). The surface pressure (π)

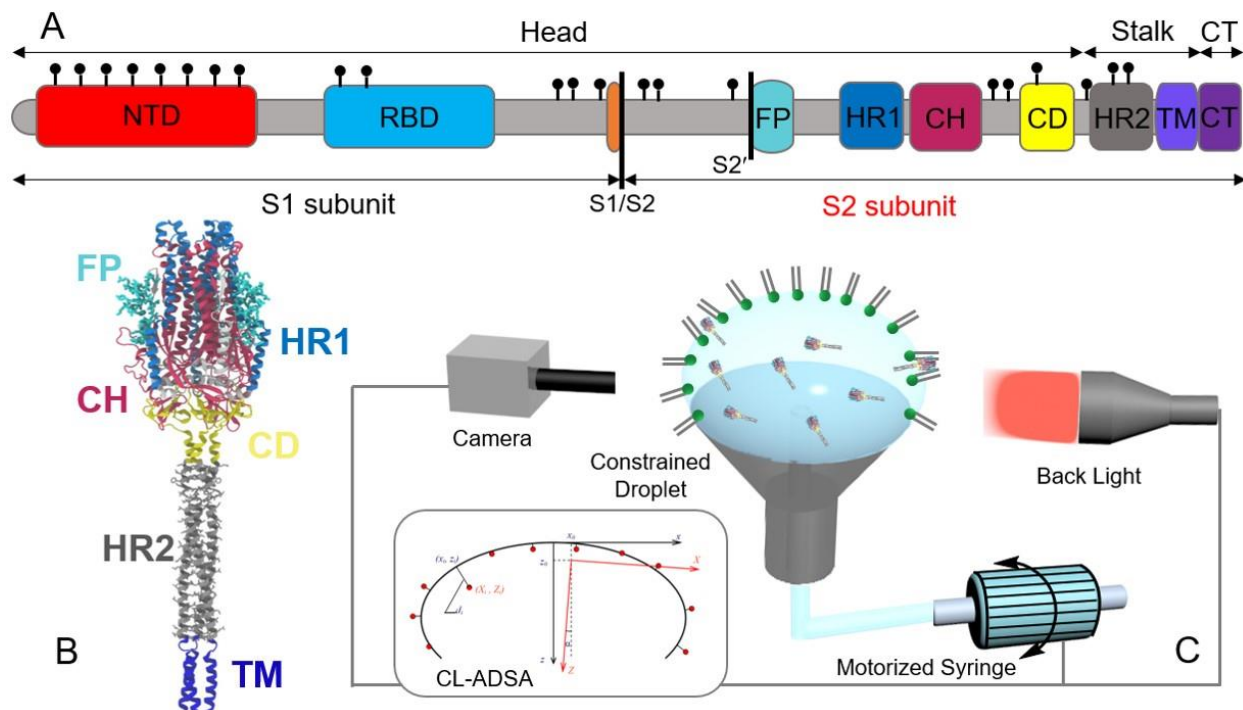


Figure 7.1 (A) Primary structure of the SARS-CoV-2 S protein. It is composed of the S1 and S2 subunits. The S1 subunit contains an N-terminal domain (NTD) and a receptor-binding domain (RBD). The S2 subunit consists of a fusion peptide (FP), central helix (CH), connecting domain (CD), heptad repeat 1 (HR1) and 2 (HR2), transmembrane (TM) domain, and cytoplasm domain (CT). (B) Cryo-EM structures of the S2 subunit from the Protein Data Bank ID 6VXX. (C) Schematic of the constrained drop surfactometry (CDS) for studying biophysical interactions between the S2 subunit and natural pulmonary surfactant.

can be calculated from surface tension (γ) using $\pi = \gamma_0 - \gamma$, where γ_0 is the surface tension of the clean surfactant-free air-water surface.

To study the biophysical impact of the S2 subunit protein on Infasurf, dynamic compression-expansion cycling of the Infasurf film was conducted with CDS at physiologically relevant temperature and humidity, *i.e.*, 37 °C and close to 100% relative humidity. The detailed experimental protocol can be found in our previous publication (194). Briefly, Infasurf was diluted to a concentration of 1.2 mM and mixed with the S2 subunit to a final concentration of 0.0017 mM or 0.0085 mM, *i.e.*, 0.15 mol% and 0.75 mol% of Infasurf. Mixtures of Infasurf and the S2 subunit

were incubated at 37 °C for 10 minutes *prior to* dynamic cycling. A 7 μL droplet of the mixture was dispensed onto the CDS pedestal, and allowed 5 min for adsorption, as indicated by reaching the equilibrium surface tension of approximately 22 mN/m. The Infasurf film was then compressed and expanded at a rate of 3 s/cycle with a controlled 20% compression ratio (CR), to simulate normal tidal breathing (311). To obtain the absolute minimum surface tension of the Infasurf film, overcompression at 30% and 40% CRs was also studied. At least ten continuous compression-expansion cycles were studied for each droplet. Dynamic surface activity was quantified with the minimum surface tension (γ_{\min}) at the end of compression, and the average isothermal film compressibility $\kappa_{\text{comp}} = \frac{1}{A} \left(\frac{\partial A}{\partial \gamma} \right)_T$. The maximum surface tension (γ_{\max}) and the film compressibility during expansion (κ_{exp}) of the Infasurf film were also recorded. All results were shown as mean \pm standard deviation ($n > 3$). One-way ANOVA with the Tukey means comparison test was used to determine group differences (OriginPro, Northampton, MA). $p < 0.05$ was considered to be statistically significant.

To study the effect of the S2 subunit protein on the spread Infasurf monolayer, $\sim 0.05 \mu\text{g}$ extracted Infasurf samples were spread onto the air-water surface of a $\sim 10 \mu\text{L}$ water droplet. The volume of the droplet was subsequently increased to $\sim 19 \mu\text{L}$, and the droplet was left undisturbed for 5 minutes to allow evaporation of chloroform and to reach equilibrium. 1 μL stock solution of the S2 subunit protein was injected into the droplet to reach a final protein concentration of 0.05 mg/mL. The spread Infasurf monolayer was then compressed at a quasi-static compression rate of 0.1 cm^2/min . The environmental temperatures were controlled at 20 °C and 37 °C, respectively.

7.2.3 Atomic Force Microscopy (AFM)

The lateral structure and topography of the Infasurf monolayer were studied at the characteristic surface pressure of 30 mN/m. The Infasurf monolayer was first Langmuir-Blodgett (LB)

transferred from the droplet by lifting a small piece of freshly peeled mica sheet at a speed of 1 mm/min. Topographical images of the immobilized Infasurf monolayer were obtained with an Innova AFM (Bruker, Santa Barbara, CA). Samples were scanned in air with the contact mode using a silicon nitride cantilever with a spring constant of 0.12 N/m and a tip radius of 2 nm. Each sample was scanned at multiple locations to ensure representativeness and reproducibility. AFM images were analyzed using Nanoscope Analysis (version 1.5).

7.3 Results and discussion

7.3.1 Effect of the S2 subunit on biophysical properties of the PS film

Figure 7.2 shows the biophysical impact of the S2 subunit on the Infasurf film under physiologically relevant conditions. To simulate normal tidal breathing, the surface area of the Infasurf film was oscillated with a 20% compression ratio (CR) and a highly dynamic rate of 3 seconds per compression-expansion cycle (311). Figure 7.2A shows typical compression-expansion cycles of 1 mg/mL Infasurf with a low 0.15 mol% or a moderate 0.75 mol% S2 subunit. It can be seen that the minimum surface tension (γ_{\min}) of Infasurf is increased from 2.9 mN/m to 4.4 mN/m with the addition of 0.15% S2 subunit, and to 6.5 mN/m with 0.75% S2 subunit, indicating significant surfactant inhibition (Figure 7.2B). κ_{comp} of the Infasurf film is increased from 0.64 m/mN to 0.71 m/mN with the addition of 0.15% S2 subunit, and to 1.06 mN/m with 0.75% S2 subunit (Figure 7.2C). The film compressibility is a quantitative measure of the “softness” of the PS film (224). Increasing film compressibility is a strong indication of biophysical inhibition of the PS, since more area reduction is needed to decrease the surface tension.

In addition to the physiologically relevant 20% CR, we have also studied the dynamic surface activity of the Infasurf film at supraphysiological levels of film compression, *i.e.*, 30% and 40% CRs (Figure 7.2D-I). Similar to 20% CR, the addition of 0.75% S2 subunit more than doubles the

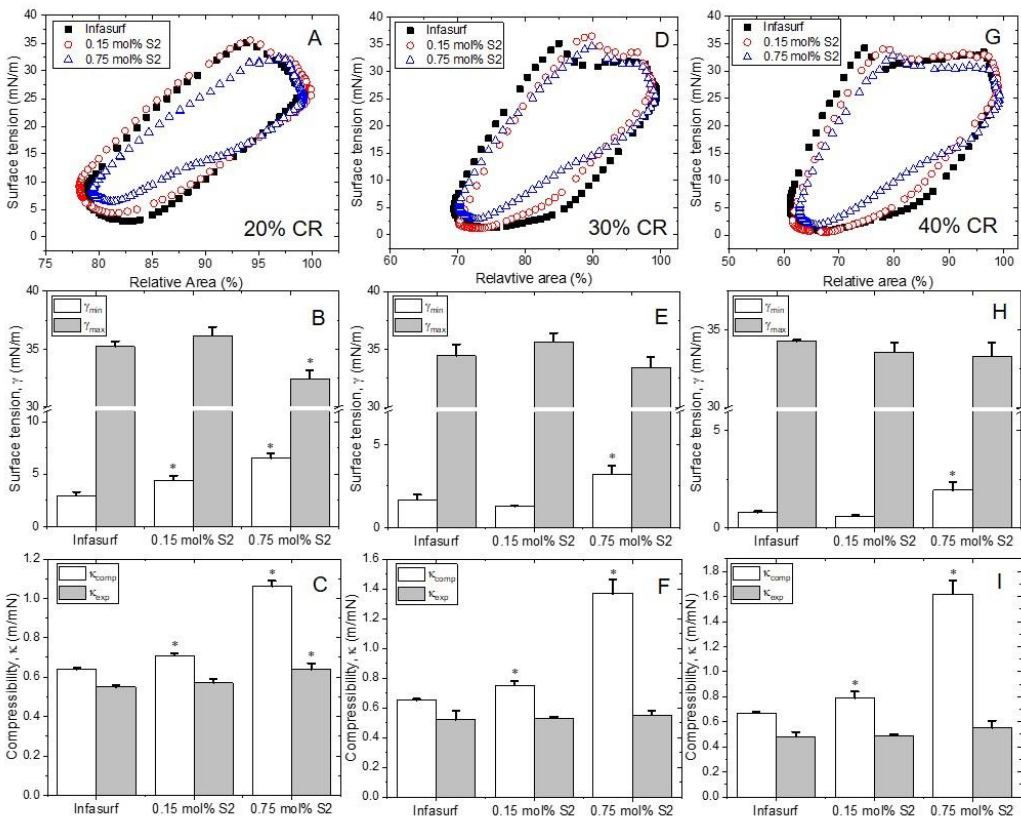


Figure 7.2 Effect of the S2 subunit (0.15 mol% and 0.75 mol%) on the biophysical properties of 1 mg/mL Infasurf, with various compression ratios (CRs). (A-C) 20% CR, (D-F) 30% CR, and (G-I) 40% CR. (A, D, G) show the dynamic compression-expansion cycles of Infasurf with/without the addition of the S subunit. (B, E, H) show the statistical analysis of the minimum (γ_{\min}) and maximum surface tension (γ_{\max}). (C, F, I) show the statistical analysis of the film compressibility during the compression (κ_{comp}) and expansion (κ_{exp}) processes. Experimental results were obtained with the CDS under physiologically relevant conditions. Results shown are the tenth compression-expansion cycle. * $p < 0.05$ suggests statistically significant differences in comparison to pure Infasurf film without the S subunit.

corresponding γ_{\min} and κ_{comp} of the Infasurf film, thus indicating significant biophysical inhibition of the PS function.

7.3.2 Effect of the S2 subunit on quasi-static compression isotherms of the PS monolayer

Figure 7.3 shows the isothermal compression of the Infasurf monolayer at a quasi-static rate of 0.1 cm²/min, with and without the S2 subunit injected into the subphase, *i.e.*, the droplet, to a final protein concentration of 0.05 mg/mL.

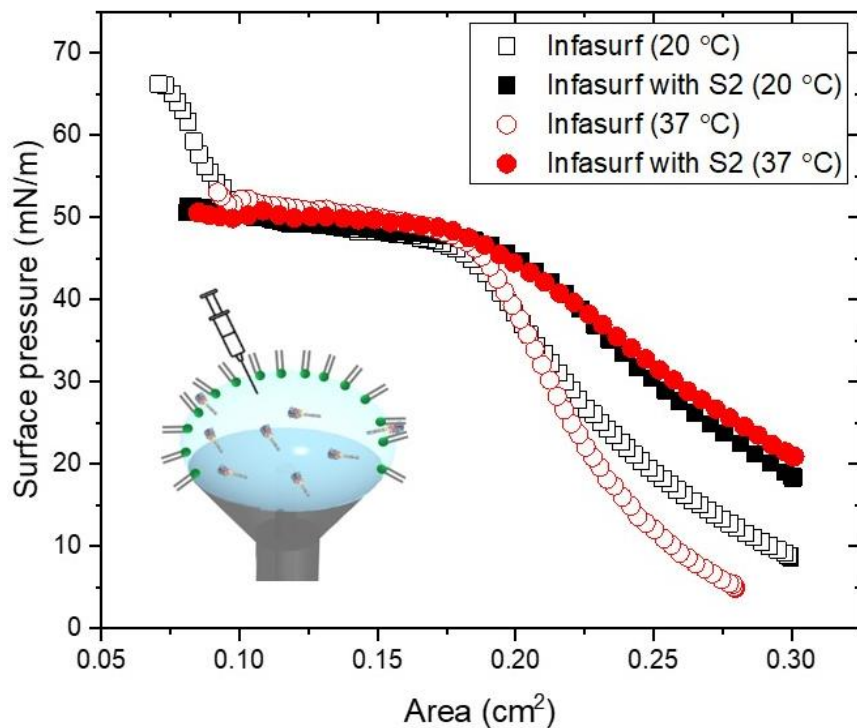


Figure 7.3 Effect of the S2 subunit on the quasi-static compression isotherms of spread Infasurf monolayers. Aqueous solution of the S2 subunit was subphase injected to a final protein concentration of 0.05 mg/mL prior to monolayer compression. The Infasurf monolayer was compressed, with a quasi-static compression rate of 0.1 cm²/min, under two environmental temperatures of 20 °C and 37 °C, respectively.

It can be seen that at two different environmental temperatures, *i.e.*, 20 and 37 °C, the S2 subunit injected into the subphase significantly increases the initial surface pressure *prior to* monolayer compression, to the surface pressure of approximately 20 mN/m, corresponding to the S2 subunit's equilibrium surface tension at 50 mN/m. At both temperatures, the compression isotherms reach a plateau region at the equilibrium spreading pressure (π_{eq}) of PS around 50 mN/m, at which the PS monolayer is transformed into a multilayer (115, 310). While the Infasurf monolayer at 20 °C can be further compressed to a metastable supracompressed state above the π_{eq} (310, 312), the Infasurf monolayer with the subphase-injected S2 subunit spontaneously collapses at π_{eq} , thus indicating the S2 subunit-induced surfactant inhibition.

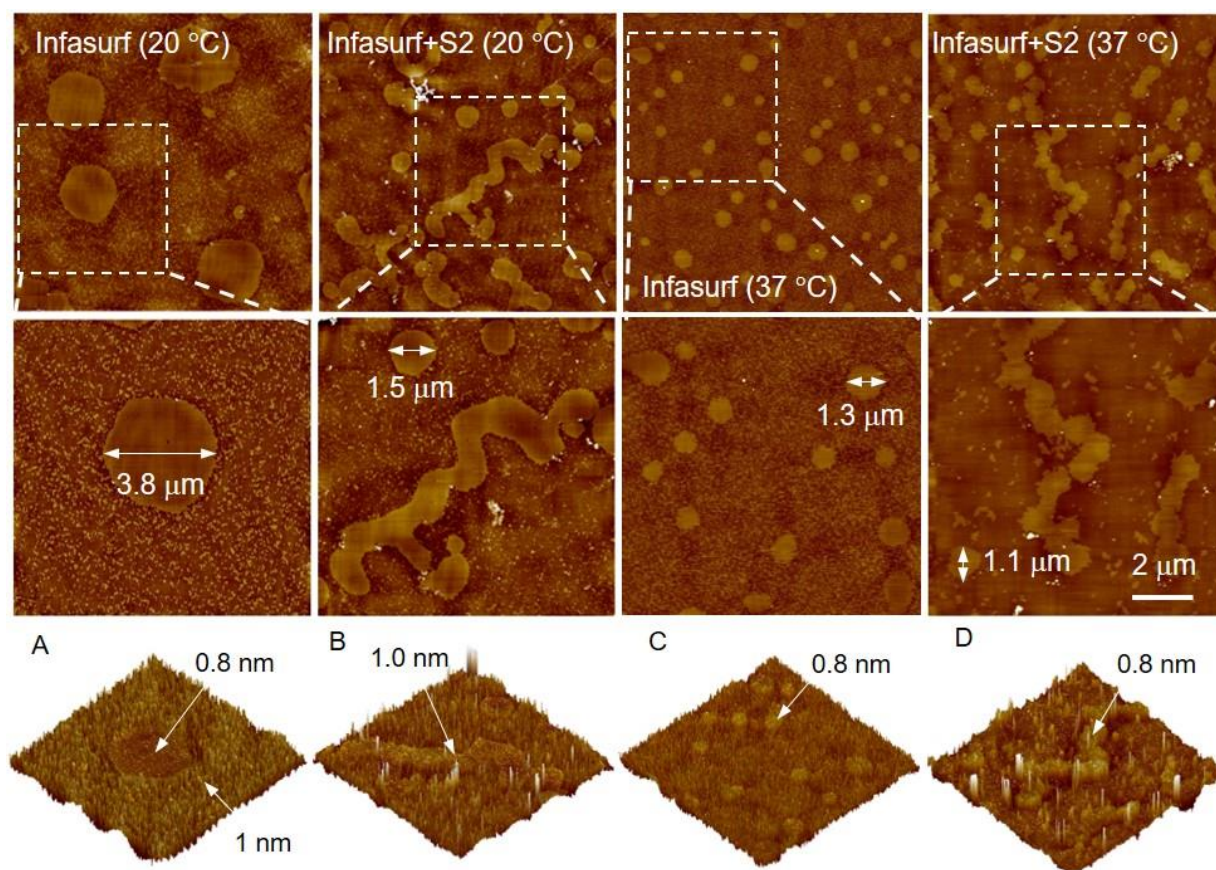


Figure 7.4 Lateral structure and topography of Infasurf with/without the addition of the S2 subunit, under two environmental temperatures of 20 °C and 37 °C, respectively. (A) Infasurf at 20 °C, (B) Infasurf with S2 at 20 °C, (C) Infasurf at 37 °C, and (D) Infasurf with S2 at 37 °C. All AFM images were obtained at a controlled characteristic surface pressure of 30 mN/m. All AFM images in the first row have the same lateral dimension of $20 \times 20 \mu\text{m}$ and a z range of 5 nm. Images in the middle row show the zoom-in of the structures indicated by the white boxes. The bottom row shows the 3D renderings of the topographic images shown in the middle row. Characteristic lateral and altitudinal dimensions are indicated by white arrows.

7.3.3 Effect of the S2 subunit on domain fusion of the PS monolayer

Figure 7.4 shows AFM topographic images of the Infasurf monolayer, at the characteristic surface pressure of 30 mN/m, with and without the S2 subunit under two environmental temperatures 20 °C and 37 °C, respectively. At 20 °C (Figure 7.4A), the Infasurf monolayer shows microscale and nanoscale tilted-condensed (TC) domains that are approximately 0.8-1.0 nm higher than the surrounding liquid-expanded (LE) phase that is mostly composed of fluid phospholipids.

These TC domains mainly consist of solid-like disaturated phospholipids, largely DPPC. The microdomains have a nearly circular shape with a diameter of 3-5 μm , in good agreement with our previous observations (310).

Addition of the S2 subunit completely alters the lateral structure of the Infasurf monolayer. The most striking change caused by the S2 subunit is the morphology of the microdomains. As shown in Figure 7.4B, the microdomains, ~ 1 nm higher than the surrounding LE phase, mostly merge into an irregular wormlike shape. A small amount of isolated circular microdomains still appears in the monolayer, but exists with a much smaller diameter than that of the Infasurf monolayer (1.5 μm vs. 3.8 μm). A similar effect of the S2 subunit on the Infasurf monolayer is also found at 37 $^{\circ}\text{C}$. As shown in Figure 7.4C, microdomains of the Infasurf monolayer at 37 $^{\circ}\text{C}$ are in general smaller than those at 20 $^{\circ}\text{C}$ (1.3 μm vs. 3.8 μm). Subphase-injected S2 subunit also causes fusion of microdomains in the Infasurf monolayer at 37 $^{\circ}\text{C}$ (Figure 7.4D).

Figure 7.5 shows the quantified domain coverage of the Infasurf monolayer. In general, addition of the S2 subunit increases the area fraction of microdomains but decreases the area fraction of the nanodomains. However, the total area fraction covered by the TC domains, *i.e.*, the sum of microdomains and nanodomains, does not appear to change with the S2 subunit.

The equilibrium morphology of microdomains (shape and size) in a phospholipid monolayer is determined by the balance between the line tension and electrostatic repulsion between lipid headgroups in the domain (224). The line tension tends to minimize the domain boundaries by producing a small number of larger domains and by imposing a round shape on the individual domains. The dipolar repulsion works in the opposite way. This mechanism explains why the size of microdomains in the Infasurf monolayer at 37 $^{\circ}\text{C}$ is much smaller than that at 20 $^{\circ}\text{C}$ (Figure 7.4A vs. C), because in general line tension decreases with temperature.

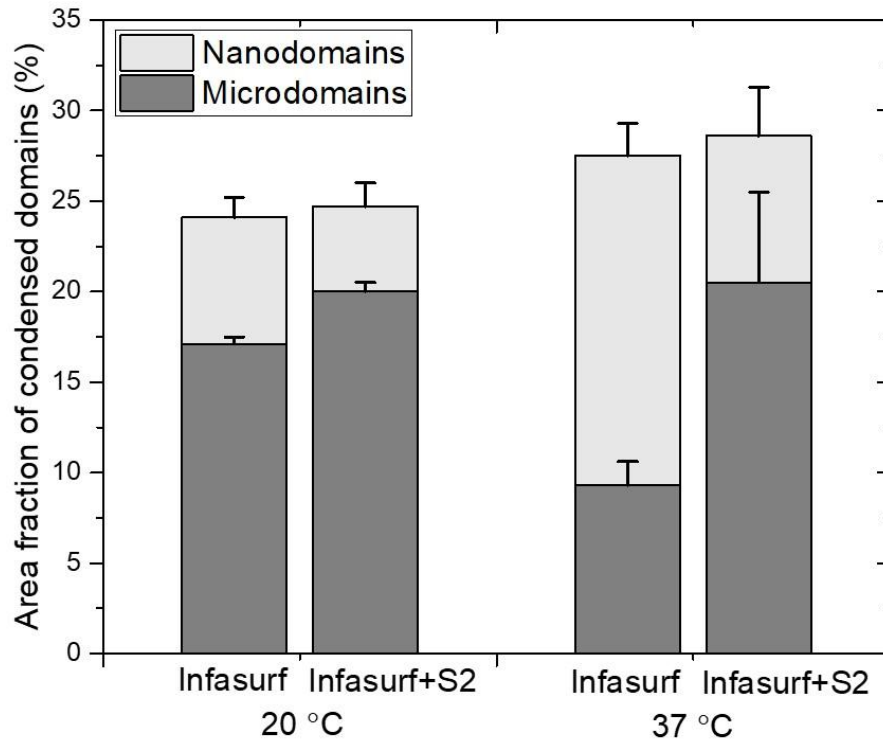


Figure 7.5 Quantification results for the Infasurf monolayer coverage of tilted-condensed (TC) microdomains and nanodomains at surface pressure 30 mN/m.

The dramatic change of microdomain morphology with the addition of the S2 subunit (Figure 7.4A *vs.* B and Figure 7.4C *vs.* D) must be caused by a significantly reduced line tension at the domain boundary. It is not unexpected that the fusion peptide (FP) of the S2 subunit selectively partitions into the microdomain boundaries to reduce line tension. It has been proposed that line tension at the lipid domain boundaries is the driving force for HIV FP-mediated fusion (313). Since the solid-like domains mostly consist of ordered lipid phases, they are energetically unfavorable for membrane fusion when it comes to infection by enveloped viruses, such as HIV and influenza. It has been found that line tension at lipid domain boundaries contributes significant energy to drive HIV gp41-FP-mediated fusion (313). Similarly, line tension has been found to be an important control factor for membrane fusion mediated by influenza hemagglutinin (314).

7.3.4 Biological implications

A critical stage of viral infection is the fusion between viral and host cell membranes. The FP of the S2 subunit plays a central role in the initial penetration of the virus into the host cell membrane (315). The FP is a relatively hydrophobic residue located at the N-terminus of the S2 subunit. Molecular dynamics simulations have shown that residues L821, L822, and F823 in the helical portion of the FP can deeply insert into the hydrophobic core of a model membrane, thus closely interacting with the membrane lipids (308). Other hydrophobic residues, *e.g.*, F817/I818, V826/T827/L828/A829, and F833/I834, may also be involved in binding to biomembrane, thus minimizing exposure of the FP to water. Once bound to the membrane, a fully conserved disulfide bridge in the FP establishes the strong anchoring required for subsequent membrane fusion (309).

In comparison to extensive studies of the FP-mediated membrane fusion, it is still unknown how the FP of enveloped virus affects the natural PS film. The endogenous PS film adsorbed at the alveolar surface is a lipid-protein biomembrane that consists of a monolayer highly enriched in disaturated phospholipids at the air-water surface, plus a multilayered surface-associated surfactant reservoir that is composed of hundreds of fluid phospholipids, closely and functionally attached to the interfacial monolayer (102, 316). In terms of membrane structures, the PS monolayer controlled at the surface pressure 30 mN/m can be loosely considered as a natural model mimicking a single leaflet of a biomembrane, since the lateral pressure of enclosed bilayers is largely conserved at 30 mN/m (317).

Using combined biophysical simulations with CDS and direct membrane imaging with AFM, we have established two experimental findings. First, the S2 subunit at a molar ratio of 0.75% with respect to phospholipids strongly inhibited the biophysical function of a natural PS (Figure 7.1). Second, the S2 subunit subphase injected at a low concentration of 0.05 mg/mL induced significant

domain fusion in the natural PS monolayer (Figure 7.4). These two biophysical findings are interrelated, since the membrane fluidization caused by the penetration of the S2 subunit is most likely responsible for the surfactant inhibition as revealed by the increase of film compressibility.

It has been shown that the FP of the S2 subunit transforms from an intrinsically disordered state in an aqueous solution into a wedge-shaped structure inserting into bilayered micelles, with the hydrophobic, narrow end of the wedge contacting the fatty acyl chains of the phospholipids and the polar end of the wedge interacting with the lipid head groups and binding calcium ions for membrane fusion (318). A similar mechanism may be also responsible for the penetration of the S2 subunit into the natural PS film. Moreover, it has been reported that the FP-mediated fusion became more favorable for membranes containing cholesterol (319), and negatively charged phospholipids (320), likely due to electrostatic interactions promoted by the positively charged FP. The natural PS contains 20% anionic phospholipids, including phosphatidylglycerol, phosphatidylinositol, and lyso-bis-phosphatidic acid, and up to 10% cholesterol (224). Hence, the FP-mediated fusion is expected to prevail in the natural PS film.

7.4 Summary

Using combined biophysical simulations and AFM imaging, we have studied the biophysical impact of the S2 subunit on a natural PS film, Infasurf. We have concluded that the S2 subunit can inhibit the biophysical properties of the PS. We have provided direct experimental evidence for S2 subunit-induced microdomain fusion in the Infasurf monolayer. The surfactant inhibition has been attributed to the membrane fluidization caused by insertion of the S2 subunit mediated by its fusion peptide. These findings may provide novel insight into the understanding of biophysical mechanisms responsible for PS interactions with SARS-CoV-2, and may have translational implications in the further development of surfactant replacement therapy for COVID-19 patients.

Chapter 8 Summary of main contributions and future directions

8.1 Summary of main contributions

1. By studying surface and dilational rheological properties of recombinant lipid films under physiologically relevant conditions, we have studied the composition-functional correlations of a model TFLL that consists of BO:CO:PC:PAHSA (40:40:15:5). We have concluded that the major biophysical function of phospholipids in the TFLL is to reduce the surface tension, while the primary function of PAHSA is to regulate interfacial rheology of the TFLL, thus optimizing the viscoelastic properties of the TFLL under physiologically relevant conditions. These findings have novel implications in better understanding the physiological and biophysical functions of the TFLL, and may offer new translational insight to the treatment of dry eye disease.
2. Using combined biophysical experiments, AFM observations, and all-atom MD simulations, we have studied the detailed biophysical properties of FAHFAs using PAHSA as a model. It is concluded that the biophysical properties of a dynamic PAHSA monolayer, under physiologically relevant conditions, depend on a balance between kinetics (mostly controlled by the speed of film compression) and thermal-relaxation (mostly controlled by temperature). We have revealed the unique lipid polymorphism and collapse mechanisms of the PAHSA monolayer at the air-water surface, under various kinetic and temperature conditions. Due to their structural similarities, the biophysical molecular mechanisms of PAHSA found here may be also applicable to OAHFAs. These findings may have novel implications in understanding biophysical functions that FAHFAs, in general, or OAHFAs, in specific, play in the TFLL.

3. We have developed a novel ventilated, closed-chamber, droplet evaporimeter with a constant surface area for studying the effect of TFL on water evaporation. This new evaporimeter is capable of a rigorous control of environmental conditions, including the temperature, relative humidity, airflow rate, surface area, and surface pressure, thus allowing for reproducible water evaporation measurements over a time period of only 5 min. The volumetric evaporation rate of this droplet evaporimeter is less than 2.7 $\mu\text{L}/\text{min}$, comparable to the basal tear production of healthy adults. With this new evaporimeter, we have established the *in vitro* evaporation resistance of a model TFL that consists of 40% wax esters, 40% cholesteryl esters, and 20% polar lipids. It was found that the TFL resists water evaporation with a combined mechanism by increasing film compactness of the polar lipid film at the air-water surface, and, to a lesser extent, by increasing film thickness of the nonpolar lipid film.
4. We have conducted a comprehensive biophysical study of the dynamic surface activity, interfacial rheology, evaporation resistance, and ultrastructure of the Meibomian lipid (ML) films extracted from wild type (WT) and *Soat1* knockout (KO) mice. By correlating the lipidomic analysis and biophysical assays of the MLs of WT and KO mice, our study revealed novel experimental evidence on the composition-structure-functional correlations of the ML films, and suggested a potential biophysical function of long-chain CEs in optimizing the surface activity, interfacial rheology, and evaporation resistance of the ML films. This study may provide novel implications to pathophysiological and translational understanding of MGD and dry eye.
5. We have studied the biophysical properties, ultrastructure and topography of the pulmonary surfactant film adsorbed from the subphase at physiologically relevant high surfactant concentrations (*i.e.*, 10-35 mg/mL) using CDS. It was found that the effect of surfactant

concentration on the dynamic surface activity of the Infasurf film was only important for the physiologically relevant compression ratio of 15%. For supraphysiological compression ratios, at which the surfactant film partially collapses at the end of compression, no statistically significant differences in the minimum surface tension and film compressibility can be found between these high surfactant concentrations and a relative low concentration of 1 mg/mL. AFM observed that the adsorbed Infasurf film depicts a multilayer conformation consisting of layer-by-layer assembly of stacked bilayers with the height of the multilayers proportional to the surfactant concentration in the subphase. At 35 mg/mL, the phospholipids stored in these multilayer structures are equivalent to 4.6 lipid bilayers throughout the entire surfactant film. Our experimental data suggest that the biophysical function of these multilayer structures formed after *de novo* adsorption is to act as a buffer zone to store surface active materials ejected from the interfacial monolayer under extreme conditions such as deep breathing.

6. We have studied the biophysical impact of the S2 subunit of the SARS-CoV-2 S protein on a natural pulmonary surfactant film, Infasurf, using combined biophysical simulations and AFM imaging. We have concluded that the S2 subunit can inhibit the biophysical properties of the pulmonary surfactant. We have provided direct experimental evidence for S2 subunit-induced microdomain fusion in the Infasurf monolayer. The surfactant inhibition has been attributed to the membrane fluidization caused by insertion of the S2 subunit mediated by its fusion peptide. These findings may provide novel insight into the understanding of biophysical mechanisms responsible for pulmonary surfactant interactions with SARS-CoV-2, and may have translational implications in the further development of surfactant replacement therapy for COVID-19 patients.

8.2 Future directions

8.2.1 Biophysical studies of Meibomian lipids of healthy donors and dry eye patients

In Chapter 5, we studied biophysical properties of Meibomian lipids of wild type (WT) and *Soat1* knockout (KO) mice. Comprehensive biophysical studies of the ML films suggested that the ML film of KO mice became stiffer than that of WT mice, revealed by reduced film compressibility, increased elastic modulus, and decreased loss tangent, thus causing more energy loss per blinking cycle of the ML film. Moreover, we found that the ultrastructure of MLs of WT mice showed a multilayer conformation at the physiologically relevant high surface pressures. The ML film consists of a compacted bilayer covering the air-water surface, and large aggregates of 50-100 nm in height atop the compacted bilayer. Comparing with mice samples, human samples show a different composition ratio of Meibomian lipids. Therefore, studying the biophysical properties of Meibomian lipids of healthy human or DED patients, such as surface activity, film stability, rheological properties, thickness, and morphology would provide a new way to distinguish dry eye disorders caused by different mechanisms.

8.2.2 Evaporation resistance of tear film lipid layer

In Chapters 4 and 5, we have developed a ventilated, closed-chamber, droplet evaporimeter to study the evaporation resistance of model TFL and Meibomian lipids of mice samples. Tear lipid films shows statistically significant evaporation resistance at high surface pressures. However, evaporation resistance found in this *in vitro* study is still much less than that found by *in vivo* studies. This might be because the temperature of the droplets inside the chamber after introducing the airflow was 30 °C (determined by an IR camera), which is lower than the ocular surface temperature of 34 °C. It would be useful to further develop the evaporimeter to have a better temperature control on the droplet.

8.2.3 Nanomedicine for ocular drug delivery

The current treatment of dry eye is mostly palliative rather than curative. It mainly relies on the use of drug-free artificial tears and over-the-counter eye drops and lubricants to hydrate the ocular surface. Nanotechnology offers the possibility to develop delivery systems particularly adapted to overcome eye-associated barriers, as a result, to improve the bioavailability of drugs. Nanoparticles interacting with proteins and biofilms establish a series of nanoparticle/biological interfaces that depend on colloidal forces as well as dynamic biophysicochemical interactions. These interactions lead to the formation of protein coronas, particle wrapping, intracellular uptake and biocatalytic processes that could have biocompatible or bioadverse outcomes. The biomolecules may induce phase transformations, free energy releases, restructuring and dissolution at the nanomaterial surface. Hence it is important to understand the nano-bio interactions at the ocular surface, and the health impact of natural, incidental, and engineered nanoparticles that enter the body *via* the eye.

8.2.4 Nanotoxicity to the eyes

The production and application of nanomaterials have grown tremendously during last few decades. The widespread exposure of nanoparticles to the public is provoking great concerns regarding their toxicity to the human body. In comparison with the extensive studies carried out to examine nanoparticle toxicity to the human body/organs, nanotoxicity to the eyes is always ignored and seldom studied. In addition, eyes usually directly interact with the surrounding environment, which may get severe damage from nanoparticles compared to inner organs. Therefore, the study of assessing the potential nanoparticle toxicity to the eyes is of great importance.

List of awards received and publications produced during the PhD

Awards

1. UH Mānoa Student Award for Excellence in Research (doctoral level), 2023
2. College of Engineering Outstanding PhD Student Award, 2022

Book chapters

1. **Xu X**, Zuo YY (2023) Nanomedicine for ocular drug delivery. In: Gu N (ed) Nanomedicine. pp. 755-786, Series of Micro/Nano Technologies, Springer, Singapore.
https://doi.org/10.1007/978-981-16-8984-0_32

Papers published in refereed journals

1. Li G, **Xu X**, Zuo YY, Phase transitions of the pulmonary surfactant film at the perfluorocarbon-water interface. *Biophys. J.* (2023). DOI: 10.1016/j.bpj.2023.04.010.
2. **Xu X**, Li G, Zuo YY, Effects of model tear film lipid layer on water evaporation. *Invest. Ophthalmol. Vis. Sci.* 64 (2023) 13.
3. Li G, **Xu X**, Zuo YY, Langmuir-Blodgett transfer from the oil-water interface. *J. Colloid Interface Sci.* 630 (2023) 21-27.
4. **Xu X***, Li G*, Sun B, Zuo YY, S2 subunit of SARS-CoV-2 spike protein induces domain fusion in natural pulmonary surfactant monolayers. *J. Phys. Chem. Lett.* 13 (2022) 8359-8364.
(*Co-first author)
5. Xu L, Yang Y, Simien JM, Kang C, Li G, **Xu X**, Haglund E, Sun R, Zuo YY, Menthol in electronic cigarettes causes biophysical inhibition of pulmonary surfactant. *Am. J. Physiol.*

Lung Cell Mol. Physiol. 323 (2022) L165-L177.

6. Matsushige C, **Xu X**, Miyagi M, Zuo YY, Yamazaki Y, RGD-modified dextran hydrogel promotes follicle growth in three-dimensional ovarian tissue culture in mice. *Theriogenology* 183 (2022) 120-131.
7. **Xu X**, Kang C, Sun R, Zuo YY, Biophysical properties of tear film lipid layer II. Polymorphism of FAHFA. *Biophys. J.* 121 (2022) 451-458.
8. **Xu X**, Li G, Zuo YY, Biophysical properties of tear film lipid layer I. Surface tension and surface rheology. *Biophys. J.* 121 (2022) 439-450. **(Front Cover)**

Papers submitted to refereed journals

1. **Xu X**, Wilkerson A, Li G, Butovich IA, Zuo YY, Comparative biophysical study of meibomian lipids of wildtype and *Soat1*-null mice: implications in meibomian gland dysfunction and dry eye. (2023)
2. **Xu X**, Zuo YY, Surface activity and ultrastructure of pulmonary surfactant films at physiologically relevant concentrations. (2023)
3. Li G, **Xu X**, Zuo YY, Biophysical function of pulmonary surfactant in liquid ventilation. (2023) under revision.

Conference presentations/posters

1. Zuo YY, **Xu X**, Wilkerson A, Butovich, IA. Comparative biophysical study of meibomian lipids of wild type and *Soat1*-knockout mice: implications to dry eye. ARVO Annual Meeting, New Orleans, LA, Apr. 23-27, 2023.
2. **Xu X**, Zuo YY, Effect of tear film lipid layer on water evaporation. 96th ACS Colloid and Surface Science Symposium, Golden, CO, Jul. 10-13, 2022.

3. **Xu X**, Zuo YY, Interfacial rheology of the tear film. 96th ACS Colloid and Surface Science Symposium, Golden, CO, Jul. 10-13, 2022.
4. **Xu X**, Zuo YY, Biophysical properties of the model tear film lipid layer. 96th ACS Colloid and Surface Science Symposium, Golden, CO, Jul. 10-13, 2022.
5. **Xu X**, Zuo YY, Biophysical properties of the tear film lipid layer. Biomedical Sciences & Health Disparities Symposium, April 7-8, 2022.
6. **Xu X**, Kang C, Run S, Zuo YY, Biophysical function of (O-acyl)- ω -hydroxy fatty acids in tear film. International Chemical Congress of Pacific Basin Societies (Pacifichem), Honolulu, HI, Dec. 16-21, 2021.
7. **Xu X**, Zuo YY, Surface thermodynamics of the phospholipid monolayer. International Chemical Congress of Pacific Basin Societies (Pacifichem), Honolulu, HI, Dec. 16-21, 2021.
8. **Xu X**, Zuo YY, Biophysical properties of model tear film lipid layer. 95th ACS Colloid and Surface Science Symposium, Jun. 14-16, 2021.
9. **Xu X**, Zuo YY, Thermodynamics of surface phase transitions. 18th East-West Center International Graduate Student Conference, Honolulu, HI, Feb. 14-16, 2019.

References

1. Snell, R. S., and M. A. Lemp. 2013. *Clinical Anatomy of the Eye*. John Wiley & Sons.
2. Bonilla, L., M. Espina, P. Severino, A. Cano, M. Ettcheto, A. Camins, M. L. García, E. B. Souto, and E. Sánchez-López. 2022. Lipid Nanoparticles for the Posterior Eye Segment. *Pharmaceutics* 14(1):90.
3. Cwiklik, L. 2016. Tear film lipid layer: A molecular level view. *Biochimica et Biophysica Acta (BBA) - Biomembranes* 1858(10):2421-2430.
4. Butovich, I. A., J. C. Wojtowicz, and M. Molai. 2009. Human tear film and meibum. Very long chain wax esters and (O-acyl)-omega-hydroxy fatty acids of meibum. *Journal of Lipid Research* 50(12):2471-2485.
5. Butovich, I. A. 2013. Tear film lipids. *Experimental eye research* 117:4-27.
6. Xu, X., G. Li, and Y. Y. Zuo. 2022. Biophysical properties of tear film lipid layer I. Surface tension and surface rheology. *Biophysical Journal* 121(3):439-450.
7. Xu, X., C. Kang, R. Sun, and Y. Y. Zuo. 2022. Biophysical properties of tear film lipid layer II. Polymorphism of FAHFA. *Biophysical Journal* 121(3):451-458.
8. Gan, L., J. Wang, M. Jiang, H. Bartlett, D. Ouyang, F. Eperjesi, J. Liu, and Y. Gan. 2013. Recent advances in topical ophthalmic drug delivery with lipid-based nanocarriers. *Drug Discovery Today* 18(5):290-297.
9. Mitra, A. K. 2013. *Ocular transporters and receptors: their role in drug delivery*. Elsevier.
10. Sánchez-López, E., M. Espina, S. Doktorovova, E. B. Souto, and M. L. García. 2017. Lipid nanoparticles (SLN, NLC): Overcoming the anatomical and physiological barriers of the eye - Part I - Barriers and determining factors in ocular delivery. *European journal of*

- pharmaceutics and biopharmaceutics : official journal of Arbeitsgemeinschaft fur Pharmazeutische Verfahrenstechnik e.V 110:70-75.
11. Thassu, D., and G. J. Chader. 2012. Ocular drug delivery systems: barriers and application of nanoparticulate systems. CRC Press.
 12. Souto, E. B., J. Dias-Ferreira, A. López-Machado, M. Ettcheto, A. Cano, A. Camins Espuny, M. Espina, M. L. Garcia, and E. Sánchez-López. 2019. Advanced Formulation Approaches for Ocular Drug Delivery: State-Of-The-Art and Recent Patents. *Pharmaceutics* 11(9):460.
 13. Reimondez-Troitiño, S., N. Csaba, M. Alonso, and M. De La Fuente. 2015. Nanotherapies for the treatment of ocular diseases. *European Journal of Pharmaceutics and Biopharmaceutics* 95:279-293.
 14. Weng, Y., J. Liu, S. Jin, W. Guo, X. Liang, and Z. Hu. 2017. Nanotechnology-based strategies for treatment of ocular disease. *Acta Pharmaceutica Sinica B* 7(3):281-291.
 15. Xu, Q., S. P. Kambhampati, and R. M. Kannan. 2013. Nanotechnology approaches for ocular drug delivery. *Middle East Afr J Ophthalmol* 20(1):26-37.
 16. Honda, M., T. Asai, N. Oku, Y. Araki, M. Tanaka, and N. Ebihara. 2013. Liposomes and nanotechnology in drug development: focus on ocular targets. *International journal of nanomedicine* 8:495.
 17. Tang, Z., X. Fan, Y. Chen, and P. Gu. 2022. Ocular Nanomedicine. *Advanced Science* 9(15):2003699.
 18. Civiale, C., M. Licciardi, G. Cavallaro, G. Giammona, and M. G. Mazzone. 2009. Polyhydroxyethylaspartamide-based micelles for ocular drug delivery. *International Journal of Pharmaceutics* 378(1):177-186.

19. Patel, A., K. Cholkar, V. Agrahari, and A. K. Mitra. 2013. Ocular drug delivery systems: an overview. *World journal of pharmacology* 2(2):47.
20. S.K. GUPTA, T. V., N. DHINGRA, and J. JAISWAL. 2000. Intravitreal Pharmacokinetics of Plain and Liposome-Entrapped Fluconazole in Rabbit Eyes. *Journal of Ocular Pharmacology and Therapeutics* 16(6):511-518.
21. Sahoo, S. K., F. Dilnawaz, and S. Krishnakumar. 2008. Nanotechnology in ocular drug delivery. *Drug discovery today* 13(3-4):144-151.
22. Amrite, A. C., H. F. Edelhauser, S. R. Singh, and U. B. Kompella. 2008. Effect of circulation on the disposition and ocular tissue distribution of 20 nm nanoparticles after periocular administration. *Mol Vis* 14:150-160.
23. Kesharwani, P., K. Jain, and N. K. Jain. 2014. Dendrimer as nanocarrier for drug delivery. *Progress in Polymer Science* 39(2):268-307.
24. Kabanov, A. V., and S. V. Vinogradov. 2009. Nanogels as pharmaceutical carriers: finite networks of infinite capabilities. *Angewandte Chemie International Edition* 48(30):5418-5429.
25. Mantelli, F., M. Massaro-Giordano, I. Macchi, A. Lambiase, and S. Bonini. 2013. The cellular mechanisms of dry eye: from pathogenesis to treatment. *Journal of cellular physiology* 228(12):2253-2256.
26. Agarwal, P., J. P. Craig, and I. D. Rupenthal. 2021. Formulation Considerations for the Management of Dry Eye Disease. *Pharmaceutics* 13(2):207.
27. Calvo, P., A. Sánchez, J. Martínez, M. I. López, M. Calonge, J. C. Pastor, and M. J. Alonso. 1996. Polyester Nanocapsules as New Topical Ocular Delivery Systems for Cyclosporin A. *Pharmaceutical Research* 13(2):311-315.

28. Shen, J., Y. Deng, X. Jin, Q. Ping, Z. Su, and L. Li. 2010. Thiolated nanostructured lipid carriers as a potential ocular drug delivery system for cyclosporine A: Improving in vivo ocular distribution. *International journal of pharmaceutics* 402(1-2):248-253.
29. Halasz, K., S. J. Kelly, M. T. Iqbal, Y. Pathak, and V. Sutariya. 2019. Micro/nanoparticle delivery systems for ocular diseases. *Assay and drug development technologies* 17(4):152-166.
30. Cetinel, S., and C. Montemagno. 2015. Nanotechnology for the prevention and treatment of cataract. *The Asia-Pacific Journal of Ophthalmology* 4(6):381-387.
31. Abdelkader, H., R. G. Alany, and B. Pierscionek. 2015. Age-related cataract and drug therapy: opportunities and challenges for topical antioxidant delivery to the lens. *Journal of Pharmacy and Pharmacology* 67(4):537-550.
32. Ohta, Y., T. Yamasaki, T. Niwa, and Y. Majima. 2000. Preventive effect of vitamin E-containing liposome instillation on cataract progression in 12-month-old rats fed a 25% galactose diet. *J Ocul Pharmacol Ther* 16(4):323-335.
33. Zhang, J., P. Guan, T. Wang, D. Chang, T. Jiang, and S. Wang. 2010. Freeze-dried liposomes as potential carriers for ocular administration of cytochrome c against selenite cataract formation. *Journal of Pharmacy and Pharmacology* 61(9):1171-1178.
34. Harmia, T., J. Kreuter, P. Speiser, T. Boye, R. Gurny, and A. Kubi. 1986. Enhancement of the myotic response of rabbits with pilocarpine-loaded polybutylcyanoacrylate nanoparticles. *International Journal of Pharmaceutics* 33(1):187-193.
35. Liao, Y.T., C.H. Lee, S.T. Chen, J.Y. Lai, and K. C. W. Wu. 2017. Gelatin-functionalized mesoporous silica nanoparticles with sustained release properties for intracameral

- pharmacotherapy of glaucoma. *Journal of Materials Chemistry B* 5(34):7008-7013. 10.1039/C7TB01217A.
36. Jain, K., R. Suresh Kumar, S. Sood, and G. Dhyanandhan. 2013. Betaxolol Hydrochloride Loaded Chitosan Nanoparticles for Ocular Delivery and their Anti-glaucoma Efficacy. *Current Drug Delivery* 10(5):493-499.
 37. Rahić, O., A. Tucak, N. Omerović, M. Sirbubalo, L. Hindija, J. Hadžiabdić, and E. Vranić. 2021. Novel Drug Delivery Systems Fighting Glaucoma: Formulation Obstacles and Solutions. *Pharmaceutics* 13(1):28.
 38. Natarajan, J. V., A. Darwitan, V. A. Barathi, M. Ang, H. M. Htoon, F. Boey, K. C. Tam, T. T. Wong, and S. S. Venkatraman. 2014. Sustained Drug Release in Nanomedicine: A Long-Acting Nanocarrier-Based Formulation for Glaucoma. *ACS Nano* 8(1):419-429.
 39. Schwartz, S. G., I. U. Scott, H. W. Flynn Jr, and M. W. Stewart. 2014. Drug delivery techniques for treating age-related macular degeneration. *Expert opinion on drug delivery* 11(1):61-68.
 40. Wong, C. W., and T. T. Wong. 2019. Posterior segment drug delivery for the treatment of exudative age-related macular degeneration and diabetic macular oedema. *British Journal of Ophthalmology* 103(10):1356-1360.
 41. Tavakoli, S., J. Puranen, S. Bahrpeyma, V. E. Lautala, S. Karumo, T. Lajunen, E. M. del Amo, M. Ruponen, and A. Urtti. 2022. Liposomal sunitinib for ocular drug delivery: A potential treatment for choroidal neovascularization. *International Journal of Pharmaceutics* 620:121725.
 42. de Cogan, F., L. J. Hill, A. Lynch, P. J. Morgan-Warren, J. Lechner, M. R. Berwick, A. F. A. Peacock, M. Chen, R. A. H. Scott, H. Xu, and A. Logan. 2017. Topical Delivery of

- Anti-VEGF Drugs to the Ocular Posterior Segment Using Cell-Penetrating Peptides. *Investigative ophthalmology & visual science* 58(5):2578-2590.
43. Fangueiro, J. F., A. M. Silva, M. L. Garcia, and E. B. Souto. 2015. Current nanotechnology approaches for the treatment and management of diabetic retinopathy. *European Journal of Pharmaceutics and Biopharmaceutics* 95:307-322.
 44. Zhu, S., L. Gong, Y. Li, H. Xu, Z. Gu, and Y. Zhao. 2019. Safety assessment of nanomaterials to eyes: an important but neglected issue. *Advanced Science* 6(16):1802289.
 45. Han, J. Y., B. Kang, Y. Eom, H. M. Kim, and J. S. Song. 2017. Comparing the effects of particulate matter on the ocular surfaces of normal eyes and a dry eye rat model. *Cornea* 36(5):605-610.
 46. Tang, Y.-J., H.-H. Chang, C.-Y. Chiang, C.-Y. Lai, M.-Y. Hsu, K.-R. Wang, H.-H. Han, L.-Y. Chen, and D. P.-C. Lin. 2019. A Murine Model of Acute Allergic Conjunctivitis Induced by Continuous Exposure to Particulate Matter 2.5. *Investigative ophthalmology & visual science* 60(6):2118-2126.
 47. Cekic, O. 1998. Effect of cigarette smoking on copper, lead, and cadmium accumulation in human lens. *British Journal of Ophthalmology* 82(2):186-188.
 48. Cosert, K. M., S. Kim, I. Jalilian, M. Chang, B. L. Gates, K. E. Pinkerton, L. S. Van Winkle, V. K. Raghunathan, B. C. Leonard, and S. M. Thomasy. 2022. Metallic Engineered Nanomaterials and Ocular Toxicity: A Current Perspective. *Pharmaceutics* 14(5):981.
 49. García-Castiñeiras, S. 2010. Iron, the retina and the lens: A focused review. *Experimental eye research* 90(6):664-678.
 50. Söderstjerna, E., P. Bauer, T. Cedervall, H. Abdshell, F. Johansson, and U. E. Johansson. 2014. Silver and Gold Nanoparticles Exposure to In Vitro Cultured Retina – Studies on

- Nanoparticle Internalization, Apoptosis, Oxidative Stress, Glial- and Microglial Activity.
PLOS ONE 9(8):e105359.
51. Butovich, I. A. 2013. Tear film lipids. *Experimental eye research* 117:4-27.
 52. Cwiklik, L. 2016. Tear film lipid layer: A molecular level view. *Biochim Biophys Acta* 1858(10):2421-2430.
 53. Creech, J., L. T. Do, I. Fatt, and C. Radke. 1998. In vivo tear-film thickness determination and implications for tear-film stability. *Current eye research* 17(11):1058-1066.
 54. E.Wolff. 1954. *The Anatomy of the Eye and Orbit*. fourth ed. H.K. Lewis and Co., London.
 55. Davidson, H. J., and V. J. Kuonen. 2004. The tear film and ocular mucins. *Veterinary Ophthalmology* 7:71-77.
 56. King-Smith, P. E., B. A. Fink, R. M. Hill, K. W. Koelling, and J. M. Tiffany. 2004. The thickness of the tear film. *Current eye research* 29(4-5):357-368.
 57. P. Ewen King-Smith, E. A. H., and Jason J. Nichols. 2010. Application of a Novel Interferometric Method to Investigate the Relation between Lipid Layer Thickness and Tear Film Thinning. *Cornea* 51:2418-2423.
 58. Chen, J., K. B. Green-Church, and K. K. Nichols. 2010. Shotgun lipidomic analysis of human meibomian gland secretions with electrospray ionization tandem mass spectrometry. *Investigative ophthalmology & visual science* 51(12):6220-6231.
 59. McCulley, J., and W. Shine. 1997. A compositional based model for the tear film lipid layer. *Transactions of the American Ophthalmological Society* 95:79.
 60. Brown SHJ, K. C., Duchoslav E, Dolla NK, Kelso MJ, Papas EB, Jara PLde la, Willcox MDP, Blanksby SJ, Mitchell TW. 2013. A Comparison of Patient Matched Meibum and Tear Lipidomes. *Cornea* 54(12):7417-7423.

61. Butovich, I. A. 2009. The Meibomian puzzle: combining pieces together. *Progress in retinal and eye research* 28(6):483-498.
62. Butovich, I. A. 2011. Lipidomics of human Meibomian gland secretions: Chemistry, biophysics, and physiological role of Meibomian lipids. *Progress in lipid research* 50(3):278-301.
63. Butovich, I. A., J. C. Wojtowicz, and M. Molai. 2009. Human tear film and meibum. Very long chain wax esters and (O-acyl)-omega-hydroxy fatty acids of meibum. *J Lipid Res* 50(12):2471-2485.
64. Chen, J., K. B. Green, and K. K. Nichols. 2013. Quantitative profiling of major neutral lipid classes in human meibum by direct infusion electrospray ionization mass spectrometry. *Investigative ophthalmology & visual science* 54(8):5730-5753.
65. Georgiev, G. A., P. Eftimov, and N. Yokoi. 2017. Structure-function relationship of tear film lipid layer: A contemporary perspective. *Experimental eye research* 163:17-28.
66. Millar, T. J., and B. S. Schuett. 2015. The real reason for having a meibomian lipid layer covering the outer surface of the tear film - A review. *Experimental eye research* 137:125-138.
67. Bron, A., J. Tiffany, S. Gouveia, N. Yokoi, and L. Voon. 2004. Functional aspects of the tear film lipid layer. *Experimental eye research* 78(3):347-360.
68. Behrens, A., and J. J. Doyle. 2006. Dysfunctional Tear Syndrome. *Cornea* 25:900-907.
69. Milner, M. S., K. A. Beckman, J. I. Luchs, Q. B. Allen, R. M. Awdeh, J. Berdahl, T. S. Boland, C. Buznego, J. P. Gira, D. F. Goldberg, D. Goldman, R. K. Goyal, M. A. Jackson, J. Katz, T. Kim, P. A. Majmudar, R. P. Malhotra, M. B. McDonald, R. K. Rajpal, T. Raviv, S. Rowen, N. Shamie, J. D. Solomon, K. Stonecipher, S. Tauber, W. Trattler, K. A. Walter,

- G. O. I. Waring, R. J. Weinstock, W. F. Wiley, and E. Yeu. 2017. Dysfunctional tear syndrome: dry eye disease and associated tear film disorders – new strategies for diagnosis and treatment. *Current Opinion in Ophthalmology* 28:3-47.
70. Stapleton, F., M. Alves, V. Y. Bunya, I. Jalbert, K. Lekhanont, F. Malet, K. S. Na, D. Schaumberg, M. Uchino, J. Vehof, E. Viso, S. Vitale, and L. Jones. 2017. TFOS DEWS II Epidemiology Report. *The ocular surface* 15(3):334-365.
71. Pflugfelder, S. C., A. Solomon, and M. E. Stern. 2000. The diagnosis and management of dry eye: a twenty-five-year review. *Cornea* 19(5):644-649.
72. Lemp, M. A., and G. N. Foulks. 2007. The definition and classification of dry eye disease. *The ocular surface* 5(2):75-92.
73. Jones, L., L. E. Downie, D. Korb, J. M. Benitez-Del-Castillo, R. Dana, S. X. Deng, P. N. Dong, G. Geerling, R. Y. Hida, Y. Liu, K. Y. Seo, J. Tauber, T. H. Wakamatsu, J. Xu, J. S. Wolffsohn, and J. P. Craig. 2017. TFOS DEWS II Management and Therapy Report. *The ocular surface* 15(3):575-628.
74. Yu J, A. C., Fairchild CJ. 2011. The Economic Burden of Dry Eye Disease in the United States: A Decision Tree Analysis. *Cornea* 30(4):379-387.
75. Kulovesi, P., A. H. Rantamäki, and J. M. Holopainen. 2014. Surface Properties of Artificial Tear Film Lipid Layers: Effects of Wax Esters. *Investigative Ophthalmology & Visual Science* 55(7):4448.
76. Kulovesi, P., J. Telenius, A. Koivuniemi, G. Brezesinski, I. Vattulainen, and J. M. Holopainen. 2012. The impact of lipid composition on the stability of the tear fluid lipid layer. *Soft matter* 8(21):5826-5834.

77. Kulovesi, P., J. Telenius, A. Koivuniemi, G. Brezesinski, A. Rantamäki, T. Viitala, E. Puukilainen, M. Ritala, S. K. Wiedmer, and I. Vattulainen. 2010. Molecular organization of the tear fluid lipid layer. *Biophysical journal* 99(8):2559-2567.
78. Butovich, I. A., J. C. Arciniega, and J. C. Wojtowicz. 2010. Meibomian lipid films and the impact of temperature. *Investigative ophthalmology & visual science* 51(11):5508-5518.
79. Leiske, D. L., S. R. Raju, H. A. Ketelson, T. J. Millar, and G. G. Fuller. 2010. The interfacial viscoelastic properties and structures of human and animal Meibomian lipids. *Exp Eye Res* 90(5):598-604.
80. Dwivedi, M., M. Brinkkotter, R. K. Harishchandra, and H. J. Galla. 2014. Biophysical investigations of the structure and function of the tear fluid lipid layers and the effect of ectoine. Part B: artificial lipid films. *Biochimica et biophysica acta* 1838(10):2716-2727.
81. Lam, S. M., L. Tong, X. Duan, A. Petznick, M. R. Wenk, and G. Shui. 2014. Extensive characterization of human tear fluid collected using different techniques unravels the presence of novel lipid amphiphiles. *J Lipid Res* 55(2):289-298.
82. Sarah E. Hancock, R. A., David L. Marshall, Simon H. J. Brown, Jennifer T. Saville, Venkateswara R. Narreddula, Nathan R. Boase, Berwyck L. J. Poad, Adam J. Trevitt, Mark D. P. Willcox, Michael J. Kelso, Todd W. Mitchell, Stephen J. Blanksby. 2018. Mass spectrometry-directed structure elucidation and total synthesis of ultra-long chain (O-acyl)- ω -hydroxy fatty acids. *J. Lipid Res.* 59:1510-1518.
83. Sophia T. Tragoulias, M., Philip J. Anderton, Gary R. Dennis, Fausto Miano and Thomas J. Millar. 2005. Surface Pressure Measurements of Human Tears and Individual Tear Film Components Indicate That Proteins Are Major Contributors to the Surface Pressure. *Cornea*.

84. Mudgil, P., M. Torres, and T. J. Millar. 2006. Adsorption of lysozyme to phospholipid and meibomian lipid monolayer films. *Colloids and surfaces B: Biointerfaces* 48(2):128-137.
85. Mudgil, P., and T. J. Millar. 2011. Surfactant properties of human meibomian lipids. *Investigative ophthalmology & visual science* 52(3):1661-1670.
86. J.M.Tiffany, N. W. a. G. B. 1989. Tear film stability and tear surface tension. *Current eye research*.
87. Miano, F., M. Calcara, T. J. Millar, and V. Enea. 2005. Insertion of tear proteins into a meibomian lipids film. *Colloids and surfaces. B, Biointerfaces* 44(1):49-55.
88. Holly FJ, P. J., Dohlman CH. . 1977. Surface Activity Determination of Aqueous Tear Components in Dry Eye Patients and Normals. *Exp. Eye Res.* 24:479-491.
89. Svitova, T. F., and M. C. Lin. 2010. Tear lipids interfacial rheology: effect of lysozyme and lens care solutions. *Optometry and vision science: official publication of the American Academy of Optometry* 87(1):10.
90. Saaren-Seppälä, H., M. Jauhiainen, T. M. Tervo, B. Redl, P. K. Kinnunen, and J. M. Holopainen. 2005. Interaction of purified tear lipocalin with lipid membranes. *Investigative ophthalmology & visual science* 46(10):3649-3656.
91. Purslow, C., and J. S. Wolffsohn. 2005. Ocular surface temperature: a review. *Eye & contact lens* 31(3):117-123.
92. Doane, M. 1980. Dynamics of the human blink. *Plastische Chirurgie der Lider und Chirurgie der Tränenwege*. Springer, pp. 13-17.
93. Cardona, G., C. Garcia, C. Seres, M. Vilaseca, and J. Gispets. 2011. Blink rate, blink amplitude, and tear film integrity during dynamic visual display terminal tasks. *Current eye research* 36(3):190-197.

94. Zuo, Y. Y., R. A. Veldhuizen, A. W. Neumann, N. O. Petersen, and F. Possmayer. 2008. Current perspectives in pulmonary surfactant--inhibition, enhancement and evaluation. *Biochimica et biophysica acta* 1778(10):1947-1977.
95. Dartt, D. A. 2011. Tear Lipocalin: structure and Function. *The ocular surface* 9(3):126-138.
96. Wizert, A., D. R. Iskander, and L. Cwiklik. 2017. Interaction of lysozyme with a tear film lipid layer model: A molecular dynamics simulation study. *Biochimica et biophysica acta. Biomembranes* 1859(12):2289-2296.
97. Flanagan, J. L., and M. D. P. Willcox. 2009. Role of lactoferrin in the tear film. *Biochimie* 91(1):35-43.
98. Valle RP, W. T., ZuoYY. 2015. Biophysical Influence of Airborne Carbon Nanomaterials on Natural Pulmonary Surfactant. *ACS nano* 9(5):5413–5421.
99. Zuo, Y. Y., R. Chen, X. Wang, J. Yang, Z. Policova, and A. W. Neumann. 2016. Phase Transitions in Dipalmitoylphosphatidylcholine Monolayers. *Langmuir : the ACS journal of surfaces and colloids* 32(33):8501-8506.
100. Yang, Y., Y. Wu, Q. Ren, L. G. Zhang, S. Liu, and Y. Y. Zuo. 2018. Biophysical Assessment of Pulmonary Surfactant Predicts the Lung Toxicity of Nanomaterials. *Small Methods* 2(4):1700367.
101. Yang, Y., L. Xu, S. Dekkers, L. G. Zhang, F. R. Cassee, and Y. Y. Zuo. 2018. Aggregation State of Metal-Based Nanomaterials at the Pulmonary Surfactant Film Determines Biophysical Inhibition. *Environmental science & technology* 52(15):8920-8929.
102. Xu, L., Y. Yang, and Y. Y. Zuo. 2020. Atomic Force Microscopy Imaging of Adsorbed Pulmonary Surfactant Films. *Biophys J* 119(4):756-766.

103. Rantamäki, A. H., J. Telenius, A. Koivuniemi, I. Vattulainen, and J. M. Holopainen. 2011. Lessons from the biophysics of interfaces: lung surfactant and tear fluid. *Progress in retinal and eye research* 30(3):204-215.
104. Butovich, I. A., T. J. Millar, and B. M. Ham. 2008. Understanding and analyzing meibomian lipids--a review. *Current eye research* 33(5):405-420.
105. Yu, K., J. Yang, and Y. Y. Zuo. 2016. Automated Droplet Manipulation Using Closed-Loop Axisymmetric Drop Shape Analysis. *Langmuir : the ACS journal of surfaces and colloids* 32(19):4820-4826.
106. Tiffany, J. M. 2006. Surface tension in tears. *Arch Soc Esp Oftalmol* 81(7):363-366.
107. Braun, R. J. 2012. Dynamics of the tear film. *Annual Review of Fluid Mechanics* 44(1):267-297.
108. Yu, K., J. Yang, and Y. Y. Zuo. 2018. Droplet Oscillation as an Arbitrary Waveform Generator. *Langmuir : the ACS journal of surfaces and colloids* 34(24):7042-7047.
109. Yang, J., K. Yu, T. Tsuji, R. Jha, and Y. Y. Zuo. 2019. Determining the surface dilational rheology of surfactant and protein films with a droplet waveform generator. *Journal of colloid and interface science* 537:547-553.
110. Nishimura, S. Y., G. M. Magana, H. A. Ketelson, and G. G. Fuller. 2008. Effect of lysozyme adsorption on the interfacial rheology of DPPC and cholesteryl myristate films. *Langmuir : the ACS journal of surfaces and colloids* 24(20):11728-11733.
111. Svitova, T. F., and M. C. Lin. 2021. Evaporation retardation by model tear-lipid films: The roles of film aging, compositions and interfacial rheological properties. *Colloids and surfaces. B, Biointerfaces* 197:111392.

112. Svitova, T. F., and M. C. Lin. 2016. Dynamic interfacial properties of human tear-lipid films and their interactions with model-tear proteins in vitro. *Advances in Colloid and Interface Science* 233:4-24.
113. Nagyova, B., and J. Tiffany. 1999. Components responsible for the surface tension of human tears. *Current eye research* 19(1):4-11.
114. Bai, X., L. Xu, J. Y. Tang, Y. Y. Zuo, and G. Hu. 2019. Adsorption of Phospholipids at the Air-Water Surface. *Biophysical Journal* 117(7):1224-1233.
115. Keating, E., Y. Y. Zuo, S. M. Tadayyon, N. O. Petersen, F. Possmayer, and R. A. Veldhuizen. 2012. A modified squeeze-out mechanism for generating high surface pressures with pulmonary surfactant. *Biochimica et biophysica acta* 1818(5):1225-1234.
116. Lee, K. Y. 2008. Collapse mechanisms of Langmuir monolayers. *Annual review of physical chemistry* 59:771-791.
117. Raju, S. R., C. K. Palaniappan, H. A. Ketelson, J. W. Davis, and T. J. Millar. 2013. Interfacial Dilatational Viscoelasticity of Human Meibomian Lipid Films. *Current Eye Research* 38(8):817-824.
118. Georgiev, G. A., N. Yokoi, S. Ivanova, V. Tonchev, Y. Nancheva, and R. Krastev. 2014. Surface relaxations as a tool to distinguish the dynamic interfacial properties of films formed by normal and diseased meibomian lipids. *Soft matter* 10(30):5579-5588.
119. Svitova, T. F., and M. C. Lin. 2016. Dynamic interfacial properties of human tear-lipid films and their interactions with model-tear proteins in vitro. *Advances in colloid and interface science* 233:4-24.

120. Wüstneck, N., R. Wüstneck, V. Fainerman, R. Miller, and U. Pison. 2001. Interfacial behaviour and mechanical properties of spread lung surfactant protein/lipid layers. *Colloids and Surfaces B: Biointerfaces* 21(1-3):191-205.
121. Yore, M. M., I. Syed, P. M. Moraes-Vieira, T. Zhang, M. A. Herman, E. A. Homan, R. T. Patel, J. Lee, S. Chen, O. D. Peroni, A. S. Dhaneshwar, A. Hammarstedt, U. Smith, T. E. McGraw, A. Saghatelian, and B. B. Kahn. 2014. Discovery of a class of endogenous mammalian lipids with anti-diabetic and anti-inflammatory effects. *Cell* 159(2):318-332.
122. Nelson, A. T., M. J. Kolar, Q. Chu, I. Syed, B. B. Kahn, A. Saghatelian, and D. Siegel. 2017. Stereochemistry of Endogenous Palmitic Acid Ester of 9-Hydroxystearic Acid and Relevance of Absolute Configuration to Regulation. *Journal of the American Chemical Society* 139(13):4943-4947.
123. Butovich, I. 2010. Biochemistry and Biophysics of Human and Animal Tear Film Lipid Layer: From Composition to Structure to Function. *Investigative ophthalmology & visual science* 51(13):4154-4154.
124. Miller, R., J. K. Ferri, A. Javadi, J. Krägel, N. Mucic, and R. Wüstneck. 2010. Rheology of interfacial layers. *Colloid and Polymer Science* 288(9):937-950.
125. Svitova, T. F., and M. C. Lin. 2013. Racial variations in interfacial behavior of lipids extracted from worn soft contact lenses. *Optometry and vision science : official publication of the American Academy of Optometry* 90(12):1361-1369.
126. Brejchova, K., L. Balas, V. Paluchova, M. Brezinova, T. Durand, and O. Kuda. 2020. Understanding FAHFAs: From structure to metabolic regulation. *Progress in lipid research* 79:101053.

127. Kolar, M. J., A. T. Nelson, T. Chang, M. E. Ertunc, M. P. Christy, L. Ohlsson, M. Härröd, B. B. Kahn, D. Siegel, and A. Saghatelian. 2018. Faster Protocol for Endogenous Fatty Acid Esters of Hydroxy Fatty Acid (FAHFA) Measurements. *Analytical Chemistry* 90(8):5358-5365.
128. Liberati-Čizmek, A.-M., M. Biluš, A. L. Brkić, I. C. Barić, M. Bakula, A. Hozić, and M. Cindrić. 2019. Analysis of Fatty Acid Esters of Hydroxyl Fatty Acid in Selected Plant Food. *Plant Foods for Human Nutrition* 74(2):235-240.
129. Zhu, Q. F., J. W. Yan, T. Y. Zhang, H. M. Xiao, and Y. Q. Feng. 2018. Comprehensive Screening and Identification of Fatty Acid Esters of Hydroxy Fatty Acids in Plant Tissues by Chemical Isotope Labeling-Assisted Liquid Chromatography-Mass Spectrometry. *Anal Chem* 90(16):10056-10063.
130. Chen, J., K. K. Nichols, L. Wilson, S. Barnes, and J. J. Nichols. 2019. Untargeted lipidomic analysis of human tears: A new approach for quantification of O-acyl-omega hydroxy fatty acids. *The ocular surface* 17(2):347-355.
131. Willcox, M. D. P., P. Argueso, G. A. Georgiev, J. M. Holopainen, G. W. Laurie, T. J. Millar, E. B. Papas, J. P. Rolland, T. A. Schmidt, U. Stahl, T. Suarez, L. N. Subbaraman, O. O. Ucakhan, and L. Jones. 2017. TFOS DEWS II Tear Film Report. *The ocular surface* 15(3):366-403.
132. Lam, S. M., L. Tong, S. S. Yong, B. Li, S. S. Chaurasia, G. Shui, and M. R. Wenk. 2011. Meibum lipid composition in Asians with dry eye disease. *PloS one* 6(10):e24339.
133. Miyamoto, M., T. Sassa, M. Sawai, and A. Kihara. 2020. Lipid polarity gradient formed by ω -hydroxy lipids in tear film prevents dry eye disease. *eLife* 9:e53582.

134. Khanal, S., Y. Bai, W. Ngo, K. K. Nichols, L. Wilson, S. Barnes, and J. J. Nichols. 2021. Human Meibum and Tear Film Derived (O-Acyl)-Omega-Hydroxy Fatty Acids as Biomarkers of Tear Film Dynamics in Meibomian Gland Dysfunction and Dry Eye Disease. *Investigative ophthalmology & visual science* 62(9):13-13.
135. Xu, X., G. Li, and Y. Y. Zuo. 2021. Biophysical properties of tear film lipid layer I. Surface tension and surface rheology. *Biophysical Journal*:Submitted as a companion paper.
136. Butovich, I. A., E. Uchiyama, and J. P. McCulley. 2007. Lipids of human meibum: mass-spectrometric analysis and structural elucidation. *Journal of lipid research* 48(10):2220-2235.
137. Butovich, I. A. 2010. Fatty acid composition of cholesteryl esters of human meibomian gland secretions. *Steroids* 75(10):726-733.
138. Zhou, P., A. Santoro, O. D. Peroni, A. T. Nelson, A. Saghatelian, D. Siegel, and B. B. Kahn. 2019. PAHSAs enhance hepatic and systemic insulin sensitivity through direct and indirect mechanisms. *J Clin Invest* 129(10):4138-4150.
139. Schuett, B. S., and T. J. Millar. 2013. An investigation of the likely role of (O-acyl) omega-hydroxy fatty acids in meibomian lipid films using (O-oleyl) omega-hydroxy palmitic acid as a model. *Experimental eye research* 115:57-64.
140. Bland, H. C., J. A. Moilanen, F. S. Ekholm, and R. O. Paananen. 2019. Investigating the Role of Specific Tear Film Lipids Connected to Dry Eye Syndrome: A Study on O-Acyl-omega-hydroxy Fatty Acids and Diesters. *Langmuir : the ACS journal of surfaces and colloids* 35(9):3545-3552.

141. Martínez, L., R. Andrade, E. G. Birgin, and J. M. Martínez. 2009. PACKMOL: a package for building initial configurations for molecular dynamics simulations. *Journal of computational chemistry* 30(13):2157-2164.
142. Martínez, J. M., and L. Martínez. 2003. Packing optimization for automated generation of complex system's initial configurations for molecular dynamics and docking. *Journal of computational chemistry* 24(7):819-825.
143. Skibinsky, A., R. M. Venable, and R. W. Pastor. 2005. A molecular dynamics study of the response of lipid bilayers and monolayers to trehalose. *Biophysical journal* 89(6):4111-4121.
144. Baoukina, S. M., L.; Marrink, S. J.; Tieleman, D. P. 2007. Pressure-Area Isotherm of a Lipid Monolayer from Molecular Dynamics Simulations. *Langmuir : the ACS journal of surfaces and colloids* 23(25):12617-12623.
145. Liu, B., M. I. Hoopes, and M. Karttunen. 2014. Molecular dynamics simulations of DPPC/CTAB monolayers at the air/water interface. *The journal of physical chemistry. B* 118(40):11723-11737.
146. Duncan, S. L., and R. G. Larson. 2008. Comparing experimental and simulated pressure-area isotherms for DPPC. *Biophysical journal* 94(8):2965-2986.
147. Nosé, S. 1984. A molecular dynamics method for simulations in the canonical ensemble. *Molecular Physics* 52(2):255-268.
148. Abraham, M. J., T. Murtola, R. Schulz, S. Páll, J. C. Smith, B. Hess, and E. Lindahl. 2015. GROMACS: High performance molecular simulations through multi-level parallelism from laptops to supercomputers. *SoftwareX* 1-2:19-25.

149. Smith, E. C., J. M. Crane, T. G. Laderas, and S. B. Hall. 2003. Metastability of a supercompressed fluid monolayer. *Biophys J* 85(5):3048-3057.
150. Yan, W., S. C. Biswas, T. G. Laderas, and S. B. Hall. 2007. The melting of pulmonary surfactant monolayers. *J Appl Physiol* 102(5):1739-1745.
151. Paananen, R. O., T. Viitaja, A. Olżyńska, F. S. Ekholm, J. Moilanen, and L. Cwiklik. 2020. Interactions of polar lipids with cholesteryl ester multilayers elucidate tear film lipid layer structure. *The ocular surface* 18(4):545-553.
152. Viitaja, T., J. E. Raitanen, J. Moilanen, R. O. Paananen, and F. S. Ekholm. 2021. The Properties and Role of O-Acyl- ω -hydroxy Fatty Acids and Type I-St and Type II Diesters in the Tear Film Lipid Layer Revealed by a Combined Chemistry and Biophysics Approach. *The Journal of organic chemistry* 86(7):4965-4976.
153. Arciniega, J. C., E. Uchiyama, and I. A. Butovich. 2013. Disruption and Destabilization of Meibomian Lipid Films Caused by Increasing Amounts of Ceramides and Cholesterol. *Investigative ophthalmology & visual science* 54(2):1352-1360.
154. Sodt, A. J., M. L. Sandar, K. Gawrisch, R. W. Pastor, and E. Lyman. 2014. The molecular structure of the liquid-ordered phase of lipid bilayers. *Journal of the American Chemical Society* 136(2):725-732.
155. Sodt, A. J., R. W. Pastor, and E. Lyman. 2015. Hexagonal Substructure and Hydrogen Bonding in Liquid-Ordered Phases Containing Palmitoyl Sphingomyelin. *Biophysical journal* 109(5):948-955.
156. Brown, S. H., C. M. Kunnen, E. Duchoslav, N. K. Dolla, M. J. Kelso, E. B. Papas, P. Lazon de la Jara, M. D. Willcox, S. J. Blanksby, and T. W. Mitchell. 2013. A comparison of

- patient matched meibum and tear lipidomes. *Investigative ophthalmology & visual science* 54(12):7417-7424.
157. Baoukina, S., L. Monticelli, H. J. Risselada, S. J. Marrink, and D. P. Tieleman. 2008. The molecular mechanism of lipid monolayer collapse. *Proceedings of the National Academy of Sciences* 105(31):10803-10808.
158. Lee, K. Y. C. 2008. Collapse Mechanisms of Langmuir Monolayers. *Annual review of physical chemistry* 59(1):771-791.
159. Davidson, H. J., and V. J. Kuonen. 2004. The tear film and ocular mucins. *Veterinary Ophthalmology* 7(2):71-77.
160. King-Smith, E., B. Fink, R. Hill, K. Koelling, and J. Tiffany. 2004. The thickness of the tear film. *Current eye research* 29(4-5):357-368.
161. Chen, J. Z., K. B. Green-Church, and K. K. Nichols. 2010. Shotgun lipidomic analysis of human meibomian gland secretions with electrospray ionization tandem mass spectrometry. *Investigative ophthalmology & visual science* 51(12):6220-6231.
162. Brown, S. H. J., C. M. E. Kunnen, E. Duchoslav, N. K. Dolla, M. J. Kelso, E. B. Papas, P. L. de la Jara, M. D. P. Willcox, S. J. Blanksby, and T. W. Mitchell. 2013. A comparison of patient matched meibum and tear lipidomes. *Investigative ophthalmology & visual science* 54(12):7417-7423.
163. Butovich, I. A. 2009. The meibomian puzzle: Combining pieces together. *Progress in retinal and eye research* 28(6):483-498.
164. Dean, A. W., and B. J. Glasgow. 2012. Mass Spectrometric Identification of Phospholipids in Human Tears and Tear Lipocalin. *Investigative ophthalmology & visual science* 53(4):1773-1782.

165. Paananen, R. O., A. H. Rantamäki, and J. M. Holopainen. 2014. Antievaporative mechanism of wax esters: implications for the function of tear fluid. *Langmuir : the ACS journal of surfaces and colloids* 30(20):5897-5902.
166. Georgiev, G. A., P. Eftimov, and N. Yokoi. 2017. Structure-function relationship of tear film lipid layer: A contemporary perspective. *Experimental eye research* 163:17-28.
167. Bron, A. J., J. M. Tiffany, S. M. Gouveia, N. Yokoi, and L. W. Voon. 2004. Functional aspects of the tear film lipid layer. *Experimental eye research* 78(3):347-360.
168. King-Smith, P. E., M. D. Bailey, and R. J. Braun. 2013. Four characteristics and a model of an effective tear film lipid layer (TFLL). *The ocular surface* 11(4):236-245.
169. King-Smith, P. E., C. G. Begley, and R. J. Braun. 2018. Mechanisms, imaging and structure of tear film breakup. *The ocular surface* 16(1):4-30.
170. Nichols, K. K., G. N. Foulks, A. J. Bron, B. J. Glasgow, M. Dogru, K. Tsubota, M. A. Lemp, and D. A. Sullivan. 2011. The International Workshop on Meibomian Gland Dysfunction: Executive Summary. *Investigative ophthalmology & visual science* 52(4):1922-1929.
171. Craig, J. P., K. K. Nichols, E. K. Akpek, B. Caffery, H. S. Dua, C.-K. Joo, Z. Liu, J. D. Nelson, J. J. Nichols, K. Tsubota, and F. Stapleton. 2017. TFOS DEWS II Definition and Classification Report. *The ocular surface* 15(3):276-283.
172. Stapleton, F., M. Alves, V. Y. Bunya, I. Jalbert, K. Lekhanont, F. Malet, K.-S. Na, D. Schaumberg, M. Uchino, J. Vehof, E. Viso, S. Vitale, and L. Jones. 2017. TFOS DEWS II Epidemiology Report. *The ocular surface* 15(3):334-365.
173. Craig, J. P., and A. Tomlinson. 1997. Importance of the lipid layer in human tear film stability and evaporation. *Optometry and vision science* 74(1):8-13.

174. Mathers, W. 2004. Evaporation from the ocular surface. *Experimental Eye Research* 78(3):389-394.
175. Wong, S., P. J. Murphy, and L. Jones. 2018. Tear evaporation rates: What does the literature tell us? *Contact Lens and Anterior Eye* 41(3):297-306.
176. Peng, C. C., C. Cerretani, Y. Li, S. Bowers, S. Shahsavarani, M. C. Lin, and C. J. Radke. 2014. Flow Evaporimeter To Assess Evaporative Resistance of Human Tear-Film Lipid Layer. *Industrial & Engineering Chemistry Research* 53(47):18130-18139.
177. Dursch, T. J., W. Li, B. Taraz, M. C. Lin, and C. J. Radke. 2018. Tear-Film Evaporation Rate from Simultaneous Ocular-Surface Temperature and Tear-Breakup Area. *Optometry and vision science : official publication of the American Academy of Optometry* 95(1):5-12.
178. Rantamäki, A. H., M. Javanainen, I. Vattulainen, and J. M. Holopainen. 2012. Do lipids retard the evaporation of the tear fluid? *Investigative ophthalmology & visual science* 53(10):6442-6447.
179. Borchman, D., G. N. Foulks, M. C. Yappert, J. Mathews, K. Leake, and J. Bell. 2009. Factors affecting evaporation rates of tear film components measured in vitro. *Eye & contact lens* 35(1):32-37.
180. Herok, G. H., P. Mudgil, and T. J. Millar. 2009. The effect of Meibomian lipids and tear proteins on evaporation rate under controlled in vitro conditions. *Current eye research* 34(7):589-597.
181. Cerretani, C. F., N. H. Ho, and C. J. Radke. 2013. Water-evaporation reduction by duplex films: application to the human tear film. *Advances in colloid and interface science* 197-198:33-57.

182. Sledge, S. M., H. Khimji, D. Borchman, A. L. Oliver, H. Michael, E. K. Dennis, D. Gerlach, R. Bhola, and E. Stephen. 2016. Evaporation and Hydrocarbon Chain Conformation of Surface Lipid Films. *The ocular surface* 14(4):447-459.
183. Kulovesi, P., A. H. Rantamäki, and J. M. Holopainen. 2014. Surface Properties of Artificial Tear Film Lipid Layers: Effects of Wax Esters. *Investigative ophthalmology & visual science* 55(7):4448-4454.
184. Borchman, D., M. C. Yappert, S. E. Milliner, D. Duran, G. W. Cox, R. J. Smith, and R. Bhola. 2013. ¹³C and ¹H NMR ester region resonance assignments and the composition of human infant and child meibum. *Experimental eye research* 112:151-159.
185. Archer, R. J., and V. K. La Mer. 1955. The Rate of Evaporation of Water through Fatty Acid Monolayers. *The Journal of Physical Chemistry* 59(3):200-208.
186. Barnes, G. T., and V. K. La Mer. 1962. The evaporation resistance of monolayers of long-chain acids and alcohols and their mixtures. *Retardation of Evaporation by Monolayers: Transport Processes*. V. K. La Mer, editor. Academic Press, New York, pp. 9-33.
187. Blank, M., and V. K. La Mer. 1962. The energy barrier for monolayer penetration. *Retardation of Evaporation by Monolayers: Transport Processes*. V. K. La Mer, editor. Academic Press, New York, pp. 59-66.
188. Tiffany, J. M., N. Winter, and G. Bliss. 1989. Tear film stability and tear surface tension. *Current eye research* 8(5):507-515.
189. Nagyová, B., and J. M. Tiffany. 1999. Components responsible for the surface tension of human tears. *Current eye research* 19(1):4-11.
190. Miano, F., M. Calcara, F. Giuliano, T. Millar, and V. Enea. 2004. Effect of meibomian lipid layer on evaporation of tears. *Journal of Physics: Condensed Matter* 16(26):S2461.

191. Svitova, T. F., and M. C. Lin. 2021. Evaporation retardation by model tear-lipid films: The roles of film aging, compositions and interfacial rheological properties. *Colloids and Surfaces B: Biointerfaces* 197:111392.
192. Mathers, W. D., G. Binarao, and M. Petroll. 1993. Ocular water evaporation and the dry eye. A new measuring device. *Cornea* 12(4):335-340.
193. Rohit, A., K. Ehrmann, T. Naduvilath, M. Willcox, and F. Stapleton. 2014. Validating a new device for measuring tear evaporation rates. *Ophthalmic & physiological optics : the journal of the British College of Ophthalmic Opticians (Optometrists)* 34(1):53-62.
194. Valle, R. P., T. Wu, and Y. Y. Zuo. 2015. Biophysical influence of airborne carbon nanomaterials on natural pulmonary surfactant. *Acs Nano* 9(5):5413-5421.
195. Zuo, Y. Y., R. Chen, X. Wang, J. Yang, Z. Policova, and A. W. Neumann. 2016. Phase Transitions in Dipalmitoylphosphatidylcholine Monolayers. *Langmuir : the ACS journal of surfaces and colloids* 32(33):8501-8506.
196. Yu, K., J. L. Yang, and Y. Y. Zuo. 2016. Automated droplet manipulation using Closed-Loop Axisymmetric Drop Shape Analysis. *Langmuir* 32(19):4820-4826.
197. Cândido, C., R. de Dear, and R. Lamberts. 2011. Combined thermal acceptability and air movement assessments in a hot humid climate. *Building and Environment* 46(2):379-385.
198. MISHIMA, S., A. GASSET, S. D. KLYCE, Jr., and J. L. BAUM. 1966. Determination of Tear Volume and Tear Flow. *Investigative ophthalmology & visual science* 5(3):264-276.
199. Kim, Y. H., A. D. Graham, W. Li, C. J. Radke, and M. C. Lin. 2019. Human Lacrimal Production Rate and Wetted Length of Modified Schirmer's Tear Test Strips. *Translational Vision Science & Technology* 8(3):40-40.

200. Xu, L., Y. Yang, and Y. Y. Zuo. 2020. Atomic Force Microscopy Imaging of Adsorbed Pulmonary Surfactant Films. *Biophysical journal* 119(4):756-766.
201. Mishima, S., and D. M. Maurice. 1961. The oily layer of the tear film and evaporation from the corneal surface. *Exp Eye Res* 1:39-45.
202. Goto, E., K. Endo, A. Suzuki, Y. Fujikura, Y. Matsumoto, and K. Tsubota. 2003. Tear Evaporation Dynamics in Normal Subjects and Subjects with Obstructive Meibomian Gland Dysfunction. *Investigative Ophthalmology & Visual Science* 44(2):533-539.
203. Zhong, X., A. Crivoi, and F. Duan. 2015. Sessile nanofluid droplet drying. *Advances in Colloid and Interface Science* 217:13-30.
204. Rosenfeld, L., C. Cerretani, D. L. Leiske, M. F. Toney, C. J. Radke, and G. G. Fuller. 2013. Structural and rheological properties of meibomian lipid. *Invest Ophthalmol Vis Sci* 54(4):2720-2732.
205. Paananen, R. O., T. Viitaja, A. Olżyńska, F. S. Ekholm, J. Moilanen, and L. Cwiklik. 2020. Interactions of polar lipids with cholesteryl ester multilayers elucidate tear film lipid layer structure. *The ocular surface* 18(4):545-553.
206. Bai, Y., W. Ngo, S. Khanal, and J. J. Nichols. 2022. Characterization of the thickness of the Tear Film Lipid Layer in Meibomian Gland Dysfunction using high resolution optical microscopy. *The ocular surface* 24:34-39.
207. Bai, Y., W. Ngo, and J. J. Nichols. 2019. Characterization of the thickness of the tear film lipid layer using high resolution microscopy. *The ocular surface* 17(2):356-359.
208. Bhamla, M. S., C. Chai, N. I. Rabiah, J. M. Frostad, and G. G. Fuller. 2016. Instability and Breakup of Model Tear Films. *Investigative ophthalmology & visual science* 57(3):949-958.

209. King-Smith, P. E., K. S. Reuter, R. J. Braun, J. J. Nichols, and K. K. Nichols. 2013. Tear Film Breakup and Structure Studied by Simultaneous Video Recording of Fluorescence and Tear Film Lipid Layer Images. *Investigative Ophthalmology & Visual Science* 54(7):4900-4909.
210. Butovich, I. A. 2017. Meibomian glands, meibum, and meibogenesis. *Experimental eye research* 163:2-16.
211. Khanna, R. K., S. Catanese, P. Emond, P. Corcia, H. Blasco, and P. J. Pisella. 2022. Metabolomics and lipidomics approaches in human tears: A systematic review. *Survey of ophthalmology* 67(4):1229-1243.
212. Sheppard, J. D., and K. K. Nichols. 2023. Dry Eye Disease Associated with Meibomian Gland Dysfunction: Focus on Tear Film Characteristics and the Therapeutic Landscape. *Ophthalmology and therapy*:doi: 10.1007/s40123-40023-00669-40121.
213. Suzuki, T., K. Kitazawa, Y. Cho, M. Yoshida, T. Okumura, A. Sato, and S. Kinoshita. 2022. Alteration in meibum lipid composition and subjective symptoms due to aging and meibomian gland dysfunction. *The ocular surface* 26:310-317.
214. Sawai, M., K. Watanabe, K. Tanaka, W. Kinoshita, K. Otsuka, M. Miyamoto, T. Sassa, and A. Kihara. 2021. Diverse meibum lipids produced by Awat1 and Awat2 are important for stabilizing tear film and protecting the ocular surface. *iScience* 24(5):102478.
215. Butovich, I. A., and A. Wilkerson. 2022. Dynamic Changes in the Gene Expression Patterns and Lipid Profiles in the Developing and Maturing Meibomian Glands. *International Journal of Molecular Sciences* 23(14):7884.
216. Oelkers, P., A. Behari, D. Cromley, J. T. Billheimer, and S. L. Sturley. 1998. Characterization of two human genes encoding acyl coenzyme A:cholesterol

- acyltransferase-related enzymes. *The Journal of biological chemistry* 273(41):26765-26771.
217. Butovich, I. A., A. Wilkerson, and S. Yuksel. 2021. Depletion of Cholesteryl Esters Causes Meibomian Gland Dysfunction-Like Symptoms in a *Soat1*-Null Mouse Model. *International Journal of Molecular Sciences* 22(4):1583.
218. Widjaja-Adhi, M. A. K., K. Chao, and M. Golczak. 2022. Mouse models in studies on the etiology of evaporative dry eye disease. *Experimental eye research* 219:109072.
219. Lu, H., J. C. Wojtowicz, and I. A. Butovich. 2013. Differential scanning calorimetric evaluation of human meibomian gland secretions and model lipid mixtures: transition temperatures and cooperativity of melting. *Chem Phys Lipids* 170-171:55-64.
220. Xu, X., G. Li, and Y. Y. Zuo. 2023. Effect of Model Tear Film Lipid Layer on Water Evaporation. *Investigative ophthalmology & visual science* 64(1):13-13.
221. Xu, X., and Y. Y. Zuo. 2023. Nanomedicine for Ocular Drug Delivery. *Nanomedicine*. N. Gu, editor. Springer Nature Singapore, Singapore, pp. 755-786.
222. Butovich, I. A., A. Wilkerson, N. Bhat, A. McMahon, and S. Yuksel. 2019. On the pivotal role of *Elovl3/ELOVL3* in meibogenesis and ocular physiology of mice. *FASEB journal : official publication of the Federation of American Societies for Experimental Biology* 33(9):10034-10048.
223. Yang, J., K. Yu, T. Tsuji, R. Jha, and Y. Y. Zuo. 2019. Determining the surface dilational rheology of surfactant and protein films with a droplet waveform generator. *Journal of Colloid and Interface Science* 537:547-553.

224. Zuo, Y. Y., R. A. W. Veldhuizen, A. W. Neumann, N. O. Petersen, and F. Possmayer. 2008. Current perspectives in pulmonary surfactant — Inhibition, enhancement and evaluation. *Biochimica et Biophysica Acta (BBA) - Biomembranes* 1778(10):1947-1977.
225. Butovich, I. A., A. Wilkerson, and S. Yuksel. 2021. Depletion of Cholesteryl Esters Causes Meibomian Gland Dysfunction-Like Symptoms in a *Soat1*-Null Mouse Model. *International journal of molecular sciences* 22(4).
226. Hjort Ipsen, J., G. Karlström, O. G. Mourtsen, H. Wennerström, and M. J. Zuckermann. 1987. Phase equilibria in the phosphatidylcholine-cholesterol system. *Biochimica et Biophysica Acta (BBA) - Biomembranes* 905(1):162-172.
227. Sankaram, M. B., and T. E. Thompson. 1991. Cholesterol-induced fluid-phase immiscibility in membranes. *Proc Natl Acad Sci U S A* 88(19):8686-8690.
228. Hung, W. C., M. T. Lee, F. Y. Chen, and H. W. Huang. 2007. The condensing effect of cholesterol in lipid bilayers. *Biophys J* 92(11):3960-3967.
229. de Meyer, F., and B. Smit. 2009. Effect of cholesterol on the structure of a phospholipid bilayer. *Proceedings of the National Academy of Sciences* 106(10):3654-3658.
230. Zhang, H., Y. E. Wang, C. R. Neal, and Y. Y. Zuo. 2012. Differential effects of cholesterol and budesonide on biophysical properties of clinical surfactant. *Pediatric research* 71(4):316-323.
231. Arciniega, J. C., E. Uchiyama, and I. A. Butovich. 2013. Disruption and destabilization of meibomian lipid films caused by increasing amounts of ceramides and cholesterol. *Invest Ophthalmol Vis Sci* 54(2):1352-1360.
232. Chhadva, P., R. Goldhardt, and A. Galor. 2017. Meibomian Gland Disease: The Role of Gland Dysfunction in Dry Eye Disease. *Ophthalmology* 124(11S):S20-S26.

233. Baudouin, C., E. M. Messmer, P. Aragona, G. Geerling, Y. A. Akova, J. Benítez-del-Castillo, K. G. Boboridis, J. Merayo-Llodes, M. Rolando, and M. Labetoulle. 2016. Revisiting the vicious circle of dry eye disease: a focus on the pathophysiology of meibomian gland dysfunction. *British Journal of Ophthalmology* 100(3):300-306.
234. Pinna, A., F. Blasetti, A. Zinellu, C. Carru, and G. Solinas. 2013. Meibomian Gland Dysfunction and Hypercholesterolemia. *Ophthalmology* 120(12):2385-2389.
235. Braich, P. S., M. K. Howard, and J. S. Singh. 2016. Dyslipidemia and its association with meibomian gland dysfunction. *International Ophthalmology* 36(4):469-476.
236. Tomioka, Y., K. Kitazawa, Y. Yamashita, K. Numa, T. Inomata, J.-W. B. Hughes, R. Soda, M. Nakamura, T. Suzuki, N. Yokoi, and C. Sotozono. 2023. Dyslipidemia Exacerbates Meibomian Gland Dysfunction: A Systematic Review and Meta-Analysis. *Journal of Clinical Medicine* 12(6):2131.
237. Nakayama, N., M. Kawashima, M. Kaido, R. Arita, and K. Tsubota. 2015. Analysis of Meibum Before and After Intraductal Meibomian Gland Probing in Eyes With Obstructive Meibomian Gland Dysfunction. *Cornea* 34(10):1206-1208.
238. Mathers, W. D., and D. Choi. 2004. Cluster Analysis of Patients With Ocular Surface Disease, Blepharitis, and Dry Eye. *Archives of Ophthalmology* 122(11):1700-1704.
239. Thébaud, B., K. N. Goss, M. Laughon, J. A. Whitsett, S. H. Abman, R. H. Steinhorn, J. L. Aschner, P. G. Davis, S. A. McGrath-Morrow, R. F. Soll, and A. H. Jobe. 2019. Bronchopulmonary dysplasia. *Nature Reviews Disease Primers* 5(1):78.
240. Castillo-Sánchez, J. C., A. Cruz, and J. Pérez-Gil. 2021. Structural hallmarks of lung surfactant: Lipid-protein interactions, membrane structure and future challenges. *Archives of biochemistry and biophysics* 703:108850.

241. Whitsett, J. A., and M. T. Stahlman. 1998. Impact of advances in physiology, biochemistry, and molecular biology on pulmonary disease in neonates. *American journal of respiratory and critical care medicine* 157(4 Pt 2):S67-71.
242. Clements, J. A., and M. E. Avery. 1998. Lung surfactant and neonatal respiratory distress syndrome. *American journal of respiratory and critical care medicine* 157(4 Pt 2):S59-66.
243. Polin, R. A., W. A. Carlo, Committee on Fetus and Newborn, and American Academy of Pediatrics. 2014. Surfactant replacement therapy for preterm and term neonates with respiratory distress. *Pediatrics* 133(1):156-163.
244. Lewis, J. F., and R. Veldhuizen. 2003. The role of exogenous surfactant in the treatment of acute lung injury. *Annu Rev Physiol* 65:613-642.
245. Kneyber, M. C. J., R. G. Khemani, A. Bhalla, R. G. T. Blokpoel, P. Cruces, M. K. Dahmer, G. Emeriaud, J. Grunwell, S. Ilia, B. H. Katira, Y. M. Lopez-Fernandez, P. Rajapreyar, L. N. Sanchez-Pinto, and P. C. Rimensberger. 2023. Understanding clinical and biological heterogeneity to advance precision medicine in paediatric acute respiratory distress syndrome. *The Lancet Respiratory Medicine* 11(2):197-212.
246. Veldhuizen, R. A. W., Y. Y. Zuo, N. O. Petersen, J. F. Lewis, and F. Possmayer. 2021. The COVID-19 pandemic: a target for surfactant therapy? *Expert Rev Respir Med* 15(5):597-608.
247. Zuo, Y. Y., W. E. Uspal, and T. Wei. 2020. Airborne Transmission of COVID-19: Aerosol Dispersion, Lung Deposition, and Virus-Receptor Interactions. *ACS Nano* 14(12):16502-16524.
248. Enhorning, G. 1977. Pulsating bubble technique for evaluating pulmonary surfactant. *J Appl Physiol* 43(2):198-203.

249. Enhorning, G. 2001. Pulmonary surfactant function studied with the pulsating bubble surfactometer (PBS) and the capillary surfactometer (CS). *Comp Biochem Physiol A Mol Integr Physiol* 129(1):221-226.
250. Bachofen, H., S. Schurch, M. Urbinelli, and E. R. Weibel. 1987. Relations among alveolar surface tension, surface area, volume, and recoil pressure. *J. Appl. Physiol.* 62(5):1878-1887.
251. Schurch, S., H. Bachofen, J. Goerke, and F. Possmayer. 1989. A captive bubble method reproduces the in situ behavior of lung surfactant monolayers. *J Appl Physiol* 67(6):2389-2396.
252. Schurch, S., H. Bachofen, J. Goerke, and F. Green. 1992. Surface properties of rat pulmonary surfactant studied with the captive bubble method: adsorption, hysteresis, stability. *Biochimica et biophysica acta* 1103(1):127-136.
253. Schurch, S., F. H. Green, and H. Bachofen. 1998. Formation and structure of surface films: captive bubble surfactometry. *Biochimica et biophysica acta* 1408(2-3):180-202.
254. Schurch, S., H. Bachofen, and F. Possmayer. 2001. Surface activity in situ, in vivo, and in the captive bubble surfactometer. *Comp Biochem Physiol A Mol Integr Physiol* 129(1):195-207.
255. Zuo, Y. Y., M. Ding, D. Li, and A. W. Neumann. 2004. Further development of Axisymmetric Drop Shape Analysis-Captive Bubble for pulmonary surfactant related studies. *Biochimica Et Biophysica Acta-General Subjects* 1675(1-3):12-20.
256. Zuo, Y. Y., C. Do, and A. W. Neumann. 2007. Automatic measurement of surface tension from noisy images using a component labeling method. *Colloids and Surfaces A: Physicochemical and Engineering Aspects* 299(1-3):109-116.

257. Codd, J. R., S. Schurch, C. B. Daniels, and S. Orgeig. 2002. Torpor-associated fluctuations in surfactant activity in Gould's wattled bat. *Biochimica et biophysica acta* 1580(1):57-66.
258. Lewis, J. F., and A. H. Jobe. 1993. Surfactant and the adult respiratory distress syndrome. *The American review of respiratory disease* 147(1):218-233.
259. Ikegami, M., C. M. Rebello, and A. H. Jobe. 1996. Surfactant inhibition by plasma: gestational age and surfactant treatment effects in preterm lambs. *J Appl Physiol* 81(6):2517-2522.
260. Rebello, C. M., A. H. Jobe, J. W. Eisele, and M. Ikegami. 1996. Alveolar and tissue surfactant pool sizes in humans. *American journal of respiratory and critical care medicine* 154(3 Pt 1):625-628.
261. Weibel, E. R. 1973. Morphological basis of alveolar-capillary gas exchange. *Physiol Rev* 53(2):419-495.
262. Bastacky, J., C. Y. Lee, J. Goerke, H. Koushafar, D. Yager, L. Kenaga, T. P. Speed, Y. Chen, and J. A. Clements. 1995. Alveolar lining layer is thin and continuous: low-temperature scanning electron microscopy of rat lung. *J Appl Physiol* 79(5):1615-1628.
263. Valle, R. P., T. Wu, and Y. Y. Zuo. 2015. Biophysical influence of airborne carbon nanomaterials on natural pulmonary surfactant. *ACS Nano* 9(5):5413-5421.
264. Yu, K., J. Yang, and Y. Y. Zuo. 2016. Automated Droplet Manipulation Using Closed-Loop Axisymmetric Drop Shape Analysis. *Langmuir* 32(19):4820-4826.
265. Cruz, A., and J. Perez-Gil. 2007. Langmuir films to determine lateral surface pressure on lipid segregation. In *Methods in molecular biology* (Clifton, N.J. 439-457.
266. Marsh, D. 1990. *CRC Handbook of Lipid Bilayers*. CRC Press, Boca Raton, FL.

267. Bachofen, H., and S. Schurch. 2001. Alveolar surface forces and lung architecture. *Comp Biochem Physiol A Mol Integr Physiol* 129(1):183-193.
268. Kharge, A. B., Y. Wu, and C. E. Perlman. 2014. Surface tension in situ in flooded alveolus unaltered by albumin. *Journal of applied physiology* 117(5):440-451.
269. Schurch, S., D. Schurch, T. Curstedt, and B. Robertson. 1994. Surface activity of lipid extract surfactant in relation to film area compression and collapse. *J. Appl. Physiol.* 77(2):974-986.
270. Dagan, M. P., and S. B. Hall. 2015. The Equilibrium Spreading Tension of Pulmonary Surfactant. *Langmuir* 31(48):13063-13067.
271. Gaines, G. L. 1966. *Insoluble Monolayers at Liquid-Gas Interfaces*. Interscience Publishers, John Wiley & Sons, New York.
272. Putz, G., J. Goerke, and J. A. Clements. 1994. Surface activity of rabbit pulmonary surfactant subfractions at different concentrations in a captive bubble. *J Appl Physiol* 77(2):597-605.
273. Veldhuizen, E. J., J. J. Batenburg, L. M. van Golde, and H. P. Haagsman. 2000. The role of surfactant proteins in DPPC enrichment of surface films. *Biophys J* 79(6):3164-3171.
274. Schurch, D., O. L. Ospina, A. Cruz, and J. Perez-Gil. 2010. Combined and independent action of proteins SP-B and SP-C in the surface behavior and mechanical stability of pulmonary surfactant films. *Biophys J* 99(10):3290-3299.
275. Rugonyi, S., S. C. Biswas, and S. B. Hall. 2008. The biophysical function of pulmonary surfactant. *Respiratory physiology & neurobiology* 163(1-3):244-255.

276. Andreev, K., M. W. Martynowycz, I. Kuzmenko, W. Bu, S. B. Hall, and D. Gidalevitz. 2020. Structural Changes in Films of Pulmonary Surfactant Induced by Surfactant Vesicles. *Langmuir* 36(45):13439-13447.
277. Diemel, R. V., M. M. Snel, A. J. Waring, F. J. Walther, L. M. van Golde, G. Putz, H. P. Haagsman, and J. J. Batenburg. 2002. Multilayer Formation upon Compression of Surfactant Monolayers Depends on Protein Concentration as Well as Lipid Composition AN ATOMIC FORCE MICROSCOPY STUDY. *J. Biol. Chem.* 277(24):21179-21188.
278. Yu, S. H., and F. Possmayer. 2003. Lipid compositional analysis of pulmonary surfactant monolayers and monolayer-associated reservoirs. *Journal of lipid research* 44(3):621-629.
279. Alonso, C., T. Alig, J. Yoon, F. Bringezu, H. Warriner, and J. A. Zasadzinski. 2004. More than a monolayer: relating lung surfactant structure and mechanics to composition. *Biophys J* 87(6):4188-4202.
280. Bachofen, H., U. Gerber, P. Gehr, M. Amrein, and S. Schurch. 2005. Structures of pulmonary surfactant films adsorbed to an air-liquid interface in vitro. *Biochimica et biophysica acta* 1720(1-2):59-72.
281. Schurch, S., R. Qanbar, H. Bachofen, and F. Possmayer. 1995. The surface -associated surfactant reservoir in the alveolar lining. *Biol Neonate* 67:61-76.
282. Martínez-Calle, M., E. Parra-Ortiz, A. Cruz, B. Olmeda, and J. Pérez-Gil. 2021. Towards the Molecular Mechanism of Pulmonary Surfactant Protein SP-B: At the Crossroad of Membrane Permeability and Interfacial Lipid Transfer. *Journal of molecular biology* 433(3):166749.

283. Sachan, A. K., and J. A. Zasadzinski. 2018. Interfacial curvature effects on the monolayer morphology and dynamics of a clinical lung surfactant. *Proceedings of the National Academy of Sciences of the United States of America* 115(2):E134-E143.
284. Chavarha, M., R. W. Loney, S. B. Rananavare, and S. B. Hall. 2015. Hydrophobic surfactant proteins strongly induce negative curvature. *Biophys J* 109(1):95-105.
285. Amrein, M., A. von Nahmen, and M. Sieber. 1997. A scanning force- and fluorescence light microscopy study of the structure and function of a model pulmonary surfactant. *European biophysics journal : EBJ* 26(5):349-357.
286. Galla, H. J., N. Bourdos, A. Von Nahmen, M. Amrein, and M. Sieber. 1998. The role of pulmonary surfactant protein C during the breathing cycle. *Thin Solid Films* 327-329(1-2):632-635.
287. Fan, Q., Y. E. Wang, X. Zhao, J. S. Loo, and Y. Y. Zuo. 2011. Adverse biophysical effects of hydroxyapatite nanoparticles on natural pulmonary surfactant. *ACS Nano* 5(8):6410-6416.
288. Xu, L., Y. Yang, J. M. Simien, C. Kang, G. Li, X. Xu, E. Haglund, R. Sun, and Y. Y. Zuo. 2022. Menthol in electronic cigarettes causes biophysical inhibition of pulmonary surfactant. *American Journal of Physiology-Lung Cellular and Molecular Physiology* 323(2):L165-L177.
289. Graham, E., L. McCaig, G. Shui-Kei Lau, A. Tejura, A. Cao, Y. Y. Zuo, and R. Veldhuizen. 2022. E-cigarette aerosol exposure of pulmonary surfactant impairs its surface tension reducing function. *PLoS ONE* 17(11):e0272475.

290. Chen, Y., Y. Yang, B. Xu, S. Wang, B. Li, J. Ma, J. Gao, Y. Y. Zuo, and S. Liu. 2017. Mesoporous carbon nanomaterials induced pulmonary surfactant inhibition, cytotoxicity, inflammation and lung fibrosis. *Journal of environmental sciences* 62:100-114.
291. Da Silva, E., U. Vogel, K. S. Hougaard, J. Pérez-Gil, Y. Y. Zuo, and J. B. Sørli. 2021. An adverse outcome pathway for lung surfactant function inhibition leading to decreased lung function. *Current research in toxicology* 2:225-236.
292. Ochs, M. 2010. The closer we look the more we see? Quantitative microscopic analysis of the pulmonary surfactant system. *Cellular physiology and biochemistry : international journal of experimental cellular physiology, biochemistry, and pharmacology* 25(1):27-40.
293. Goerke, J. 1998. Pulmonary surfactant: Functions and molecular composition. *Biochimica et biophysica acta* 1408(2-3):79-89.
294. Yao, H., Y. Song, Y. Chen, N. Wu, J. Xu, C. Sun, J. Zhang, T. Weng, Z. Zhang, Z. Wu, L. Cheng, D. Shi, X. Lu, J. Lei, M. Crispin, Y. Shi, L. Li, and S. Li. 2020. Molecular Architecture of the SARS-CoV-2 Virus. *Cell* 183(3):730-738.e713.
295. Hoffmann, M., H. Kleine-Weber, S. Schroeder, N. Krüger, T. Herrler, S. Erichsen, T. S. Schiergens, G. Herrler, N.-H. Wu, A. Nitsche, M. A. Müller, C. Drosten, and S. Pöhlmann. 2020. SARS-CoV-2 Cell Entry Depends on ACE2 and TMPRSS2 and Is Blocked by a Clinically Proven Protease Inhibitor. *Cell* 181(2):271-280.e278.
296. Turoňová, B., M. Sikora, C. Schürmann, W. J. H. Hagen, S. Welsch, F. E. C. Blanc, S. v. Bülow, M. Gecht, K. Bagola, C. Hörner, G. v. Zandbergen, J. Landry, N. T. D. d. Azevedo, S. Mosalaganti, A. Schwarz, R. Covino, M. D. Mühlebach, G. Hummer, J. K. Locker, and M. Beck. 2020. In situ structural analysis of SARS-CoV-2 spike reveals flexibility mediated by three hinges. *Science* 370(6513):203-208.

297. Ou, X., Y. Liu, X. Lei, P. Li, D. Mi, L. Ren, L. Guo, R. Guo, T. Chen, J. Hu, Z. Xiang, Z. Mu, X. Chen, J. Chen, K. Hu, Q. Jin, J. Wang, and Z. Qian. 2020. Characterization of spike glycoprotein of SARS-CoV-2 on virus entry and its immune cross-reactivity with SARS-CoV. *Nature Communications* 11(1):1620.
298. Jackson, C. B., M. Farzan, B. Chen, and H. Choe. 2022. Mechanisms of SARS-CoV-2 entry into cells. *Nature Reviews Molecular Cell Biology* 23(1):3-20.
299. Meyer, N. J., L. Gattinoni, and C. S. Calfee. 2021. Acute respiratory distress syndrome. *The Lancet* 398(10300):622-637.
300. Hamming, I., W. Timens, M. Bulthuis, A. Lely, G. Navis, and H. van Goor. 2004. Tissue distribution of ACE2 protein, the functional receptor for SARS coronavirus. A first step in understanding SARS pathogenesis. *The Journal of Pathology* 203(2):631-637.
301. Hsieh, M.-H., N. Beirag, V. Murugaiah, Y.-C. Chou, W.-S. Kuo, H.-F. Kao, T. Madan, U. Kishore, and J.-Y. Wang. 2021. Human Surfactant Protein D Binds Spike Protein and Acts as an Entry Inhibitor of SARS-CoV-2 Pseudotyped Viral Particles. *Frontiers in Immunology* 12. Original Research.
302. Madan, T., B. Biswas, P. M. Varghese, R. Subedi, H. Pandit, S. Idicula-Thomas, I. Kundu, S. Rooge, R. Agarwal, D. M. Tripathi, S. Kaur, E. Gupta, S. K. Gupta, and U. Kishore. 2021. A Recombinant Fragment of Human Surfactant Protein D Binds Spike Protein and Inhibits Infectivity and Replication of SARS-CoV-2 in Clinical Samples. *American journal of respiratory cell and molecular biology* 65(1):41-53.
303. Schousboe, P., A. Ronit, H. B. Nielsen, T. Benfield, L. Wiese, N. Scoutaris, H. Verder, R. M. G. Berg, P. Verder, and R. R. Plovsing. 2022. Reduced levels of pulmonary surfactant in COVID-19 ARDS. *Scientific Reports* 12(1):4040.

304. Herman, L., S. C. De Smedt, and K. Raemdonck. 2022. Pulmonary surfactant as a versatile biomaterial to fight COVID-19. *Journal of controlled release : official journal of the Controlled Release Society* 342:170-188.
305. Piva, S., R. M. DiBlasi, A. E. Slee, A. H. Jobe, A. M. Roccaro, M. Filippini, N. Latronico, M. Bertoni, J. C. Marshall, and M. A. Portman. 2021. Surfactant therapy for COVID-19 related ARDS: a retrospective case–control pilot study. *Respiratory Research* 22(1):20.
306. Heching, M., S. Lev, D. Shitenberg, D. Dicker, and M. R. Kramer. 2021. Surfactant for the Treatment of ARDS in a Patient With COVID-19. *CHEST* 160(1):e9-e12.
307. Cai, Y., J. Zhang, T. Xiao, H. Peng, S. M. Sterling, R. M. Walsh, S. Rawson, S. Rits-Volloch, and B. Chen. 2020. Distinct conformational states of SARS-CoV-2 spike protein. *Science* 369(6511):1586-1592.
308. Gorgun, D., M. Lihan, K. Kapoor, and E. Tajkhorshid. 2021. Binding mode of SARS-CoV-2 fusion peptide to human cellular membrane. *Biophysical journal* 120(14):2914-2926.
309. Schaefer, S. L., H. Jung, and G. Hummer. 2021. Binding of SARS-CoV-2 Fusion Peptide to Host Endosome and Plasma Membrane. *The Journal of Physical Chemistry B* 125(28):7732-7741.
310. Zhang, H., Q. Fan, Y. E. Wang, C. R. Neal, and Y. Y. Zuo. 2011. Comparative study of clinical pulmonary surfactants using atomic force microscopy. *Biochimica et biophysica acta* 1808(7):1832-1842.
311. Bachofen, H., S. Schurch, M. Urbinelli, and E. R. Weibel. 1987. Relations among alveolar surface tension, surface area, volume, and recoil pressure. *Journal of Applied Physiology* 62(5):1878-1887.

312. Zhang, H., Y. E. Wang, Q. Fan, and Y. Y. Zuo. 2011. On the Low Surface Tension of Lung Surfactant. *Langmuir* 27(13):8351-8358.
313. Yang, S.-T., V. Kiessling, and L. K. Tamm. 2016. Line tension at lipid phase boundaries as driving force for HIV fusion peptide-mediated fusion. *Nature Communications* 7(1):11401.
314. Risselada, H. J., G. Marelli, M. Fuhrmans, Y. G. Smirnova, H. Grubmüller, S. J. Marrink, and M. Müller. 2012. Line-Tension Controlled Mechanism for Influenza Fusion. *PLOS ONE* 7(6):e38302.
315. Xia, S., Y. Zhu, M. Liu, Q. Lan, W. Xu, Y. Wu, T. Ying, S. Liu, Z. Shi, S. Jiang, and L. Lu. 2020. Fusion mechanism of 2019-nCoV and fusion inhibitors targeting HR1 domain in spike protein. *Cellular & Molecular Immunology* 17(7):765-767.
316. Castillo-Sánchez, J. C., A. Cruz, and J. Pérez-Gil. 2021. Structural hallmarks of lung surfactant: Lipid-protein interactions, membrane structure and future challenges. *Archives of Biochemistry and Biophysics* 703:108850.
317. Marsh, D. 1996. Lateral pressure in membranes. *Biochimica et biophysica acta* 1286(3):183-223.
318. Koppiseti, R. K., Y. G. Fulcher, and S. R. Van Doren. 2021. Fusion Peptide of SARS-CoV-2 Spike Rearranges into a Wedge Inserted in Bilayered Micelles. *Journal of the American Chemical Society* 143(33):13205-13211.
319. Santamaria, A., K. C. Batchu, O. Matsarskaia, S. F. Prévost, D. Russo, F. Natali, T. Seydel, I. Hoffmann, V. Laux, M. Haertlein, T. A. Darwish, R. A. Russell, G. Corucci, G. Fragneto, A. Maestro, and N. R. Zaccai. 2022. Strikingly Different Roles of SARS-CoV-2 Fusion

- Peptides Uncovered by Neutron Scattering. *Journal of the American Chemical Society* 144(7):2968-2979.
320. Guillén, J., R. F. M. d. Almeida, M. Prieto, and J. Villalaín. 2008. Structural and Dynamic Characterization of the Interaction of the Putative Fusion Peptide of the S2 SARS-CoV Virus Protein with Lipid Membranes. *The Journal of Physical Chemistry B* 112(23):6997-7007.